

---

# Crystal structure of fiber structured pentacene thin films

Stefan Schiefer

---



München 2007



---

# **Crystal structure of fiber structured pentacene thin films**

**Stefan Schiefer**

---

Dissertation  
an der Fakultät für Physik  
der Ludwig–Maximilians–Universität  
München

vorgelegt von  
Stefan Schiefer  
aus Freilassing (Obb.)

München, den 31.07.2007

Erstgutachter: Prof. Dr. Joachim Rädler

Zweitgutachter: Prof. Dr. Wolfgang Schmahl

Tag der mündlichen Prüfung: 22.10.2007

# Contents

<b>Summary</b>	<b>1</b>
<b>1 Introduction and Motivation</b>	<b>3</b>
1.1 Organic semiconductors	3
1.2 Crystal structure of organic molecules	6
1.3 Pentacene, a promising organic semiconductor	9
1.4 Aim of this thesis	10
<b>2 Sample preparation</b>	<b>13</b>
2.1 Cleaning procedures of Si wafers	13
2.1.1 RCA cleaning	13
2.1.2 Plasma cleaning	15
2.2 Spin coating of polymeric thin films	15
2.3 Gate dielectric materials	16
2.3.1 Amorphous silicon dioxide ( $a - SiO_2$ )	16
2.3.2 Octadecyltrichlorosilane (OTS) treated $a - SiO_2$	16
2.3.3 Topas	17
2.3.4 Polystyrene	18
2.4 Characterization by X-ray reflectivity and AFM	19
2.4.1 Atomic force microscopy	19
2.4.2 Specular X-ray reflectivity	21
2.4.3 In-house 4-circle X-ray setup	23
2.4.4 Results	24
2.4.5 Summary	32
2.5 Organic molecular beam deposition (OMBD)	32
2.5.1 Purification of pentacene	33
2.5.2 Portable, ultra high vacuum growth chamber (PGC)	34
2.5.3 OMBD of pentacene thin films	44
<b>3 Solving the crystal structure of a fiber structured thin film</b>	<b>49</b>
3.1 Kinematical theory of X-ray diffraction	49
3.1.1 Crystal axes and the reciprocal lattice	49
3.1.2 Diffraction intensity of a thin film	55

---

3.1.3	Diffraction intensity of a pentacene thin film . . . . .	57
3.2	Experimental setup and measurement techniques . . . . .	65
3.2.1	HASYLab beamline W1 setup . . . . .	65
3.2.2	X-ray measurement techniques . . . . .	70
3.2.3	Diffraction intensity correction factors . . . . .	75
3.3	Implementation in Matlab . . . . .	83
3.3.1	Solving the unit-cell using FiberRod . . . . .	85
3.3.2	Solving the molecular orientation using FiberRod . . . . .	88
<b>4</b>	<b>Results</b>	<b>93</b>
4.1	Crystal structure on $a - SiO_2$ substrate . . . . .	93
4.2	Crystal structure on OTS substrate . . . . .	98
4.3	Crystal structure on Topas substrate . . . . .	98
4.4	Crystal structure on PS substrate . . . . .	101
<b>5</b>	<b>Discussion</b>	<b>107</b>
5.1	Crystal structure . . . . .	107
5.2	Charge transport mechanism . . . . .	108
<b>6</b>	<b>Outlook</b>	<b>115</b>
<b>A</b>	<b>Detailed Parratt32 fit results</b>	<b>117</b>
<b>B</b>	<b>Detailed fit results of Bragg peak positions</b>	<b>125</b>
<b>C</b>	<b>Cif files of pentacene <i>thin-film</i> polymorphs</b>	<b>129</b>
C.1	Cif Header . . . . .	129
C.2	Atomic positions for $a - SiO_2$ substrate . . . . .	131
C.3	Atomic positions for OTS substrate . . . . .	131
C.4	Atomic positions for Topas substrate . . . . .	132
C.5	Atomic positions for polystyrene substrate . . . . .	133
C.6	Comments on cif file checking . . . . .	134
<b>D</b>	<b>Publications</b>	<b>135</b>
	<b>Bibliography</b>	<b>137</b>
	<b>Acknowledgement</b>	<b>155</b>

# Summary

This PhD thesis presents a technique based on the grazing incidence crystal truncation rod (GI-CTR) X-ray diffraction method used to solve the crystal structure of substrate induced fiber structured organic thin films. The crystal structures of pentacene thin films grown on technologically relevant gate dielectric substrates are reported.

It is widely recognized, that the intrinsic charge transport properties in organic thin film transistors (OTFTs) depend strongly on the crystal structure of the organic semiconductor layer. Pentacene, showing one of the highest charge carrier mobilities among organic semiconductors, is known to crystallize in at least four polymorphs, which can be distinguished by their layer periodicity  $d_{(001)}$ . Only two polymorphs (14.4 Å and 14.1 Å), grow as single crystals and their detailed crystal structure has been solved with standard crystallography techniques. The substrate induced 15.4 Å polymorph, the so called pentacene *thin-film* phase, is the most relevant for OTFT applications, since it grows at room temperature on technologically relevant gate dielectrics. However, the crystal structure of the pentacene *thin-film* phase has remained incomplete as it only grows as a fiber structured thin film. In this thesis, the GI-CTR X-ray diffraction technique is extended to fiber structured thin films. The X-ray diffraction experiments were carried out at the synchrotron source beamline W1 at HASYLAB in Hamburg, in order to obtain enough diffraction data for the determination of the crystal structure as pentacene thin films only grow as ultra thin films with crystal grains as small as 0.4  $\mu\text{m}$ . Pentacene thin films are also known to be sensitive to environmental conditions, such as light and oxygen. For this reason, the X-ray synchrotron measurements were performed in-situ. A portable ultra high vacuum growth chamber equipped with a rotatable sample holder and a beryllium window was built in order to perform X-ray measurements of up to four samples right after the thin film growth process without breaking the vacuum. Parallel to this, a versatile software package coded with Matlab in order to simulate, analyze and fit the complex data measured at the synchrotron source was developed. The complete crystal structure of the 15.4 Å pentacene *thin-film* polymorph grown on four model types of gate dielectric materials, amorphous silicon dioxide ( $a - \text{SiO}_2$ ), octadecyltrichlorosilane-treated  $a - \text{SiO}_2$  (OTS), Topas (“thermoplastic olefin polymer of amorphous structure”) and polystyrene films, was solved. It was found, that the unit cell parameters are identical within measurement precision on all measured substrates. The crystal structure belongs to the space group P-1 and was found to be triclinic with the following lattice parameters:  $a = 5.958 \pm 0.005 \text{ \AA}$ ,  $b = 7.596 \pm 0.008 \text{ \AA}$ ,  $c = 15.61 \pm 0.01 \text{ \AA}$ ,  $\alpha = 81.25 \pm 0.04^\circ$ ,  $\beta = 86.56 \pm 0.04^\circ$  and

$\gamma = 89.80 \pm 0.10^\circ$ . The unit cell volume  $V = 697 \text{ \AA}^3$  is the largest of all pentacene polymorphs reported so far. However, the molecular arrangement within the unit cell was found to be substrate dependent. Here, the following parameters are reported: The herringbone angle ( $\theta_{hr gb}$ ) is  $54.3^\circ$ ,  $55.8^\circ$ ,  $59.4^\circ$  and  $55.1^\circ$  for  $a - SiO_2$ , OTS, Topas and polystyrene, respectively. The tilts of the two molecular axes ( $\varphi_A, \varphi_B$ ) are  $(5.6^\circ, 6.0^\circ)$ ,  $(6.4^\circ, 6.8^\circ)$ ,  $(5.6^\circ, 6.3^\circ)$  and  $(5.7^\circ, 6.0^\circ)$  for  $a - SiO_2$ , OTS, Topas and polystyrene, respectively.

To conclude, it was shown that the molecular orientation in the unit cell differs among substrates while the unit cell dimensions of the  $15.4 \text{ \AA}$  pentacene polymorph are identical. This indicates that substrate effects have to be included if one aims on understanding the molecular structure of the *thin-film* phase in detail. The crystal structures reported here provide a basis to apply techniques such as density functional methods to investigate intrinsic charge transport properties and optical properties of organic thin film devices on a molecular level. In previous studies it was observed that different substrates vary the charge carrier mobility in OTFTs. The substrate dependent crystal structures observed here could be one reason for this variation. This topic may lead ultimately to a controlled fine-tuning of intrinsic charge transport properties. The experimental approach to determine the crystal structure developed here can be easily applied to a wide range of organic thin film systems used in organic electronic devices.



# Chapter 1

## Introduction and Motivation

### 1.1 Organic semiconductors

Organic semiconductors can be divided into two groups, small molecules and polymers. For a long time, polymers were thought of as insulators, because their electrical conductivity was observed to be as low as  $< 10^{-5} S/cm$ . But in 1976, Heeger, MacDiarmid and Shirakawa discovered conducting polymers and a way to dope these polymers from insulator to metal[8, 9]. This discovery was awarded in 2000 the Nobel prize for chemistry, because it created a new field of research and offered the promise of achieving a new generation of polymers: Materials which exhibit the electrical and optical properties of semiconductors and which retain the attractive mechanical properties and low cost processing advantages of polymers. Scientists and industry all over the world were attracted to this new field of organic semiconductors. The scientists were attracted mainly because of intellectual interests and to gain insight into the conduction mechanism of these new materials, industry was attracted because these materials promised utility in a wide variety of applications. The standard silicon based semiconductor technology requires clean rooms and high temperature processing, which makes the process rather expensive, whereas most of the polymers can be dissolved and can therefore be spin coated, which makes the processing much cheaper, especially when high volumes or large areas are needed. Promising applications include radio frequency identification tags (RFID tags), large-area lighting, flexible flat panel displays and electronic papers, which are illustrated in figure 1.1.

An RFID tag is an object that can be attached to or incorporated into a product, animal, or person for the purpose of identification using radio waves. The production costs of conventional silicon-based RFID tags are still too high to replace bar codes that are currently used for large volume applications like “over the counter” products. RFID tags made from polymer semiconductors are currently being developed by several companies globally and prototypes have already been demonstrated by PolyIC (Germany) and Philips (The Netherlands). If successfully commercialized, polymer tags will be roll-printable, like a magazine, and much less expensive than silicon-based tags.

Electronic reusable paper is a polymer display material that has many of the properties

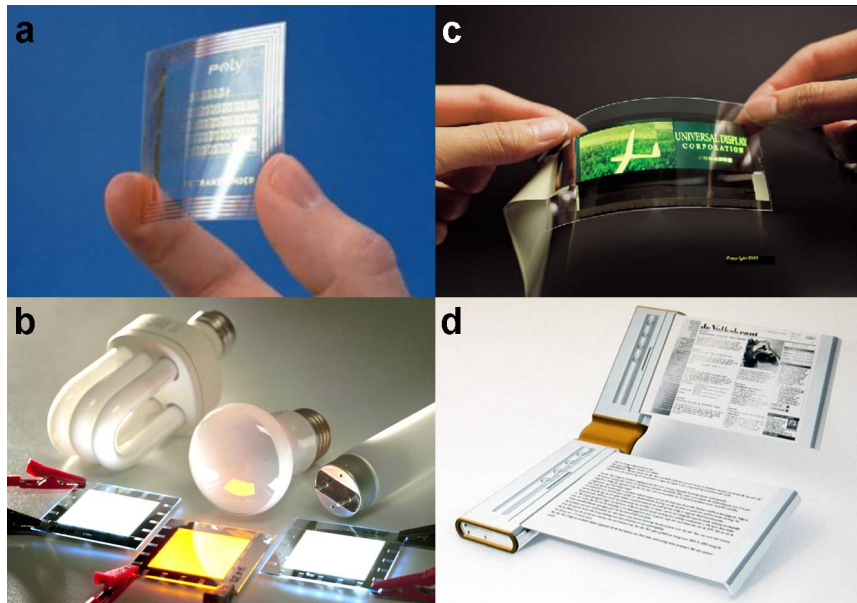


Figure 1.1: a) Passive polymer RFID tag (Source: PolyIC). b) Four generations of lighting technologies: incandescent light bulb, fluorescent, compact fluorescent and the new Organic Light Emitting Diode in different colors (Source: Philips). c) Flexible Display (Source: Universal Display Corporation). d) Electronic paper device (Source: Philips).

of paper. It stores an image, is viewed in reflective light, has a wide viewing angle, is rollable, is as thin as paper and is relatively inexpensive. Unlike conventional paper, however, it is electrically writable and erasable. This material has many potential applications in the field of information display including always up-to-date newspapers, digital books and wall-sized displays. A flexible flat panel display has the same properties as electronic paper, except that it is not a light modulating device, but a light emitting device which requires the use of organic light emitting diodes (OLEDs). Many companies like Polymer Vision are currently working on mass production processes of electronic paper and flexible displays.

IDTechEx estimates that organic electronics will be a \$30 billion dollar business in 2015 mainly due to logic, displays and lighting. It will be a \$250 billion dollar business in 2025, with sales from logic, memory, displays for electronic products, billboard, signage etc, non-emissive organic displays, lighting, batteries and photovoltaics. Almost all of these products will be printed, flexible, laminar constructions using the same or similar processes. However, Henning Sirringhaus, a Cambridge University physicist who co founded Plastic Logic, recently stated in a February 2007 interview with MIT Technology Review: "Silicon is so advanced and sophisticated, that it's hard to see how plastic electronics could replace it. So it seems inevitable that the polymer-electronic startups will have to stick with flexible applications, where silicon is unable to compete."

Almost all of these applications employ either organic thin film transistors (OTFTs), organic light emitting diodes or both. To be used for device applications, the organic

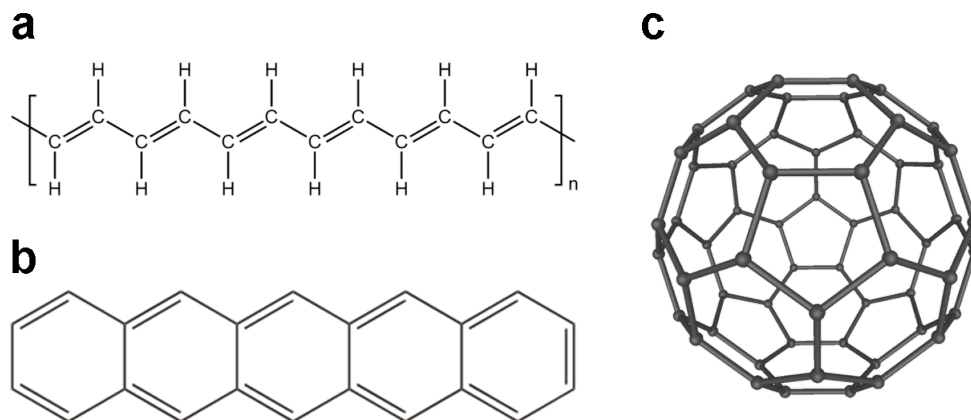


Figure 1.2: Lewis structure of a) polyacetylene b) pentacene and c) C60.

materials have to attain minimal conductivity values. If conduction is low, impractical high voltages are needed to operate these devices. Hence, the most important performance factors of an OTFT are the charge carrier mobility  $\mu$  and the stability of the active organic layer. The first OTFT based on polythiophene was fabricated in 1986[10], but the carrier mobility  $\mu = 10^{-5} \text{ cm}^2/\text{Vs}$  was too low for practical use. It has been stated, that  $\mu$  should be in the range of  $\sim 1 \text{ cm}^2/\text{V} \cdot \text{s}$ , a value which is common for the well established amorphous silicon (a-Si:H) technology, that is currently used for large-area applications like TFT displays and photovoltaics. In the last 20 years, there has been an impressive increase in charge carrier mobility, which came about either by improving the processes used for the fabrication of the transistors or by synthesizing new organic materials. However, charge carrier mobilities on the order of  $\sim 1 \text{ cm}^2/\text{V} \cdot \text{s}$  and even above could only be achieved by small organic molecules and not by polymers. Both polymers and molecular conductors are conjugated materials, i.e. they have alternating single and double bonds in their chemical structure. One of the most promising materials is pentacene (shown in figure 1.2b), which exhibits charge carrier mobilities of up to  $\sim 3 \text{ cm}^2/\text{V} \cdot \text{s}$  [11]. In this material the chemical bonding leads to one unpaired electron (the  $\pi$ -electron) per carbon atom. Moreover,  $\pi$ -bonding, in which the carbon orbitals are in  $sp^2p_z$  configuration and the orbitals of successive carbon atoms overlap, leads to electron delocalization along the molecule. This  $\pi$ -system is responsible for an important part of the intramolecular conduction. In polymers, the intramolecular transport is very important and the long conjugated length of the chains (shown in figure 1.2a) provides the “highway” for charge carrier mobility along the backbone of the polymer chain. However, polymer thin films are typically amorphous and considered to be rather disordered systems. This makes modeling of the intra and intermolecular transport difficult.

In small organic conducting molecules, the conductivity is determined by the intermolecular transport. Unlike polymers, these molecular conductors often form ordered crystal structures. This opens up the possibility to relate the observed electronic properties to the crystal structure [3, 12, 13, 14], which is a powerful method to get insight in

the intrinsic charge transport processes.

Molecular conductors have been studied since the 1950s [15]. In the mid 1970s the high conductivity and superconductivity of TTF-TCNQ<sup>1</sup> renewed the interest in these organic materials. In 1985 the buckminsterfullerene  $C_{60}$  (shown in figure 1.2c) was discovered, which gained big attention in the 1990s, as this material was shown to become metallic and even superconducting with doping [16].

Various techniques like pulsed laser deposition, vacuum evaporation and processing from solution [17, 18, 19, 20] have been used to induce high crystalline order in the thin films of molecular conductors. High vacuum sublimation is a technique which is often used to prepare thin films. The vacuum prevents, to a certain degree, the inclusion of impurities in the material. Having a well defined structure makes the material a model system for the study of the intrinsic charge transport. The presence of chemical defects and impurities, however, masks the intrinsic physical properties, like the charge transport [21].

## 1.2 Crystal structure of organic molecules

To investigate the intrinsic charge transport properties in organic crystals by numerical methods, the crystal structure has to be determined. Depending on the growth method, organic materials can have high crystallinity in thin films (figure 1.3) and even single crystals with a size in the order of  $\sim 1\text{ cm}$  have been grown. However, it is still not possible to predict the structure in which they crystallize.

While interactions between the atoms in covalent and ionic crystals are strong, in covalent crystals, the electron pairs are shared between atoms, resulting in an electronic distribution which has localized preferred directions. For example in diamond, all carbon atoms participate in four covalent bonds, which form tetrahedrons with fixed angles. In ionic crystals, the ions can be approximated as charged spheres, which are bonded by electrostatic interaction. Due to the spherical nature of the atom and the relatively strong interactions between them, these crystals can be seen as a formation of closely packed anions (cations) with the cations (anions) filling the tetrahedral and octahedral holes.

The crystal structures formed by organic and inorganic materials are quite different. Organic materials form their crystal structure not by atoms, but by weakly bonded molecules. In ionic and covalent crystals, the atomic positions can be predicted by the strong interactions and the spherical nature of the atoms. In organic molecular crystals, such an approach is in general not possible, partly due to the complicated shape of the molecules and partly because of the presence of chemical forces which are on the same order as the weak bonds. Those crystals are so called *van der Waals crystals*, as the crystal structure is mainly formed by this weak force.

Nevertheless, Gavezotti et. al. performed a database study on the crystal structure formed by several representative aromatic hydrocarbons. These compounds have been chosen since they adopt a few sharply defined packing types. They are planar or almost

---

<sup>1</sup>Tetrathiafulvalenium tetracyanoquinodimethane

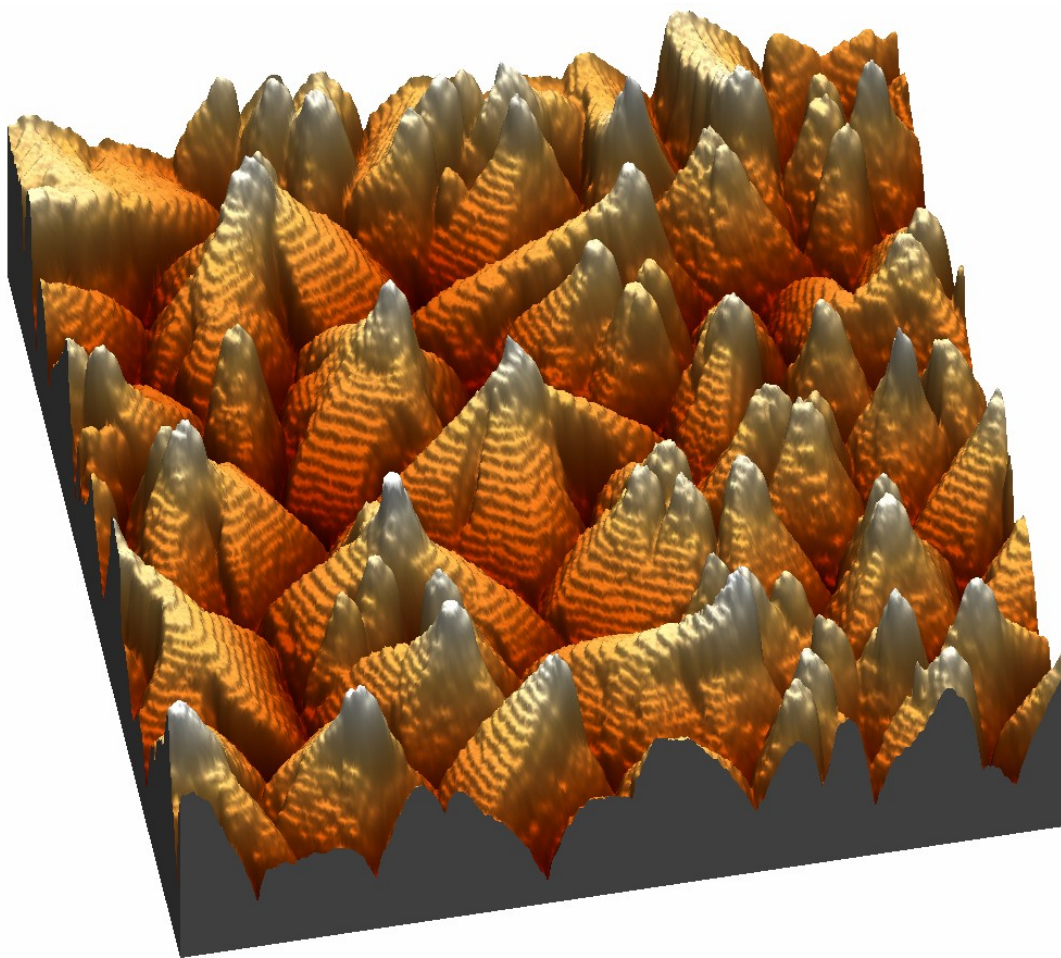


Figure 1.3: 3D Atomic force microscopy (AFM) micrograph of a 480 Å pentacene thin film on a Topas substrate. Edge length is  $5\ \mu\text{m}$ . The crystalline areas (grains) with a diameter of  $\sim 2\ \mu\text{m}$  are clearly visible. Terrace height corresponds to a pentacene monolayer with a  $d_{(001)}$  spacing of 15.4 Å. The crystal grains are forming a typical fiber structure. The fiber axes are parallel to the substrate surface normal. Also clearly visible is the surface roughness, that characteristically shapes the whole thin film.

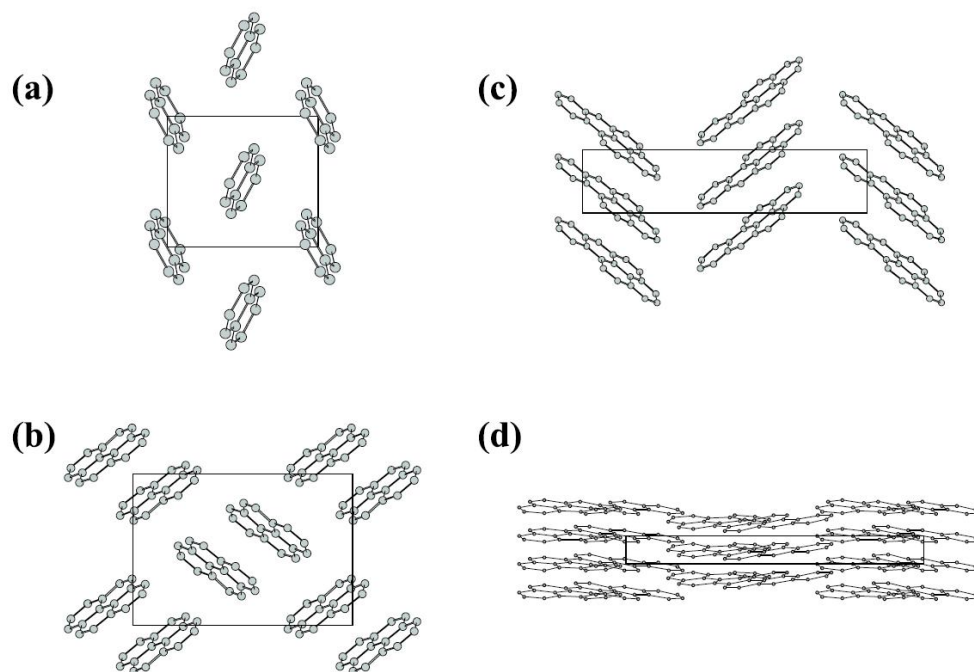


Figure 1.4: The four crystal packings observed for (almost) planar aromatic hydrocarbon crystals. a) Classical herringbone structure (Naphthalene) b) Sandwich herringbone (Pyrene) c)  $\gamma$ -structure (Benzopyrene) d)  $\beta$ -structure (Violanthrene).

planar molecules and this lack of conformational flexibility allows a clear-cut definition of molecular shape. Based on this study, four basic structural types for aromatic hydrocarbons were defined [22, 23]. These basic structural types are all layered structures and may be clearly differentiated by geometrical criteria (shown in figure 1.4). The simplest pattern is the herringbone structure, where the molecules are arranged on alternating angles. A classic example is Naphthalene shown in figure 1.4a. In the second type, called “sandwich herringbone” or “sandwich”, the herringbone motif is made up of two molecules. This structure is adopted by Pyrene, shown in figure 1.4b. In the third type, the herringbone structure is flattened in one direction, giving a  $\gamma$ -structure. Benzopyrene exhibits this structure and is illustrated in figure 1.4c. The last type, the  $\beta$ -structure, is a layered structure made up of “graphitic” planes. Violanthrene grows in this orientation and is illustrated in figure 1.4d.

The geometrical criteria used to distinguish between these crystal structures are the length of the shortest axis and the angle between the molecules. The length of the shortest axis is increased in order rank as follows:  $\beta$ -structure,  $\gamma$ -structure, herringbone structure and sandwich herringbone structure. Some general trends could be identified for the preferred crystal structure of aromatic hydrocarbons [23]: elongated molecules with H-atoms on the rim prefer herringbone structure, while disk shaped molecules mainly crystallize in

$\beta$ -structures. The study also shows that the relative strength of the interactions between the molecules are a driving force for the adoption of a specific crystal structure. There are two main interactions between two molecules in organic thin films: C-C and C-H interactions. C-C interactions induce parallel stacking, while C-H interactions induce herringbone stacking. For  $\gamma$  and  $\beta$ -structures C-C interactions are dominant, while in herringbone and sandwich herringbone structures C-H interactions are dominant. C-C interactions are associated with  $\pi$ -system interactions of neighboring molecules, while C-H interactions are associated with weak bonds between hydrogens of one molecule and a  $\pi$ -system of a neighboring molecule. However, a clear-cut prediction of the structure is difficult, since organic molecules often show polymorphism, i.e. they crystallize in various structures.

### 1.3 Pentacene, a promising organic semiconductor

Among the various materials used for OTFTs, pentacene has been established as a model system, as it readily forms polycrystalline thin films with a charge carrier mobility among the highest reported for an organic semiconductor [24]. In this thesis, the crystal structure and the relation to charge transport properties of pentacene (figure 1.2b) is studied. Pentacene is known to crystallize in at least four polymorphs, which can be distinguished by their layer periodicity[4]  $d_{(001)}$ : 14.1, 14.4, 15.0 and 15.4 Å. The first analysis of the crystal structure of pentacene was done by Campbell et.al. in 1961 [25, 26] and slightly modified in 1962. The single crystals used in his study were grown from solution and yielded a characteristic  $d_{(001)}$  value of 14.4 Å. In 1991, Minakata et.al. reported  $d_{(00l)}$  values of 15.0 and 15.4 Å for thin films [27, 28]. It was not until 1996 that Dimitrakopoulos et.al. noticed, that these thin film polymorphs are different from the single crystal phase determined by Campbell [29]. They also observed the coexistence of two phases, the 14.4 Å and 15.4 Å, which they called the “single crystalline phase” or “bulk phase” and the “thin film phase” respectively. These former names are incorrect as more recent studies showed, that the single crystal structure has a  $d_{(001)}$  value of 14.1 Å [30, 31] and that all four pentacene polymorphs can be grown in thin film form, depending on the growth conditions [4]. The 14.1 Å single crystal phase was first solved by Homes et. al. [30] and confirmed by Mattheus et.al. [31].

The 15.0 and 15.4 Å polymorphs are substrate induced, as they are only observed near the substrate for film thicknesses of up to 50 nm at 300 K. Moreover, they are metastable, as they transform into 14.1 and 14.4 Å polymorphs at elevated temperatures, respectively [4]. The substrate induced 15.4 Å polymorph is the most relevant for OTFT applications, since it grows at room temperature on technologically relevant gate dielectrics. However, the crystal structure of the pentacene *thin-film* phase has remained incomplete as it only grows as a fiber structured thin film[29, 4, 32, 33, 34, 35, 7]. Moreover, in theoretical calculations based on a simulated crystal structure of the *thin-film* phase, it was predicted that the 15.4 Å polymorph is the polymorph of choice when fabricating OTFTs since its mobility tensor is much less isotropic when compared to the other pentacene polymorphs[3].

This PhD thesis presents a technique based on the grazing incidence crystal trunca-

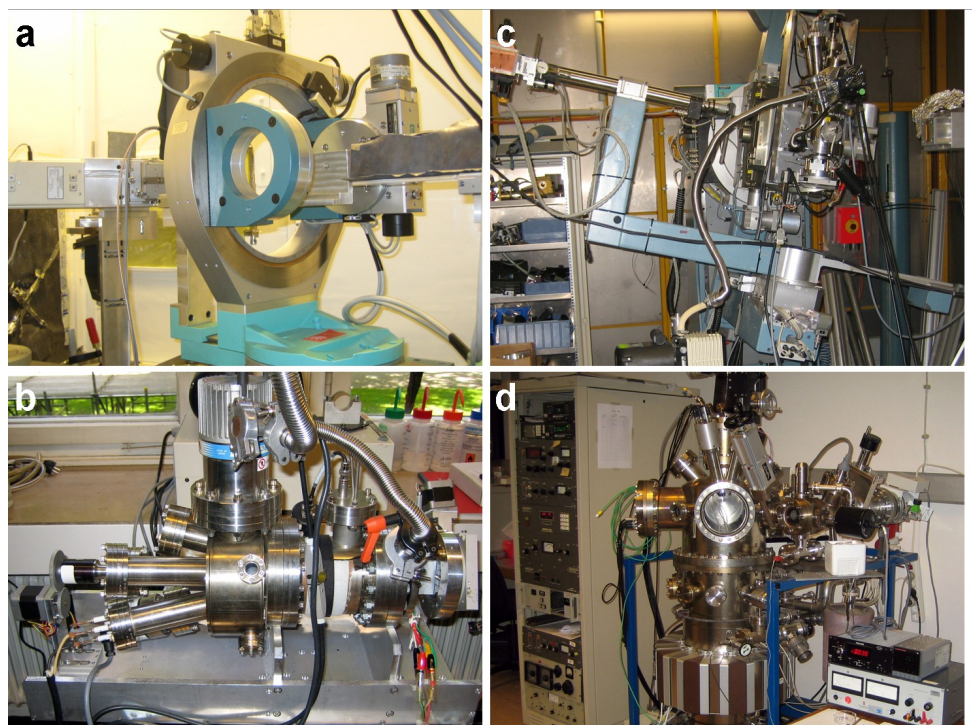


Figure 1.5: Equipment built during this thesis: a) In-house 4-circle X-ray diffractometer. b) Mobile ultra high vacuum growth chamber. c) Mobile ultra high vacuum growth chamber mounted on W1 diffractometer at HASYLab, Hamburg. d) Reconstructed molecular beam deposition chamber.

tion rod (GI-CTR) X-ray diffraction method to solve the crystal structure of substrate induced fiber structured organic thin films. The crystal structures of the 15.4 Å pentacene polymorphs grown on technologically relevant gate dielectric substrates are reported.

## 1.4 Aim of this thesis

A consistent picture of all the processes contributing to charge transport properties can only be gained if different methods with different points of view on the big picture are used. Some methods such as I-V measurements are standard methods already in use for the characterization of inorganic semiconductors. Other methods, like the structural characterization by X-ray diffraction have first to be developed and adopted for the specific properties of organic semiconductors. Since this is a complex and large project on its own, the determination of the crystal structure was carried out within this thesis and aims to provide a basis for a better understanding between the crystal structure of pentacene thin films and its relation to charge transport properties.

Substrates where a thin film of pentacene can be grown and investigated by X-ray diffraction require certain properties such as low surface roughness [36]. To insure a low

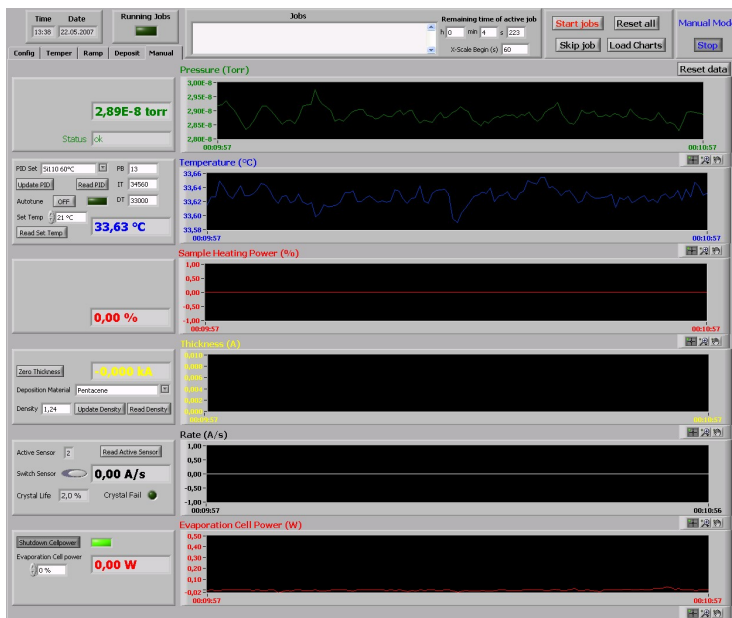


surface roughness, an in-house 4-circle X-ray diffractometer (figure 1.5a) which is controlled by a lab computer using the command-line interface SPEC, was setup in order to perform reflectivity studies from surfaces and thin films.

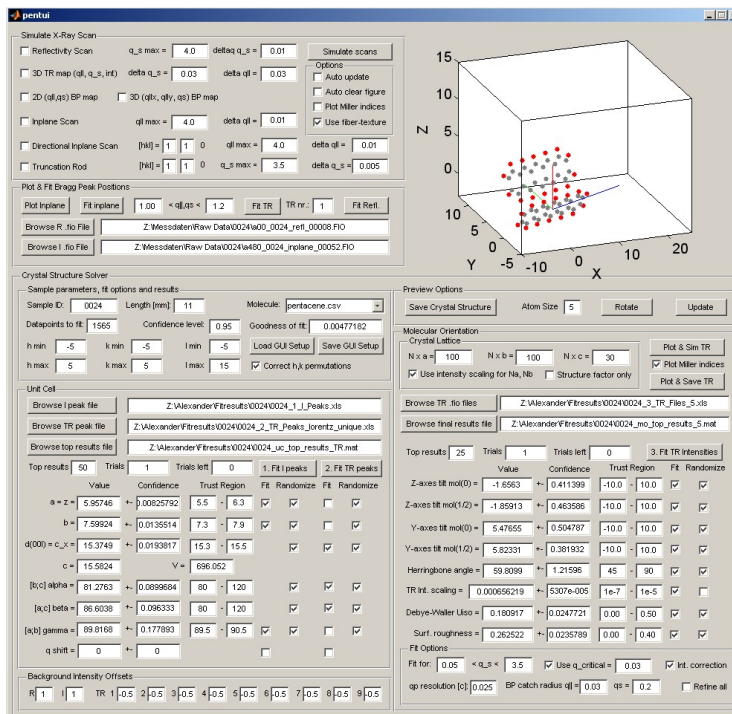
As the 15.4 Å pentacene polymorph investigated in this thesis only grows as an ultra thin film with crystal grains as small as  $0.4\mu m$ , it is inevitable that X-ray measurements must be carried out at a synchrotron source to obtain enough diffraction data for the determination of the crystal structure. Pentacene thin films are also known to be sensitive to environmental conditions, such as light and oxygen. For this reason, X-ray synchrotron measurements were performed in-situ and a portable ultra high vacuum growth chamber was built (PGC, figure 1.5b and c), equipped with a rotatable sample holder and a beryllium window in order to perform X-ray measurements of up to four samples right after the thin film growth process without breaking the vacuum. Many steps were needed to build and operate the custom-made portable growth chamber at the synchrotron. These include the chambers mechanical construction, the electronic circuits and equipment, and the automation by a custom made thin film growth software (figure 1.6a) that had to be built and tested for portable use. Since this is a steady learning process, we went several times a year to the synchrotron source for up to 10 days to test and improve our custom made equipment step by step for in-situ thin film measurements. Parallel to this, we developed a versatile software package with Matlab (figure 1.6b) in order to simulate, analyze and fit the complex data measured at the synchrotron source. This gave us the opportunity to simulate new measurement methods at the synchrotron source in our home lab and test them at the next synchrotron beam time, because beam time slots are too short to develop a new method on-site. There are only a very few groups worldwide, who have all the expertise needed from thin film growth to X-ray diffraction to carry out such a project.

It should be noted, that while the focus of this thesis is on structural properties of pentacene thin films, ideas, data and samples were constantly exchanged with the groups of P. Lugli from the Technische Universität München (modeling and simulation), S. Lochbrunner from the BMO München (optical characterization) and U. Beierlein & J. Kotthaus (electronic characterization), which resulted in a number of joint publications (appendix D). Some of these results will also be discussed in this thesis.

A last project was begun towards the end of this thesis. The molecular beam deposition chamber was customized for in-situ I-V measurements (figure 1.5d) as they can be better related to the intrinsic charge transport properties derived from the crystal structure which was also measured in-situ. The project is being continued by a diploma student, so initial results are expected in summer 2007.



(a)



(b)

Figure 1.6: Screenshots of versatile software packages, that have been developed throughout this thesis. (a) Manual mode of thin film deposition software (TFDS) developed for the portable vacuum growth chamber (PGC) coded with NI LabView 6. (b) Software developed to solve the crystal structure of fiber structured organic thin films by X-ray diffraction.

# Chapter 2

## Sample preparation

A simple bottom contact OTFT consists of a layered structure, where the pentacene layer is grown on the gate dielectric material as illustrated in figure 2.1. A promising path to high-mobility and low-voltage organic transistors is the use of gate dielectrics, that provide a low capacitance per area. Inorganic materials, self-assembled mono- and multilayers (SAMs) and polymeric materials are promising materials and have already been demonstrated as gate dielectrics in OTFTs [36, 37, 38, 39, 40]. The charge transport is confined to a thin film region adjacent to the gate dielectric insulator[41], referred to as the “active region”. Growing a specific organic semiconducting layer on different gate dielectrics may lead to a different crystal structure, referred to as polymorphism. Thus, the intrinsic charge transport properties may be altered and affecting the mobility. Here, the crystal structures of pentacene grown on the three model types of gate dielectric materials suited for OTFT applications are investigated. As model systems four widely used gate dielectrics were chosen: amorphous silicon dioxide ( $a - SiO_2$ , inorganic), octadecyltrichlorosilane-treated  $a - SiO_2$  (OTS, SAM), Topas and polystyrene films (both polymeric).

### 2.1 Cleaning procedures of Si wafers

To prevent the inclusion of impurities during sample preparation and thin film growth, it is important that the samples undergo certain cleaning processes . For maximum purity, well established standard cleaning procedures known from inorganic semiconductor technology were used which will be discussed below.

#### 2.1.1 RCA cleaning

RCA clean was used for  $a - SiO_2$  substrates and for samples that were further processed with a SAM of OTS.

The RCA clean is the industry standard for removing contaminants from wafers. Werner Kern developed the basic procedure in 1961 while working for RCA (Radio Corporation of America) in Princeton, New Jersey - hence the name. In 1966 it was patented

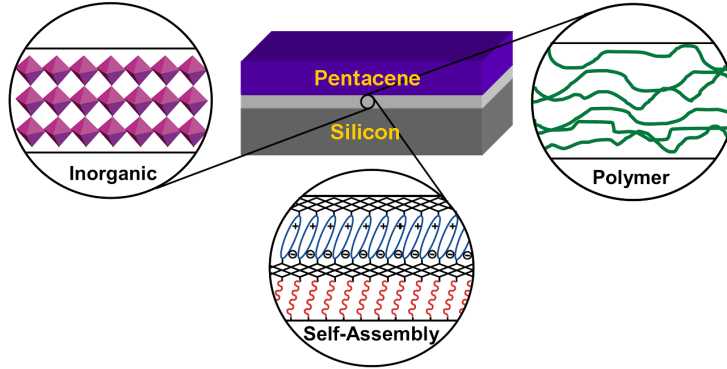


Figure 2.1: Illustration of the layered structure used in OTFTs. The structure consists of the silicon substrate, gate dielectric layer and the pentacene thin film layer. The insulating gate dielectric materials can be divided into three main categories: inorganic, self-assembled mono and multilayers (SAMs) and polymers.

and published in 1970 in RCA review[42]. The RCA cleaning procedure has two major steps used sequentially, denoted by SC-1 and SC-2 (Standard clean step one and two) and an optional step after SC-1:

- *SC-1*: Removal of insoluble organic contaminants with a 1:1:5  $NH_4OH : H_2O_2 : H_2O$  solution.
- *Optional step*: Removal of a thin silicon oxide layer that may have built up in SC-1 with a 1:50  $HF : H_2O$  solution
- *SC-2*: Removal of ionic and heavy metal atomic contaminants using a solution of 1:1:6  $H_2O_2 : HCl : H_2O$ .

The mix-ratios of the solutions given in SC-1 and SC-2 represent the original ratios. Over the years these ratios were altered up to 1:4:50 by the semiconductor industry to be more cost effective as the used chemicals are rather expensive. Here, the original mix-ratios and deionized water is used, to ensure that the wafers are as clean as possible. Each solution is prepared in a separate polypropylene beaker. After the wafers are placed in a teflon carrier, they are cleaned as follows:

- submerged in the SC-1 solution for 10 minutes at a temperature of 75-85°C.
- rinsed in a DI water beaker for 1 minute.
- submerged in the optional step solution for 15 seconds at room temperature.
- rinsed in a DI water beaker for 1 minute.
- submerged in the SC-2 solution for 10 minutes at a temperature of 75-85°C.

- rinsed in a DI water beaker for 1 minute.
- removed from the DI water beaker and blown dry with nitrogen.

In SC-1, hydrogen peroxide oxidizes the wafer and contaminants on the wafer. This lowers the adhesion forces between them, such that the contaminants become soluble in the solution. The ammonium hydroxide etches the silicon dioxide that may have built up on the wafer surface and undercuts the contaminants. The hydroxide ions build up a negative charge on the wafer and on the contaminants, resulting in electrostatic repulsion between them and preventing new adhesion of contaminants.

The optional step removes the silicon dioxide layer of some Angstroms that may have built up in SC-1. It is only used for native silicon wafers, but not necessary for  $a - SiO_2$  wafers.

SC-2 is used to remove ionic and heavy metal atomic contaminants from the wafer. The combination of a low pH and a high oxidation potential ionizes metals and makes them soluble in the solution.

The RCA cleaning technique does not attack silicon, and only a very thin layer of silicon dioxide is removed in the optional step.

### 2.1.2 Plasma cleaning

Plasma cleaning is also a commonly used process in the semiconductor industry which has the advantage of being solvent free, thus producing less waste when compared to RCA cleaning. It removes mainly organic contaminants from the wafer surface through the use of a highly reactive gas plasma. It is important to choose the correct plasma gas as gases react and work in different ways when removing contaminants. Here, oxygen was chosen as it removes organic contaminants like hydrocarbons by oxidation and reduction. The plasma is created by using GHz frequency electric fields which ionize the gas in an oxygen atmosphere at a pressure of about 2 Torr. When the free oxygen radicals react with the organic contaminants, gaseous products like carbon dioxide and carbon monoxide are produced and removed by the vacuum system.

Plasma cleaning was used for samples that were further processed by spin coating. The samples were cleaned with oxygen plasma for five minutes at 50 W.

## 2.2 Spin coating of polymeric thin films

In order to investigate the crystal structure of an organic thin film grown on polymer surfaces by X-ray diffraction, it is mandatory to produce flat and smooth thin films of these polymers. A standard and easy to use method is spin coating. Here, a thin film is produced on top of a silicon wafer by spin coating a solution with the polymer dissolved in an organic solvent.

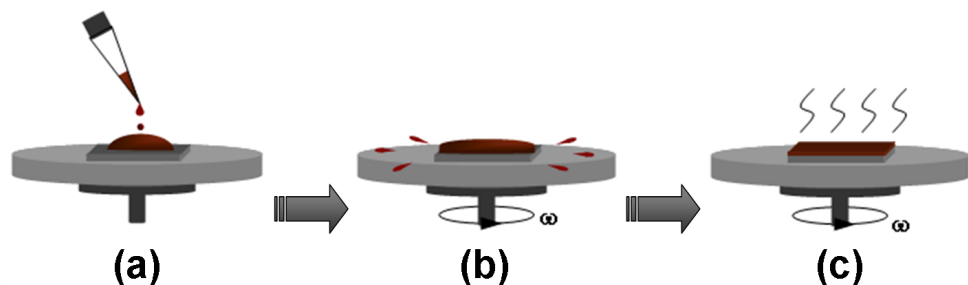


Figure 2.2: Spin coating a dissolved polymer on a substrate is a three step process a) Dispense: defines initial amount of solution b) Ramp-up (accelerating  $\omega$ ): spreads the solution c) Constant  $\omega$ : dry spin coated thin film.

Spin coating is a three step process, illustrated in figure 2.2. The residual film thickness depends not only on the spinning velocity  $\omega$  and concentration  $c$  of the dissolved polymer, but also on molar mass and molar mass distribution[43].

For spin coating the polymer gate dielectrics, a Delta 10 BM spin coater was used.

## 2.3 Gate dielectric materials

### 2.3.1 Amorphous silicon dioxide ( $a - SiO_2$ )

Amorphous silicon dioxide is the most common inorganic gate dielectric material. It was the first gate dielectric material which was successfully used for the production of pentacene OTFTs[44].

The substrates are prepared from highly n-doped silicon (110) wafers. First, the samples are cleaned by the RCA method. Then, the  $a - SiO_2$  layer with a thickness of 200 nm is grown by heating the wafer in a dry oxygen environment in an RTP-oven. The wafers are then cut into rectangular pieces with a size of 10x10 mm using a diamond scribing tool.

### 2.3.2 Octadecyltrichlorosilane (OTS) treated $a - SiO_2$

It is well known, that the treatment of  $a - SiO_2$  with OTS (figure 2.3) prior to pentacene deposition results in increased mobilities and drain current on/off ratios at room temperature when compared to untreated  $a - SiO_2$ , while dramatically reducing the average pentacene grain size[45]. To investigate if these effects are partly induced by improved intrinsic charge transport properties, we investigate the crystal structure of pentacene grown on a SAM of OTS.

Silanizing [46, 47]  $a - SiO_2$  surfaces is a well known process in semiconductor physics. OTS changes the surface chemistry of the sample, makes it hydrophobic and thus prevents the formation of a water layer on the surface. To silanize the samples with a SAM of OTS, a method developed by Christoph Strobel was used, which is well documented in his PhD thesis[48]:

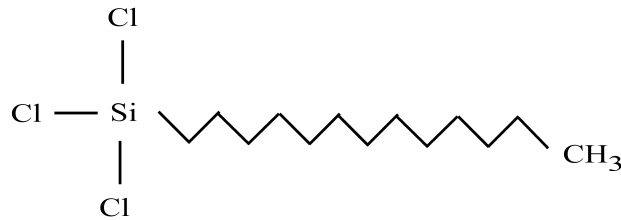
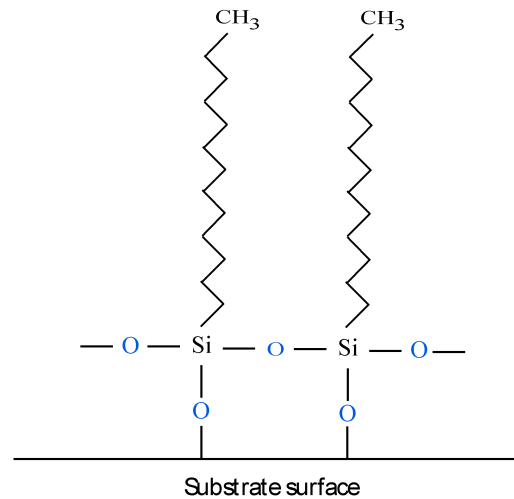


Figure 2.3: Structure of octadecyltrichlorosilane (OTS).

Figure 2.4: Self assembled monolayer of OTS on  $a - SiO_2$  substrate.

- a solution of 30 ml n-hexane and 24  $\mu$ l OTS (purchased from Sigma-Aldrich) is filtered
- the previously RCA cleaned  $a - SiO_2$  samples are put upside down in the solution for 30 min at a temperature of 4°C (refrigerator)
- the samples are cleaned by dipping them consecutively in clean solutions of n-hexane I, n-hexane II, chloroform I, chloroform II

The solution is filtered and the samples are put upside down in the OTS n-hexane solution to prevent contamination of the surface by polymerized OTS. During the silanization process, the chlorine atoms are substituted by OH groups. In a second step, the OTS molecules bind covalently with the help of oxygen bridges to the substrate surface. The  $CH_3$  termination of OTS is nonpolar, which makes the surface hydrophobic (figure 2.4).

### 2.3.3 Topas

Topas is the trade name for “thermoplastic olefin polymer of amorphous structure” from Ticona, Germany. As the name suggests, Topas consists of amorphous, transparent copolymers based on cyclo olefins and linear olefins (figure 2.5). This material exhibits a unique combination of properties, which are beneficial when producing organic electronic devices:

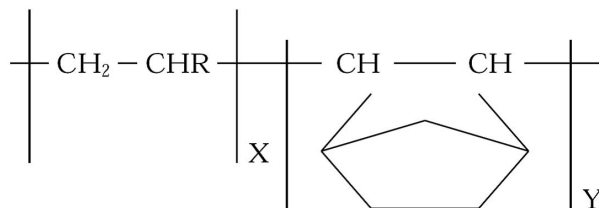


Figure 2.5: Chemical structure of Topas, purchased from Ticona, Germany.

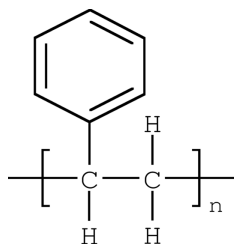


Figure 2.6: Chemical structure of the aromatic polymer polystyrene.

- Flexible, high strength and hardness
- Low density and therefore lightweight
- Low birefringence and high transparency for the use in optical devices
- Extremely low water absorption and excellent water vapor barrier properties
- Variable heat deflection temperature up to 170 °C
- Very good resistance to acids and alkalis
- Very good electrical insulating properties
- Very good blood compatibility and biocompatibility [49]

In this study Topas grade 6013 with a heat deflection temperature of 130°C purchased from Ticona, Germany was used.

### 2.3.4 Polystyrene

Another promising substrate is polystyrene, a very inexpensive and common aromatic polymer (figure 2.6). Just like Topas, polystyrene is flexible, optically transparent, water resistant and electrically insulating and therefore interesting for the use in flexible electronics. Studies showed that the use of polystyrene in organic TFTs resulted in high mobilities [50].



## 2.4 Characterization by X-ray reflectivity and AFM

The produced gate dielectric substrates exhibit different surface roughnesses and film thicknesses. Both parameters are of great importance when producing OTFTs. Different studies observed that dielectric materials with higher surface roughness exhibit a much lower carrier mobility[36]. The insulating properties are dependent on the film thickness. To investigate surface roughness, film thickness and surface morphology of the gate dielectrics used, X-ray reflectivity and atomic force microscopy (AFM) measurements were performed.

### 2.4.1 Atomic force microscopy

AFM was has been invented by Binnig, Quate and Gerber in 1986[51], and has become a standard tool for imaging surface morphologies on the nanoscale.

The AFM consists of a microscale cantilever with a sharp tip at its end that is used to scan the sample surface. When the tip is brought into proximity of a sample surface, forces between the tip and the sample lead to a deflection of the cantilever. The deflection is measured using a laser spot reflected from the top of the cantilever into an array of photodiodes. A feedback mechanism is employed to adjust the tip-to-sample distance to maintain a constant force between the tip and the sample. The sample is mounted on a piezoelectric tube, that can move the sample in the z direction for maintaining a constant force, and the x and y directions for scanning the sample. The 3D morphology of the sample surface is calculated from the three measured coordinates x,y and z and visualized by a computer. The resolution of an AFM is generally limited by the end radius of its tip.

AFM measurements in this thesis were performed with the Dimension 3000 from Digital instruments. The Dimension 3000 can be operated in two modes, “contact mode” and “tapping mode”.

#### Contact mode

In contact mode, the tip slightly touches the surface and is dragged over the area to be scanned (figure 2.7). This mode is suitable, if the sample surface is rigid and stable or is covered by a fluid.

#### Tapping mode

If the surface is soft as in organic thin films, the tapping mode (figure 2.8) is more convenient. Tapping mode operates by scanning a tip attached to the end of an oscillating cantilever across the sample surface. The cantilever is oscillated at or near its resonance frequency with an amplitude ranging typically from 20nm to 100nm. The frequency of oscillation can be at or on either side of the resonant frequency. The tip lightly taps on the sample surface during scanning, contacting the surface at the bottom of its swing. The feedback loop maintains a constant oscillation amplitude and thus a constant tip-sample interaction.

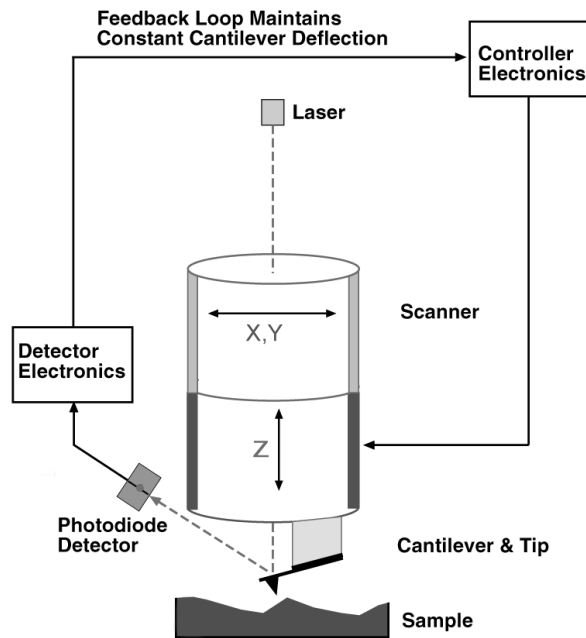


Figure 2.7: AFM contact mode.

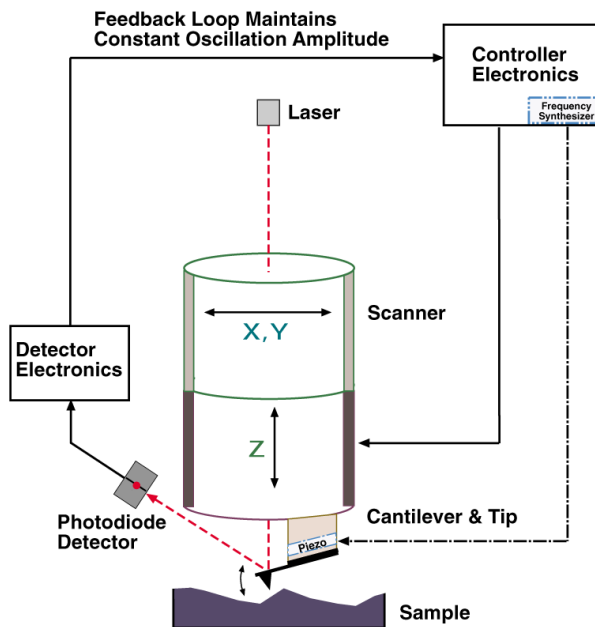


Figure 2.8: AFM tapping mode.

All AFM measurements shown in this thesis were performed in tapping mode.

### 2.4.2 Specular X-ray reflectivity

With X-ray reflectivity buried surfaces and the properties of interfaces in thin film systems can be investigated on a micro- and nanoscale. During a reflectivity measurement, the angle  $\alpha_i$  between the incident wave  $\vec{k}_i$  and the surface is varied, while the reflected intensity of  $\vec{k}_f$  is measured with a detector at the same exit angle  $\alpha_f$  (inset of figure 2.9). This results in a momentum transfer  $q_\perp = \vec{k}_f - \vec{k}_i = \frac{4\pi}{\lambda} \sin\alpha_{i,f}$ , which is perpendicular to the surface. Specular X-ray reflectivity can be described with the laws of classical optics when the appropriate index of refraction  $n$  is used. For X-rays with a wavelength  $\lambda$  around 1 Å,  $n$  is given by:

$$\begin{aligned} n &= 1 - \delta + i\beta \\ \delta &= \frac{\lambda^2}{2\pi} r_e \rho \\ \beta &= \frac{\lambda}{4\pi} \mu \end{aligned}$$

where  $r_e$  is the classical electron radius,  $\rho$  is the electron density of the material, and  $\mu$  is the absorption length. If  $\delta > 0$  then the index of refraction  $n < 1$ , which leads to the so-called total external reflection for incident angles  $\alpha_i$  below the critical angle  $\alpha_c = \sqrt{2\delta}$ .

The index of refraction  $n$  is typically in the range  $10^{-5} - 10^{-6}$ , and therefore the critical angle  $\alpha_c$  is in the range of  $0.1^\circ - 0.5^\circ$ .  $\beta$  is usually much smaller and is ignored for further considerations.

The intensity  $R_F$  of the reflected X-ray wave for an ideal, sharp interface can be derived by Fresnel's equations and is called the Fresnel Reflectivity:

$$R_F = r^2 = \left( \frac{k_{i\perp} - k_{t\perp}}{k_{i\perp} + k_{t\perp}} \right)^2$$

where  $k_{i\perp}$  and  $k_{t\perp}$  are the vertical components of the incident and the transmitted wave (inset of figure 2.10). When  $\alpha_i$  is close to the critical angle  $\alpha_c$ , then  $k_{t\perp}$  is strongly affected by refraction effects:

$$k_{t\perp} = \sqrt{\alpha_i - \alpha_c}$$

If  $\alpha_i$  is smaller than  $\alpha_c$ , then  $k_{t\perp}$  is imaginary. If  $\alpha_i$  is above the critical angle  $R_F$  falls off rapidly by

$$R_F \propto 1/\alpha_i^4$$

and the penetration depth into the sample diverges. Here it becomes possible to collect information on the surface up to a depth of some hundreds of nanometers. For  $\alpha_i > 3\alpha_c$ ,  $R_F$  can be approximated by:

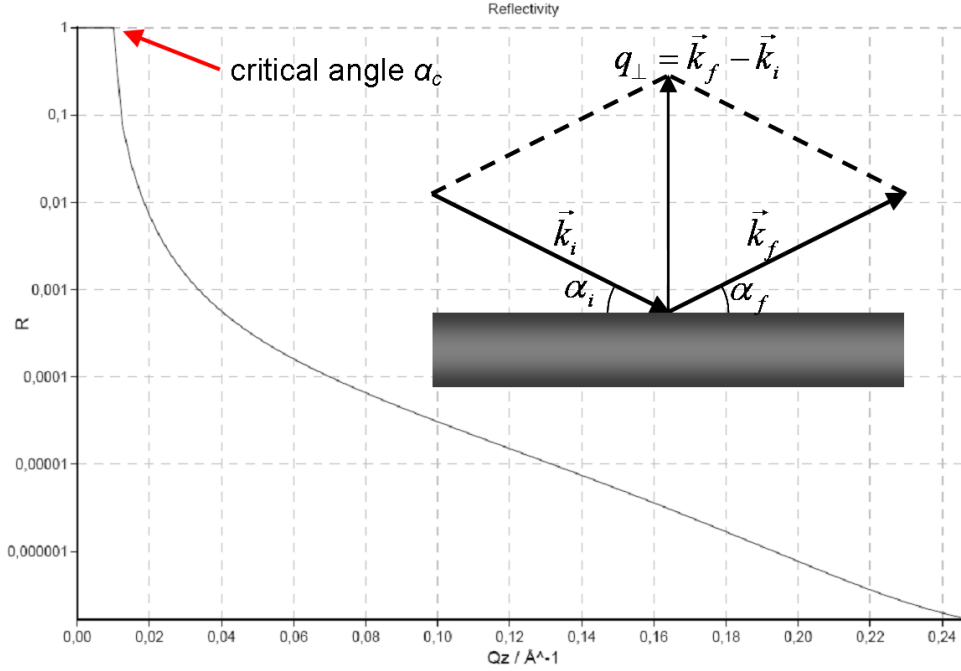


Figure 2.9: Fresnel X-ray reflectivity of a bare substrate with a surface roughness of 5 Å.

$$R_F = (\alpha_c/2\alpha_i)^4$$

Surface roughness  $\sigma$  can be included by:

$$r_\sigma = r \cdot \exp(k_{i\perp} k_{t\perp} \sigma^2)$$

An example of Fresnel Reflectivity with surface roughness is shown in figure 2.9.

If the sample has more than one interface (e.g. thin film on a substrate, inset of figure 2.10), the scattering from all interfaces has to be taken into account. For this purpose, Parratt developed a recursion formalism [52] which relates the reflected and transmitted amplitude. Due to the interference of waves, which are reflected from different interfaces, intensity oscillations in the reflectivity, the so-called Kiessig fringes (figure 2.10), can be observed. In the case of a flat substrate covered homogeneously by a thin layer (e.g.  $d=100$  Å), incident waves may be reflected by the interface air/layer or layer/substrate. At distances far away from the sample, the reflectivity interference effects caused by superposition of the waves  $k'_f$  and  $k''_f$  (inset figure 2.10) can be measured by the detector. If the additional path by the wave scattered at the layer/substrate interface is a multiple of the X-ray wavelength, constructive interference occurs. Otherwise, if the path difference equals an uneven multiple of half the wavelength, the waves interfere destructively and the signal completely vanishes. Usually, full destructive interference is not observed, since the interfaces always exhibit a certain roughness  $\sigma$ . The spacing between adjacent minima or maxima of the Kiessig fringes give direct information about the layer thickness  $d$ :

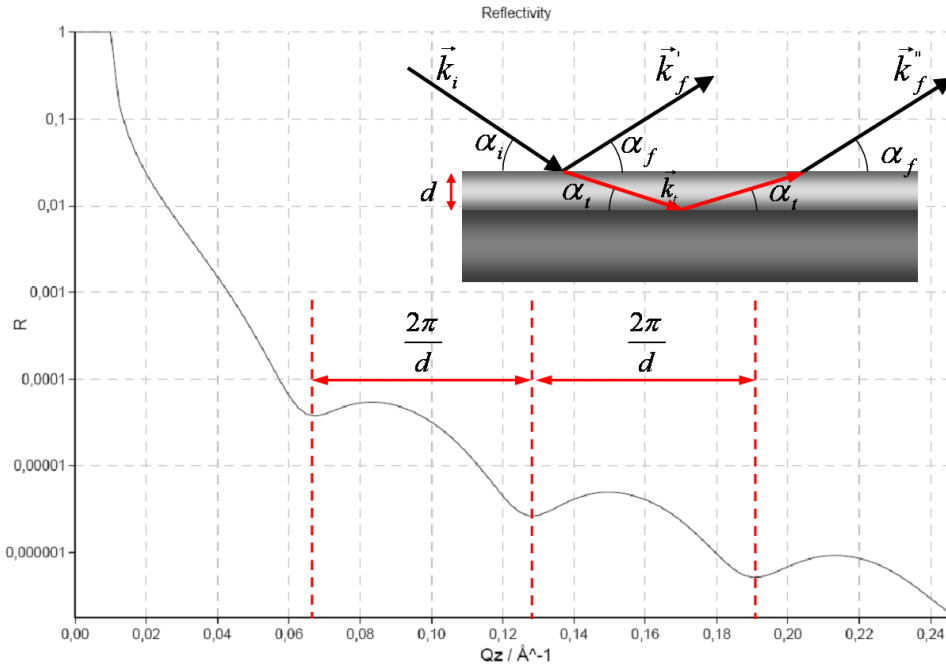


Figure 2.10: X-ray reflectivity of a flat surface covered with a surface layer of  $d=100$  Å thickness and an interface roughness of 5 Å.

$$d = 2\pi/\Delta q_{\perp}$$

For a quantitative data fit, the software tool Parratt32 developed by the Hahn Meitner Institut in Berlin was used to fit the optical reflectivity of X-rays from flat surfaces. It uses Parratt's recursion scheme for stratified media [52] to fit the layer thickness  $d$ , the interface roughness  $\sigma$ , and the average density of the different layers.

### 2.4.3 In-house 4-circle X-ray setup

For a quick analysis of thin films (e.g. spin coated polymer gate dielectrics), an in-house X-ray setup was used. The Huber 424 X-ray diffractometer (figure 1.5a) has a 4-circle geometry (figure 2.11) and is employed for reflectivity studies from surfaces and thin films. The X-ray tube using a copper anode which is powered by a Seifert ISO-Debyelex 3003 X-ray generator with a maximum power of 2.2 kW. It produces an X-ray beam of 8.04 keV energy at a wavelength of  $\lambda_{K_{\alpha}} = 1.54$  Å. The X-ray beam is sent through a Huber Guinier system 611 monochromator using a bent Ge(111) crystal. As a detector a NaI scintillator from Rich-Seifert is used. Several beam and detector slits are used to maximize the signal to noise ratio. The Huber 424 diffractometer as well as the power of the X-ray generator are controlled by a lab computer using the standard command-line interface SPEC from Certified Scientific Software.

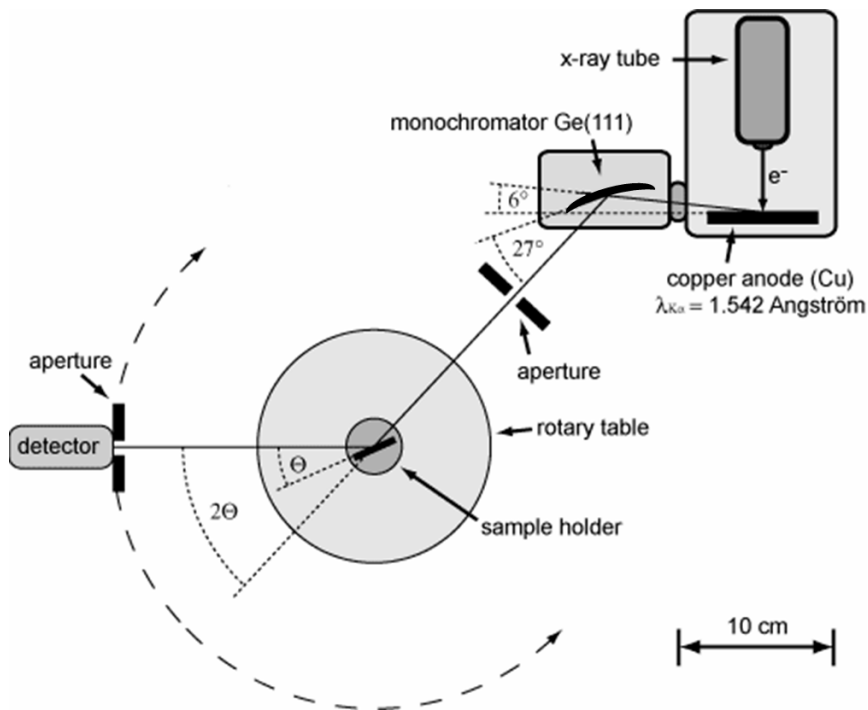


Figure 2.11: Schematic drawing of the in-house 4-circle X-ray setup. The diffractometer is employed for reflectivity studies from surfaces and thin films (figure by C. Reich).

## 2.4.4 Results

### $a - SiO_2$

Commercially purchased silicon wafers exhibit a very low surface roughness typically  $< 5 \text{ \AA}$ . However, when an  $a - SiO_2$  layer is produced, the surface roughness increases depending on the method used to grow the layer. Thus, the surface roughness of commercially purchased  $a - SiO_2$  and custom-made  $a - SiO_2$  which was grown in our RTP-oven was measured and compared.

Before the measurements, the wafers were cleaned by the RCA method. Using AFM measurements, it was found, that the surface roughness of custom-made  $a - SiO_2$  remains unchanged at  $R_q = 1.7 \text{ \AA}$  before and after the growth of 200 nm (figure 2.12). Due to the size of the cantilever tip, surface roughness measurements by AFM are difficult when the roughness is in the sub nm range. Thus the roughness was also measured by X-ray reflectivity measurements at the HASYLab synchrotron source W1 beamline. Commercially purchased  $a - SiO_2$ , custom-made  $a - SiO_2$  before and after the growth of a  $SiO_2$  layer was measured and compared. The X-ray reflectivity fits are shown in figure 2.13. As expected, the surface roughness  $\sigma$  measured by X-ray reflectivity is much higher when compared to the surface roughness  $R_q$  measured by AFM. Nevertheless,  $\sigma$  also remained constant at  $3.7 \text{ \AA}$  before and after the growth of a 200nm  $a - SiO_2$  layer. The surface roughness of the commercially purchased  $a - SiO_2$  is with  $\sigma = 5.3 \text{ \AA}$  significantly higher. Thus,

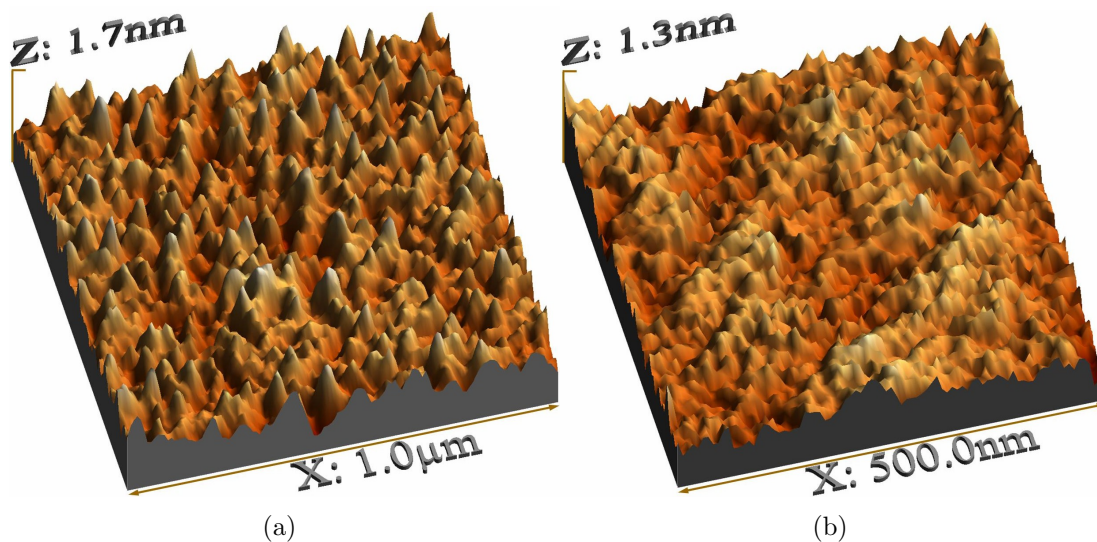


Figure 2.12: 3D AFM micrographs of wafers before (a) and after (b) the growth of 200 nm of  $a - \text{SiO}_2$  in our RTP oven. (note that the z-axis scaling is different from the x- and y-axis scaling).

substrate	$R_q[\text{\AA}]$	$\sigma[\text{\AA}]$	$d_{\text{layer}}[\text{\AA}]$
$a - \text{SiO}_2$ (before growth)	1.7	3.7	7.5
$a - \text{SiO}_2$ (after growth)	1.7	3.7	2012
$a - \text{SiO}_2$ (commercial)	-	5.3	4053

Table 2.1: Comparison of surface roughnesses of  $a - \text{SiO}_2$  wafers before and after the growth of a  $a - \text{SiO}_2$  layer and commercially purchased  $a - \text{SiO}_2$  wafers measured by AFM ( $R_q$ ) and X-ray reflectivity  $\sigma$ .

custom-made  $a - \text{SiO}_2$  wafers were used for further pentacene thin film growth studies.

### OTS treated $a - \text{SiO}_2$

Immediately after the treatment of the custom-made  $a - \text{SiO}_2$  with OTS in the clean-room, AFM measurements were performed. The 3D AFM micrograph in figure 2.14 shows a needle-like surface with a roughness of  $R_q = 7.9 \text{\AA}$ , which is significantly higher than for  $a - \text{SiO}_2$ . This suggests that the OTS may have polymerized or cross-linked and that the surface is not fully covered by an OTS monolayer.

X-ray reflectivity measurements were performed at the HASYLab synchrotron source W1 beamline. A data fit of the measurements reveal an OTS monolayer of  $d = 21.8 \text{\AA}$  and a roughness of  $\sigma = 8.2 \text{\AA}$  (figure 2.15a), which is significantly higher than for  $a - \text{SiO}_2$  substrates.

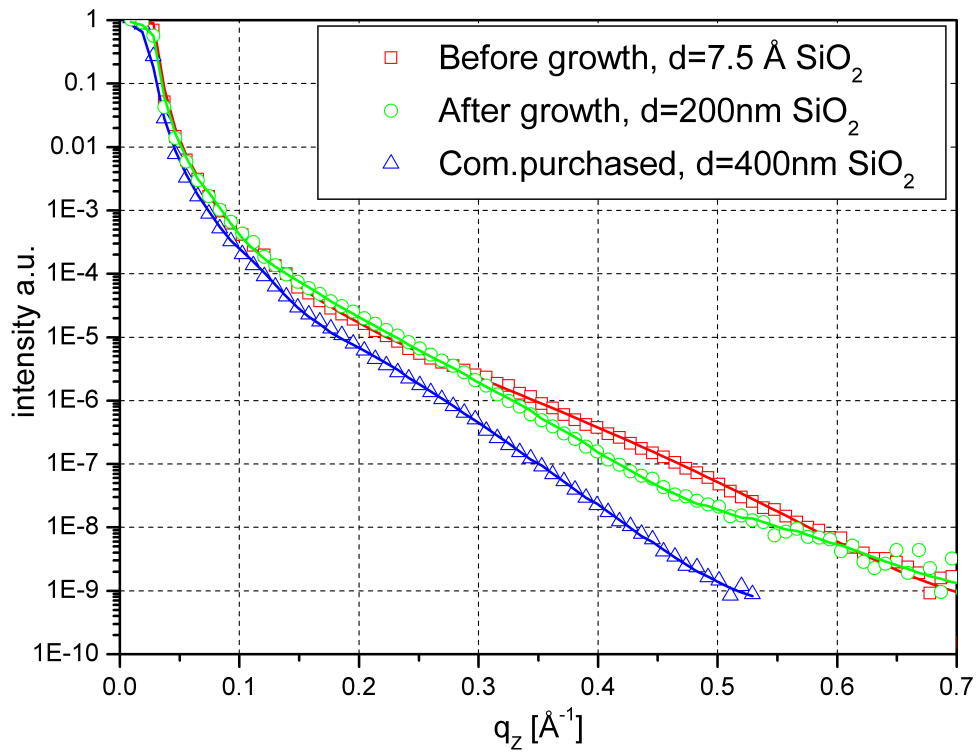


Figure 2.13: X-ray reflectivity (W1). Silicon wafer with an initially 7.5 Å native  $a - SiO_2$  layer, after the growth of 200 nm  $a - SiO_2$  in the RTP oven and for comparison a commercially purchased wafer with a 400 nm  $a - SiO_2$  layer. Data fits are illustrated by solid lines.



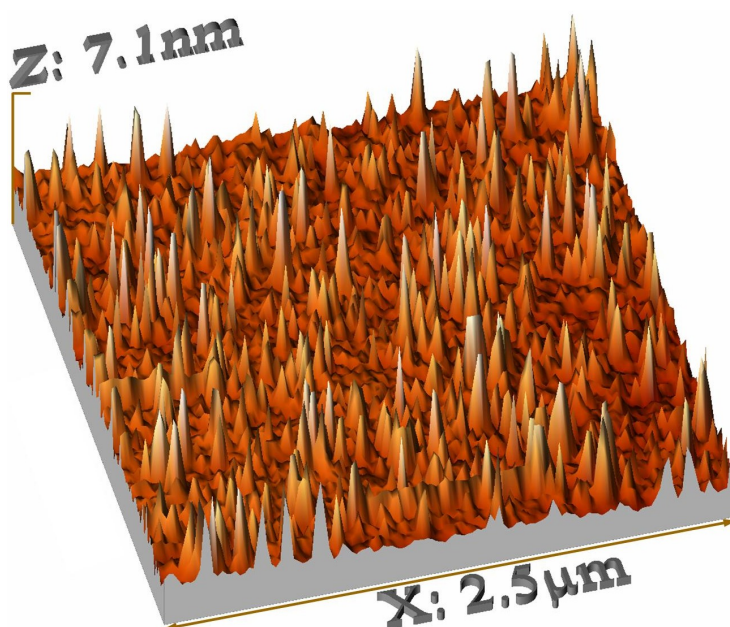


Figure 2.14: 3D AFM micrograph of an OTS treated  $a - SiO_2$  wafer. The needle like surface is clearly visible, which suggests, that the surface is not fully covered with an OTS monolayer. (note that the z-axis scaling is different from the x- and y-axis scaling).

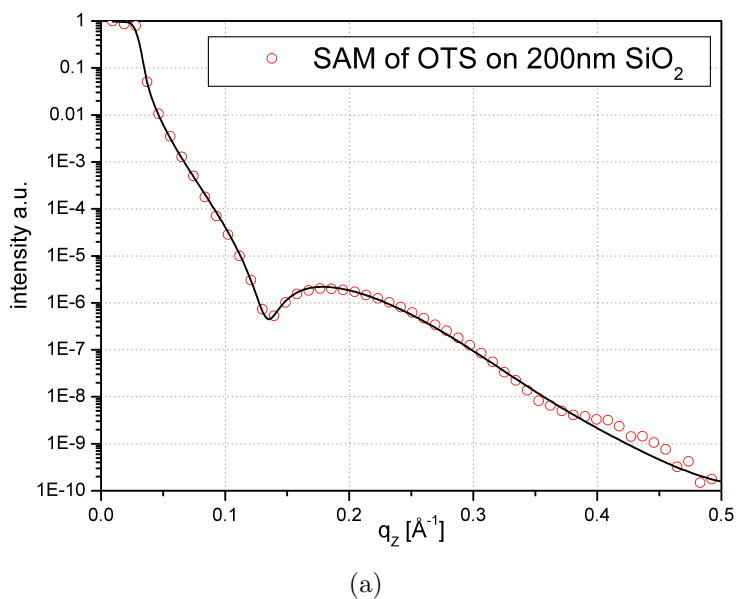


Figure 2.15: (a) X-ray reflectivity (W1). OTS treated  $a - SiO_2$  sample (circles). The data fit (solid line) revealed an OTS monolayer of  $d = 21.8 \text{\AA}$  and a surface roughness of  $8.2 \text{\AA}$ .

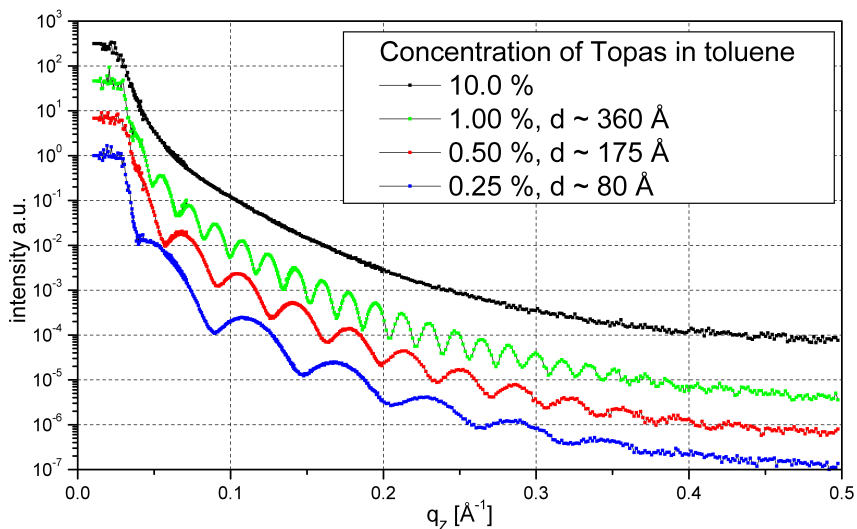


Figure 2.16: X-ray reflectivity measurements (in-house). Topas films coated on  $a - SiO_2$  wafers with concentrations of Topas dissolved in toluene as indicated. The thickness can be tuned almost linearly within a concentration range of 5.00 % down to 0.25 %. Concentrations  $> 5$  % were beyond the resolution of the in-house 4-circle X-ray setup.

### Topas

A thin film of Topas was produced by spin coating a solution of Topas dissolved in the nonpolar organic solvent toluene. As there is no literature available about spin coating Topas thin films, the relation of film thickness and concentration of dissolved Topas by in-house X-ray reflectivity measurements was investigated. Toluene dries very fast during spin coating, thus the parameters at the Delta 10 BM spin coater were set to maximum. Acceleration was set to 5 and  $\omega$  to 6000 rpm for 30s. It was found, that the thickness of the Topas layer depends almost linearly on the concentration in the investigated range of 5.00 % down to 0.25 %. In figure 2.16 some selected reflectivity measurements and their respective film thickness calculated from the periodicity of the Kiessig fringes are shown. Film thicknesses for concentrations  $> 5$  % could not be resolved due to resolution restrictions of the in-house 4-circle setup, illustrated by the black line for a reflectivity measurement of a Topas film with 10% concentration (figure 2.16).

Before the growth process of a pentacene thin film can be started, it is necessary to anneal the sample surface in vacuum by heating up to  $100^\circ\text{C}$  in order to desorb impurities and especially to desorb a thin water layer on the sample surface, which might affect the thin film growth process of pentacene. To verify the thermal stability of Topas during the annealing process, X-ray reflectivity measurements were performed before and after the treatment of 10min on a hotplate with a temperature of  $T=110^\circ\text{C}$  shown in figure 2.17. The periodicity of the Kiessig fringes didn't change, which indicates that the Topas layer thickness is not affected by heating up to  $110^\circ\text{C}$ .

For a quantitative analysis of the surface roughness, X-ray reflectivity measurements

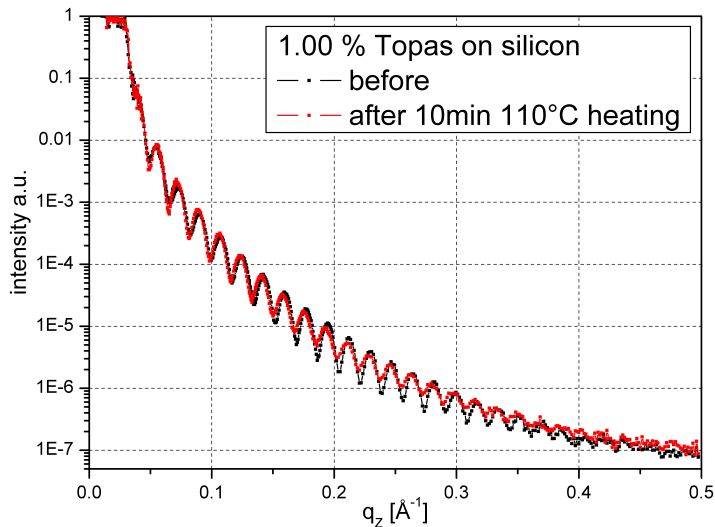


Figure 2.17: X-ray reflectivity measurements (in-house). Topas film before (black line) and after the treatment of 10min on a hotplate with  $T=110^{\circ}\text{C}$  (red line). The periodicity of the Kiessig fringes indicates that the Topas layer thickness is not affected by heating up to  $110^{\circ}\text{C}$ .

at the HASYLAB synchrotron source beamline W1 were performed and analyzed. Figure 2.19 shows a fit of an X-ray reflectivity measurement of a spin coated Topas film with a concentration of 0.25% after one minute of annealing at a surface temperature of  $T=80^{\circ}\text{C}$ . The surface roughness  $\sigma = 2.5 \text{ \AA}$  is about 50% lower than the surface roughness of the underlying silicon wafer. This in consequence means, that Topas is able to flatten the already very smooth silicon wafer surface, which makes Topas an ideal surface for growth studies of pentacene thin films. The surface roughness of  $R_q = 2.0 \text{ \AA}$  determined by AFM (figure 2.18) confirmed the low surface roughness measured by X-ray reflectivity (figure 2.19)

## Polystyrene

Just like Topas, polystyrene was dissolved in toluene and spin coated on commercially purchased  $a - \text{SiO}_2$  with a surface roughness of  $5.3 \text{ \AA}$ , measured by X-ray reflectivity. A solution of 0.10 weight % of polystyrene was spin coated with an acceleration of five and 300 rpm for 5 seconds and subsequent with 2000 rpm for 30 seconds.

With AFM measurements a surface roughness of  $R_q = 3.4 \text{ \AA}$  shown in figure 2.20 was determined. X-ray reflectivity measurements (figure 4.11) performed at the synchrotron source beamline W1 were fitted and revealed a film thickness of  $63.5 \text{ \AA}$  and a surface roughness  $\sigma = 5.1 \text{ \AA}$ . Similar to Topas, the surface roughness of a polystyrene film is lower than the one of the underlying substrate. However, this flattening effect of about 5 % is not as drastic as for Topas films. The surface roughness is still low enough for pentacene thin film growth experiments.

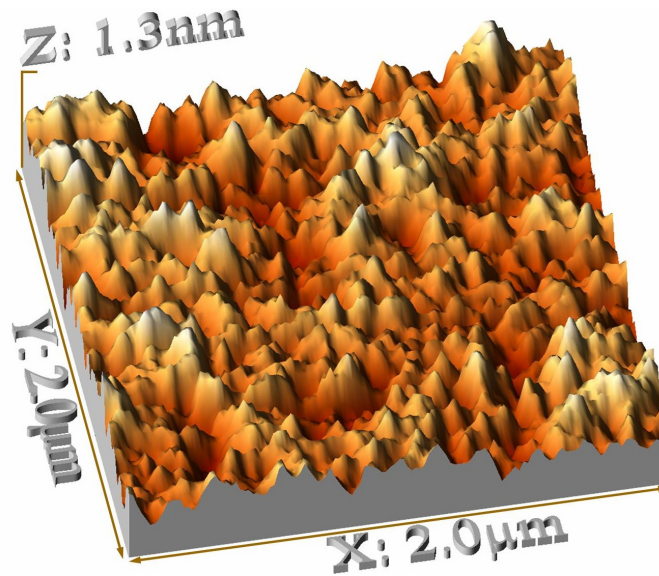


Figure 2.18: 3D AFM micrograph of a Topas film spin coated on a silicon wafer. The polymer film has surface roughness of  $R_q = 2.0 \text{ \AA}$  measured by AFM. (note that the z-axis scaling is different from the x- and y-axis scaling).

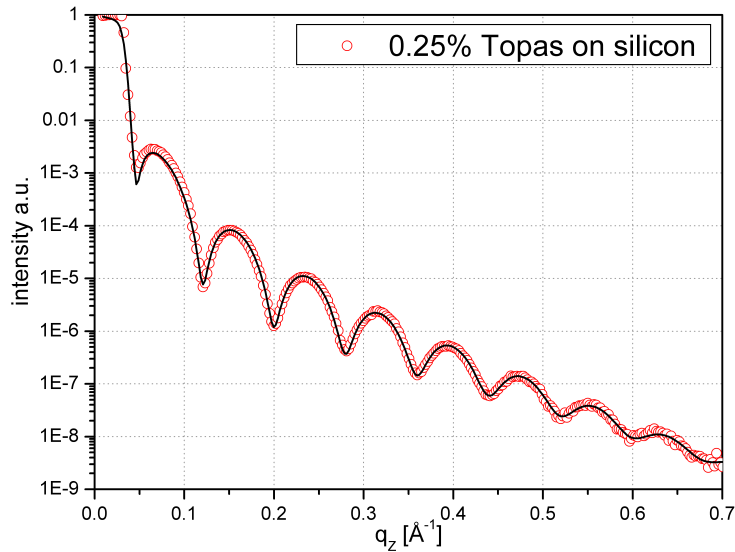


Figure 2.19: X-ray reflectivity (W1). Spin coated Topas film with a concentration of  $c = 0.25\%$  dissolved in toluene after one minute of annealing at a temperature of  $T = 80^\circ\text{C}$ . The data fit (solid line) revealed a film thickness of  $d = 78.9 \text{ \AA}$  and a surface roughness of  $2.5 \text{ \AA}$ .

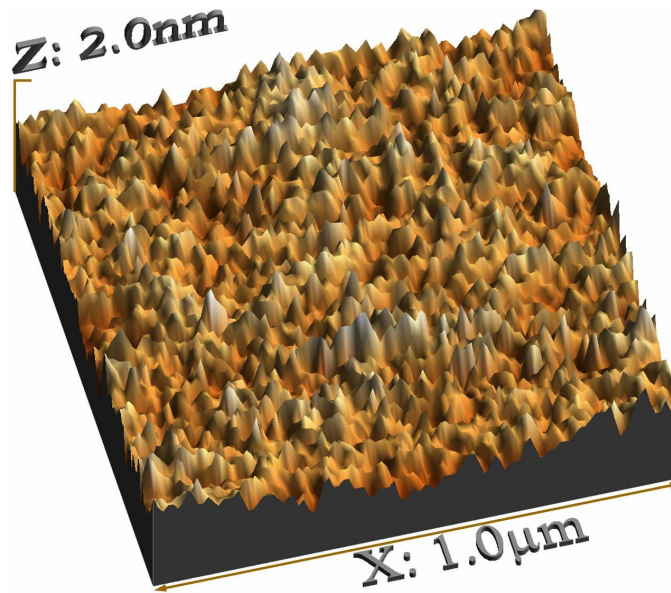


Figure 2.20: 3D AFM micrograph of a polystyrene film spin coated on a  $a - SiO_2$  wafer. The polymer film has a surface roughness of  $R_q = 3.4 \text{ \AA}$  measured by AFM. (note that the  $z$ -axis scaling is different from the  $x$ - and  $y$ -axis scaling).

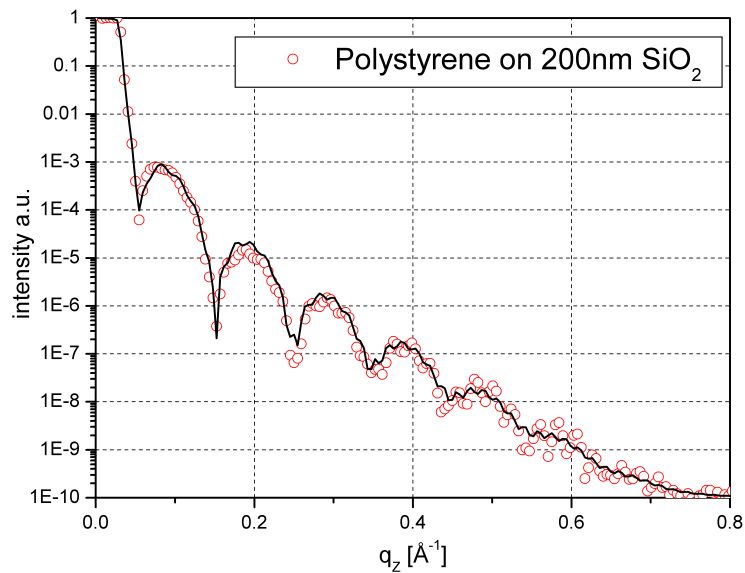


Figure 2.21: X-ray reflectivity (W1). Polystyrene film spin coated on a commercially purchased  $a - SiO_2$  wafer with a concentration of 0.10 weight % dissolved in toluene after one minute of annealing at a temperature of  $T = 80^\circ\text{C}$ . The data fit (solid line) revealed a film thickness of  $d = 63.6 \text{ \AA}$  and a surface roughness of  $5.1 \text{ \AA}$ .

substrate	$R_q$ [Å]	$\sigma$ [Å]	$d_{layer}$ [Å]
$a - SiO_2$ (custom-made)	1.7	3.7	2012
OTS	7.9	8.2	21.8
Topas	2.0	2.5	78.9
polystyrene	3.4	5.1	63.6

Table 2.2: Comparison of the surface roughness  $R_q$  measured by AFM,  $\sigma$  measured by X-ray reflectivity and layer thickness  $d_{layer}$ , also measured by X-ray reflectivity. Topas has the lowest surface roughness, followed by custom-made  $a - SiO_2$ , polystyrene and OTS.

### 2.4.5 Summary

In table 2.2, the results of surface roughness and layer thickness of all gate dielectrics used for pentacene thin film growth are summarized. It can be concluded, that Topas has the lowest surface roughness, followed by custom-made  $a - SiO_2$ , polystyrene and OTS. Detailed fit results of the gate dielectrics can be found in appendix A.

Now that the gate dielectrics are characterized by layer thickness and surface roughness, they are ready for the pentacene thin film growth process in the portable vacuum growth chamber.

## 2.5 Organic molecular beam deposition (OMBD)

Here the growth of a well defined pentacene thin film, which can later be used as a model system for X-ray diffraction studies is discussed.

So far, the best performing thin film devices utilizing organic semiconductors such as pentacene were fabricated by thermal molecular beam deposition under vacuum [53]. This technique involves heating the organic semiconductor using a heating source in a vacuum environment with a pressure in the range of  $10^{-8}$  to  $10^{-6}$  Torr [54, 29]. The technique has the advantages of excellent thin film formation, high reproducibility and purity of the thin films. The disadvantage of this method are the relatively high material consumption and also the high cost for equipment setup. In 2003 a new vacuum deposition method called organic vapor phase deposition (OVPD) was presented, which was developed by Aixtron AG and Stephen Forrest in Princeton. Here, a carrier gas like nitrogen is used to carry the pentacene molecules and transport them directly on the substrate surface. OVPD is a cost optimized version of OMBD as the material consumption during the growth process is reduced by 90%. On the other hand, OTFTs produced by OVPD could not reach the high charge mobilities of OMBD produced devices [45, 55]. In addition the OVPD technique is way more complex than OMBD and can therefore not be reconstructed easily to be suitable for in-situ X-ray diffraction measurements. Even though OVPD and OMBD are different vacuum deposition techniques, they share several factors that should be considered when selecting the deposition conditions in order to achieve high OTFT performance. Deposition rate, substrate temperature, base pressure and purity of the

organic semiconducting material directly affect the crystallinity and morphology of the resulting thin film.

Purification is essential, because impurities (“chemical defects”) can strongly influence the electrical as well as the optical properties of the organic thin film. The situation here is not so different from inorganic semiconductors, where a lot of efforts are made to get down to impurity levels as low as 1 ppm and even below. Subsequent controlled doping allows the creation of specific properties such as n- or p-type conduction. Uncontrolled doping can lead to charge-carrier scattering and trapping, which leads to the reduction of mobilities. In different studies it was shown that even ppm traces of impurities in the organic model compound anthracene can lead to drastically reduced electron and hole mobilities [56].

To control deposition rate, substrate temperature and base pressure, a portable ultra high vacuum growth chamber (figure 2.24), equipped with a rotatable sample holder and a beryllium window in order to perform X-ray measurements of up to four different gate dielectrics right after the thin film growth process without breaking the vacuum was built.

### 2.5.1 Purification of pentacene

The purification process of pentacene was performed by the group of Jens Pflaum, Universität Stuttgart, who purified pentacene using temperature gradient sublimation.

Temperature gradient sublimation is an easy to handle and fast purification process, when compared to other purification processes. The concept behind temperature gradient sublimation is that the various components of the starting material in vapor phase condense at different temperatures. The starting material is placed at the one end of a glass tube surrounded by a conical tubular metal furnace and heated up slightly above the melting point (figure 2.22). While the other end of the glass tube is kept at a constant temperature, a temperature gradient is established. A stream of well-purified inert gas ( $N_2$ ,  $Ar$ ) transports the sublimating molecules along the glass tube. Due to their different condensation temperatures, the various components of the raw material condense at different places in the glass tube. For further purification, the process may be repeated several times with the purest fraction as a new starting material.

The purification of pentacene for electronic devices is a challenging field of organic electronics, because pentacene is capable of significant impurity-forming reactions at relatively low temperatures. In flowing gas, pentacene undergoes a disproportionation reaction to produce 6,13-dihydropentacene (DHP) and a series of polycondensed aromatic hydrocarbons like peripentacene. The process requires activation by heating to 320 °C and is catalyzed by impurities such as DHP, 6,13-pentacenequinone (figure 2.23), Al, or Fe found in the starting material. Subsequent purifications remove such impurities, thus inhibiting the formation of the disproportionation products [57].

The single crystal structure of 6,13-pentacenequinone is significantly different from the pentacene single crystal structure [58]. It has been shown, that the number of traps in pentacene single crystals is reduced by two orders of magnitude after a purification process in which 6,13-pentacenequinone was removed by vacuum sublimation. The hole mobility increased from  $\mu = 35 \text{ cm}^2/V$  at room temperature to  $\mu = 58 \text{ cm}^2/V$  at 225 K indicating

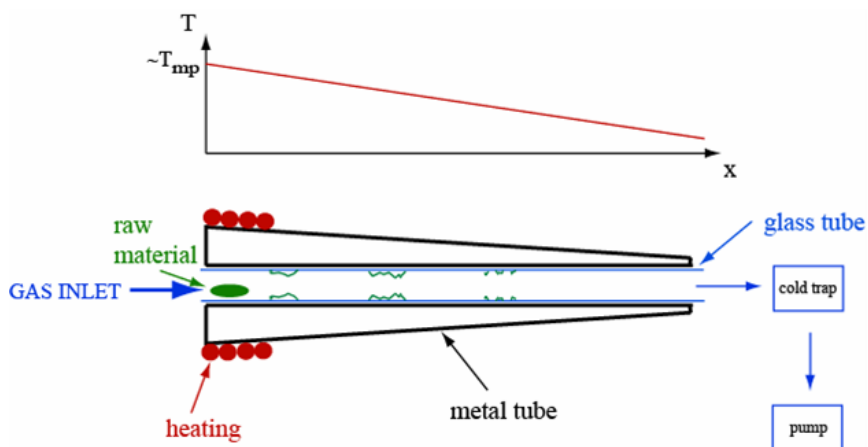


Figure 2.22: Sketch of the setup used for temperature gradient sublimation.

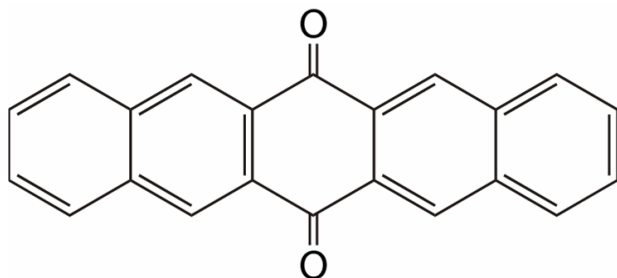


Figure 2.23: Lewis structure of 6,13-pentacenequinone. When pentacene is exposed to light and oxygen, it oxidizes to 6,13-pentacenequinone.

a band like electronic transport in the crystal [59].

These results clarify the importance of purifying semiconductive materials for measurements of intrinsic mobility and optimal device performance.

### 2.5.2 Portable, ultra high vacuum growth chamber (PGC)

To build and operate a portable growth chamber (figure 2.24) at a synchrotron source requires much effort. Mechanical construction, software programming and testing at the synchrotron source were completed over a period of about 2 years. The growth chamber builds the “heart” of our science network collaboration, as all organic samples used in different groups were processed using this chamber.

The PGC is able to produce a base pressure  $< 10^{-8}$  torr, monitored by a Balzers PKR250 compact full-range pressure sensor, providing a mean free path  $> 1$  km for the organic molecules inside the chamber, which is much larger than the dimensions of the chamber. The vacuum is produced by a combination of a rotary vane pump and a Varian V 70LP turbopump. A tantalum bag, produced by spot-welding of tantalum foil (figure 2.25) filled with the purified organic semiconducting material, is used as a thermal evaporation



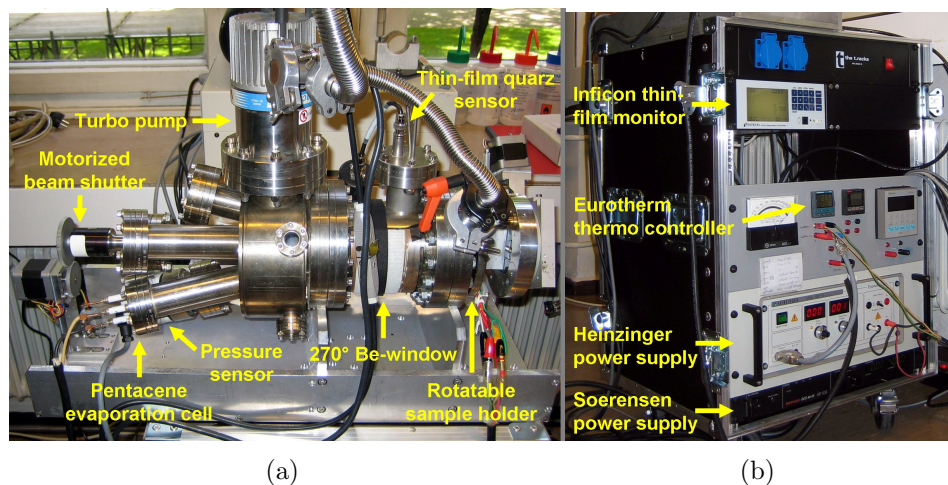


Figure 2.24: (a) Custom-made, portable vacuum growth chamber (PGC). (b) Rack of electric equipment used to operate the PGC.

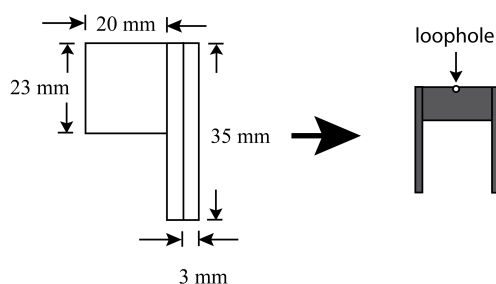


Figure 2.25: Sketch of the evaporation source. A tantalum bag is produced by spot-welding a tantalum foil and is filled with the previously purified organic semiconducting material. The bag is heated by an electric current and the organic material evaporates and streams out of the loophole producing a point-source organic molecular beam.

source. The molecular deposition beam is produced by applying a well defined electric current, supplied by a Soerensen power supply and collimated by a vacuum tube, which heats the tantalum bag and thus sublimates the organic material. Tantalum was chosen as an evaporation source, because it is a very clean and supple UHV compatible metal and heat resistant to temperatures as high as 3290 K. A custom made motorized beam shutter, equipped with a thin film quartz crystal sensor allows the beam to become stable before the growth process is started. Next to the samples, a second thin film quartz crystal sensor monitors the deposition rate near the substrate surface. Both thin film sensors are read out by an Inficon XTM/2 thin film monitor. The XTM/s controls both rates using a built-in proportional-integral-derivative (PID) control feedback circuit (figure 2.27, indicated with green lines).

The samples are mounted on a custom-made multi sample holder (figure 2.26), which can hold up to four sample substrates. A 20W halogen light bulb purchased from Conrad

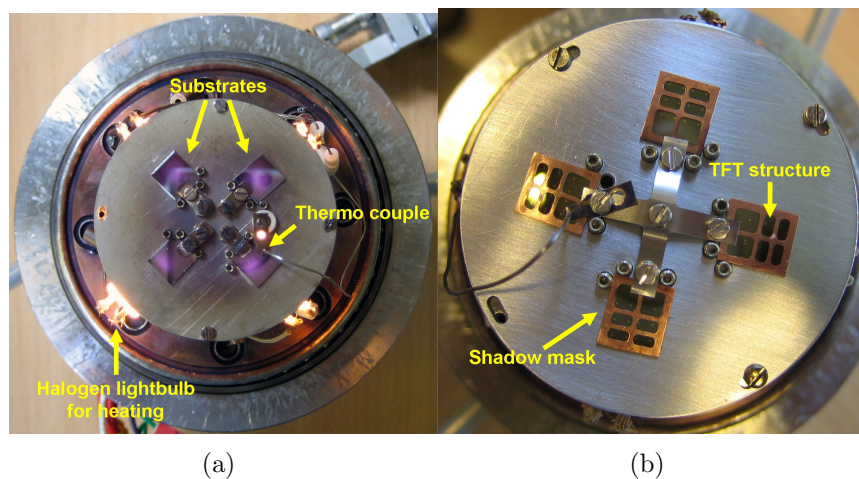


Figure 2.26: Custom-made rotatable sample holder. (a) Mounted with four samples. Each sample is heated using a 20W halogen light bulb. The temperature of the substrate surface is measured by a thermo couple. (b) Mounted with shadow masks for growing organic thin films on TFT structures.

Electronics is placed directly below each substrate. The samples are heated through holes in the sample holder cap, such that the substrate surfaces are not directly exposed to light. The temperature is measured directly on the substrate surface by a thermo couple type K, made of chromel (a nickel chromium alloy) and alumel (a nickel aluminium alloy) which is optimized for temperatures between  $-200$  and  $+1200$  °C. The temperature is controlled by a built-in PID circuit using an Eurotherm 2416 thermo controller and a Heinzinger power supply (figure 2.27, indicated with red lines). With the help of a  $270^\circ$  beryllium window (figure 2.24) an X-ray beam can be sent through the chamber for in-situ X-ray diffraction measurements. As the sample holder can be rotated using a stepping motor, up to four samples can be rotated into the X-ray beam and measured without breaking the vacuum (figure 2.26).

The electric wiring of the two major PID circuits for temperature (red) and deposition rate (green) control are illustrated in figure 2.27. The equipment used in the setup is connected either digitally or by analog connection via a multi I/O box purchased from National Instruments to the PC. This allows the TFDS software to monitor and control the thin film deposition process parameters directly. When using pentacene, the setup allows the deposition rate at the sample to be tuned in the range of  $0.1 \text{ \AA}/s$  up to  $5 \text{ \AA}/s$  with a precision of  $\pm 0.1 \text{ \AA}/s$ . The resulting film thickness has an accuracy of 0.5% with a resolution of  $1 \text{ \AA}$ . The substrates can be heated up to  $400^\circ\text{C}$  and can be kept stable within a temperature range of  $\pm 0.01^\circ\text{C}$ . The compact fullrange gauge PKR 250 from Balzers allows measurements in the range of  $1 \cdot 10^{-9} - 750 \text{ torr}$  with a precision of  $\pm 30\%$  in air.

The software can be configured to use any organic deposition material and any substrate (figure 2.28a). The quartz crystal sensor is capable of precisely measuring the mass added to the face of the oscillating quartz crystal. By entering the density of this added material

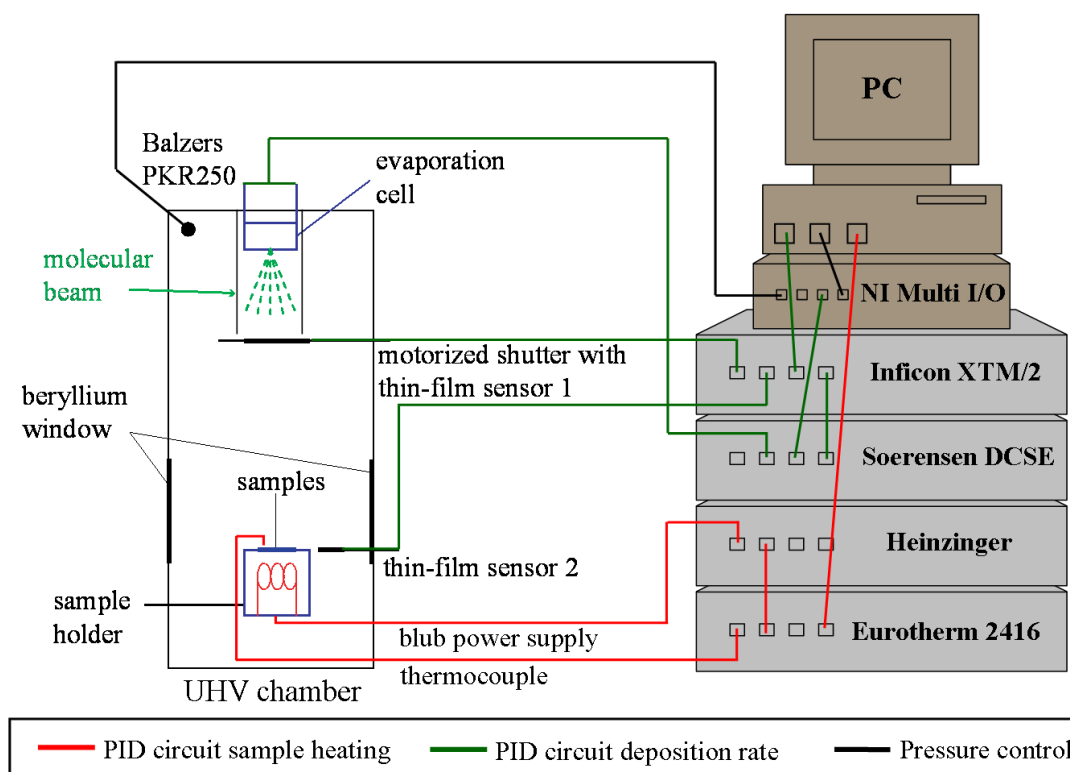
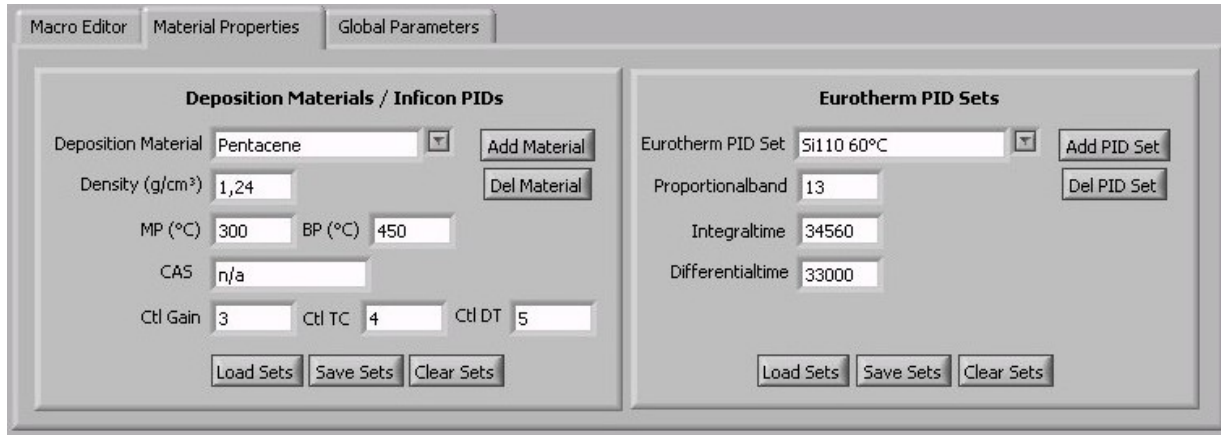
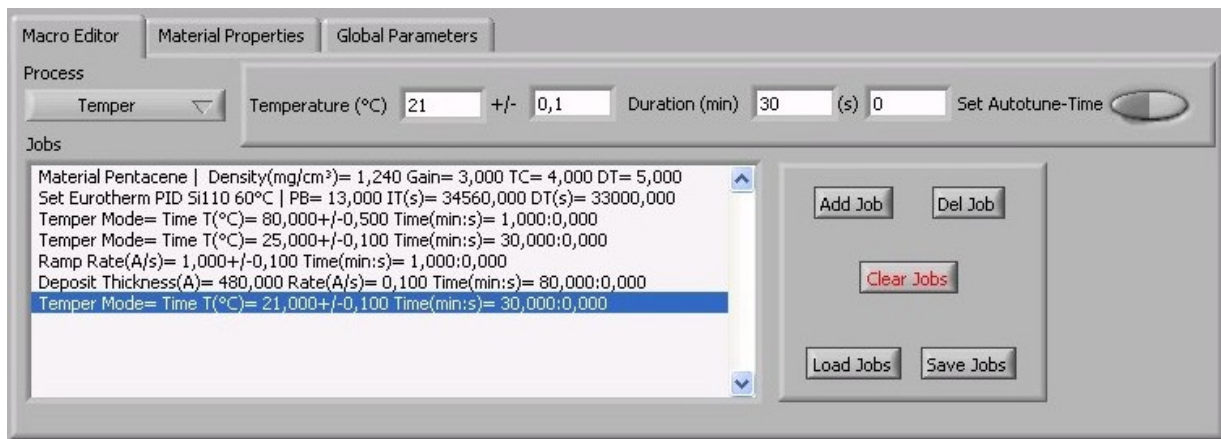


Figure 2.27: Electric wiring of the PGC setup. The setup consists of two major proportional-integral-derivative (PID) control loop feedback circuits indicated in red and green.



(a)



(b)

Figure 2.28: TFDS configuration: (a) Configuration of deposition material (left) and substrate material (right). (b) Macro script editor to enter commands for the deposition process, that are executed one after another in macro-mode.

in the configuration, the instrument converts the mass information into film thickness. Every material to be evaporated exhibits its characteristic melting and boiling point, thus different PID parameters can be configured to get a stable deposition rate. Depending on the thermal conduction and the target temperature, different PID parameters for the sample heating can be configured in order to get a stable substrate temperature. Both PID parameters sets can be gained automatically by a built in autotune command.

A thin film deposition process can be operated in two modes: Automated macro mode and manual mode. The macro-mode allows the user to enter commands with a macro-editor (figure 2.28b), which are then executed one after an other. Typically, a thin film deposition macro consists of three major tasks. Each task is assign to a command in the macro-editor and to a graphical user interface (GUI), which is displayed, when the command is executed:

1. Temper (figure 2.29): The temperature of the substrate can be set to a specific value for a certain time. This command allows controlled predeposition treatments, such as annealing. The GUI displays pressure, temperature and used heating power over time. In figure 2.29, the substrate surface was annealed at  $T=80^{\circ}\text{C}$  for 60 seconds. The increasing pressure at the beginning of the annealing process indicates, that contaminants like water or dust are desorbing from the substrate surface. The dropping pressure indicates that the contaminants evaporated and were exhausted by the turbopump.
2. Ramp (figure 2.30): The deposition rate at the beam shutter can be set to a specific value. This allows the molecular beam to become stable before the thin film is deposited on the sample. The GUI displays pressure, rate and heating power of the evaporation source over time. Here, not only the stability of the deposition rate can be monitored, but also contaminants with lower evaporation temperature than the deposition material can be detected during the heating process of the evaporation source, when the pressure is monitored over time.
3. Deposit (figure 2.31): With this command, the actual thin film deposition process is executed. Deposition rate at the substrate surface, final film thickness and deposition time can be set. The GUI displays pressure, substrate temperature, deposition rate, heating power of the evaporation source and thin film thickness.

With the help of these three commands and additional material configuration commands, any thin film deposition process with pre- and postdeposition treatments can automatically be executed.

In manual mode (figure 2.32), all deposition parameters must be entered manually during the thin film deposition process. All parameters like pressure, temperature, electric power of the substrate heating, film-thickness, deposition rate and electric power of the evaporation source are displayed over time in six diagrams. This mode allows the user to experiment with deposition parameters and to react directly during the deposition process.

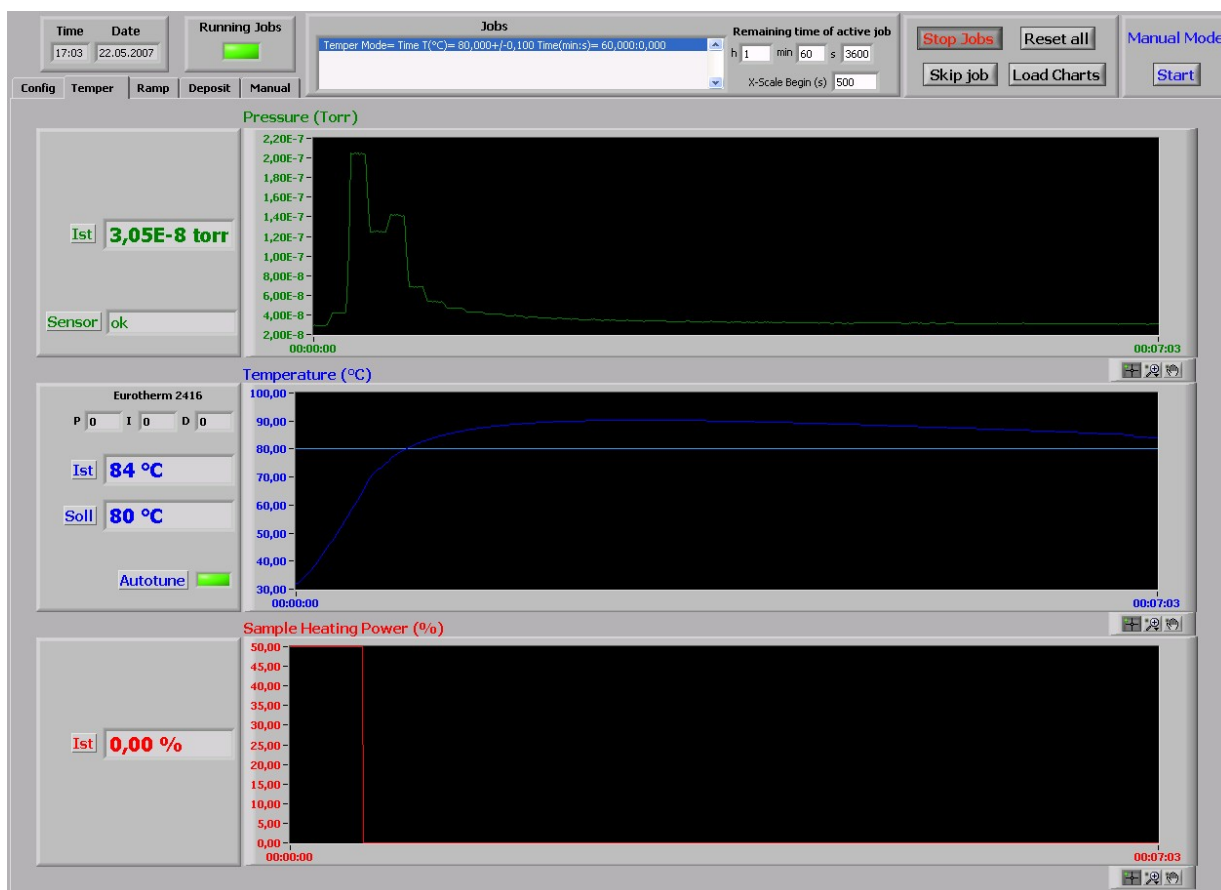


Figure 2.29: Screenshot of temper GUI. The temper command allows controlled predeposition treatments, such as annealing. It displays pressure, temperature and used heating power over time.

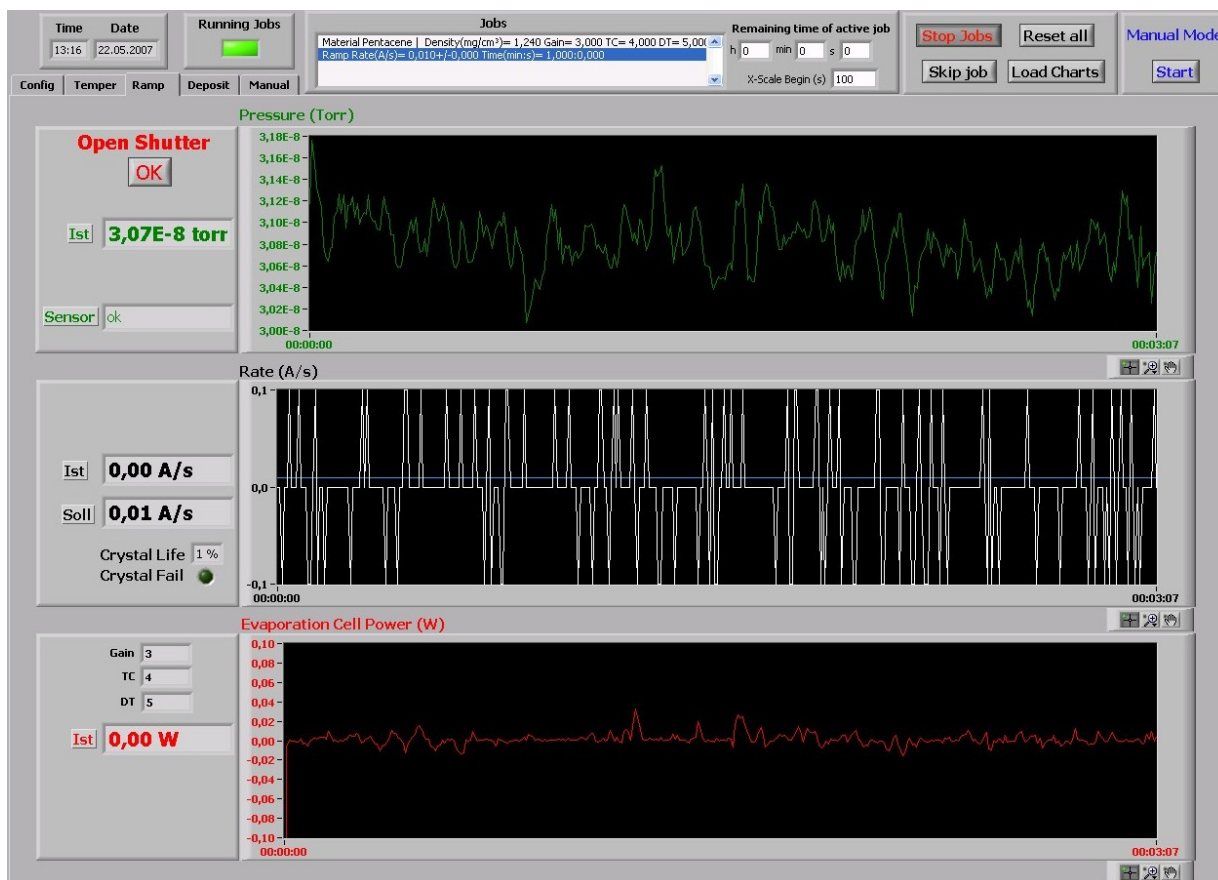


Figure 2.30: Screenshot of ramp GUI. The ramp command allows the deposition rate at the beam shutter to be set to a specific value and to become stable before the thin film deposition.

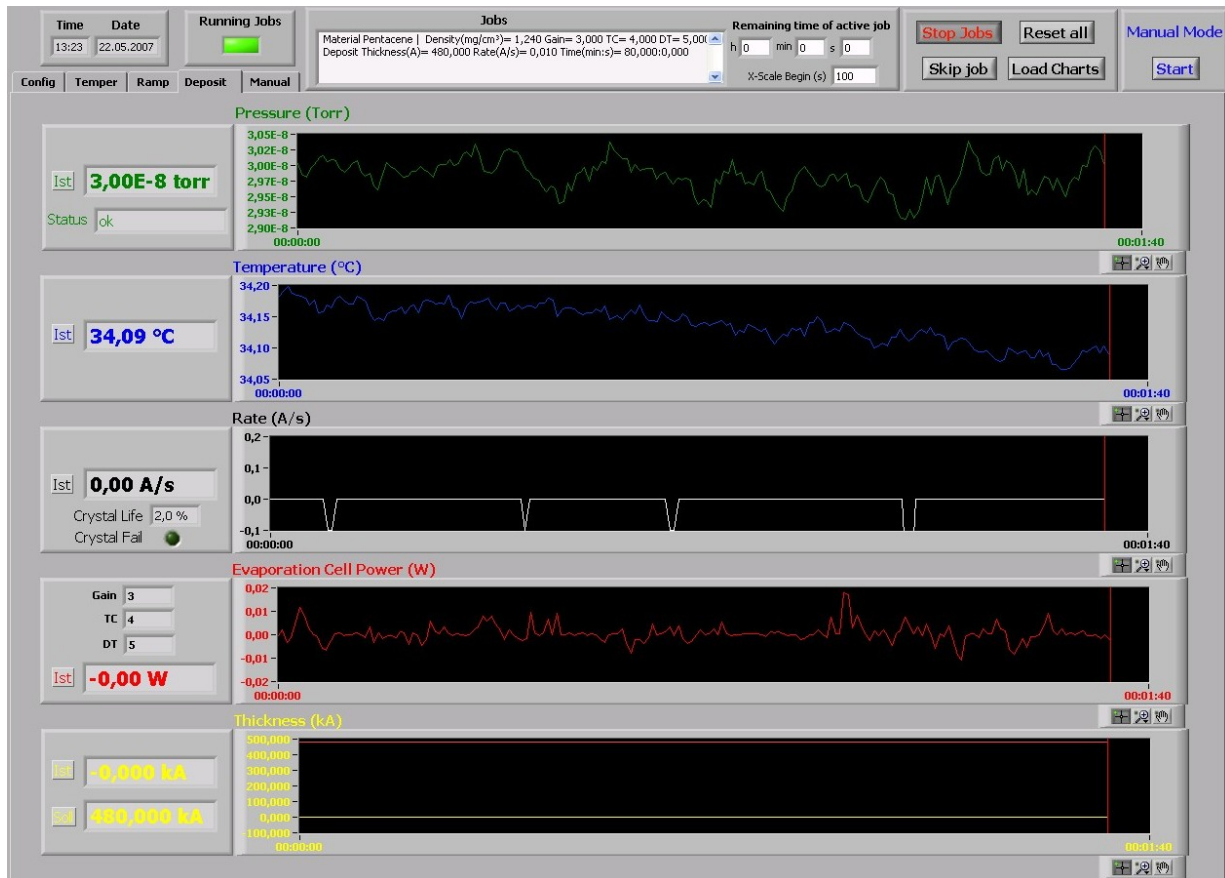


Figure 2.31: Screenshot of deposit GUI. The deposition command is responsible for the actual thin film deposition process and allows the user to set deposition rate at the substrate surface, thin film thickness and/or deposition time.



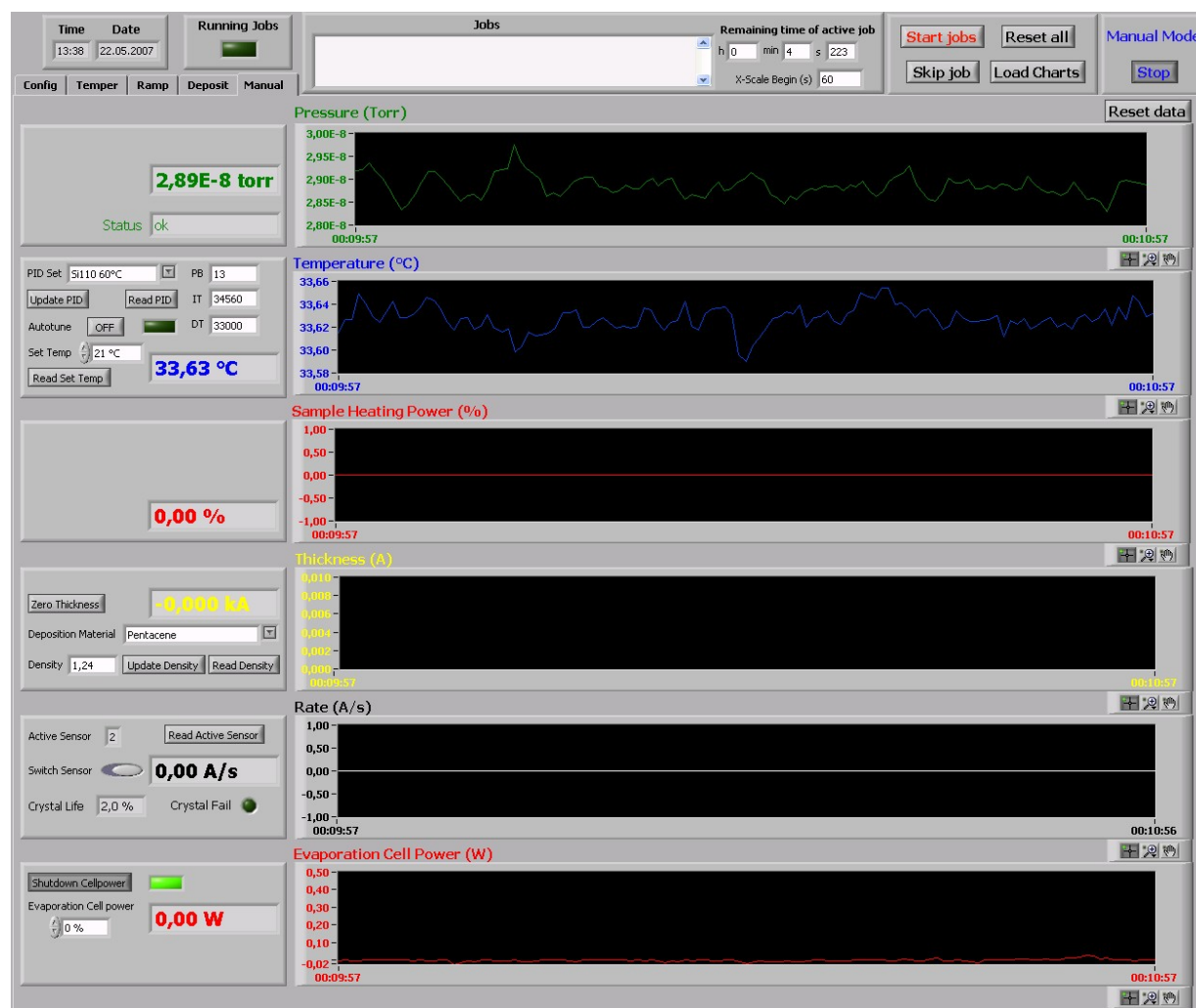


Figure 2.32: Screenshot of the manual mode. All parameters like pressure, temperature, electric power of the substrate heating, film-thickness, deposition rate and electric power of the evaporation source are displayed over time. The control buttons are located on the left of each diagram, that allow the user to experiment with deposition parameters.

### 2.5.3 OMBD of pentacene thin films

Pentacene is one of the most studied organic semiconductors in terms of deposition parameters. A number of groups have studied nucleation and growth dynamics of pentacene and the results have provided a deep insight into the thin film formation of organic materials in general [60, 33, 61, 45]. A study of the impact of deposition rate and substrate temperature on morphology of pentacene thin films has been published by Yanagisawa [1]. Figure 2.33 from this work shows the influence of growth temperature and deposition rate on the average grain size of a pentacene thin films grown on  $a - SiO_2$  with a surface roughness of 6 Å. They also measured the X-ray diffraction intensity of the 15.4 Å *thin-film* phase and the 14.4 Å bulk phase against growth temperature shown in the top diagram. The red dot marks the growth conditions that were chosen for pentacene thin films in this thesis. These were carefully selected in order to achieve the maximal diameter of pure 15.4 Å *thin-film* crystal grains. The substrate temperature was set to  $T = 30.0^\circ C$ , which is about  $10^\circ C$  lower than the temperature where the 14.4 Å bulk phase becomes detectable by X-ray reflectivity. A superimposed X-ray diffraction signal of the 14.4 Å bulk phase with the 15.4 Å *thin-film* phase would make the analysis of the crystal structure much more complicated and almost impossible. The optimal deposition rate with a predicted grain size of  $4 \mu m$  would be around  $1.5 \text{ \AA}/\text{min}$ . Unfortunately, the deposition rate had to be set to  $5 \text{ \AA}/\text{min}$ , since this represents the lowest detectable deposition rate, that can be monitored by the XTM/2 thin film monitor. The predicted crystal grain size under these growth conditions is about  $2 \mu m$  on  $a - SiO_2$ .

In order to get the maximum 3D crystal size, the 15.4 Å polymorph also needs to be maximized perpendicular to the substrate. It has been shown that on different substrates such as  $a - SiO_2$ , the 15.4 Å polymorph is formed in the first 30 monolayers. If the film becomes thicker the 14.4 Å structure appears, which was erroneously referred to as the bulk phase by some authors. If the film becomes extremely thick ( $>1300$  monolayers), the 14.1 Å phase is observed [4]. The 14.1 Å structure is observed in single crystals and on thin films grown on polyimide. This substrate does, therefore, not seem to influence the growth. However, the appearance of the 14.1 Å polymorph on thick films on a  $a - SiO_2$  substrate indicates that the 14.4 and 15.4 Å polymorphs are substrate induced. Therefore, pentacene thin films with a thickness of  $d_{tf} = 480 \text{ \AA}$  ( $\sim 30$  monolayers) represents the maximum thickness for the substrate induced 15.4 Å grains. The maximum 3D crystal size is mandatory to achieve the maximum signal to noise ratio by subsequent X-ray diffraction measurements.

The size of the 15.4 Å crystal grains are not just influenced by the substrate temperature, deposition rate and thin film thickness influence. The surface roughness of the used gate dielectrics where pentacene is deposited plays an important role. Knipp et.al. found, that the average size of the pentacene grains deposited on smooth silicon nitride with a surface roughness of  $3.5 \text{ \AA}$  increased by a factor of 30 to  $4.5 \mu m$ , when compared to rough silicon nitride with a surface roughness of  $8.0 \text{ \AA}$  [62, 63]. To investigate this effect on  $a - SiO_2$ , we deposited a  $240 \text{ \AA}$  pentacene thin film on custom-made  $a - SiO_2$  with a surface roughness of  $3.7 \text{ \AA}$  and commercially purchased  $a - SiO_2$  with a surface roughness

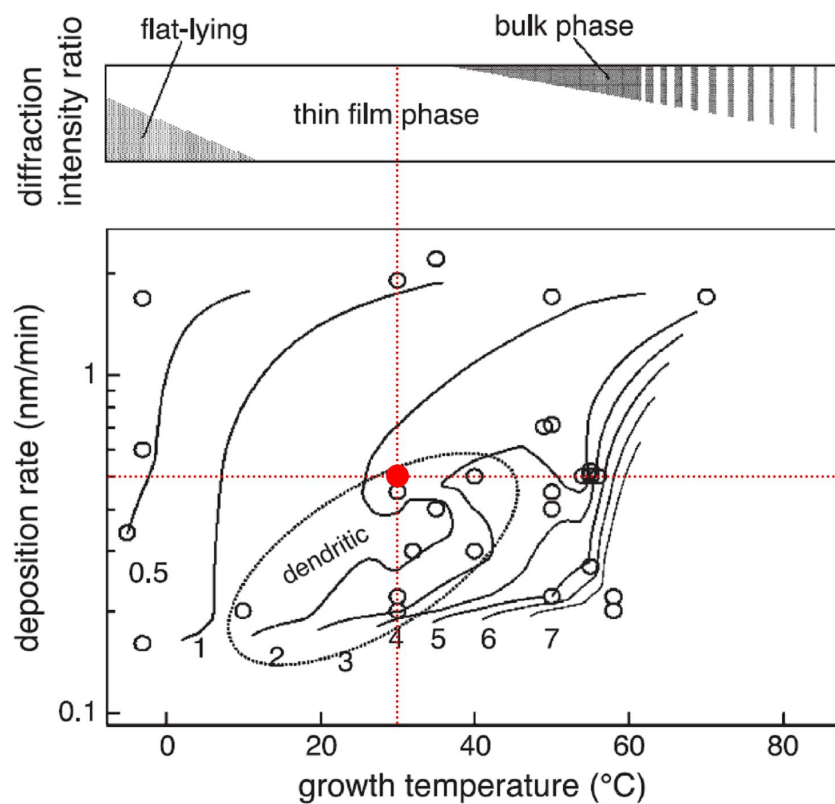


Figure 2.33: Effect of growth temperature and deposition rate on average grain size and polymorph of the resulting pentacene thin film grown on  $a - SiO_2$  with surface roughness of  $6 \text{ \AA}$  (figure from [1]). The red dot indicates the parameters used to grow pentacene thin films in this thesis.

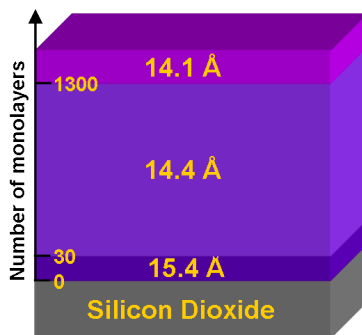
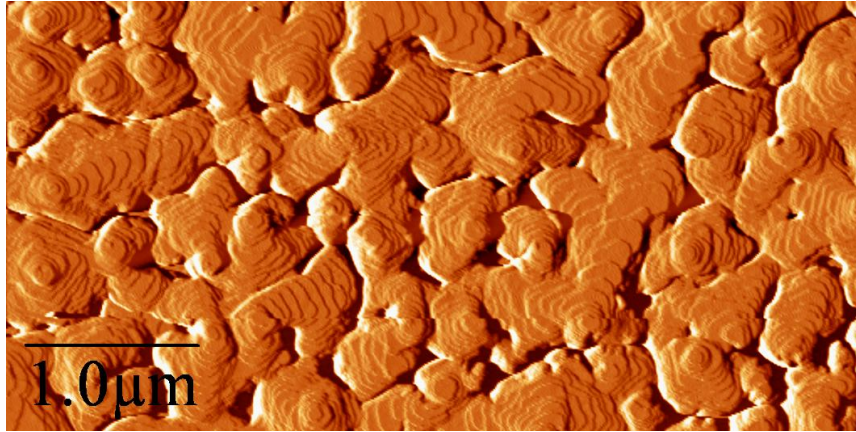
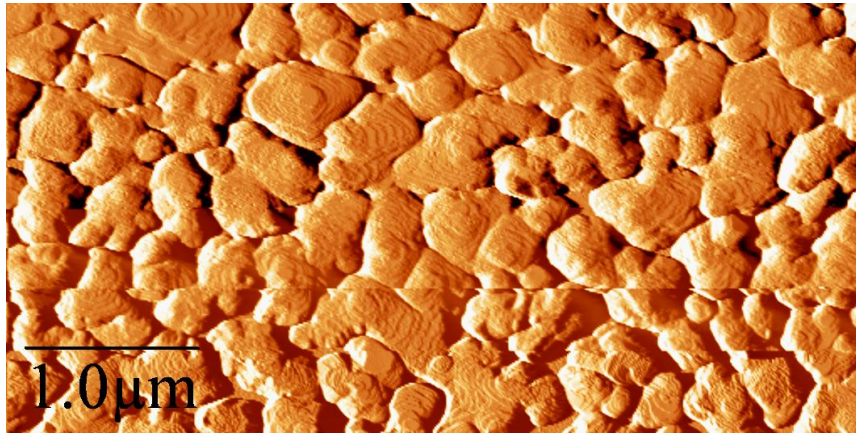


Figure 2.34: Schematic illustration of the growth of the different pentacene polymorphs on  $a - SiO_2$ .



(a)



(b)

Figure 2.35: AFM micrograph of a 240 Å pentacene thin film deposited on (a) custom-made  $a - SiO_2$  and (b) commercially purchased  $a - SiO_2$ .

of 5.3 Å. The thin film was deposited at an elevated temperature of  $T = 50^\circ C$  and a deposition rate of 10 Å/min. Subsequent AFM measurements showed, that the average grain size of pentacene on cusom-made  $a - SiO_2$  is  $1.4 \mu m$ , about twice as large as on commercially purchased  $a - SiO_2$  (figure 2.35). This result emphasizes the importance of the use of smooth gate dielectric substrates.

The gate dielectric substrates used for X-ray diffraction in this thesis were grown in the PGC on site at the synchrotron source beamline W1 at HasyLab, Hamburg in the following order: The substrates were mounted on the multi sample holder and the pressure was pumped down to  $5 \cdot 10^{-8} torr$ , which takes about 15 hours. The substrates were annealed for one minute at a substrate surface temperature of  $T_{an} = 80^\circ C$ . During annealing the base pressure increased to  $1 \cdot 10^{-7} torr$  and dropped to  $5 \cdot 10^{-8} torr$  about 2 hours after annealing. The substrate surface temperature was set to  $T_{gr} = 30^\circ C$ . A pentacene thin film with a thickness of  $d_{tf} = 480 \text{ \AA}$  ( $\sim 30$  monolayers) was deposited at a deposition rate

Gate dielectric	Bare gate dielectric			After deposition of pentacene	
	Thickness [Å]	Roughness [Å]		Grain diameter [ $\mu m$ ]	
		by X-ray	by AFM	by X-ray	by X-ray
$a - SiO_2$	2012	1.7	3.7	7.3	$\sim 2.0$
OTS	21.8	7.9	8.2	6.1	$\sim 0.8$
Topas	78.7	2.0	2.5	6.7	$\sim 2.2$
polystyrene	63.6	3.4	5.1	7.3	$\sim 1.0$

Table 2.3: Comparison of surface roughnesses and layer thickness of the gate dielectric substrates measured by AFM and X-ray reflectivity . Also given the average crystal grain diameter and the thin film roughness after the growth of a 480 Å pentacene thin film. Deposition rate was set to 1.7 nm/min for polystyrene and 0.5 nm/min for the other substrates. Substrate temperature was set to 30°C.

of 0.5 nm/min, which took about 96 minutes. The pentacene thin film on a polystyrene substrate was grown with 1.7 nm/min.

After the substrates were measured in-situ by X-ray diffraction at the synchrotron source, AFM measurements were performed to analyze the pentacene thin film morphology. The knowledge of the thin film morphology is essential to analyze the X-ray diffraction data and to solve the crystalline structure of the grains. 3D AFM micrographs of the different substrates are shown in figure 2.36. Clearly visible on every substrate are the single steps of the pentacene terraces, which corresponds to a pentacene monolayer with a  $d_{(001)}$  spacing of 15.4 Å. The crystal grains are forming a fiber structure with the fiber axes parallel to the substrate surface normal. Moreover, the grains have a dendritic pyramid like shape, with a height almost as big as the nominal film thickness. As expected from literature, the grains on  $a - SiO_2$  substrate have an average diameter of  $d_{gr} \sim 2.0 \mu m$  (figure 2.36a). Also, a reduced grain size  $d_{gr} \sim 0.8 \mu m$  on OTS treated  $a - SiO_2$  could be observed (figure 2.36b). This is the smallest grain size of the substrates measured. The grains on Topas however (figure 2.36a) show an average size of  $d_{gr} \sim 2.2 \mu m$ , which makes them the largest of all substrates. Polystyrene exhibited bigger grains than OTS treated  $a - SiO_2$ , but significantly smaller grains than Topas and  $a - SiO_2$ , which can be attributed to the relatively high growth rate.

A comparison of the surface roughness  $\sigma_{subs}$  of the gate dielectric surface with the resulting pentacene grain size shows the same trend, which Knipp et.al. observed for silicon nitride surfaces[63, 62]. Here, it can be formulated more general: The lower the surface roughness of the underlying gate dielectric, the bigger the grains. The surface roughness of the resulting pentacene thin film is not correlated with the average grain size or the gate dielectric surface roughness. It should be noted, that the pentacene thin film grown on OTS treated  $a - SiO_2$  exhibits the lowest surface roughness, although it has the smallest grains and biggest gate dielectric surface roughness. A comparison of the surface roughnesses, crystalline grains and growth conditions is given in table 2.3.

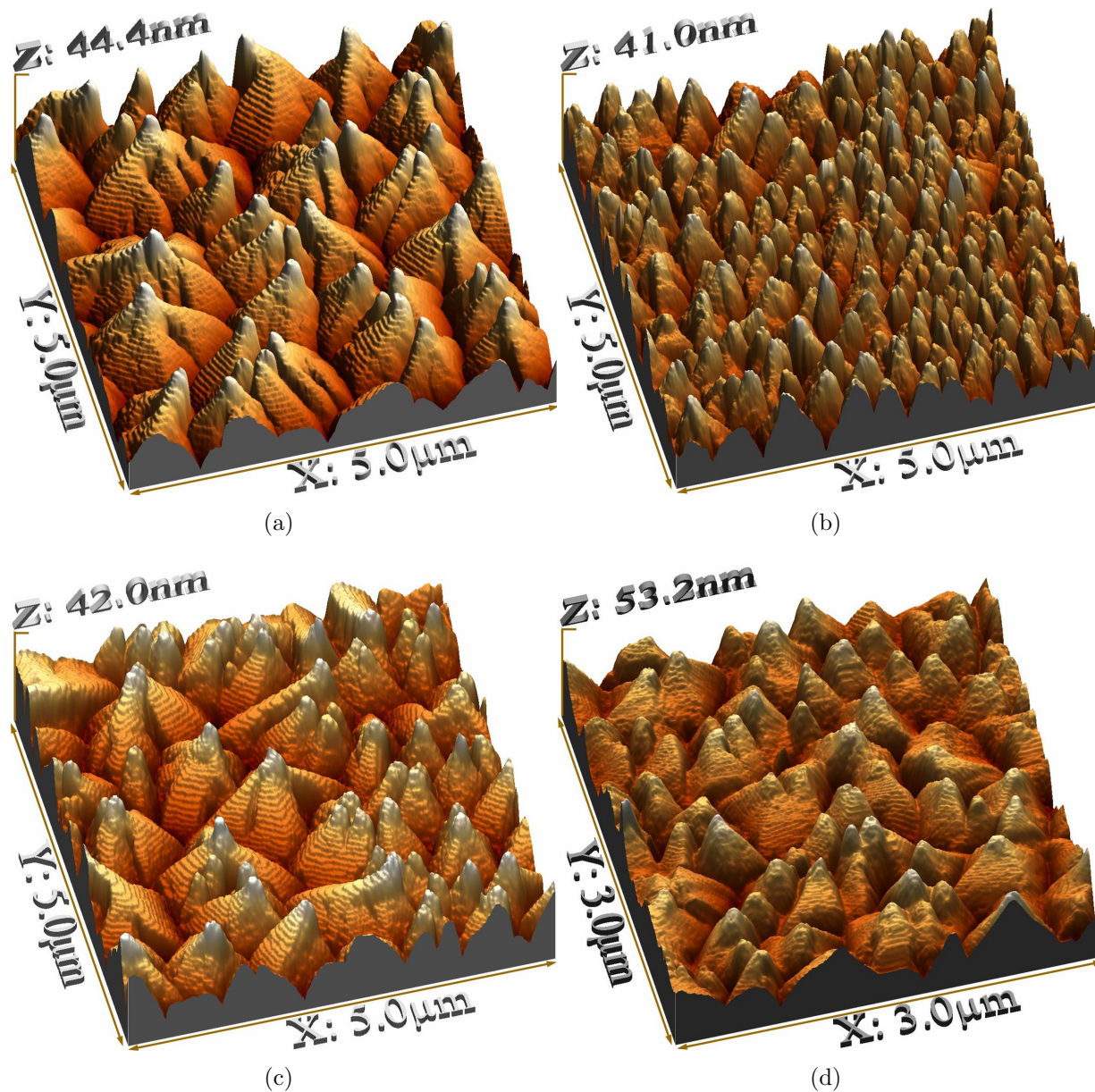


Figure 2.36: 3D AFM micrographs of a 480 Å pentacene thin film deposited at  $T=30^{\circ}\text{C}$  on different gate dielectric substrates: (a)  $\text{SiO}_2$  (b) OTS treated  $\text{SiO}_2$  (c) Topas (d) Polystyrene. The terraces correspond to a pentacene monolayer with a  $d_{(001)}$  spacing of 15.4 Å. (note, that (d) is only a  $3 \times 3 \mu\text{m}$  section, resulting in optical smaller grains when compared to  $5 \times 5 \mu\text{m}$  sections).

# Chapter 3

## Solving the crystal structure of a fiber structured thin film

In this chapter, the methodology to solve the unit-cell and the molecular arrangement of the 15.4 Å pentacene *thin-film* polymorph by X-ray diffraction grown in-situ on the model gate dielectrics as mentioned in the previous chapter is developed. The physical theory and its implementation in a Matlab software package called FiberRod to reproduce the observed X-ray diffraction patterns from fiber structured thin films is developed step by step using the kinematical scattering theory. First, a general theory to describe X-ray diffraction from single crystalline thin films based on the standard textbooks for X-ray scattering [64] is given. The theory is then extended to fit the observed characteristics of pentacene thin films like fiber structure and surface roughness. Hereafter, the experimental setup and the X-ray measurement techniques at HASYLab beamline W1 are presented and its effects on the observed X-ray diffraction patterns are derived. After that, the implementation of these findings in the software package “FiberRod” coded in Matlab is discussed.

### 3.1 Kinematical theory of X-ray diffraction

#### 3.1.1 Crystal axes and the reciprocal lattice

A crystal is composed of a unit cell (figure 3.1), which is repeated in three independent directions, defined by the unit cell vectors  $\vec{a}$ ,  $\vec{b}$  and  $\vec{c}$ . The volume of the unit cell is then given by  $V = \vec{a} \cdot \vec{b} \times \vec{c}$ . The unit cell itself can be composed of  $n$  units of atoms or molecules, whose positions are given by  $r_n^{\vec{}}$  relative to the unit cell origin.

Directions with repeating units in crystals are described by the Miller indices  $h, k$  and  $l$ , which define a set of lattice planes  $(hkl)$ <sup>1</sup> in that direction (figure 3.2). This set of lattice

---

<sup>1</sup>There are also several related notations:  $[hkl]$  with square instead of round brackets, denotes a direction in the basis of the direct lattice vectors instead of the reciprocal lattice. The notation  $\{hkl\}$  denotes all planes that are equivalent to  $(hkl)$  by the symmetry of the crystal. Similarly, the notation  $\langle hkl \rangle$  denotes all directions that are equivalent to  $[hkl]$  by symmetry.

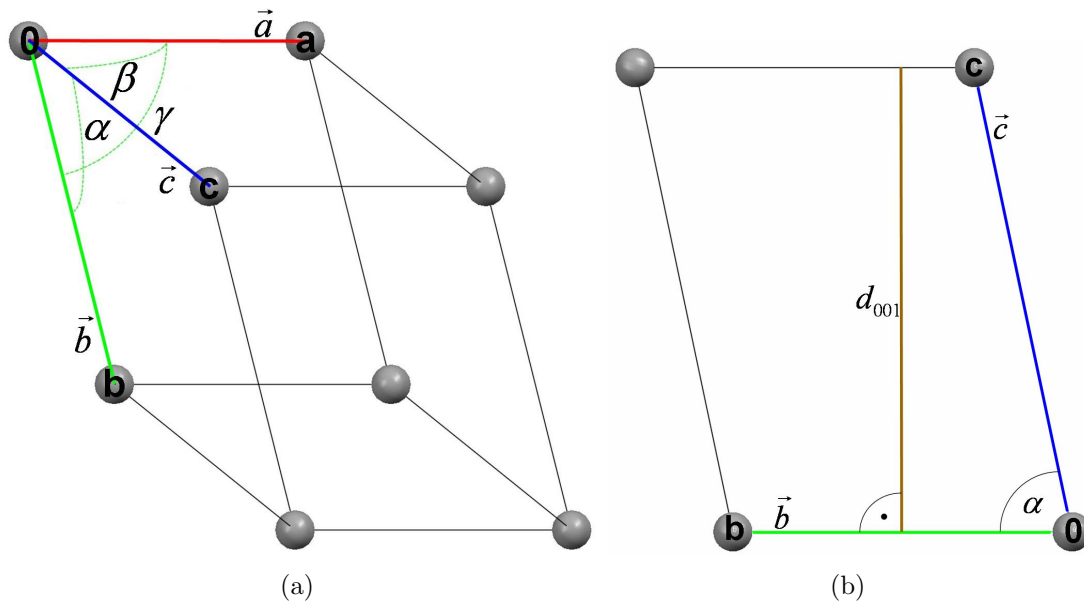


Figure 3.1: (a) Schematic representation of the unit cell, illustrating the unit cell vectors  $\vec{a}$ ,  $\vec{b}$  and  $\vec{c}$  and their respective angles  $\alpha$ ,  $\beta$  and  $\gamma$ . (b) Schematic representation of  $d_{001}$ .

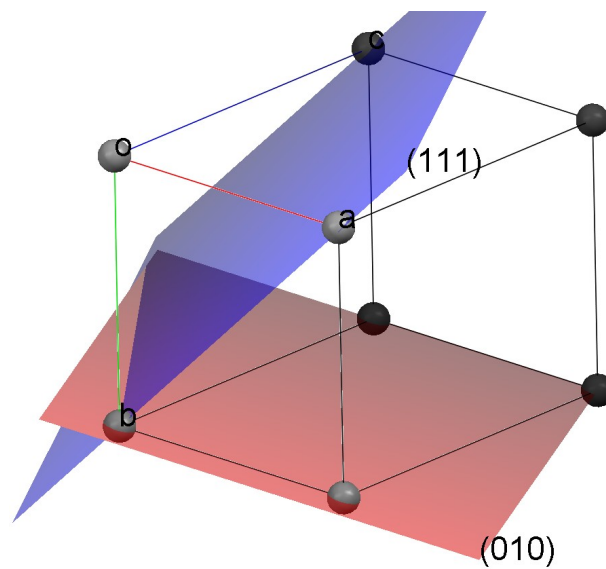


Figure 3.2: Illustration of crystallographic planes with their corresponding Miller indices notation  $(1\ 1\ 1)$  and  $(0\ 1\ 0)$ .



planes, determined by the three integers  $h$ ,  $k$  and  $l$ , define a set of equidistant planes. One which passes through the origin and the next nearest which makes intercepts at  $\vec{a}/h$ ,  $\vec{b}/k$  and  $\vec{c}/l$  on the three crystallographic axes. By convention, negative integers are written with a bar, as  $\bar{3}$  for  $-3$ . The integers are usually written in lowest terms, i.e. their greatest common divisor should be 1. The Miller notation is particularly useful, when using Bragg's law in the reciprocal lattice notation. The three reciprocal vectors, which form the reciprocal lattice, are defined by:

$$\vec{a}_r = 2\pi \frac{\vec{b} \times \vec{c}}{V}, \quad \vec{b}_r = 2\pi \frac{\vec{c} \times \vec{a}}{V}, \quad \vec{c}_r = 2\pi \frac{\vec{a} \times \vec{b}}{V} \quad (3.1)$$

Each reciprocal vector is perpendicular to the plane defined by the two crystal axes in the numerator. Next, a vector  $\vec{H}_{hkl}$  is defined, which is perpendicular to the set of planes  $hkl$ , and whose magnitude is the reciprocal of the spacing using the equations 3.1 and the Miller indices  $hkl$ :

$$\vec{H}_{hkl} = h\vec{a}_r + k\vec{b}_r + l\vec{c}_r \quad (3.2)$$

Hence, the  $d_{hkl}$  spacing between two consecutive planes in a set of planes  $hkl$  is given by:

$$d_{hkl} = \frac{2\pi}{|\vec{H}_{hkl}|} \quad (3.3)$$

Next, the wave vectors  $\vec{k}_i$  and  $\vec{k}_f$ , which specify the wavenumber and direction of propagation for a wave are defined for the incident and the diffracted beam:

$$\vec{k}_{i,f} = \frac{2\pi}{\lambda} \vec{s}_{i,f} \quad (3.4)$$

where  $\vec{s}$  is the unit vector pointing in the direction of the wave. The magnitude of the wave vector indicates the wavenumber. If  $\vec{k}_i$  and  $\vec{k}_f$  are the wave vectors in the directions of the incident and diffracted beam and  $\theta$  is the angle between  $\vec{k}_{i,f}$  and  $\vec{H}_{hkl}$  with the diffracting planes (figure 3.3), Bragg's law is given by the vector equation:

$$\vec{k}_f - \vec{k}_i = \vec{q} = \vec{H}_{hkl} \quad (3.5)$$

where  $\vec{q}$  is the momentum transfer perpendicular to the diffracting planes.

The vector equation 3.5 implies two conditions: (1)  $\vec{q}$  and  $\vec{H}_{hkl}$  are parallel; (2) the magnitudes  $|\vec{q}|$  and  $|\vec{H}_{hkl}|$  are equal, which leads to the equation:

$$\frac{4\pi \sin(\theta)}{\lambda} = |\vec{q}| = |\vec{H}_{hkl}| = \frac{2\pi}{d_{hkl}} \Rightarrow \lambda = 2d_{hkl} \sin \theta \quad (3.6)$$

Equation 3.6 is equivalent to the classical form of Bragg's law. To conclude, the reciprocal lattice provides a simple representation of Bragg's law. Reflection spots observed in the diffraction image correspond to Bragg peaks. The Bragg peak positions in the reciprocal lattice allow one to solve and construct the three unit cell vectors  $\vec{a}$ ,  $\vec{b}$  and  $\vec{c}$ . The

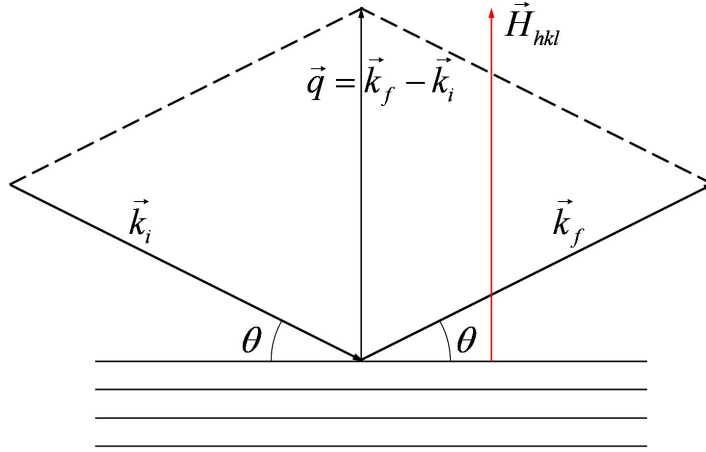


Figure 3.3: Vector representation of Bragg's Law.

three unit-cell vectors are determined by six parameters: the magnitudes  $a$ ,  $b$  and  $c$ , and the three angles  $\alpha$ ,  $\beta$  and  $\gamma$  between the vectors (figure 3.1). In the Cartesian coordinate system, which will be used for further calculations, the unit-cell vectors were defined as follows:

$$\vec{a} = \begin{pmatrix} 0 \\ 0 \\ a \end{pmatrix} \quad (3.7)$$

$$\vec{b} = \begin{pmatrix} 0 \\ b \cdot \sin \gamma \\ b \cdot \cos \gamma \end{pmatrix} \quad (3.8)$$

$$\vec{c} = d_{001} \begin{pmatrix} 1 \\ (\cos \alpha - \cos \beta \cdot \cos \gamma) \cdot w \\ \cos \beta \cdot \sin \gamma \cdot w \end{pmatrix} \quad (3.9)$$

$$w = 1/\sqrt{2 \cos \alpha \cdot \cos \beta \cdot \cos \gamma - \cos^2 \alpha - \cos^2 \beta + \sin^2 \gamma}.$$

The equations imply that  $\vec{a}$  starts at the coordinate origin and is fixed in z-axis direction. Unit cell vector  $\vec{b}$  makes an angle  $\gamma$  with  $\vec{a}$  in the  $\vec{y}$ ,  $\vec{z}$ -plane. For several reasons the unit cell vector  $\vec{c}$  is defined by using the  $d_{001}$ -spacing. First, pentacene polymorphs are identified their typical  $d_{001}$ -spacing, which is 15.4 Å for the *thin-film* phase. Therefore, this parameter is very well known from literature and has been examined in great detail by many groups. Last and maybe most importantly,  $d_{001}$  can be calculated easily and precisely from X-ray reflectivity measurements. The magnitude of  $\vec{c}$  can be derived by calculating its norm given by equation 3.9. The definition of the unit cell vectors imply that the substrate surface is in the  $\vec{y}$  –  $\vec{z}$ -plane and thus also the  $\vec{a}$  –  $\vec{b}$ -plane. The growth direction of the

thin film is in direction of the x-axis, which is parallel to the  $\vec{d}_{00l}$  spacing vector and the surface normal  $\vec{n} = (1, 0, 0)$ .

The reciprocal vectors defined in equation 3.1 can now be expressed with the six unit cell parameters  $a$ ,  $b$ ,  $d_{00l}$ ,  $\alpha$ ,  $\beta$  and  $\gamma$  using the equations 3.7-3.9:

$$\vec{a}_r = \frac{2\pi}{a} \begin{pmatrix} (\cos \alpha \cdot \cos \gamma - \cos \beta) \cdot u \\ -\cot \gamma \\ 1 \end{pmatrix} \quad (3.10)$$

$$\vec{b}_r = \frac{2\pi}{b} \begin{pmatrix} (\cos \beta \cdot \cos \gamma - \cos \alpha) \cdot u \\ \sin^{-1} \gamma \\ 0 \end{pmatrix} \quad (3.11)$$

$$\vec{c}_r = \frac{2\pi}{d_{00l}} \begin{pmatrix} 1 \\ 0 \\ 0 \end{pmatrix} \quad (3.12)$$

$$u = \sin^{-1} \gamma \cdot w = 1 / \left( \sin \gamma \cdot \sqrt{2 \cos \alpha \cdot \cos \beta \cdot \cos \gamma - \cos^2 \alpha - \cos^2 \beta + \sin^2 \gamma} \right)$$

Using these equations, Bragg's law can now be expressed in terms of the six unit cell parameters and the Miller indices using the equations 3.2 and 3.5:

$$\begin{aligned} \vec{q} &= 2\pi \left[ \frac{h}{a} \begin{pmatrix} (\cos \alpha \cdot \cos \gamma - \cos \beta) \cdot u \\ -\cot \gamma \\ 1 \end{pmatrix} + \frac{k}{b} \begin{pmatrix} (\cos \beta \cdot \cos \gamma - \cos \alpha) \cdot u \\ \sin^{-1} \gamma \\ 0 \end{pmatrix} + \frac{l}{d_{00l}} \begin{pmatrix} 1 \\ 0 \\ 0 \end{pmatrix} \right] \\ &= 2\pi \left[ \begin{array}{c} \frac{l}{d_{00l}} + u \cdot \left( \frac{h}{a} (\cos \alpha \cos \gamma - \cos \beta) + \frac{k}{b} (\cos \beta \cos \gamma - \cos \alpha) \right) \\ \sin^{-1} \gamma \left( \frac{k}{b} - \frac{h}{a} \cos \gamma \right) \\ \frac{h}{a} \end{array} \right] \quad (3.13) \end{aligned}$$

The  $\vec{q}$ -vector's magnitude can be split into the momentum transfer perpendicular to the surface  $q_{\perp}$  and parallel to the surface  $q_{\parallel}$ :

$$q_{\perp} = \vec{q} \cdot \vec{n} = 2\pi \cdot \left[ u \cdot \left( \frac{h}{a} (\cos \alpha \cos \gamma - \cos \beta) + \frac{k}{b} (\cos \beta \cos \gamma - \cos \alpha) \right) + \frac{l}{d_{00l}} \right] \quad (3.14)$$

$$q_{\parallel} = |\vec{q} - \vec{q}_{\perp}| = \frac{2\pi}{ab \cdot \sin \gamma} \sqrt{h^2 b^2 + k^2 a^2 - 2hkba \cdot \cos \gamma} \quad (3.15)$$

From these two equations, several correlations between  $q_{\perp}$  and  $q_{\parallel}$  (or Bragg peak positions) and the six unit cell parameters can be seen:

Equation 3.15 shows that  $q_{\parallel}$  only depends on  $a$ ,  $b$  and  $\gamma$ . Thus, X-ray measurement techniques such as grazing incidence X-ray diffraction (GIXD), that are based on momentum transfer parallel to the surface, only allow unit cell parameters  $a$ ,  $b$  and  $\gamma$  to be solved

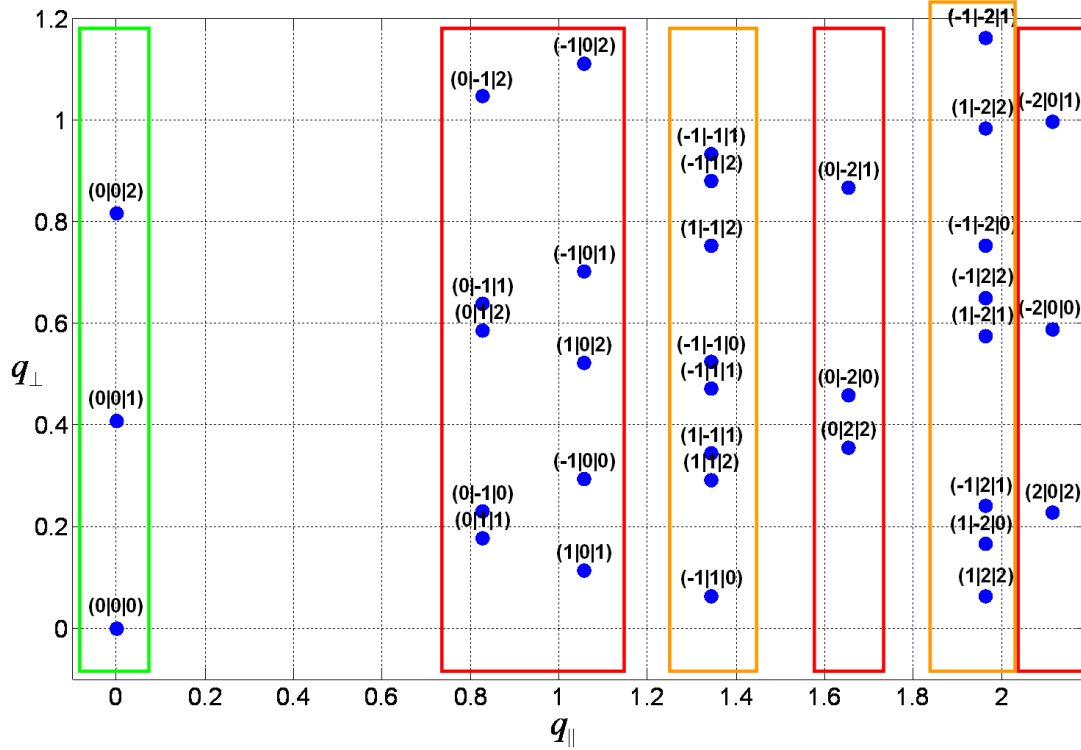


Figure 3.4: Simulated Bragg peak positions and their corresponding Miller indices found using equations 3.14 and 3.15. As  $\gamma = 90^\circ$ , Bragg peaks with equal modulus of  $h$  and  $k$  share the same  $q_{||}$  (marked by orange boxes). Bragg peaks with  $h = 0$  or  $k = 0$  always share the same  $q_{||}$  independent of  $\gamma$  (marked by red boxes). For Bragg peaks with  $h = k = 0$ ,  $q_{||} = 0$  (marked by green boxes). These peaks are observed in X-ray reflectivity measurements.

for. The most interesting term of this equation is the last term in the root  $2hkb a \cdot \cos \gamma$ . This term equals zero, if either of the Miller indices  $h$  or  $k$  equals zero. Thus, Bragg peaks with these indices always have the same magnitude of parallel momentum transfer  $q_{||}$  independent of  $l$  as illustrated by red boxes in figure 3.4. The simulation in this figure was done for  $\gamma = 90^\circ$ , which means that  $2hkb a \cdot \cos \gamma = 0$ . In this case, Bragg peaks with indices of  $\pm h$  and  $\pm k$  share the same parallel momentum transfer, as  $h$  and  $k$  are always squared in the remaining terms of equation 3.15. These Bragg peaks are marked with yellow boxes, also illustrated in figure 3.4.

If  $\gamma \neq 90^\circ$ , then  $2hkb a \cdot \cos \gamma$  is  $\neq 0$ . As  $h$  and  $k$  are not squared in this term, Bragg peaks with equal modulus of  $h$  and  $k$  split up in  $q_{||}$  by  $\pm 2hkb a \cdot \cos \gamma$  in the root term. This is illustrated by the yellow boxes in figure 3.5, where Bragg peaks were simulated with  $\gamma = 85^\circ$ . The other Bragg peaks marked by red and green boxes do not split up in  $q_{||}$ . The perpendicular momentum transfer  $q_{\perp}$  of all Bragg peaks, except the ones observed in X-ray reflectivity measurements (marked by a green box), changed according to equation 3.14. The X-ray reflectivity Bragg peaks will be used later to determine the  $d_{001}$ -spacing.

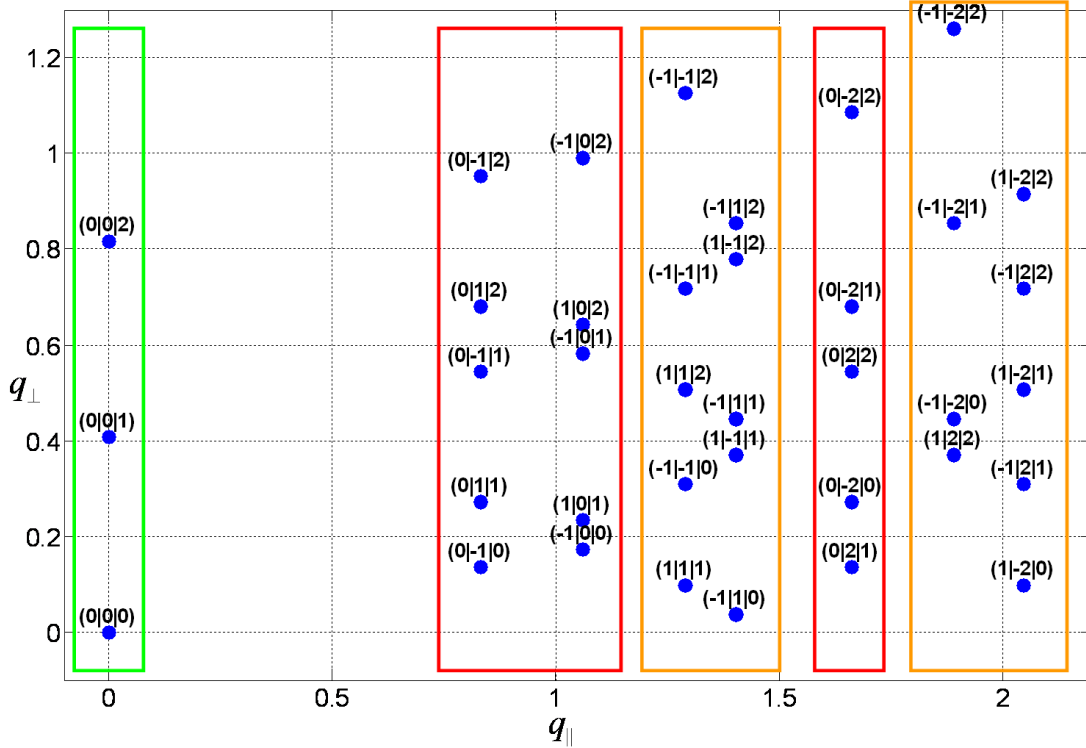


Figure 3.5: Simulated Bragg peak positions and their corresponding Miller indices found using equations 3.14 and 3.15 and  $\gamma = 85^\circ$ . Bragg peaks with equal modulus of  $h$  and  $k$  (marked by orange boxes) now split up in  $q_{||}$  by  $\pm 2hkb a \cdot \cos \gamma$  when compared to  $\gamma = 90^\circ$  (figure 3.4), while the other Bragg peaks do not split up in  $q_{||}$ .

In this case equation 3.14 reduces to:

$$q_{\perp} = 2\pi \frac{l}{d_{00l}} \Rightarrow d_{00l} = 2\pi \cdot \frac{l}{q_{\perp}} \quad (3.16)$$

Equation 3.14 shows that  $q_{\perp}$  depends on all six unit cell parameters. Therefore, the knowledge of Bragg peaks positions with a perpendicular momentum transfer and a parallel momentum transfer when  $h, k > 0$  is mandatory to resolve the full set of unit cell parameters.

### 3.1.2 Diffraction intensity of a thin film

In the previous chapter the Bragg peak positions in reciprocal space, which are determined by the six unit cell parameters, were examined. In this chapter, the diffracted intensity of a thin film is derived to resolve the molecular orientation in the unit cell.

A plane monochromatic X-ray wave  $A_0 \cdot \exp(i \cdot q_i \cdot \vec{r})$  is incident on a crystal (figure 3.3). The direction of the wave is given by  $\vec{r}$ . The position of the  $n$ -th atom of type  $m$

Atom type m	C	H.
$c$	0.2156	0.001305
$a_1$	2.31	0.489918
$a_2$	1.02	0.262003
$a_3$	1.5886	0.196767
$a_4$	0.865	0.049879
$b_1$	20.8439	20.6593
$b_2$	10.2075	7.74039
$b_3$	0.5687	49.5519
$b_4$	51.6512	2.20159

Table 3.1: Cromer-Mann coefficients of carbon (C) and hydrogen (H).

in the unit cell relative to the unit cell origin is given by  $r_n^m$ . Assuming for simplicity that the crystal has a shape of a parallelepipedon with edges  $N_a \vec{a}$ ,  $N_b \vec{b}$ , and  $N_c \vec{c}$  parallel to the crystal axes, the amplitude  $A(\vec{q})$  of the scattered X-ray wave along  $q_f$  is given by the lattice sum:

$$A(\vec{q}) = A_0 \frac{r_e}{R_0} F(\vec{q}) \sum_{n_a=0}^{N_a-1} \sum_{n_b=0}^{N_b-1} \sum_{n_c=0}^{N_c-1} \exp(i \cdot n_a \vec{q} \cdot \vec{a}) \exp(i \cdot n_b \vec{q} \cdot \vec{b}) \exp(i \cdot n_c \vec{q} \cdot \vec{c}) \quad (3.17)$$

$$F(\vec{q}) = \sum_m f_m(q) \sum_n \exp(i \cdot \vec{q} \cdot \vec{r}_n^m) \quad (3.18)$$

$$f_m(|\vec{q}|) = \sum_{i=1}^4 a_i \cdot \exp\left(-b_i \left(\frac{|\vec{q}|}{4\pi}\right)^2\right) + c \quad (3.19)$$

$A_0$  represents the incident beam amplitude,  $r_e$  the classical electron radius,  $R_0$  the distance of the scattering center to the detector and  $N_a$ ,  $N_b$ ,  $N_c$  the number of unit cells in the direction of the unit cell axes given by the indices.  $N_a \cdot N_b$  represents the typical size of a crystal along the surface given in square unit-cells.  $N_c$  is the thickness of the thin film, which is  $\sim 30$  unit-cells for the pentacene *thin-film* phase. The summations over  $n_{a-c}$  in equation 3.17 can be simplified by calculating the geometric progression:

$$\sum_{n=0}^{N-1} \exp(n \cdot x) = \frac{\exp(N \cdot x) - 1}{\exp(x) - 1} \quad (3.20)$$

Using this simplification,  $A(\vec{q})$  in equation 3.17 becomes:

$$A(\vec{q}) = A_0 \frac{r_e}{R_0} F(\vec{q}) \cdot \frac{\exp(i \cdot N_a \cdot \vec{q} \cdot \vec{a}) - 1}{\exp(i \cdot \vec{q} \cdot \vec{a}) - 1} \cdot \frac{\exp(i \cdot N_b \cdot \vec{q} \cdot \vec{b}) - 1}{\exp(i \cdot \vec{q} \cdot \vec{b}) - 1} \cdot \frac{\exp(i \cdot N_c \cdot \vec{q} \cdot \vec{c}) - 1}{\exp(i \cdot \vec{q} \cdot \vec{c}) - 1} \quad (3.21)$$

The observable intensity  $I(\vec{q})$  is given by multiplying  $A(\vec{q})$  with its complex conjugate  $A^*(\vec{q})$ :

$$I(\vec{q}) = A(\vec{q}) \cdot A^*(\vec{q}) \quad (3.22)$$

$F(\vec{q})$  describes the structure factor (equation 3.18) which plays a very important role for the determination of the crystal structure, since it is only in the structure factor, that atomic positions  $\vec{r}_n^m$  appear. The incoming X-rays are scattered by the electrons of the atoms. As the wavelength of the X-rays is on the order of the atom diameter, most of the scattering is in the forward direction. It is also obvious that the X-ray scattering power will depend on the number of electrons in the particular atom. The X-ray scattering power of an atom decreases with increasing scattering angle and is higher for heavier atoms. The normalized scattering curves have been fitted to a 9-parameter equation  $f_m(q)$  3.19 by Don Cromer and J. Mann ([65] p. 500-502). Knowing the 9 coefficients,  $a_i$ ,  $b_i$  and  $c$ , and the X-ray wavelength, the atomic scattering factor of each atom type at any given scattering angle can be calculated.  $f_m(q)$  only describes the non-dispersive part of the atomic scattering factor of an atom of type  $m$ . The atomic scattering factor contains additional complex contributions from anomalous dispersion effects (essentially resonance absorption) which become substantial in the vicinity of the X-ray absorption edge of the scattering atom (see figure 3.6). As pentacene is composed of hydrogen and carbon atoms and the X-ray energy of 10500 eV used throughout this study is far beyond the absorption edges, the changes in the intensities caused by the anomalous scattering are very small and were neglected. The Cromer-Mann coefficients for carbon and hydrogen are given in table 3.1.

Atoms are never residing at fixed lattice sites, they are thermally vibrating around an average position. This is accounted for by the Debye-Waller factor in the structure factor given equation 3.18:

$$F(\vec{q}) = \exp\left(-B \left(\frac{|\vec{q}|}{4\pi}\right)^2\right) \cdot \sum_m f_m(|\vec{q}|) \sum_n \exp(i \cdot \vec{q} \cdot \vec{r}_n^m) \quad (3.23)$$

where  $B$  is called the  $B$ -factor. For isotropic vibrations the  $B$ -factor is given by:

$$B = 8\pi^2 u^2 = 8\pi^2 U_{iso} \quad (3.24)$$

where  $u^2$  is the real absolute mean square displacement, which is also equivalent to the crystallography standard  $U_{iso}$ . Replacing  $B$  in the structure factor yields:

$$F(\vec{q}) = \exp(-U_{iso} \cdot |\vec{q}|^2/2) \cdot \sum_m f_m(|\vec{q}|) \sum_n \exp(i \cdot \vec{q} \cdot \vec{r}_n^m) \quad (3.25)$$

### 3.1.3 Diffraction intensity of a pentacene thin film

In the previous chapter, an analytical expression of the diffraction intensity of a monocrystalline thin film with a shape of a parallelepipedon with edges  $N_a \vec{a}$ ,  $N_b \vec{b}$ ,  $N_c \vec{c}$  (equation

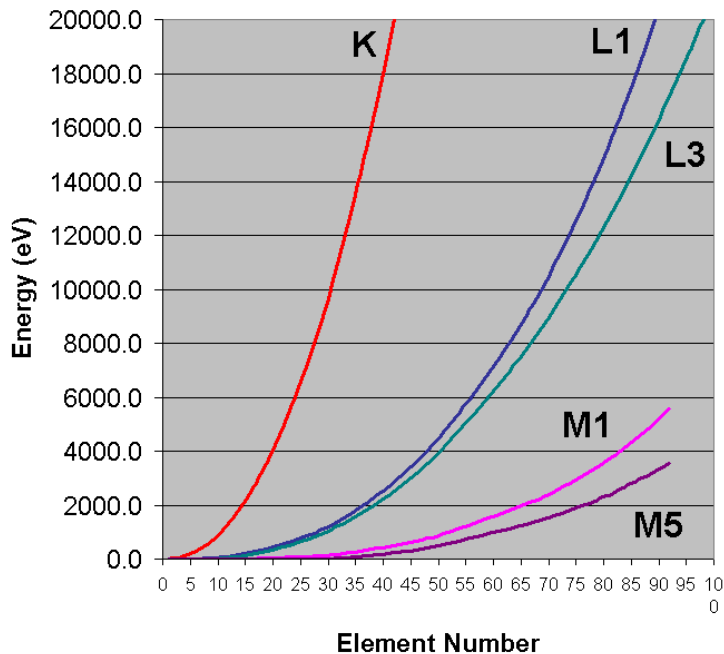


Figure 3.6: X-ray absorption edges of the elements.

3.21) was derived. Here, the theory of the diffracted intensity is extended to fit the specific properties of pentacene thin films.

### Surface morphology

AFM measurements of pentacene thin films (figure 2.36) show, that the surface morphology of a typical crystal grain has a dendritic pyramid like shape with a height almost as big as the nominal film thickness. An analysis of the height profile along a pyramid plane suggests, that the observed terraces correspond to a pentacene monolayer (figure 3.7) as the height of a terrace step corresponds closely to the length of a pentacene molecule of  $1.54 \text{ nm}$ . Since X-ray reflectivity measurements of the pentacene *thin-film* phase only showed  $(00l)$  Bragg reflections associated with a spacing of  $d_{(00l)} = 15.4 \text{ \AA}$ , the crystallites are supposed to form a fiber structure with their  $\vec{a} - \vec{b}$  plane oriented parallel to the substrate surface and the fiber axes oriented parallel to the substrate normal [29]. Accordingly, the terraces are oriented parallel to the substrate surface. This surface morphology can be described by introducing an exponential decaying profile function  $\rho(n_c)$  in the direction of the  $\vec{c}$ -axis, which is defined for  $0 \leq n_c \leq N_c$ :

$$\rho(n_c) = \exp(-n_c \cdot \sigma) \quad (3.26)$$

$\sigma$  is the slope or the inverse length of the decay profile function. The pentacene monolayers in  $\vec{c}$ -axis direction are numbered by the integer variable  $n_c$  which runs from 0 (first monolayer on the gate dielectric) to  $N_c - 1$  (top layer of the thin film).  $N_c$  is the total



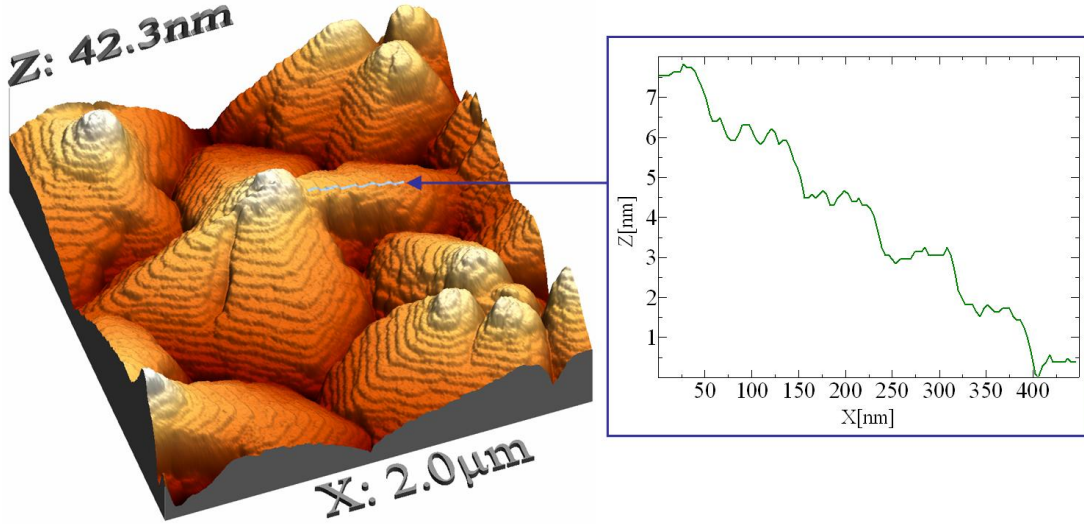


Figure 3.7: 3D AFM micrograph of a pentacene crystal grain grown on a Topas. The graph on the left shows a height profile along a pyramid plane marked in blue. The steps of the pyramid terraces have a height of  $\sim 1.5 \text{ nm}$  which corresponds to the length of a pentacene molecule.

number of monolayers of the thin film, which is  $N_c = 30$  for the pentacene *thin film* phase. The profile function assumes that the first pentacene monolayer fully covers the surface ( $\rho(n_c = 0) = 1$ ). To calculate the different intensity contributions of the pentacene terraces, the profile function is multiplied with the lattice sum given in equation 3.17 and is integrated in the sum over  $n_c$ :

$$\sum_{n_c=0}^{N_c-1} \exp(i \cdot n_c \vec{q} \cdot \vec{c}) \cdot \exp(-n_c \cdot \sigma) = \sum_{n_c=0}^{N_c-1} \exp(n_c(i \cdot \vec{q} \cdot \vec{c} - \sigma))$$

This sum can be further simplified using equation 3.20:

$$\sum_{n_c=0}^{N_c-1} \exp(n_c(i \cdot \vec{q} \cdot \vec{c} - \sigma)) = \frac{\exp(N_c(i \cdot \vec{q} \cdot \vec{c} - \sigma)) - 1}{\exp(i \cdot \vec{q} \cdot \vec{c} - \sigma) - 1} \quad (3.27)$$

A simulation of the intensity  $I(\vec{q})$  along a  $(11l)$  Bragg peak series with low surface roughness  $\sigma = 0.05$  and the structure factor intensity  $F(\vec{q}) \cdot F^*(\vec{q})$  of a pentacene thin film is given in figure 3.8. As the structure factor amplitude is multiplied with the lattice amplitude, it modulates the Bragg peak intensities generated by the lattice. The small oscillations along a Bragg peak are the so called Laue oscillations [64], which can only be seen if the surface roughness is low.

The Laue oscillations are completely damped out if the surface roughness gets larger. In general, pentacene thin films exhibit a surface roughness of  $\sigma > 0.2$ , so that no Laue oscillations can be observed (figure 3.9). Moreover, an increased surface roughness leads,

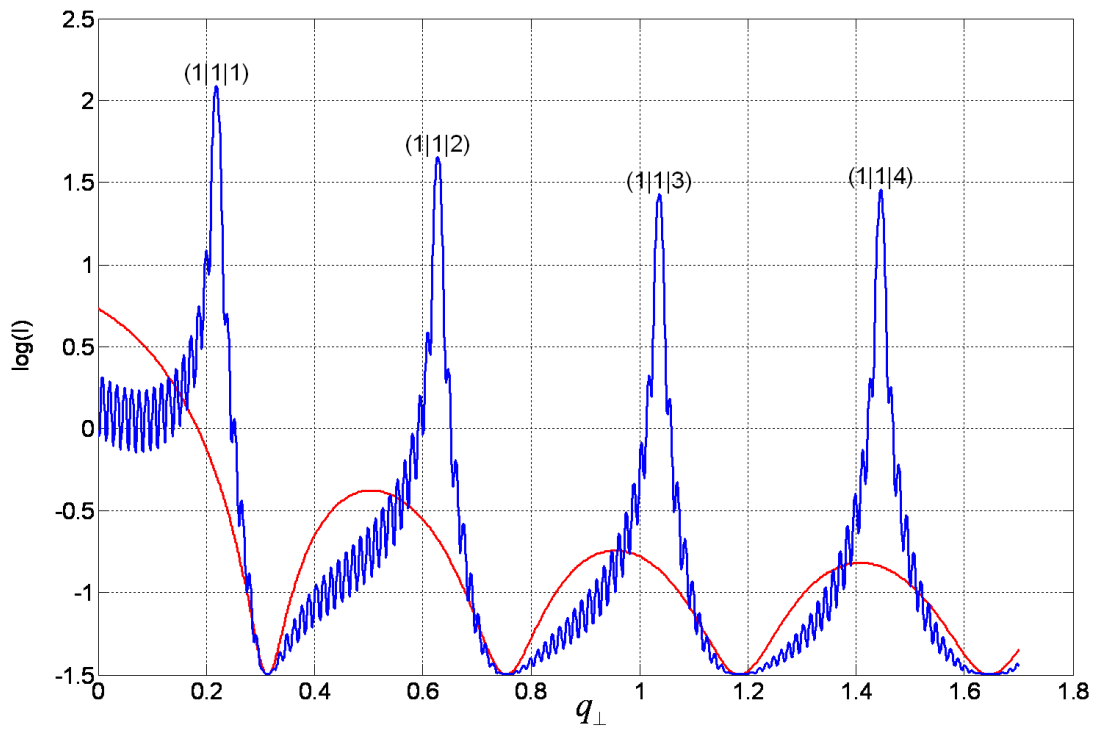


Figure 3.8: Simulation of the intensity  $I(\vec{q})$  along a  $(11l)$  Bragg peak series with surface roughness  $\sigma = 0.05$  (blue line) and  $N_c = 30$ . The structure factor is plotted in red and masks the intensity  $I(\vec{q})$ .

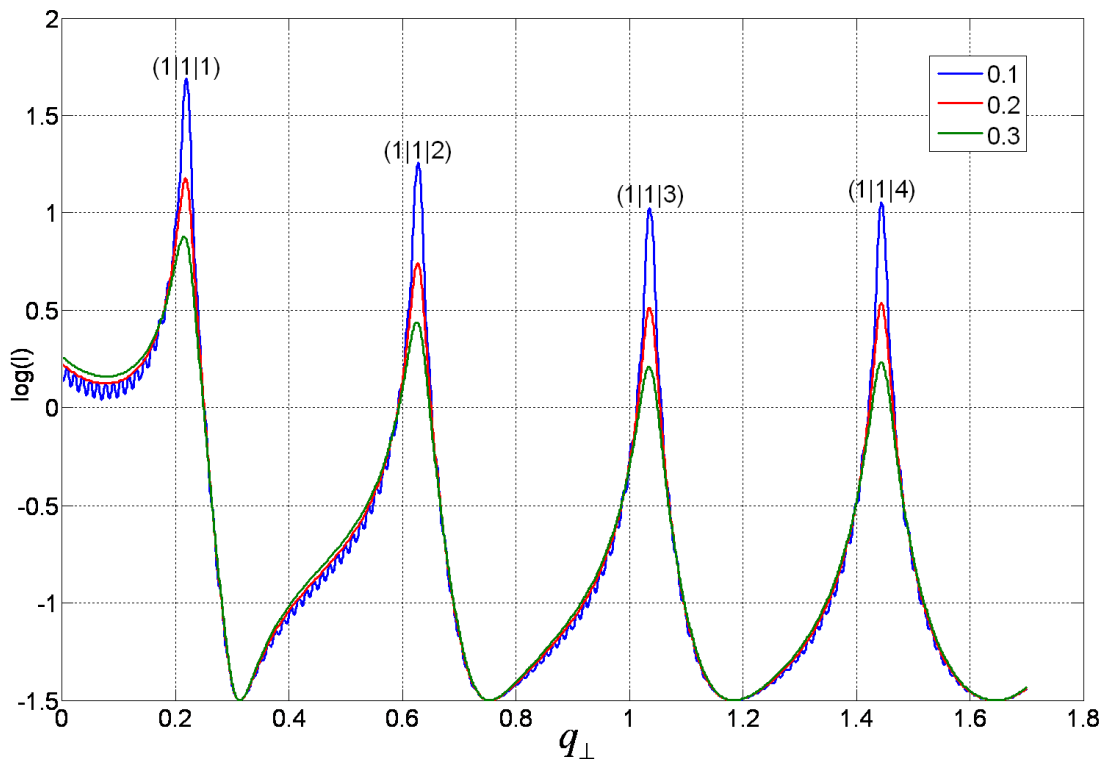


Figure 3.9: Simulation of the intensity  $I(\vec{q})$  along a  $(11l)$  Bragg peak series with different surface roughness  $\sigma$  and  $N_c = 30$ .

similar to the Debye-Waller factor, to a dampening of the observed Bragg peak intensities.

### Fiber structure

The inplane size of pentacene crystal grains can be as small as a fraction of a micrometer. Up to now, there is no microfocus or nanofocus synchrotron beamline available that is able to produce a beam size in the sub micron regime and simultaneously is able to carry the PGC. Apart from this, such measurements would require an extensive precision mechanical construction to adjust the center of rotation to a specific crystal grain of the fiber structure. Moreover, the measurements would require X-ray transparent substrates, which makes substrate dependent investigations almost impossible. Therefore, it is more convenient to develop an analytical tool to analyze the diffraction pattern of a fiber structure, rather than measuring the diffraction pattern of a single crystal grain and analyze it with standard crystallography software.

The area which is illuminated by the X-ray beam at synchrotron beamline W1 is about 6-7 orders of magnitudes larger than a typical  $1 \mu m^2$  pentacene grain. Thus, the observed diffracted intensity at the beamline W1 emerges from several million crystal grains forming a fiber structure with their  $\vec{a} - \vec{b}$  plane oriented parallel to the substrate surface and the

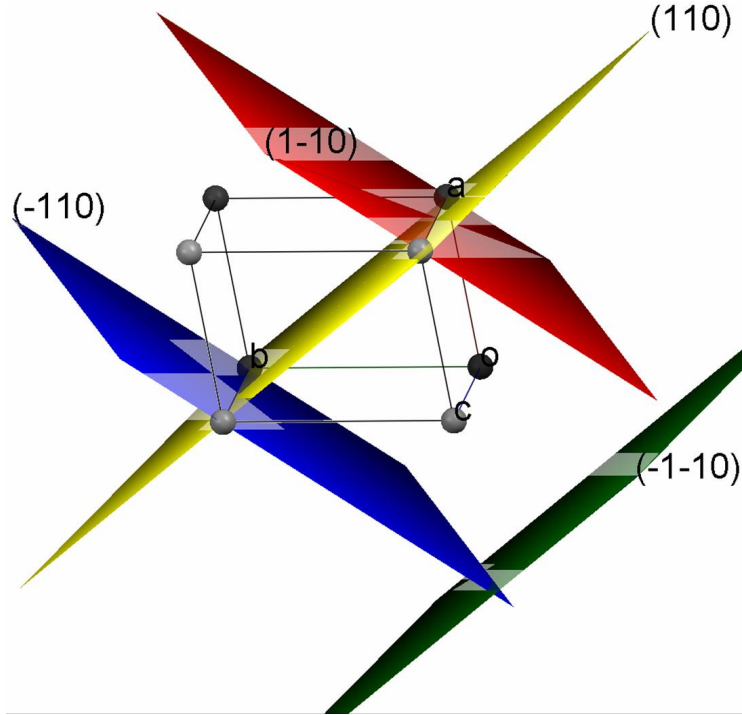


Figure 3.10: Illustration of planes defined by Miller indices in the unit cell. The red plane  $(1,-1,0)$  is parallel to the blue  $(-1,1,0)$  plane. The crystal directions are oriented in opposite directions, which also applies for the parallel planes  $(1,1,0)$  in yellow and  $(-1,-1,0)$  in green.

fiber axes parallel to the substrate normal. The impact on the observed diffraction pattern due to this fiber structure can be described as follows. Since the number of crystallites illuminated by the X-ray beam is much larger compared to those in the X-ray coherence volume, no interference between the signals of individual crystallites is assumed. Thus, the observed diffraction pattern coming from randomly oriented crystal grains in the  $\vec{a} - \vec{b}$  plane is a superposition of all diffraction patterns that can be observed when rotating a single crystal in the  $\vec{a} - \vec{b}$  plane continuously by an angle  $\vartheta$  from  $0^\circ$  to  $180^\circ$ .

Now, all diffraction patterns, which occur when a single crystal is rotated around the  $\vec{a} - \vec{b}$  plane, are identified and discussed. If Bragg's law is satisfied under a certain angle  $\vartheta$  for a set of planes with Miller indices  $(hkl)$ , then it is also satisfied for any set of planes with Miller indices  $(h'k'l)$  that have the same  $d_{hkl}$  spacing as  $(hkl)$  and which can be brought parallel to  $(hkl)$  by rotating the planes an angle  $\vartheta$ . Obviously this is the case if  $(h'k'l)$  is oriented in the opposite direction, such that  $(h'k'l) = (\bar{h}\bar{k}l)$  as illustrated in figure 3.10. If the  $d_{hkl}$  spacings for these planes are equal, then the parallel momentum transfers are equivalent, too. This can be verified by using equation 3.15:

$$q_{\parallel} = \frac{2\pi}{ab \cdot \sin \gamma} \sqrt{h^2 b^2 + k^2 a^2 - 2hkba \cdot \cos \gamma}$$

and substituting  $h := -h$  and  $k := -k$ :

$$\begin{aligned}
&= \frac{2\pi}{ab \cdot \sin \gamma} \sqrt{(-h)^2 b^2 + (-k)^2 a^2 - 2(-h)(-k)ba \cdot \cos \gamma} \\
&= \frac{2\pi}{ab \cdot \sin \gamma} \sqrt{h^2 b^2 + k^2 a^2 - 2hkba \cdot \cos \gamma}
\end{aligned}$$

From this equation it can also be seen that if  $\gamma = 90^\circ$ , then  $q_{\parallel}$  remains unchanged if only  $h = -h$  or  $k = -k$  is substituted alone:

$$\begin{aligned}
q_{\parallel}(\gamma = 90^\circ) &= \frac{2\pi}{ab} \sqrt{h^2 b^2 + k^2 a^2} \\
&= \frac{2\pi}{ab} \sqrt{(-h)^2 b^2 + k^2 a^2} \\
&= \frac{2\pi}{ab} \sqrt{h^2 b^2 + (-k)^2 a^2}
\end{aligned}$$

To conclude, if a set of Bragg peaks ( $hkl$ ) ( $h$  and  $k$  fixed,  $l$  variable) is observed for a single crystal under a fixed angle  $\vartheta$ , then at least one additional set of Bragg peaks with the Miller indices  $(h'k'l) = (\bar{h}\bar{k}l)$  can be observed in the fiber structure diffraction pattern. If  $\gamma = 90^\circ$ , then three additional set of Bragg peaks  $(\bar{h}kl)$ ,  $(h\bar{k}l)$  and  $(\bar{h}\bar{k}l)$  can be observed. A typical diffraction pattern of a fiber structure for  $\gamma \neq 90^\circ$  is shown in figure 3.5 and for  $\gamma = 90^\circ$  in figure 3.4. The Bragg peak positions were simulated in a range of  $h = [-1, 1]$ ,  $k = [-2, 2]$  and  $l = [0, 2]$ .

Now that the Bragg peak positions emerging from a fiber structure with the fiber axis parallel to the substrate normal are known, their diffracted intensities are discussed. As mentioned before, a fiber structure diffraction pattern consists of several superimposed single crystal diffraction patterns. Thus, it is much more likely that some Bragg peaks overlap, depending on their size and distance from each other. The intensities of a fiber structure diffraction pattern is calculated by simply adding up all  $m$  individual single crystal intensity contributions:

$$I(\vec{q}) = \sum_m A(\vec{q}_m) \cdot A^*(\vec{q}_m) \quad (3.28)$$

Here,  $\vec{q}_m$  is the three dimensional scattering vector associated with a Bragg peak position. The individual intensity contributions and their sum  $I(\vec{q})$  of a fiber structured pentacene thin film with  $\gamma = 90^\circ$  is simulated in figure 3.11 for the  $(\pm 1, \pm 1, l)$  direction. The simulation shows, that the peak intensity of some Bragg peaks cannot be observed due to an overlap with neighboring Bragg peaks with higher intensity (e.g.  $(\bar{1}\bar{1}0)$  and  $(111)$ ).

### Semi-kinematic approximation

As optical waves, X-rays show refraction when they pass the interface from one medium into an other. In general, the refraction index of X-rays with matter is very low when

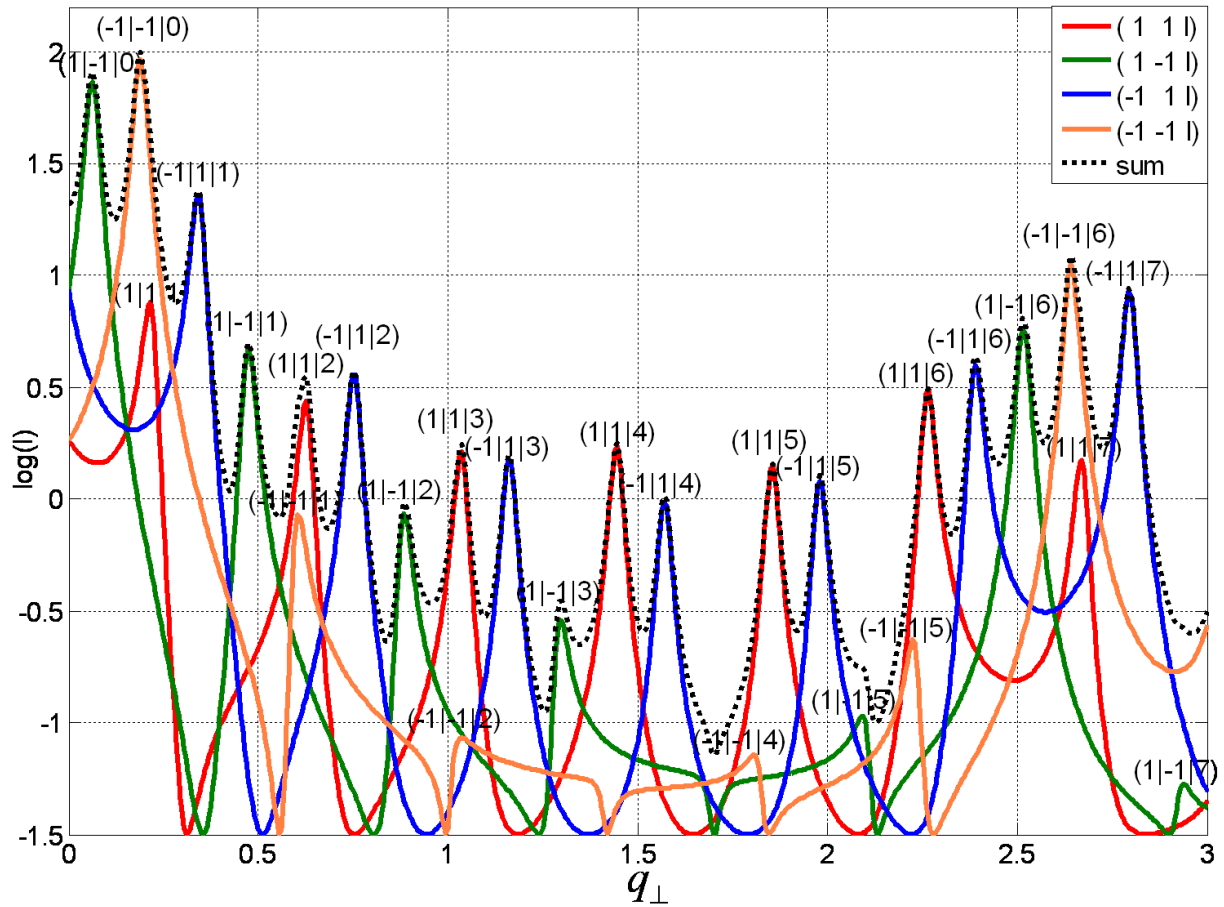


Figure 3.11: Simulation of the individual intensity contributions of the fiber structure and their sum  $I(\vec{q})$  of a pentacene thin film using equation 3.28 along the  $(|1| |1| l)$  direction. ( $\sigma = 0.3$ ,  $U_{iso} = 0.05$ ).

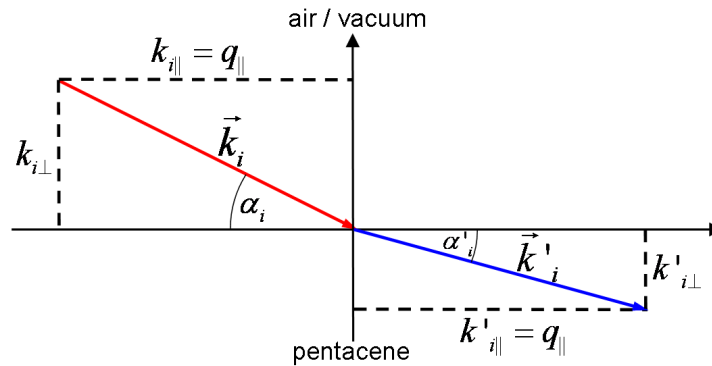


Figure 3.12: Refraction of the incoming wavevector  $\vec{k}_i$  at the air/vacuum - pentacene thin film interface.

compared to optical waves, but for the precise determination of the unit-cell, the effect has to be considered. With the so called semi-kinematic approximation, the refraction at the vacuum-pentacene thin film interface of the X-ray beam is taken into account. The critical angle  $\alpha_c = 0.131^\circ$  for total external reflection of a pentacene thin film was calculated using the “X-ray Interaction with Matter Calculator” of the Lawrence Berkeley National Laboratory, California. The perpendicular momentum transfer of the incoming wave vector  $k_{i\perp}$  has to be corrected due to refraction (figure 3.12) by

$$k'_{i\perp} = \sqrt{k_{i\perp}^2 - \left(\frac{2\pi}{\lambda} \sin \alpha_c\right)^2} \quad (3.29)$$

The same correction has to be applied to the outgoing wavevector  $k_f$ . The equation can simply be derived by using Pythagoras’ theorem and the assumption that  $k_{i\perp} = \frac{2\pi}{\lambda} \sin \alpha_c$  and  $k'_{i\perp} = 0$  at total external reflection.

## 3.2 Experimental setup and measurement techniques

In the previous chapter, Bragg peak positions and their intensities resulting from thin films with respect to fiber structure and surface roughness were discussed. However, the observed intensities in a scattering experiment also depend on the experimental setup. In this chapter, the experimental setup at the synchrotron beamline W1 and the measurement techniques used are presented and the influence of the setup during a measurement on the observed intensity are discussed.

### 3.2.1 HASYLab beamline W1 setup

The X-ray diffraction experiments were carried out at the HASYLab synchrotron beamline W1 in Hamburg. DORIS III, a storage ring for charged particles, was used as synchrotron radiation source. Its 289 meters of circumference facilitates the storing of positrons or electrons at an energy of 4.45 GeV in bunched packages. Typically 2 or 5 bunches of positrons are stored in DORIS III with an initial beam current of up to 120 mA. The corresponding time interval between the bunches is 480 ns or 192 ns, respectively. Synchrotron radiation is produced with a wiggler insertion device. The wiggler generates a horizontally polarized X-ray beam. The energy of the X-ray beam was set to 10500 eV; here the photon flux reaches its maximum brilliance of  $2 \cdot 10^{15} \text{ photons/s} \cdot \text{mrad}^2 \cdot 0.1\% \text{ bandwidth}$  (figure 3.13).

The setup of the W1 beamline is illustrated in figure 3.14. This sketch is not drawn to scale, and the distances are rather approximate values (the Johann spectrometer illustrated in the sketch was not used). The white X-ray beam from the 32-pole wiggler is monochromated using a double-crystal Si(111) monochromator. The toroidal mirror focuses the divergent beam into a spot of approximately  $1.6 \text{ mm} \times 4 \text{ mm}$  at the position of the sample.

The growth chamber is mounted on a heavy-load diffractometer as illustrated in figure 3.15. The built-in  $270^\circ$  beryllium window allows the X-ray beam to enter and leave the

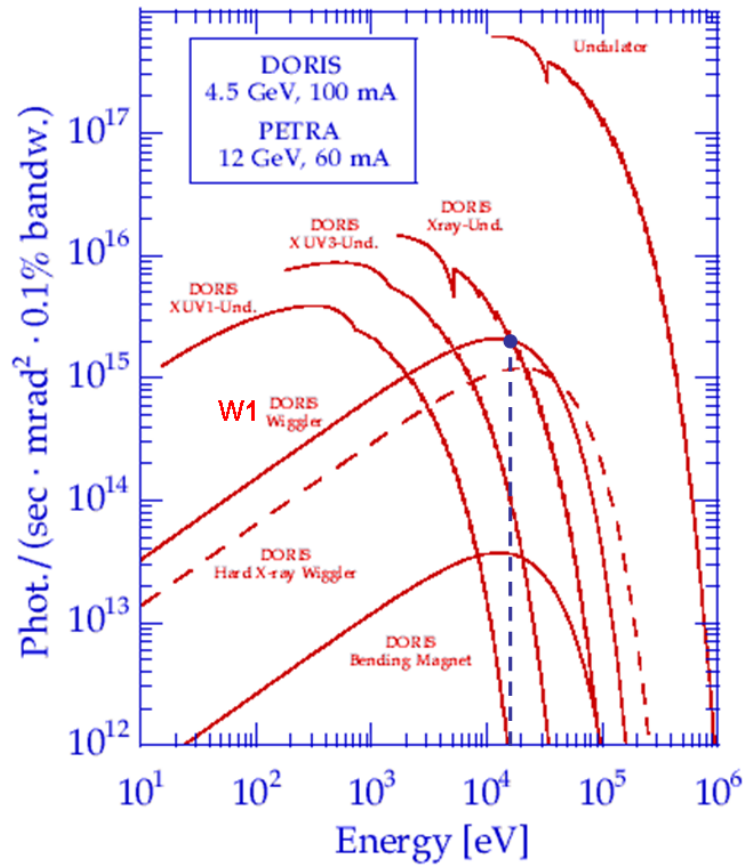


Figure 3.13: Photon flux of the DORIS W1 wiggler. The experiments were carried out at an energy of 10500 eV, where the photon flux reaches a maximum of  $2 \cdot 10^{15}$  photons/s ·  $mrad^2 \cdot 0.1\%$  bandwidth (figure by P. Gürtler, HASYLab).

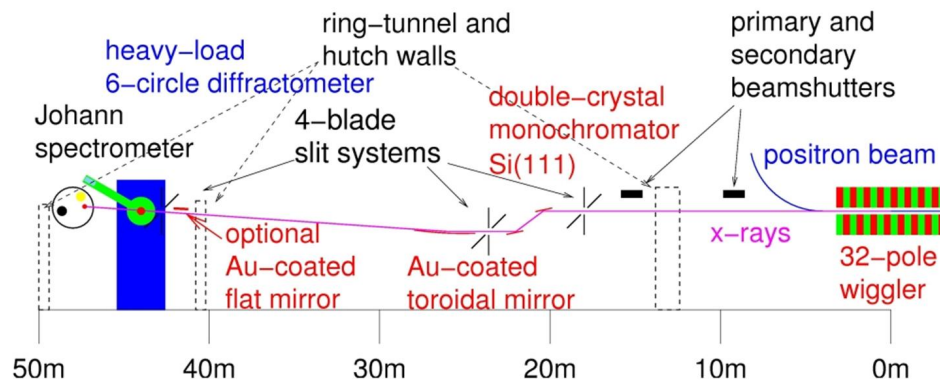


Figure 3.14: Sketch of W1 beamline (sketch from HASYLab homepage).



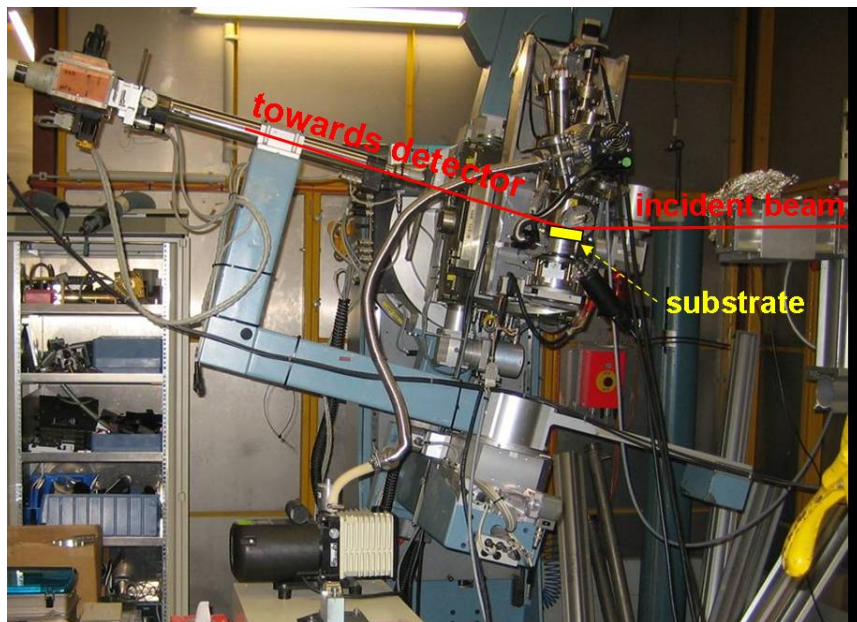


Figure 3.15: PGC mounted on W1 diffractometer.

chamber with almost no loss of intensity, such that in-situ measurements right after the pentacene thin film growth can be made.

A schematic sketch of the W1 diffractometer setup is illustrated in figure 3.16. All diffractometer and monochromator movements are performed by stepper motors controlled by a Linux PC using the HASYLab OnLine control software. The intensity of the primary beam is measured by a monitor detector to correct for variations in the incident beam intensity. A highly collimated signal with low background is produced by a system of several vertical and horizontal slits and a flight tube. The incident beam is defined by the vertical and horizontal beam slits SSV and SSH. The diffracted beam passes first a vertical defining slit FTS (which is open in horizontal direction), and at the end of the flight tube the vertical and horizontal slits DSV ( $\leq$  FTS) and DSH. By using a scintillating point detector and an autoabsorber mechanism, the full dynamic intensity range can be measured. The diffractometer in combination with the  $270^\circ$  Beryllium windows of the UHV chamber gives access to reciprocal space using the three angles FTR (flight tube rotation), TT (two theta) and OM (omega) which can be moved within a range of FTR =  $[-40^\circ, 40^\circ]$ , TT =  $[0^\circ, 90^\circ]$  and OM =  $[0^\circ, 45^\circ]$ . Note, that the angle FTR is not equal to the detector azimuth  $\delta$  (figure 3.19) in spherical coordinates, which are used for convenience in diffraction intensity correction calculations later.

Now, a general expression for the momentum transfer  $\vec{q}$  is derived. The calculations assume that the sample surface is perfectly aligned, i.e. parallel to the X-ray beam polarization in off position (all angles set to  $0^\circ$ ). We further assume, that the direction of propagation of the beam is in z-direction. The substrate normal is aligned in x-direction in the off position. During a measurement, the incident X-ray beam makes an angle OM

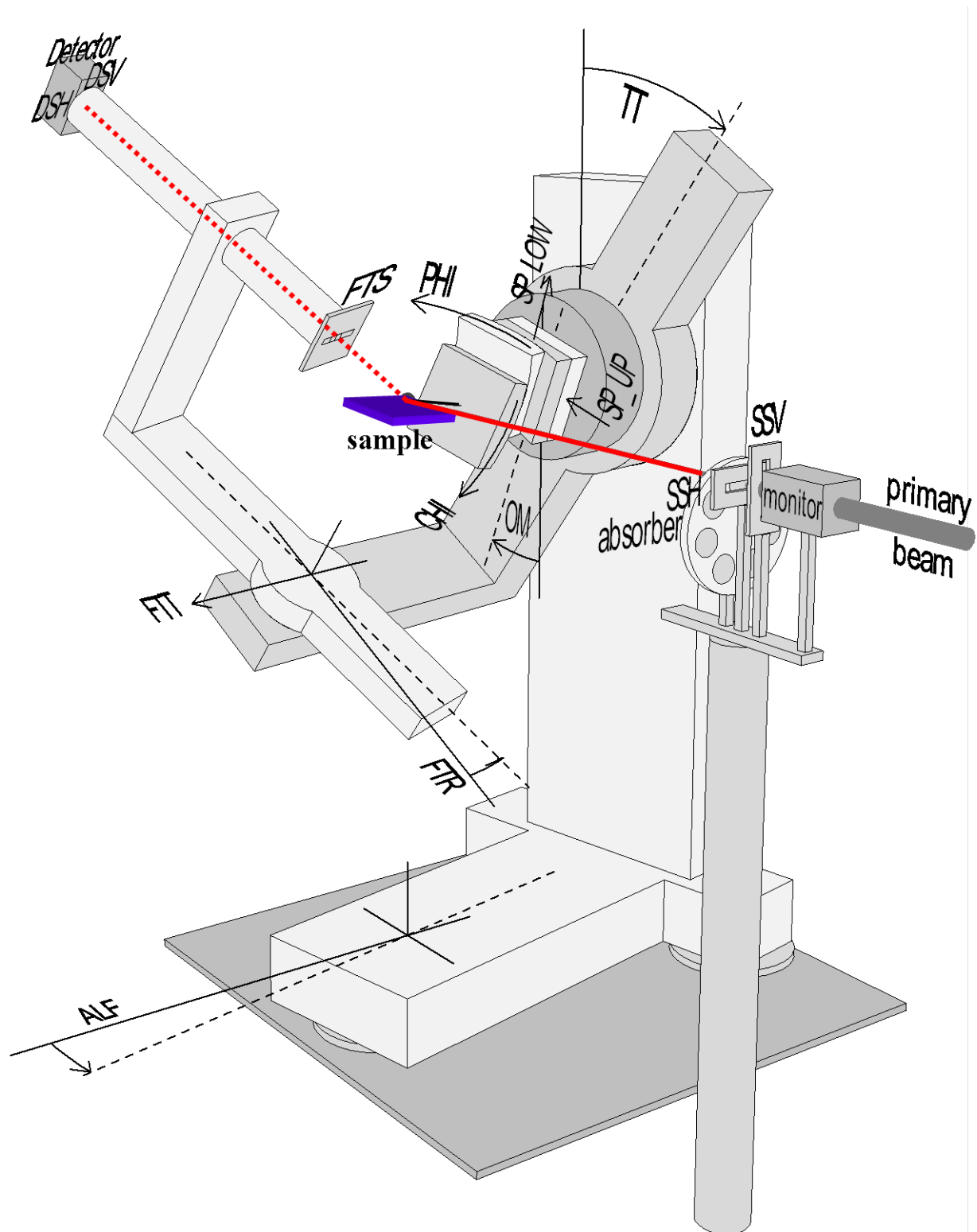


Figure 3.16: Setup of W1 diffractometer at HASYLab W1 beamline, Hamburg and motor names as used in calculations.

with the substrate surface and the exit beam is measured using the detector angles FTR and TT. The incoming wave vector  $k_i$  is given by:

$$\vec{k}_i = \frac{2\pi}{\lambda} \cdot \text{rotOM} \cdot \begin{pmatrix} 0 \\ 0 \\ 1 \end{pmatrix}$$

$$\text{rotOM} = \begin{pmatrix} \cos(\text{OM}) & 0 & -\sin(\text{OM}) \\ 0 & 1 & 0 \\ \sin(\text{OM}) & 0 & \cos(\text{OM}) \end{pmatrix}$$

Here rotOM is the rotation matrix for the angle OM. The scattered wave vector  $k_f$  is given by:

$$\vec{k}_f = \frac{2\pi}{\lambda} \cdot \text{rotOM} \cdot \text{rotTT} \cdot \text{rotFTR} \cdot \begin{pmatrix} 0 \\ 0 \\ 1 \end{pmatrix}$$

$$\text{rotTT} = \begin{pmatrix} \cos(\text{TT}) & 0 & \sin(\text{TT}) \\ 0 & 1 & 0 \\ -\sin(\text{TT}) & 0 & \cos(\text{TT}) \end{pmatrix}$$

$$\text{rotFTR} = \begin{pmatrix} 1 & 0 & 0 \\ 0 & \cos(\text{FTR}) & -\sin(\text{FTR}) \\ 0 & \sin(\text{FTR}) & \cos(\text{FTR}) \end{pmatrix}$$

where rotTT is the rotation matrix of the angle TT and rotFTR of the angle FTR, respectively. For the calculation of geometry dependent intensity correction factors in grazing incidence geometry,  $\vec{k}_f$  will be transformed into spherical coordinates using the azimuth angle  $\delta$ , the polar angle  $\gamma$  and the radius  $r$  as illustrated in figure 3.19. The conversion into the sphere coordinate system uses the equations:

$$r = \sqrt{x^2 + y^2 + z^2}$$

$$\delta = \arccos \frac{z}{\sqrt{z^2 + y^2}}$$

$$\gamma = \text{arccot} \frac{x}{\sqrt{z^2 + y^2}}$$

where x, y and z are vector components of  $\vec{k}_f$ .

Using equation 3.5, the momentum transfer  $\vec{q}$  is given by:

$$\begin{aligned} \vec{q} &= \vec{k}_f - \vec{k}_i \\ &= \frac{2\pi}{\lambda} \cdot \begin{bmatrix} 0.5 \cdot (\sin u + \sin w) + \sin(\text{OM}) \\ -\sin(\text{FTR}) \\ 0.5 \cdot (\cos u + \cos w) - \cos(\text{OM}) \end{bmatrix} \end{aligned} \quad (3.30)$$

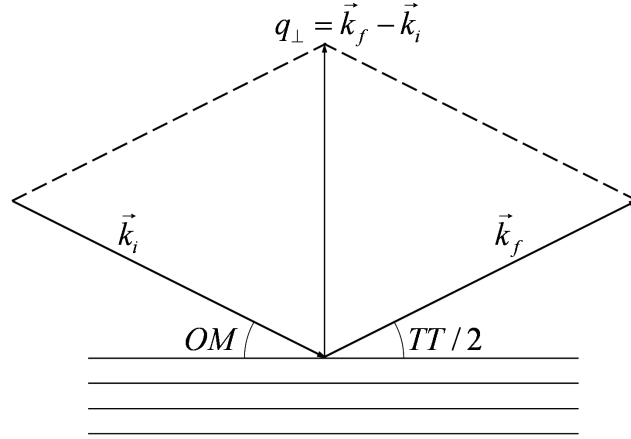


Figure 3.17: Momentum transfer during an X-ray reflectivity measurement.

$$u = \text{FTR} - \text{OM} + \text{TT}, \quad w = -\text{FTR} - \text{OM} + \text{TT}$$

The magnitude of the parallel momentum transfer is calculated by norm of the y and z components of  $\vec{q}$ :

$$q_{\parallel} = \frac{2\pi}{\lambda} \cdot \sqrt{\sin^2(\text{FTR}) + (0.5 \cdot (\cos u + \cos w) - \cos(\text{OM}))^2} \quad (3.31)$$

### 3.2.2 X-ray measurement techniques

In this chapter, the basic X-ray measurement techniques performed at the W1 beamline are presented.

#### X-ray reflectivity

An optical approach of specular X-ray reflectivity using the Parratt formalism was already given in chapter 2.4.2. When performing X-ray reflectivity measurements on ordered structures like pentacene thin films, Bragg peaks appear which can be used to investigate the ordering of pentacene thin films perpendicular to the surface.

During an X-ray reflectivity measurement, OM (the angle between the incident wave vector  $k_i$  and the substrate surface) is varied and the reflected beam is measured under the same angle  $\text{TT}/2 = \text{OM}$ . Using equation 3.30, the momentum transfer  $\vec{q}$  on the substrate surface is given by:

$$\vec{q} = \frac{2\pi}{\lambda} \cdot \begin{bmatrix} 2 \sin(\text{OM}) \\ 0 \\ 0 \end{bmatrix}$$

It is obvious, that during a reflectivity measurement, only a perpendicular momentum transfer  $q_{\perp}$  is present:

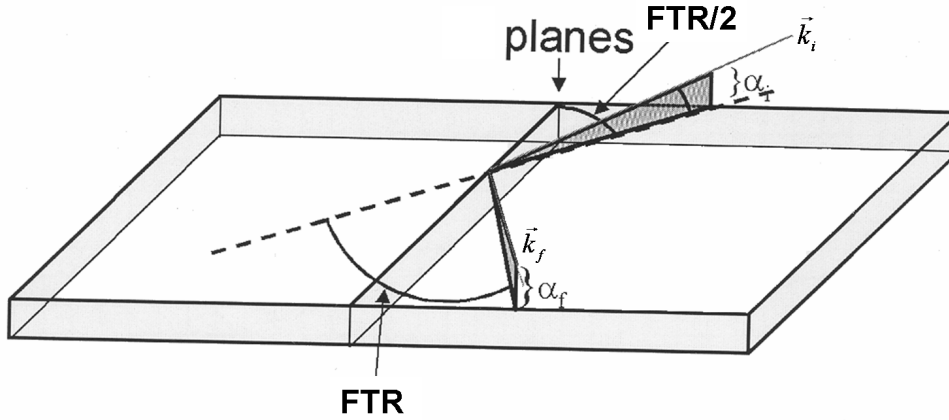


Figure 3.18: Sketch of a GIXD geometry.

$$q_{\perp} = \frac{4\pi}{\lambda} \cdot \sin(\text{OM}) = \frac{4\pi}{\lambda} \cdot \sin(\text{TT}/2) \quad (3.32)$$

If the parallel momentum transfer  $q_{\parallel} = 0$ , then the miller indices  $h$  and  $k$  have to be 0 as well according to equation 3.15.

Then  $q_{\perp}$  reads:

$$q_{\perp} = 2\pi \frac{l}{d_{00l}} \Rightarrow d_{00l} = 2\pi \cdot \frac{l}{q_{\perp}} \quad (3.33)$$

To conclude, the appearance of Bragg peaks measured in an X-ray reflectivity measurement can be used to determine the  $d_{00l}$  spacing of the unit cell. The FWHM  $\Delta q_{\perp}$  of such Bragg peaks can be used to calculate the average crystalline film thickness  $D_{\perp}$  along the surface normal. The relation is given by using equation 3.3:

$$D_{\perp} = 2\pi/\Delta q_{\perp} \quad (3.34)$$

### Grazing incidence X-ray diffraction (GIXD)

Laterally ordered structures can be investigated with grazing incidence X-ray diffraction (GIXD). The incident X-ray beam is kept at a grazing angle  $\alpha_i(\text{OM})$  on the sample near the critical angle  $\alpha_c$  for total external reflection of the substrate. An advantage of GIXD is that the electric field at the critical angle is amplified locally by a factor of four compared to other incident angles. It also reduces the scattering background from the bulk of the substrate[66].

Here, the intensity is measured at  $\alpha_i = \alpha_f$  (TT/2) while FTR is varied. Assuming, that  $\text{OM} \sim 0^\circ$ , the momentum transfer  $\vec{q}$  on the substrate surface using equation 3.30 is given by:

$$\vec{q} = \frac{2\pi}{\lambda} \cdot \begin{bmatrix} 0 \\ -\sin(\text{FTR}) \\ \cos(\text{FTR}) - 1 \end{bmatrix}$$

Thus, a GIXD measurement only exhibits a parallel momentum transfer  $q_{\parallel}$  (given by the norm of  $\vec{q}$ ):

$$q_{\parallel} = \frac{2\pi}{\lambda} \cdot \sin(\text{FTR}/2) \quad (3.35)$$

According to equation 3.14, the perpendicular momentum transfer  $q_{\perp}$  of Bragg peaks with miller index  $l = 0$  is not necessarily 0 (e.g. in a triclinic crystal structure) and therefore not a priori detectable with GIXD. In practice, the local amplification of the electric field due to the ordered inplane structure at grazing incidence allows the detection of GIXD peaks. According to equation 3.15, the vertical momentum transfer  $q_{\parallel}$  of peaks measured by GIXD can be used to solve the unit cell parameters  $a$ ,  $b$ , and  $\gamma$ .

The unit cell volume  $V$  can be calculated, when X-ray reflectivity and GIXD measurements are combined:

$$V = d_{00l} \cdot ab \cdot \cos \gamma$$

Analog to reflectivity measurements, the average diameter  $D_{\parallel}$  of a crystalline domain along the surface can be derived using equation 3.3 and the FWHM  $\Delta q_{\parallel}$  of a typical GIXD peak. The relation is then given by:

$$D_{\parallel} = 2\pi/\Delta q_{\parallel} \quad (3.36)$$

### Grazing incidence crystal truncation rod (GI-CTR) diffraction

Since the mid 80s, crystal truncation rod (CTR) scattering has proved to be a powerful technique for investigating surface and interface structures. The method is the most powerful of the used measurement techniques, as it covers the biggest section of reciprocal space. During a GI-CTR measurement, the diffracted intensity along a set of Bragg peaks sharing the same lateral momentum transfer  $q_{\parallel}$  by increasing the perpendicular momentum transfer  $q_{\perp}$  is measured. A sketch of the GI-CTR geometry in spherical coordinates is given in figure 3.19. The incident X-ray beam is kept at a grazing angle  $\alpha_i$  on the sample near the critical angle  $\alpha_c$  for total external reflection. The detector azimuth angle  $\delta$  is set to  $\delta'$ , an in-plane Bragg peak position of interest measured by GIXD. A scan is performed by measuring the diffracted intensity while increasing  $\gamma$  and simultaneously adjusting  $\delta$  by:

$$\delta = \arccos \left( \frac{2 \cos \delta' \cos \alpha_i + \cos^2 \gamma - 1}{2 \cos \gamma \cos \alpha_i} \right) \quad (3.37)$$

This keeps the lateral momentum transfer  $q_{\parallel}$  constant while the perpendicular momentum transfer  $q_{\perp}$  is varied. The evolution of the detector position ( $\delta$ ,  $\gamma$ ) is illustrated as red

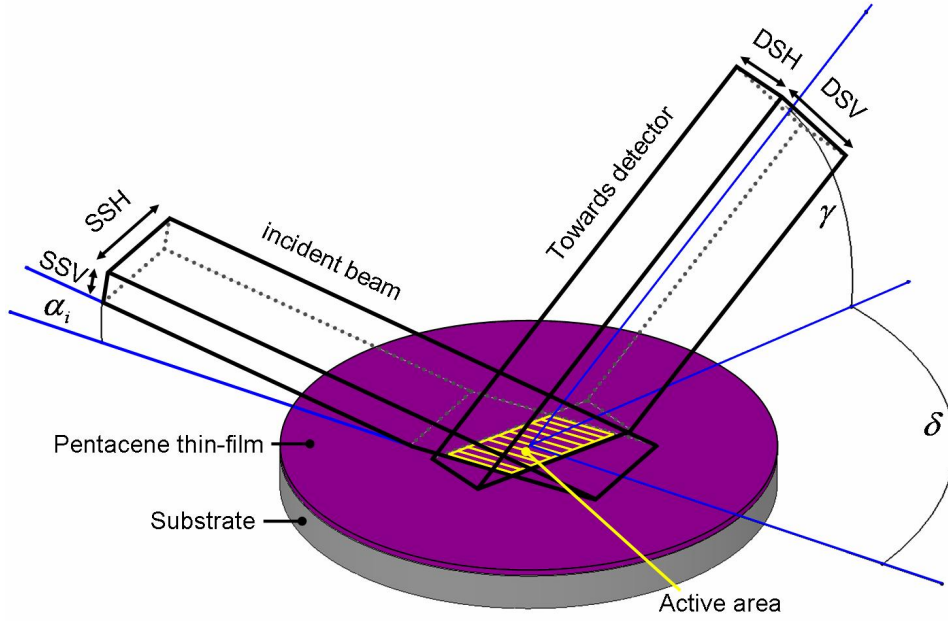


Figure 3.19: Sketch of the GI-CTR geometry using spherical coordinates.

lines in figure 3.20 for different fixed  $q_{\parallel}$  values according to equation 3.37. It shows, that for same values of  $\gamma$  the correction of  $\delta$  can be small or large, depending on  $\delta'$ .

As the W1 diffractometer angle FTR is not equal to the detector azimuth  $\delta$  in spherical coordinates, the correction of FTR to keep  $q_{\parallel}$  constant is given by:

$$\text{FTR} = -\arccos \frac{-b - \sqrt{b^2 - 4ac}}{2a} \quad (3.38)$$

$$a = -\sin^2(\text{TT} - \text{OM})$$

$$b = -2 \cos(\text{TT} - \text{OM}) \cdot \cos \text{OM}$$

$$c = 1 + \cos^2 \text{OM} - \sin^2 \text{FTR}' - (\cos \text{OM} \cdot \cos \text{FTR}' - \cos \text{OM})^2$$

The evolution of the detector position (FTR, TT) is illustrated in figure 3.20 as blue lines and compared to the evolution of the detector position in spherical coordinates for different fixed  $q_{\parallel}$  values according to equation 3.38.

A GI-CTR scan starts at an in-plane Bragg peak of interest with a fixed lateral momentum transfer  $q_{\parallel}$  determined by a GIXD measurement. Thus,  $\vec{q}$  satisfies the Bragg condition with Miller indices  $(hk)$  and reads according to equation 3.2:

$$\vec{q} = h\vec{a}_r + k\vec{b}_r + l\vec{c}_r$$

The lattice sum given in equation 3.17 is simplified by calculating the scalar products of  $\vec{q}$  with the unit cell axes  $\vec{a}$  and  $\vec{b}$ :

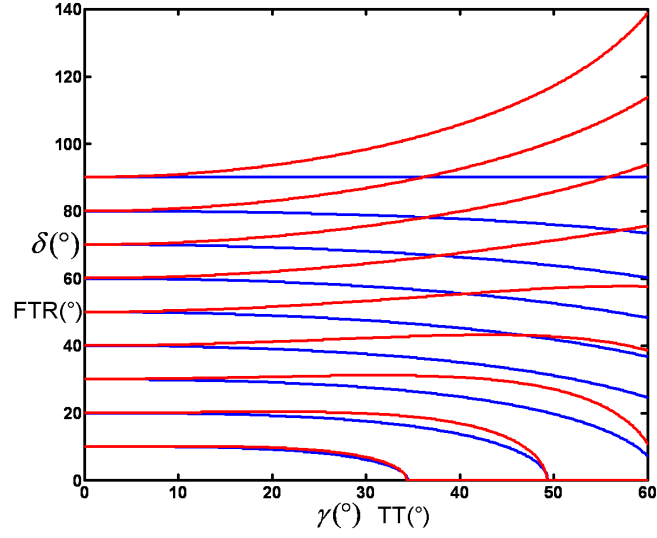


Figure 3.20: Evolution of the detector position when traveling in  $q_{\perp}$  along a given rod for different fixed  $q_{\parallel}$  values according to equations 3.37 ( $\delta$ ,  $\gamma$ ) as red lines and 3.38 (FTR, TT) as blue lines.  $\alpha_i$  is fixed at  $0.15^{\circ}$ .

$$\begin{aligned}\vec{q} \cdot \vec{a} &= (h\vec{a}_r + k\vec{b}_r + l\vec{c}_r) \cdot \vec{a} \\ \vec{q} \cdot \vec{b} &= (h\vec{a}_r + k\vec{b}_r + l\vec{c}_r) \cdot \vec{b}\end{aligned}$$

The scalar product of a unit cell vector with its corresponding reciprocal vector equals  $2\pi$ , and is 0 for any other reciprocal vector given by definition of the reciprocal vectors in equation 3.1. Therefore, the two scalar products simplify to:

$$\begin{aligned}\vec{q} \cdot \vec{a} &= 2\pi h \\ \vec{q} \cdot \vec{b} &= 2\pi k\end{aligned}$$

Inserting these results in the lattice sum given in equation 3.21 and integrating the expression for surface roughness (equation 3.27), the lattice sum reads:

$$A(\vec{q}) = A_0 \frac{r_e}{R_0} F(\vec{q}) N_a N_b \frac{\exp(N_c(i \cdot \vec{q} \cdot \vec{c} - \sigma)) - 1}{\exp(i \cdot \vec{q} \cdot \vec{c} - \sigma) - 1} \quad (3.39)$$

The intensity is derived by multiplying the amplitude  $A(\vec{q})$  with its complex conjugate  $A^*(\vec{q})$ . Using the modification of the intensity for fiber structures given in equation 3.28, the intensity  $I(\vec{q})$  reads:

$$I(\vec{q}) = I_0 \left( \frac{r_e}{R_0} N_a N_b \right)^2 \sum_m \left( F F^*(\vec{q}) \cdot \frac{\exp(N_c(i \cdot \vec{q} \cdot \vec{c} - \sigma)) - 1}{\exp(i \cdot \vec{q} \cdot \vec{c} - \sigma) - 1} \cdot \frac{\exp(N_c(-i \cdot \vec{q} \cdot \vec{c} - \sigma)) - 1}{\exp(-i \cdot \vec{q} \cdot \vec{c} - \sigma) - 1} \right) \quad (3.40)$$



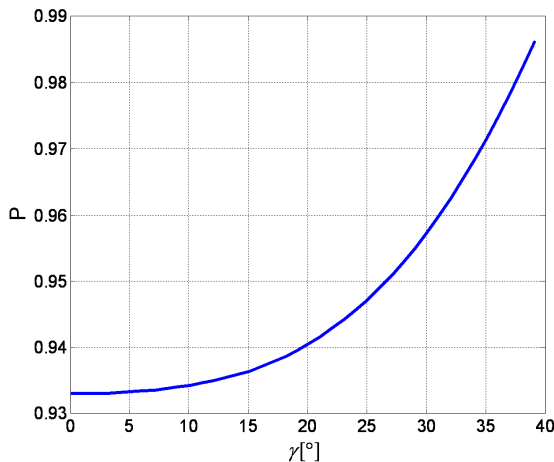


Figure 3.21: Evolution of the Polarization factor  $P$  plotted vs. the detector angle  $\gamma$  during a GI-CTR measurement. The detector position  $(\delta, \gamma)$  was simulated as illustrated in figure 3.20 for  $\delta' = 15^\circ$ ,  $\gamma = [0^\circ, 40^\circ]$  and  $\alpha_i$  fixed at  $0.15^\circ$ .

Since the amplitude  $A(\vec{q})$  grows linearly with the number  $N$  of scatterers, the observed intensity grows quadratically with  $N$ . In other words, using a crystal concentrates the weak scattering of the individual unit cells into a much more intense, coherent reflection that can be observed above background noise.

### 3.2.3 Diffraction intensity correction factors

In this section, various correction factors due to the setup for GI-CTR scattering will be derived. The calculations for polarization factor, Lorenz factor and interception of scattering rod are based on the work by D. Smilgies [66].

#### Polarization factor

Synchrotron light is linearly polarized in the horizontal plane and perpendicular to the beam direction  $\vec{k}$ . The polarization factor  $P$  describes the dependence of the electric field in the crystal on the polarization of the incoming wave. For large exit angles  $\gamma$  (figure 3.19) as used during a GI-CTR measurement[67], a polarization correction is necessary.

$$P = \cos^2 \gamma \cos^2 \delta + \sin^2 \gamma$$

A simulation of  $P$  plotted vs. the detector angle  $\gamma$  during a GI-CTR measurement is shown in figure 3.21. The plot shows, that the Polarization factor changes the intensity less than 5% over the whole measurement range used in this study.

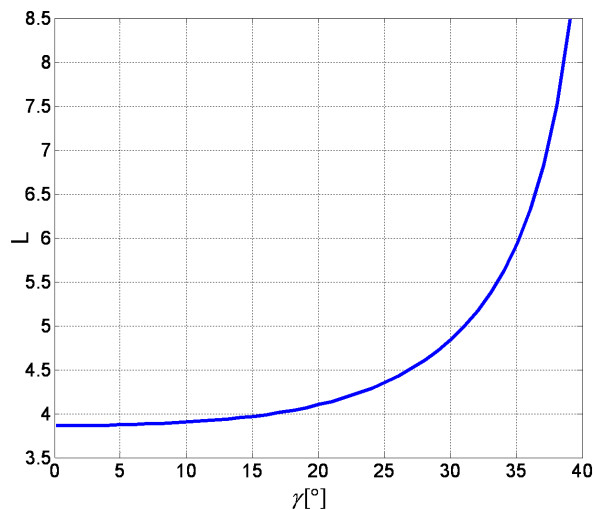


Figure 3.22: Evolution of the Lorentz factor  $L$  plotted vs. the detector angle  $\gamma$  during a GI-CTR measurement. The detector position  $(\delta, \gamma)$  was simulated as illustrated in figure 3.20 for  $\delta' = 15^\circ$ ,  $\gamma = [0^\circ, 40^\circ]$  and  $\alpha_i$  fixed at  $0.15^\circ$ .

### Lorentz factor

When a crystal is rotated around its  $\vec{a} - \vec{b}$ -plane in a beam of monochromatic X-rays, the various planes of the crystal pass through positions in which they satisfy the condition for reflection. In general, the various planes do not occupy such positions for equal lengths of time. The total amount of X-ray radiation in each reflection is proportional to this time opportunity to reflect. In the rotating single crystal method, the Lorentz factor  $L$  is essentially this time factor. The Lorentz factor is proportional to the permitted reflection time of each reflection, or inversely proportional to the velocity with which the plane passes through the condition of reflection. For GIXD and GI-CTR other than the  $(00l)$  reflectivity rod,  $L$  can be written as:

$$L = 1 / \cos \alpha_i \sin \delta \cos \gamma$$

An analog expression can be found in the International Tables of X-ray crystallography for the “equi-inclination method”. In figure 3.22 shows a simulation of  $L$  plotted vs. the detector angle  $\gamma$  during a GI-CTR measurement. It is obvious, that the slope of the Lorentz factor increases quickly towards higher  $\gamma$  values.

### Area factor

This factor normalizes the integrated intensity with respect to the scattering area on the sample. This is given by the intersection of the illuminated area of the incident beam, the area that the detector “sees” at a given slit settings and the sample surface area (figure 3.19). The incident beam is limited by pre-sample slits (SSH and SSV) and the

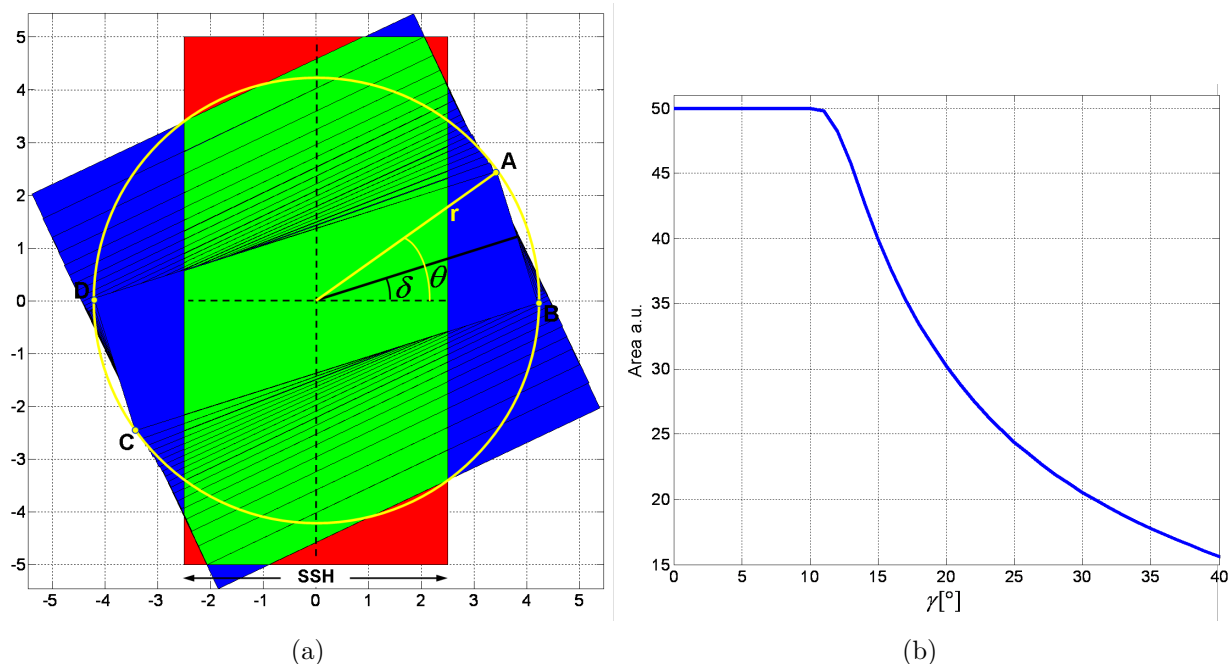


Figure 3.23: (a) Evolution of the active area  $A$  during a GI-CTR measurement. The substrate area illuminated by the incident beam is red. The area, that the detector “sees” is blue. The intersection of the two rectangles is green. The detector position  $(\delta, \gamma)$  was simulated as illustrated in figure 3.20 for  $\delta' = 15^\circ$  and  $\gamma = [14^\circ, 40^\circ]$ .  $\alpha_i$  is fixed at  $0.15^\circ$ . (b) Plot of the active area vs.  $\gamma$  (as simulated on the left) during a GI-CTR measurement.

diffracted beam is limited by the detector aperture (DSH and DSV). The flighttube slit FTS does not limit the beam, as it is open in horizontal direction and bigger than DSV in vertical direction. This set of slits defines an active surface on the sample for diffraction. The projections on the sample surface plane of the pre-sample slits along the direction of the average incident beam and of the detector slits along the direction of the average diffracted beam define two rectangles on the surface. These two rectangles of dimensions  $[SSH \cdot SSV / \sin \alpha_i]$  and  $[DSH \cdot DSV / \sin \gamma]$  are rotated by the angle  $\delta$  with respect to each other. The intersection between these two rectangles and the sample surface gives the diffracting surface area, i.e. the area that contributes to the detected signal. Note that in grazing incidence, the diffracting area becomes independent of the value of SSV, except if SSV is very small.

Even with the simple assumption used above that the incident and diffracted beams are perfectly collimated, the diffracting area  $A$  must generally be calculated numerically, since there is no general expression for arbitrary sample shapes. The shapes of the samples used in this study were all of rectangular shape. Here, a numerical approach is given to calculate the active area during a GI-CTR measurement. Figure 3.23 shows a graphical simulation (right) and a plot (left) of the active area  $A$  vs. the detector angle  $\gamma$ . The substrate area illuminated by the incident beam is red. The area, that the detector “sees”

is blue. The intersection of the two rectangles is green. It is clear that the area factor  $A$  is the most important intensity correction factor during a GI-CTR measurement, as  $A$  reduces the intensity significantly at high angles. The coordinates of the corners of the rectangle ABCD that the detector sees, can be calculated as follows:

$$\begin{aligned} A &= (P1x, P1y) \\ B &= (P2x, P2y) \\ C &= (-P1x, -P1y) \\ D &= (-P2x, -P2y) \end{aligned}$$

$$\begin{aligned} P1x &= r \cdot \cos(\theta + \delta) \\ P1y &= r \cdot \sin(\theta + \delta) \\ P2x &= r \cdot \cos(-\theta + \delta) \\ P2y &= r \cdot \sin(-\theta + \delta) \end{aligned}$$

$$\begin{aligned} r &= \sqrt{(\text{DSH}/2 \sin \gamma)^2 + (\text{DSH}/2)^2} \\ \theta &= \arctan((\text{DSV}/(2 \sin \gamma))/(\text{DSH}/2)) \end{aligned}$$

The coordinates of the two overlapping rectangles were used as input for a numerical polygon area intersection algorithm from the Geometry 2D Matlab toolkit provided by the Institute of Applied Mathematics at INRA, France.

### Interception of scattering rods

Intensities during a GI-CTR experiment are measured with a fixed slit size DSV. However, the slit is not fixed in reciprocal space. Thus, the intensity has to be corrected by the “Interception of scattering rods” -factor, called R-factor. The R-factor is given by:

$$R = \text{DSV} \cdot \cos \gamma$$

A simulation of  $R$  plotted vs. the detector angle  $\gamma$  during a GI-CTR measurement together with the L-, P- and A-factors for comparison is shown in figure 3.24. The product of those four correction factors is plotted as a solid line and shows the evolution of the four factors combined.

### Scanned area in reciprocal space

The intensity for small crystal particles is given by equation 3.21. The finite peak width is observable when the crystal is small so that it produces broad Bragg peaks. For large single crystals, the Bragg peaks are sharp delta functions and only the integrated intensity

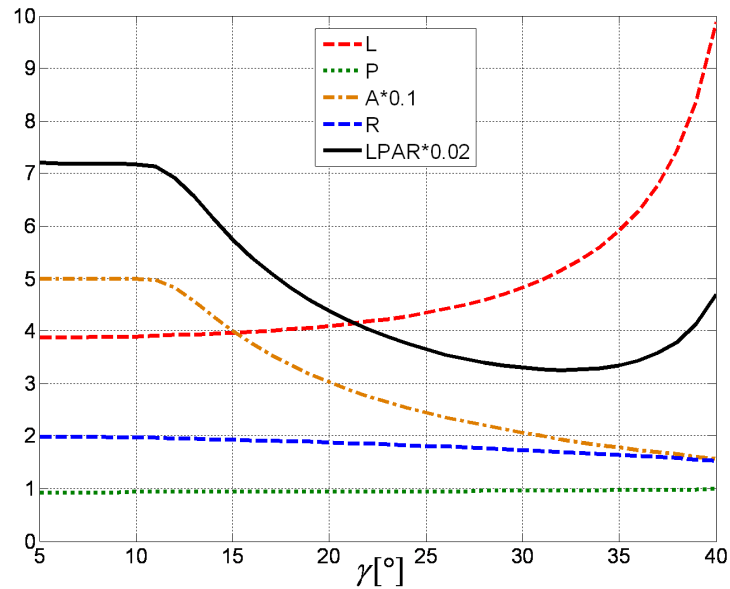


Figure 3.24: Evolution of the L-, P-, A- and R-factor plotted vs. the detector angle  $\gamma$  during a GI-CTR measurement. The detector position  $(\delta, \gamma)$  was simulated as illustrated in figure 3.20 for  $\delta' = 15^\circ$ ,  $\gamma = [0^\circ, 40^\circ]$  and  $\alpha_i$  fixed at  $0.15^\circ$ . The solid line represents the product of L, P, A, and R factors. Note: For better visualization, the A factor was multiplied by 0.1 and the LPAR factor by 0.02.

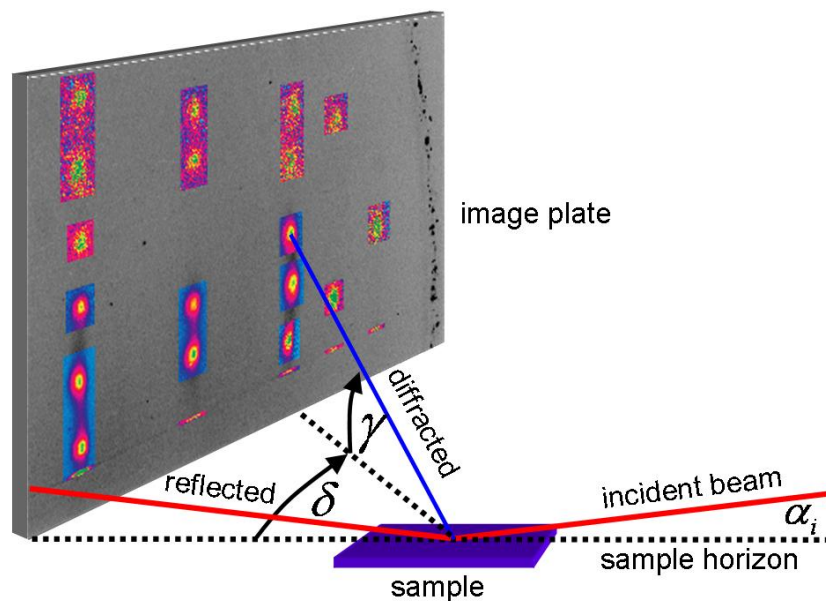


Figure 3.25: Schematic drawing of the X-ray setup for GIXD and GI-CTR measurements using an image plate to record the Bragg peaks.

can be observed e.g. by the crystal rotation method [64]. To make sure that the Bragg peaks of a pentacene thin film are sufficiently broad to be described by equation 3.21 and to get an overview of the of the Bragg peak positions and their size, an X-ray sensitive image plate was used to record the diffraction pattern in grazing incidence geometry (figure 3.25). The image plate was scanned with an image plate scanner at HASYLab. For better visualization, the intensities of the Bragg peaks are contrast enhanced. In figure 3.26, the image plate scan is superimposed with a simulated Bragg peak pattern (blue dots). The corresponding Miller indices are included to the right of each Bragg peak. Each was fitted from the observed Bragg peak positions using equation 3.13. There are several conclusion, that can be drawn from this Bragg peak pattern: (1) There are four pairs of Bragg peaks that overlap each other, such that their exact individual  $q_{\perp}$  value cannot be determined unambiguously:  $(111)$  &  $(\bar{1}\bar{1}0)$ ,  $(112)$  &  $(\bar{1}\bar{1}1)$ ,  $(1\bar{2}0)$  &  $(\bar{1}\bar{2}1)$ ,  $(1\bar{2}1)$  &  $(\bar{1}\bar{2}2)$ . (2) The first two pairs of Bragg peaks are shifted slightly towards lower  $q_{\parallel}$  and the last two pairs slightly towards higher  $q_{\parallel}$ . This indicates, that the unit-cell angle  $\gamma$  is slightly smaller than  $90^{\circ}$ . (3) Bragg peaks with higher  $q_{\perp}$  values are so weak, that their position can barely be identified. (4) The Bragg peaks are broad and not delta function like, such that equation 3.21 can be used to describe their intensities.

When performing a GI-CTR measurement, one has to make sure that the whole Bragg peak is integrated in  $q_{\parallel}$ . Therefore, the width of a Bragg peak in  $q_{\parallel}$  was analyzed by taking a profile scan from the image plate scan. The profile and a 3D visualization of the image plate scan to illustrate the size of the Bragg Peaks is shown in figure 3.27. The profile exhibits a Gauss like shape with a broadness of  $2\sigma = 0.024 \text{ \AA}^{-1}$ . The 3D image plate figure also shows, that the Bragg peaks exhibit all the same width in  $q_{\parallel}$ . The width of the horizontal detector slit DSH was set to a maximum of 8mm, which corresponds to a width of  $q_{\parallel\text{DSV}} = 0.042 \text{ \AA}^{-1}$ . When compared to the Bragg peak width of  $2\sigma = 0.024 \text{ \AA}^{-1}$ , the DSH slit has a horizontal width of  $3.5\sigma$ . This in consequence means, that 99.95% of the Bragg peak signal is integrated by the detector slits. Even if some Bragg peaks in one measurement are shifted in  $q_{\parallel}$  by about 10% of the detector slit width as it is the case for some Bragg peaks of the pentacene *thin-film* phase (figure 3.26), the measured intensity reduces less than 0.03%. Therefore, no intensity corrections were made due to the finite slit width of DSH or Bragg peaks shifted in  $q_{\parallel}$  for pentacene thin films.

The slit width of DSV, which masks the area scanned in perpendicular direction to the surface, was set to 2mm. This corresponds to an angle of  $0.1^{\circ}$  in TT direction. Therefore, the angle step width during a GI-CTR in this direction was set to  $0.1^{\circ}$ , such that no intensity is lost or added.

It should be noted, that the intensities in this 3D plot were not enhanced as it was performed in figure 3.26 for better visualization. As Bragg peaks with higher  $q_{\perp}$  can hardly be identified, this clarifies once more, that the image plate technique is not suitable to measure the weak scattering signal of a pentacene thin film.

Before a GI-CTR scans can be further processed and fitted, the diffuse background signal of the scan has to be analyzed and subtracted from the rod scan. This was done by performing a GI-CTR scan shifted in  $q_{\parallel}$  next to the area where the original scan was

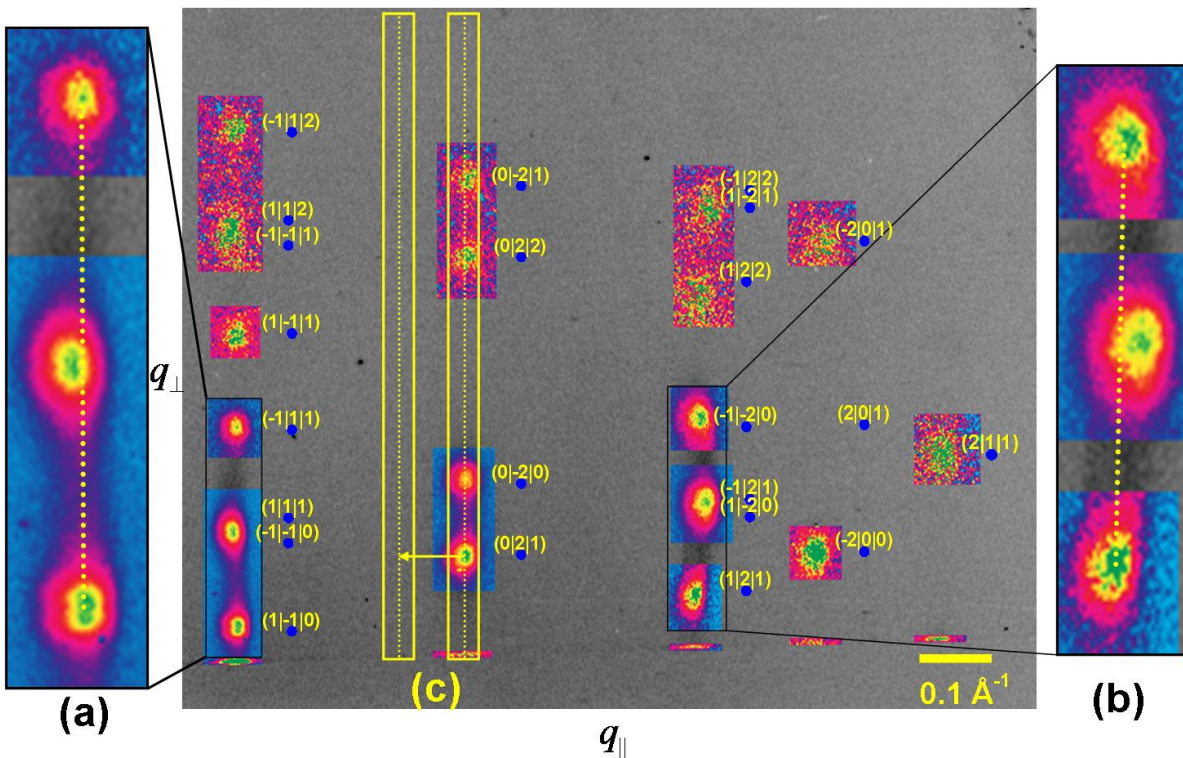


Figure 3.26: 2D image plate scan of a 480 Å pentacene thin film and simulated Bragg peak pattern (shifted to the right). (a) Zoom of the  $(\pm 1, \pm 1, 1)$  rod indicating a left shifted Bragg peak. (b) Zoom of  $(\pm 1, \pm 2, 1)$  rod indicating a right shifted Bragg peak. (c) The yellow boxes mark the area scanned by a GI-CTR measurement. The left shifted box marks the area, where the background scan of the  $(0, \pm 2, 1)$  rod was performed.

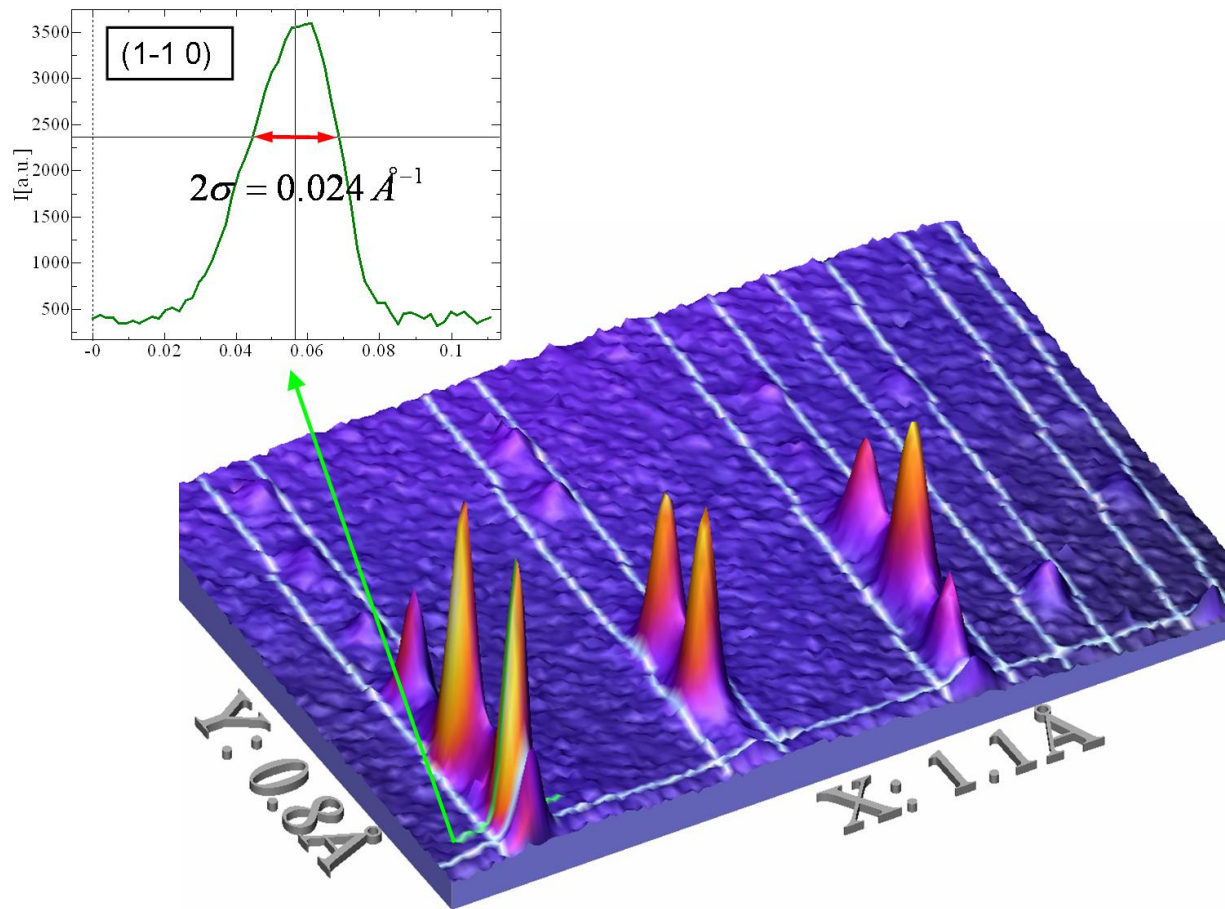


Figure 3.27: 3D visualization of a image plate scan of  $480 \text{ \AA}$  pentacene thin film. The green line indicates a profile scan, which is inset in the top left. The lines left and right of the Bragg peaks series mark the relevant area scanned during a GI-CTR measurement.



made (figure 3.26). The distance in  $q_{\parallel}$  was carefully selected, such that only diffuse signal is detected. This GI-CTR background scan is subtracted from its corresponding GI-CTR scan that was used as the basis dataset to estimate the crystal structure.

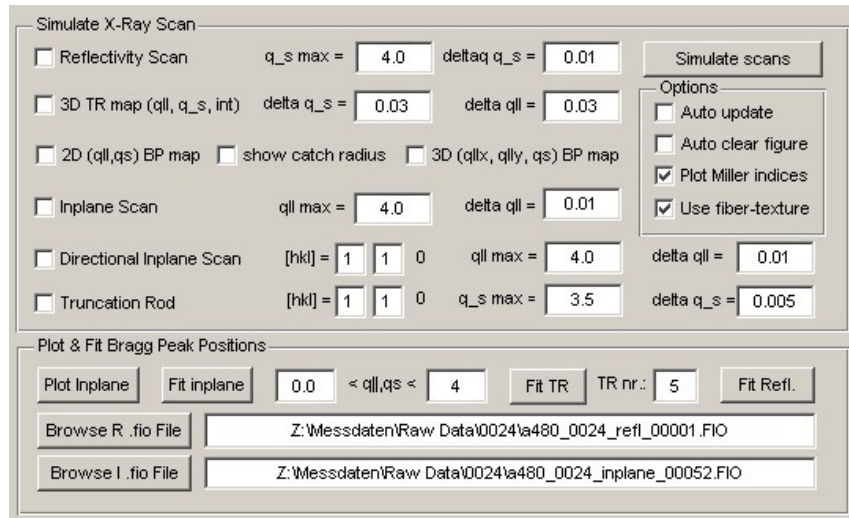
### 3.3 Implementation in Matlab

In the previous chapter, the theory and measurement techniques to solve the crystal structure of the pentacene *thin-film* phase were discussed. As there is no commercially available software package that is able to analyze GI-CTR measurements from a thin film fiber structure, the versatile software package “FiberRod” was developed and coded with the platform independent standard software suite Matlab, purchased from Mathworks. The length of the source code is several thousand lines long. FiberRod uses a user friendly graphical user interface (figure 3.28) and consists of several modules:

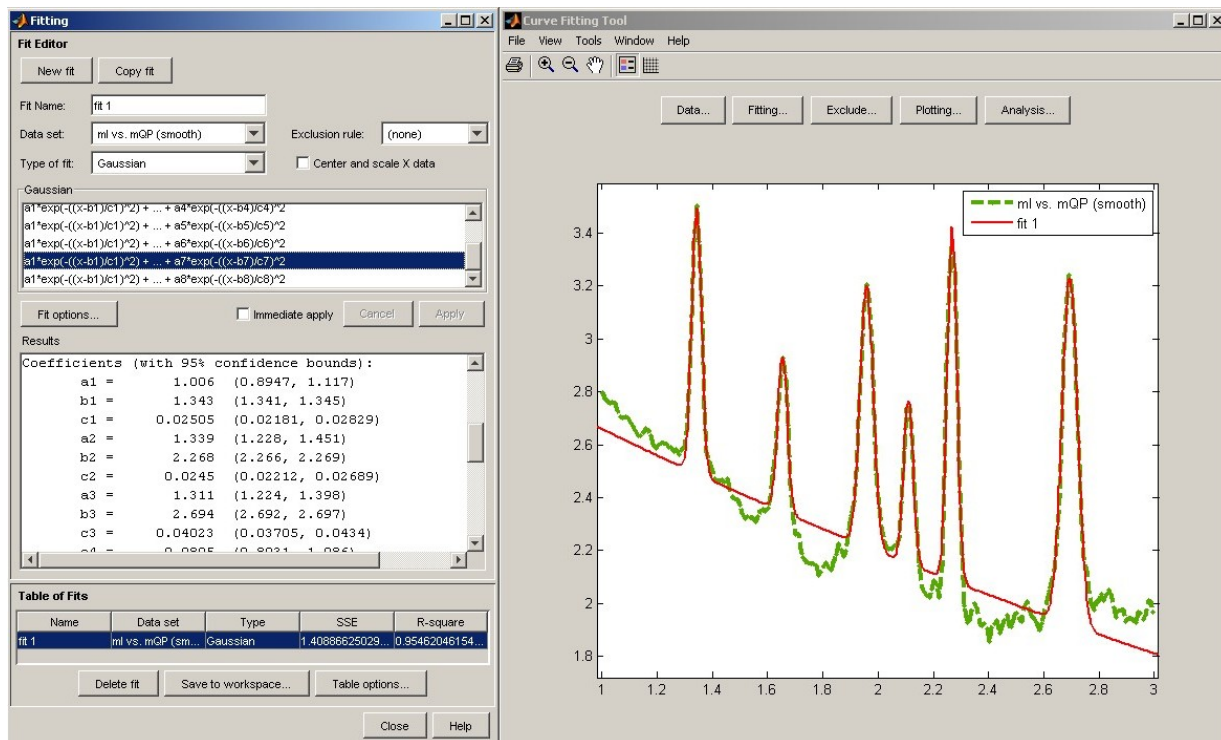
1. X-ray diffraction simulation module: to simulate Bragg peaks patterns and intensities from X-ray diffraction experiments.
2. Bragg peak position fit module: to estimate the exact Bragg peak positions from an X-ray diffraction scan.
3. Unit-cell solver module: to solve the unit-cell from the Bragg peak positions.
4. Molecular orientation solver module: to solve the molecular orientation of the molecules within the unit-cell using the previously determined unit-cell and by fitting the measured GI-CTR intensities .
5. Crystal structure visualizer: to visualize the solved crystal structure.
6. Crystal structure export module: to export the crystal structure to the Excel file format in order to create a .cif file (Crystallographic interchange format).

The X-ray diffraction simulation module shown in figure 3.28a is self explaining. It can be used to simulate X-ray reflectivity measurements, GIXD measurements, GI-CTR measurements and is able to plot Bragg peaks patterns. All simulation figures in this thesis were produced by the simulation module.

FiberRod is able to read the .fio file format used at W1 HasyLab directly and converts it into the reciprocal space using equations 3.30 and 3.29. To solve the crystal structure, a strategy with two steps was used: First, the unit-cell is solved by fitting the Bragg peak positions according to equations 3.14 and 3.15. Second, the molecular arrangement of the pentacene molecules within the previously determined unit-cell is solved by fitting the intensities of GI-CTR measurements according to equation 3.40. The two steps are now explained in the following two chapters using the six modules of FiberRod.



(a)



(b)

Figure 3.28: Screenshot of the (a) X-ray diffraction simulation module and the (b) Bragg peak position fit module using the curve fitting tool from the curve fitting toolbox by Mathworks.

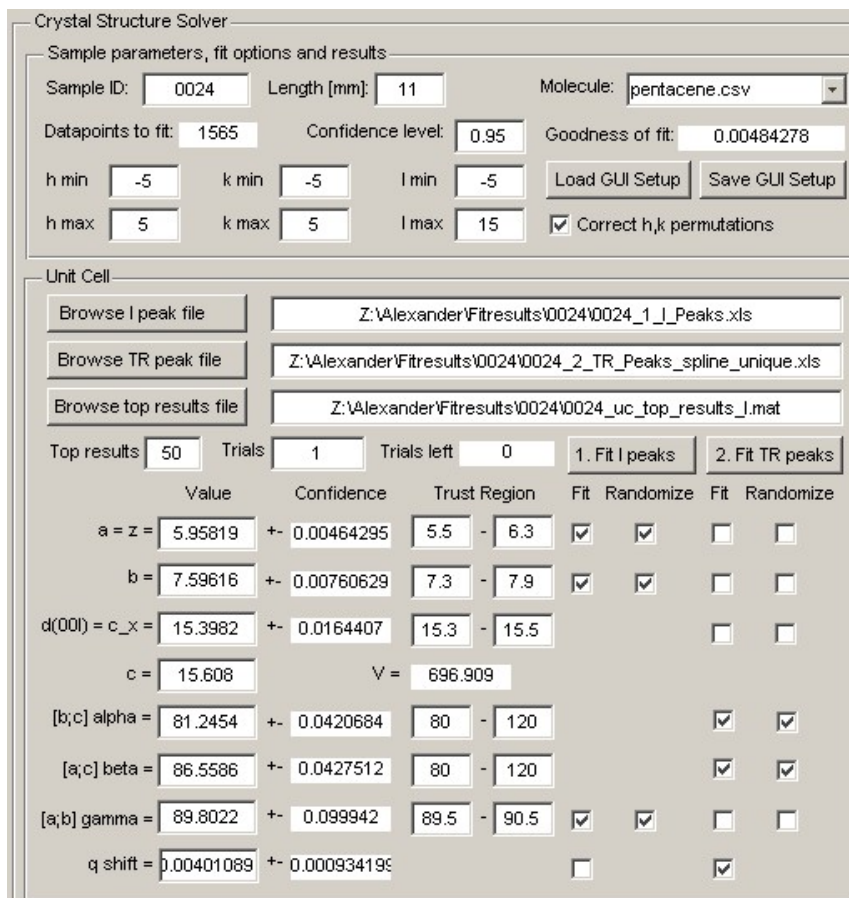


Figure 3.29: Screenshot of the unit-cell solver module.

### 3.3.1 Solving the unit-cell using FiberRod

To solve the unit-cell, a three step strategy is used:

(1) The  $(00l)$  Bragg peaks from an X-ray reflectivity measurement are used to calculate the  $d_{00l}$  spacing using equation 3.33. The measurement path is selected by the “Browse R .fio File” button and it is displayed and fitted using the “Fit Refl.” button in the Bragg peak position fit module (figure 3.28(a)). The button loads the reflectivity measurement automatically in the curve fitting tool (figure 3.28(b)) from the curve fitting toolbox, which can be used to fit the peaks.

(2) The inplane peaks from an GIXD measurement are used to fit the unit cell parameters  $a$ ,  $b$  and  $\gamma$  using equation 3.15. The measurement path is selected by the “Browse I .fio File” button. To display the measurement and to fit the peak positions within a selectable  $q$ -range is done clicking the “Fit Inplane” button (figure 3.28a). This loads the inplane measurement automatically in the curve fitting tool. In figure 3.28b, the fit result of an inplane measurement of a pentacene thin film with six peaks using a sum of seven Gauss functions is shown. The fitted inplane peak positions are given in the results

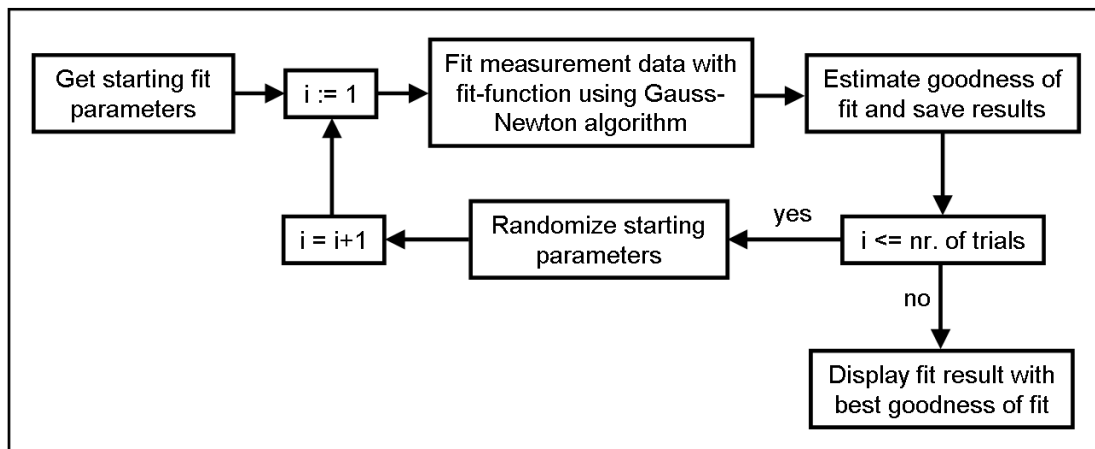


Figure 3.30: Flowchart of the algorithm to fit data in FiberRod.

window, which must be entered manually in an excel file in [ $\text{\AA}^{-1}$ ] units. The path of the excel file must be selected by clicking “Browse I peak file” in the unit-cell solver module (figure 3.29). After that, a results file path must be entered by clicking the “Browse top results file” button. This is the file where the fit results are saved by storing the complete graphical user interface of FiberRod. Before the inplane unit-cell fit can be started, it is mandatory to enter some parameters: A range of Miller indices ( $hkl$ ) have to be chosen, which cover the range of the Bragg peak positions to be fitted. To fit a fiber structure, the range of  $h$  and  $k$  must be symmetric around 0. The unit-cell parameters to be fitted and to be randomized can be chosen by clicking the corresponding “Fit” and “Randomize” flags. Last, the number of Monte Carlo trials have to be entered in the “Trials” field. Optionally, a “sample ID” can be entered to identify the fit and the corresponding sample. The fit process is started by clicking the “Fit I peaks” button. FiberRod automatically detects the best set of Bragg peak indices for the given Bragg peak positions by minimizing the sum of all distances from the measured peak positions to the simulated peaks positions within the given ( $hkl$ )-range. The fitting algorithm uses an iterative Gauss-Newton nonlinear least-squares data fitting model combined with a variation of the initial fit parameters by a Monte Carlo method within a given trust region for each unit-cell parameter, to ensure global minimization. After each trial, the “Goodness of the fit” is evaluated, the best fit out of the given number of trials is displayed at the end of the fit procedure and the assigned Miller indices and the error for each Bragg peak is output in the command window. The fit algorithm is shown as a flowchart in figure 3.30. Additionally, in the field “Top results” a number of the best  $x$  results can be entered, which are saved in a .mat (Matlab binary format) file for comparison. When the fit procedure is finished, the confidence intervals for each parameter are shown based on the confidence level given in the field “Confidence level”, which is set to 95% ( $2\sigma$ ) by default.

(3) The GI-CTR Bragg peaks are used to fit any unit-cell parameters (usually the remaining parameters  $\alpha$  and  $\beta$ ) using equation 3.13. First an excel file must be created where the file names of the GI-CTR measurements and their background scan are entered.

**Molecular Orientation**

Crystal Lattice

N x a =  N x b =  N x c =

Use intensity scaling for Na, Nb  Structure factor only

Plot Miller indices

Top results  Trials  Trials left

	Value	Confidence	Trust Region	Fit	Randomize
Z-axes tilt mol(0) =	<input type="text" value="-1.6608"/>	+ 0.419672	-10.0 - 10.0	<input checked="" type="checkbox"/>	<input checked="" type="checkbox"/>
Z-axes tilt mol(1/2) =	<input type="text" value="-1.80234"/>	+ 0.228311	-10.0 - 10.0	<input checked="" type="checkbox"/>	<input checked="" type="checkbox"/>
Y-axes tilt mol(0) =	<input type="text" value="5.49315"/>	+ 0.519808	-10.0 - 10.0	<input checked="" type="checkbox"/>	<input checked="" type="checkbox"/>
Y-axes tilt mol(1/2) =	<input type="text" value="5.81003"/>	+ 0.522201	-10.0 - 10.0	<input checked="" type="checkbox"/>	<input checked="" type="checkbox"/>
Herringbone angle =	<input type="text" value="59.841"/>	+ 1.65101	45 - 90	<input checked="" type="checkbox"/>	<input checked="" type="checkbox"/>
TR Int. scaling =	<input type="text" value="0.000662123"/>	+ 5.32028e-0	1e-7 - 1e-5	<input checked="" type="checkbox"/>	<input type="checkbox"/>
Debye-Waller Uiso =	<input type="text" value="0.0914024"/>	+ 0.0126972	0.00 - 0.50	<input checked="" type="checkbox"/>	<input checked="" type="checkbox"/>
Surf. roughness =	<input type="text" value="0.264532"/>	+ 0.0121487	0.00 - 0.40	<input checked="" type="checkbox"/>	<input checked="" type="checkbox"/>

**Fit Options**

Fit for:  <  $q_s$  <   Use  $q_{critical}$  =   Int. correction

$q_p$  resolution [c]:  BP catch radius  $q_{||}$  =   $q_s$  =   Refine all

**Background Intensity Offsets**

R  |  TR

Figure 3.31: Screenshot of the molecular orientation solver module.

The path of the excel file must be entered by clicking the “Browse TR .fio files” button in the Molecular Orientation Solver module (figure 3.31). As for reflectivity and GIXD measurements, the Bragg peak positions can be fitted by clicking the “Fit TR” button. The GI-CTR measurement with the line number in the excel file entered in the field “TR nr.” is then loaded in the curve fitting toolbox. Once the Bragg peak positions are determined by using e.g. Gauss- or Lorentz fit functions, their  $(q_{\perp}, q_{||})$  values must be entered in an excel file. The file path of this excel file must be entered by clicking “Browse TR peak file”. The fit process is started by clicking “Fit TR peaks”. The fit algorithm works in the same way as for inplane Bragg peaks by minimizing the sum of the distances of the measured and simulated peaks.

### 3.3.2 Solving the molecular orientation using FiberRod

Once the unit-cell is determined, the molecular orientation is solved by fitting the GI-CTR intensities with the Molecular orientation solver module (figure 3.31) using equation 3.40. The fit algorithm works as illustrated in figure 3.30. FiberRod constructs a pentacene unit-cell consisting of two pentacene molecules, called A and B in the following manner: The structure of the plain pentacene molecule was taken from the 14.1 Å crystal structure [31] and is assumed to be rigid in the *thin-film* phase, as only weak forces are present in the crystal. The positions of both molecules are fixed with their center of mass to the relative unit-cell coordinates to (0, 0, 0) for molecule A and (1/2, 1/2, 0) for molecule B. The initial orientation of the molecules is set with their molecular plane parallel to the  $\vec{a} - \vec{b}$  plane and their long molecular axes (LMAs, see figure 3.32a) oriented parallel to the x-axis. During a fit, each molecule can be rotated by its three angular degrees of freedom independently. The respective molecule is rotated around the center of mass by the x-, y- and z-axis. The molecular orientation in the graphical user interface is parametrized as follows: The angle between the two molecular planes is called the herringbone angle  $\theta_{hrgb}$  as illustrated in figure 3.32b. The tilt angle around the z-axis of the molecule coordinate system is called  $\theta_z$  and around the y-axis  $\theta_y$ . The angles are indexed with A or B for the two pentacene molecules.

When the “Fit TR Intensities” button is pressed, the molecular orientation fit is started. Before the measurement data is parsed into the fit-function, several tasks are performed: (1) The measured data is smoothed by the Savitzky-Golay method [68] with degree = 2 and span = 5 to reduce background noise. (2) After conversion into reciprocal space, the background signal of each GI-CTR measurement is linearized by subtracting the corresponding GI-CTR background measurement. (3) The resulting datasets are corrected by the LPAR intensity correction factors as described in chapter 3.2.3. The geometric parameters needed for the corrections are stored in the .fio files. The length of the sample in mm is entered in the unit-cell module (figure 3.29) in the field “Length of Sample”. (4) To simulate the whole line shape of a GI-CTR measurement, it is necessary to simulate the intensity for each measured data point. Therefore it is necessary to identify all Bragg peaks of which the GI-CTR is composed. FiberRod automatically detects these Bragg peaks. The peaks are identified by superimposing the calculated Bragg peak pattern with the GI-CTR measurements. All Bragg peaks within a ellipse defined by the semimajor axis  $r_{q_{\parallel}}$  and the semimajor axis  $r_{q_{\perp}}$  entered in the field “BP catch radius  $q_{\parallel}$ ” and “qs” are assigned to each data point (figure 3.33). The catch radius  $r_{q_{\parallel}}$  is especially important when several crystal rods are close in  $q_{\parallel}$  and are measured in one GI-CTR measurement due to the finite slit width of the detector slit DSH in  $q_{\parallel}$ . The semimajor axis  $r_{q_{\perp}}$  is set to a value, such that every data point is within at least one ellipse.

Once all Miller indices are assigned to each data point, the GI-CTR measurements are combined to one big dataset and parsed into the fit function. The fit function simulates the intensity of every data point by constructing a  $\vec{q}$  vector by using the  $q_{\perp}$  value from the actual measured data point and the  $\vec{q}_{\parallel}$  vector from the assigned Miller indices h and k and evaluating the intensity using equation 3.40. When “Use intensity scaling for Na, Nb” is

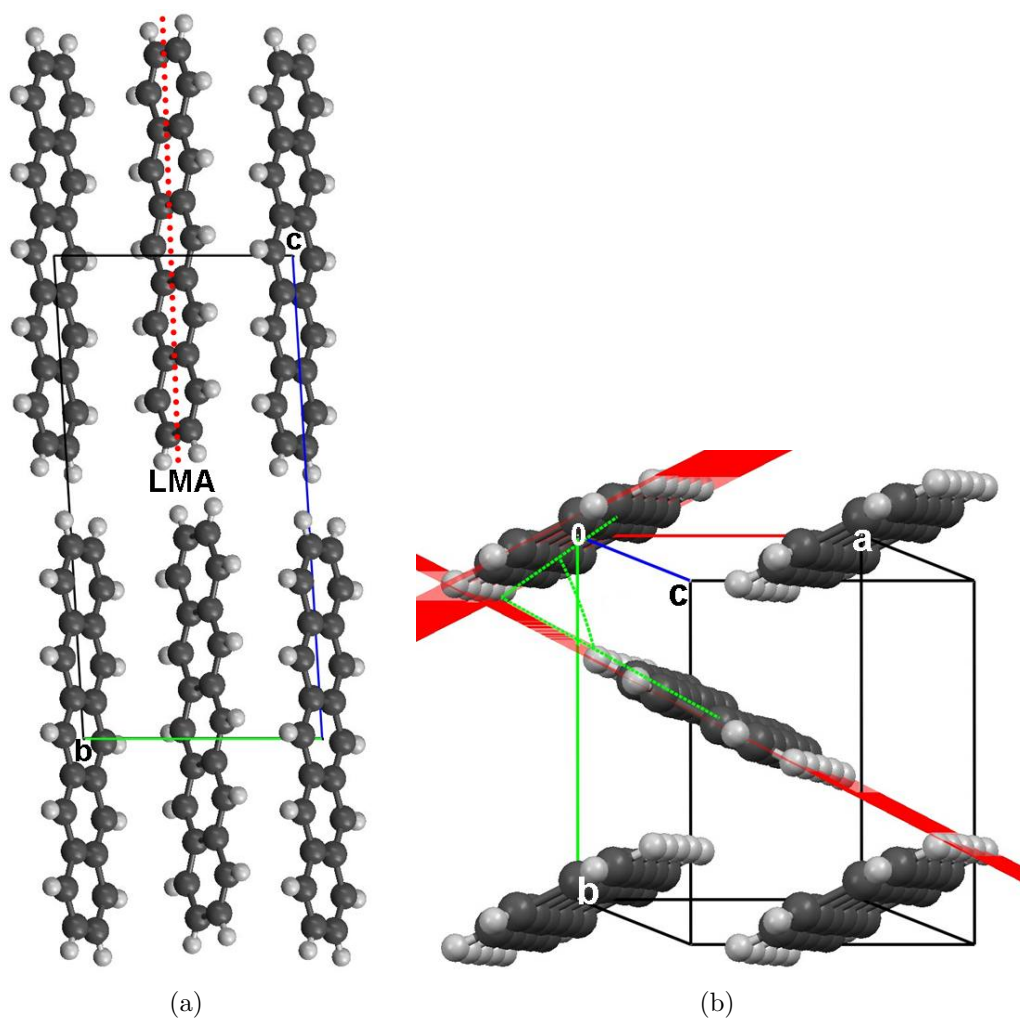


Figure 3.32: (a) Side view and (b) top view of a pentacene unit-cell arranged in a herringbone structure. The long molecular axis (LMA) is illustrated as a red dotted line. The herringbone angle between the two molecule planes is illustrated in green.

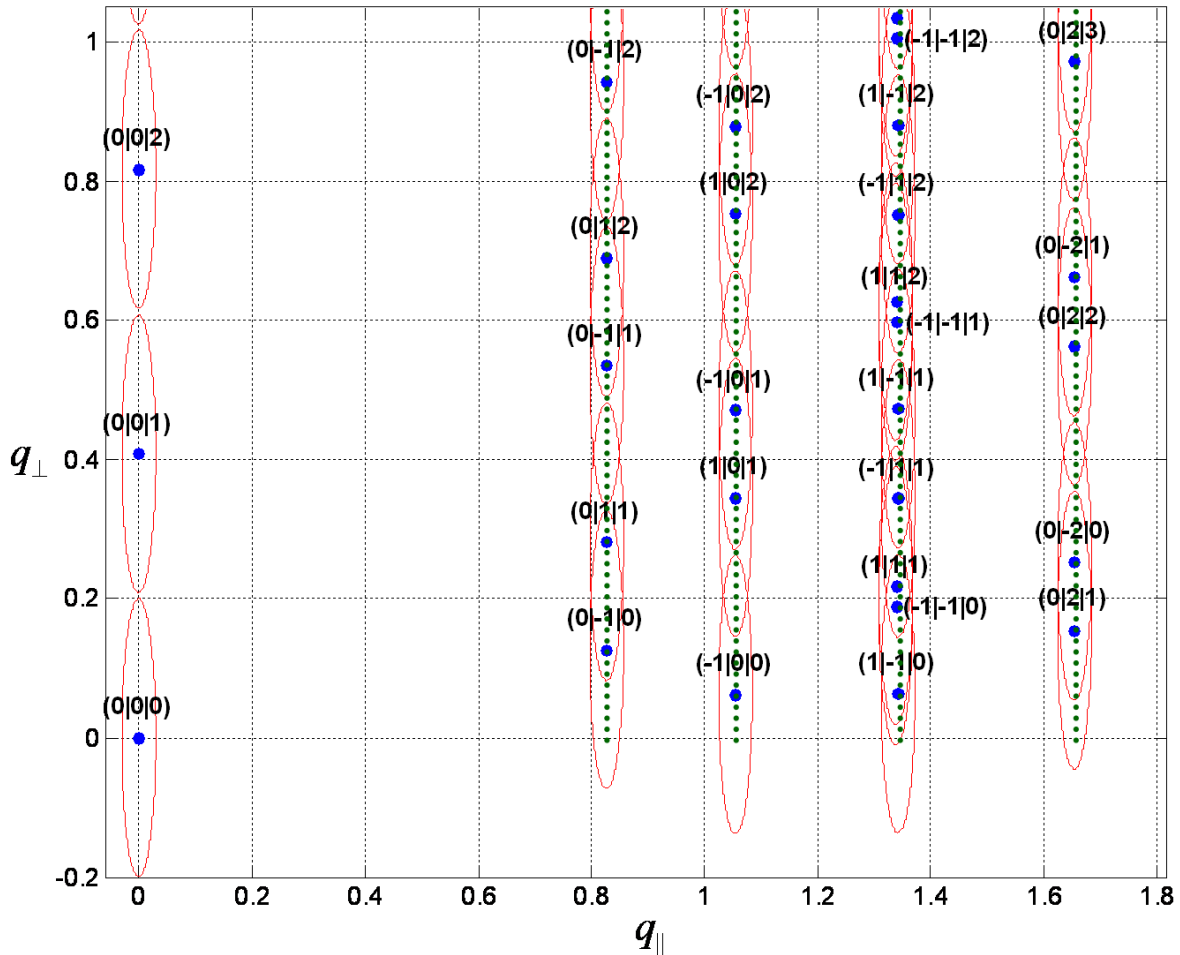


Figure 3.33: Schematic illustration of the automatic assignment of Miller indices to a measured data point. The green dotted line illustrates the path of a GI-CTR measurement. The blue dots represent the centers of the Bragg peaks. Data points within the red ellipses, illustrating the “catch area”, are assigned the Miller indices of the respective Bragg peak.



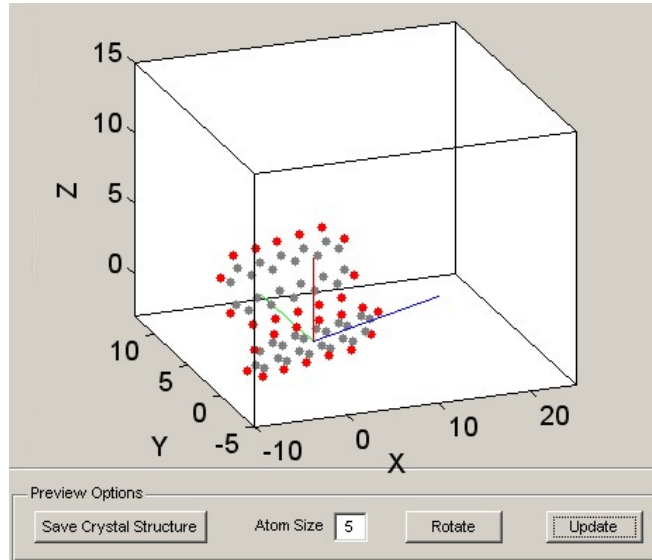


Figure 3.34: Screenshot of the crystal structure visualizer and the crystal structure export module.

activated, the pre factor of equation 3.40

$$I_{TR} = I_0 \left( \frac{r_e}{R_0} N_a N_b \right)^2$$

is treated as one fit parameter, called “TR intensity scaling”  $I_{TR}$  and is used for the whole dataset. The thickness of the film is entered in the field “Nc”, which was set to 30 in unit cells.

As the signal to noise ratio during a measurement is finite, a constant background which can be set individually for each measurement is added to the simulated GI-CTR dataset. The values for constant background are entered in the section “Background Intensity Offsets” in the Molecular Orientation Module. The backgrounds are estimated by plotting the GI-CTR measurements and selecting an intensity value, where background noise is dominant and no more Bragg peaks are identified.

The fit algorithm is able to fit all nine molecular orientation parameters, the six orientation angles, the  $U_{iso}$  factor, the surface roughness  $\sigma$  and the “TR intensity scaling”  $I_{TR}$  at the same time.

When the fit is completed, the fit results of the crystal parameters, the measurements and the simulations of the GI-CTRs can be plotted by clicking the “Plot & Sim TR” button (figure 3.35).

The unit-cell and the molecular orientation is visualized in the “Crystal structure visualizer” module as shown in figure 3.34. Here, the crystal structure can be exported in an excel file for further processing.

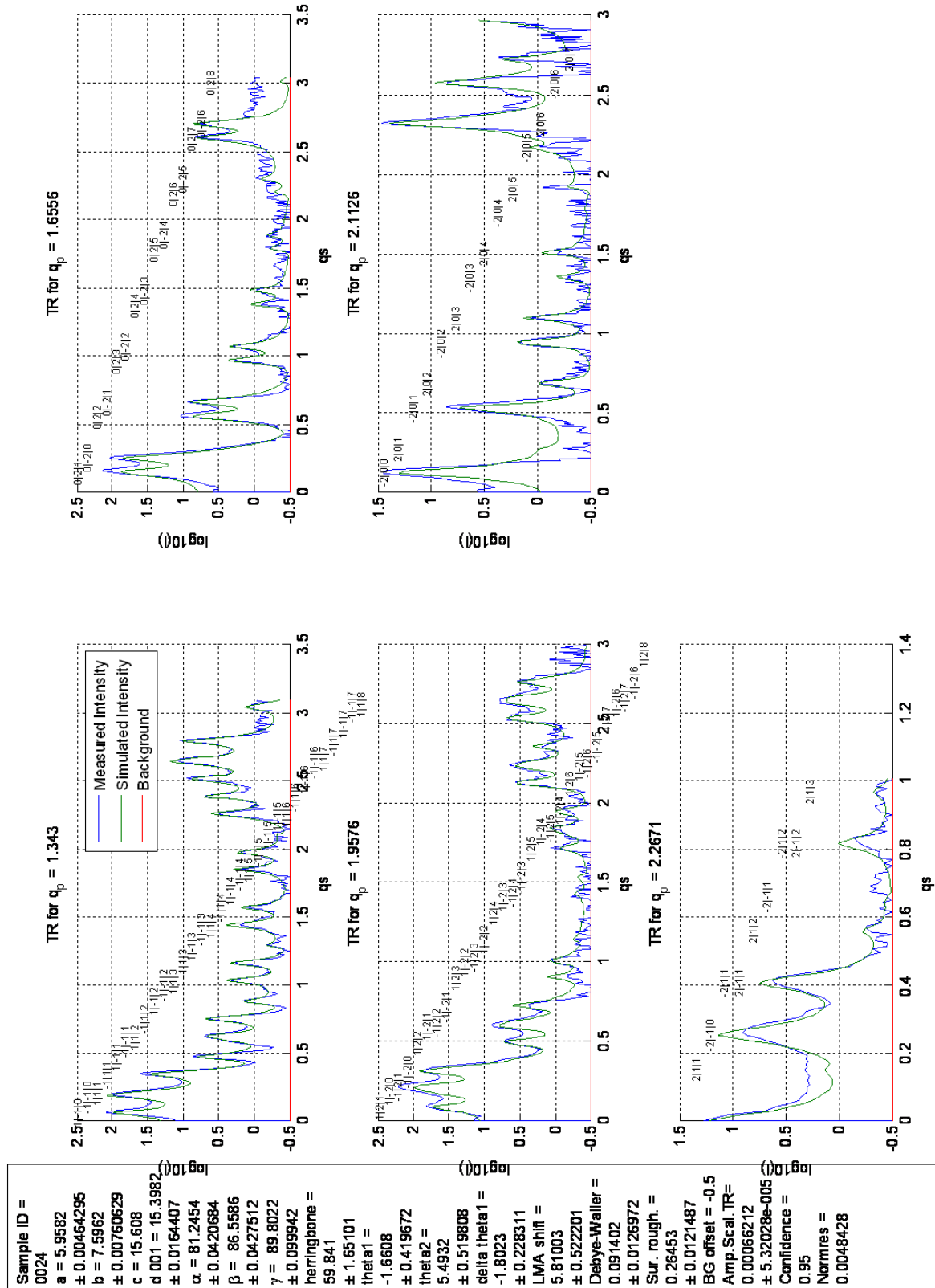


Figure 3.35: Plot of the GI-CTR fit results after clicking the “Plot & Sim TR” button.

# Chapter 4

## Results

In this chapter, the fit results of the X-ray diffraction measurements at HasyLab beamline W1 and the corresponding crystal structures pentacene *thin-film* polymorphs grown on four gate dielectric materials is presented. Detailed atomic positions are given in appendix C in cif (crystallographic interchange format) format.

### 4.1 Crystal structure on $a - SiO_2$ substrate

After the thin film is grown in situ as described in chapter 2.5.3, an X-ray reflectivity measurement was performed (figure 4.1). The measurement shows five distinct Bragg peaks. The Miller indices were identified as  $d_{00l}$  peaks, where  $l = [1, 5]$  associated with  $d_{001}$  interlayer spacing of 15.40 Å. As expected from literature, the reflectivity measurement showed, that solely the 15.40 Å *thin-film* phase is present on the substrate.

Hereafter, a GIXD measurement was performed (figure 4.2). The GIXD Bragg peak positions were fitted with a Gauss function. The precise knowledge of the  $q_{||}$  positions is important, as  $a$ ,  $b$  and  $\gamma$  are very sensitive to these positions. For the fit process, only GIXD peaks which could be explicitly assigned to Miller indices were used. Figure 4.2 shows a GIXD measurement of the pentacene *thin-film* phase on  $a - SiO_2$  and the corresponding Miller indices. Two peaks consist of two Miller indices (marked red), which are slightly shifted against each other, such that the peak is broadened. This makes an explicit association to a specific Miller index impossible, and these peaks are omitted in the first step of the analysis. However, the six remaining peaks are sufficient to solve for  $a$ ,  $b$  and  $\gamma$ . The unit-cell parameters were found to be  $a = 5.958 \pm 0.005 \text{Å}$ ,  $b = 7.596 \pm 0.008 \text{Å}$  and  $\gamma = 89.80 \pm 0.1^\circ$ . The unit cell volume was calculated to  $V = 697 \text{Å}^3$ .

GI-CTR measurements were performed using the first five GIXD peaks as a starting position (figure 4.2). The other GIXD peaks were omitted, because the corresponding GI-CTRs are too broad in  $q_{||}$  to be integrated properly by the slit system. The two remaining unit-cell parameters  $\alpha$  and  $\beta$  were determined from Bragg peak positions measured by GI-CTR. Again, some Bragg peaks are too close in  $q_{\perp}$  to resolve the exact position. Only the unique Bragg peak positions have been chosen for the subsequent analysis of  $\alpha$  and

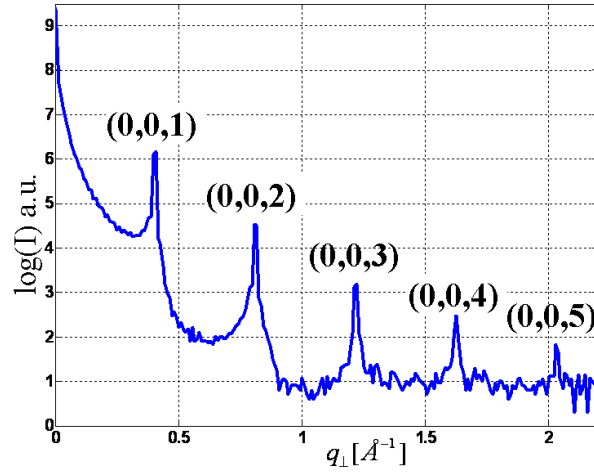


Figure 4.1: X-ray reflectivity measurement of a 480  $\text{\AA}$  pentacene thin film on  $a - \text{SiO}_2$  gate dielectric.

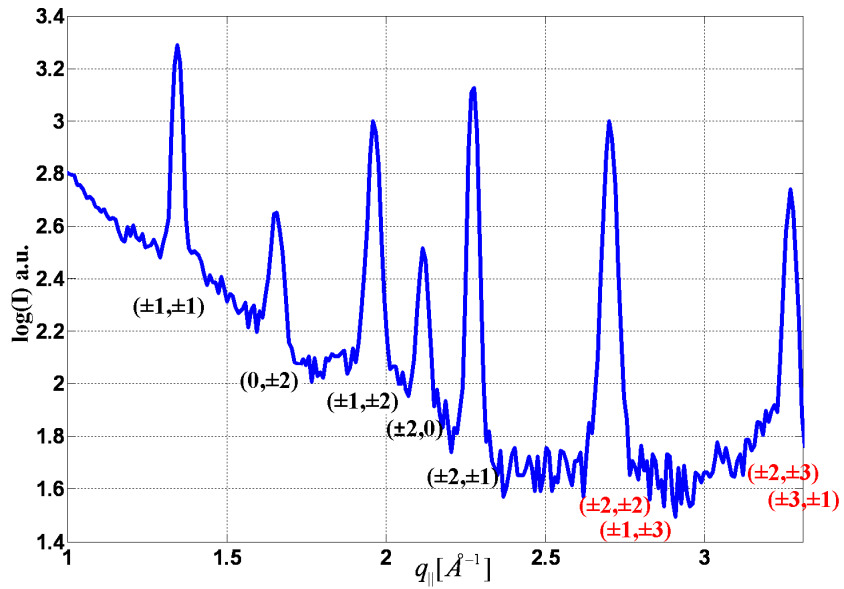


Figure 4.2: GIXD measurement of a 480  $\text{\AA}$  pentacene thin film on  $a - \text{SiO}_2$  gate dielectric.

Substrate: $a - SiO_2$	
a	$5.958 \pm 0.005 \text{ \AA}$
b	$7.596 \pm 0.008 \text{ \AA}$
c	$15.61 \pm 0.01 \text{ \AA}$
$d_{001}$	$15.40 \pm 0.01 \text{ \AA}$
$\alpha$	$81.25 \pm 0.04^\circ$
$\beta$	$86.56 \pm 0.04^\circ$
$\gamma$	$89.80 \pm 0.1^\circ$
V	$697.0 \text{ \AA}^3$

Table 4.1: Unit-cell parameters of the pentacene *thin-film* phase grown on  $a - SiO_2$ .

Substrate: $a - SiO_2$	
$\theta_{hr gb}$	$54.3 \pm 1.3^\circ$
$\theta_{zA}$	$-1.0 \pm 0.4^\circ$
$\theta_{yA}$	$5.6 \pm 0.5^\circ$
$\theta_{zB}$	$-1.6 \pm 0.4^\circ$
$\theta_{yB}$	$5.8 \pm 0.4^\circ$
$U_{iso}$	$0.04 \pm 0.01$
$\sigma$	$0.23 \pm 0.02$

Table 4.2: Molecular orientation parameters of the pentacene *thin-film* phase grown on  $a - SiO_2$ .

$\beta$ . After that, it was verified that the as determined unit-cell parameters cover all peaks omitted accordingly. The unit-cell parameters were found to be  $\alpha = 81.25 \pm 0.04^\circ$  and  $\beta = 86.56 \pm 0.04^\circ$ . To double check, all six unit-cell parameters were fitted from the GI-CTR Bragg peak positions and found to be equal to the values determined by X-ray reflectivity and GIXD measurements. The unit-cell parameters are summarized in table 4.1.

The molecular orientation was solved by fitting the intensities of the five GI-CTR measurements shown in figure 4.3. Using model simulations of GI-CTRs shown in figure 4.4, it was verified that these five GI-CTRs are sensitive to the molecular orientation fitting parameters, if the signal to noise ratio of  $10^3$  provided by the X-ray setup at the W1 beamline is assumed. Note, that the model simulations also show that in this case it is not possible to fit the molecular orientation by the data provided by an image plate, which is only sensitive to regions of  $q_\perp < 0.8 \text{ \AA}^{-1}$  including a signal-to-noise ratio as low as  $10^{1.5}$ . The fit results of the molecular orientation are summarized in table 4.2.



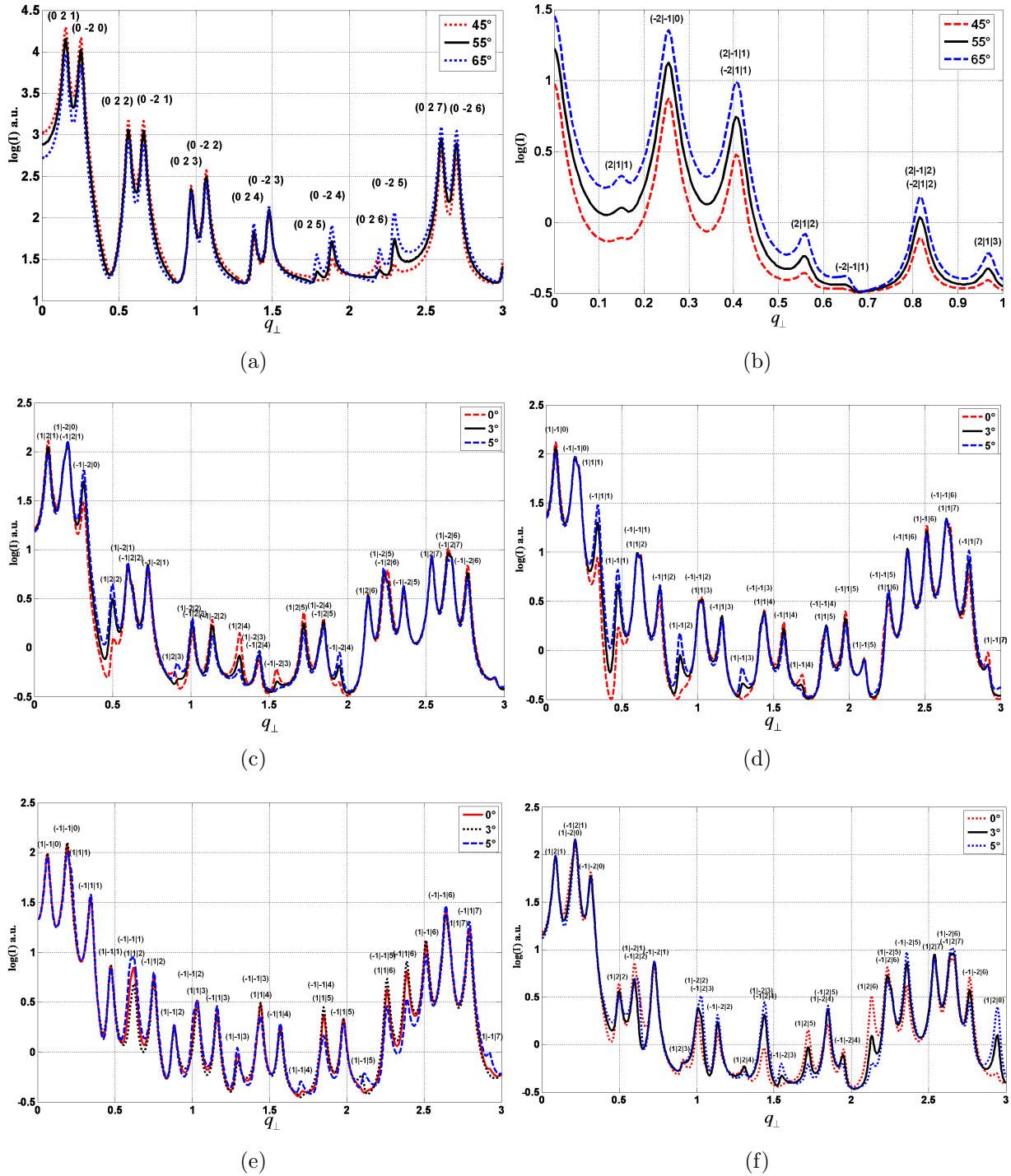


Figure 4.4: Impact of the herringbone angle  $\theta_{hr gb}$  on the (a)  $(0, \pm 2)$  and (b)  $(\pm 2, \pm 1)$  rods. Impact of the tilt angle (c)  $\theta_{AY}$  on the  $(\pm 1, \pm 2)$  and (d)  $\theta_{BY}$  on the  $(\pm 1, \pm 1)$  rod. (e) Impact of the tilt angle  $\theta_{AZ}$  on the  $(\pm 1, \pm 1)$  and (f)  $\theta_{BZ}$  on the  $(\pm 1, \pm 2)$  rod.

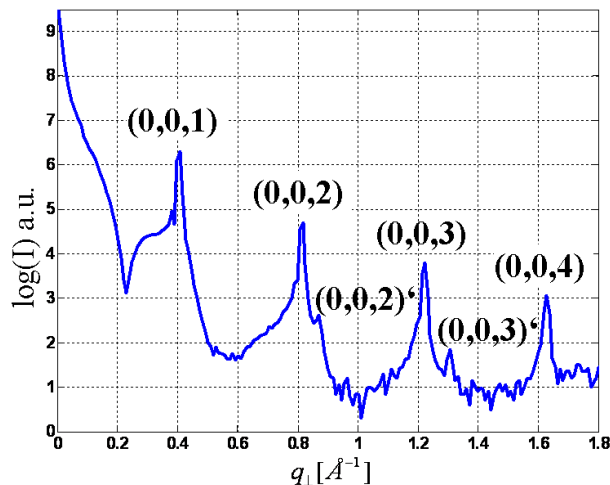


Figure 4.5: X-ray reflectivity measurement of a 480 Å pentacene thin film on OTS gate dielectric.

## 4.2 Crystal structure on OTS substrate

Figure 4.5 shows the X-ray reflectivity measurement of the pentacene *thin-film* phase on the OTS gate dielectric. As expected, the  $d_{00l}$  Bragg peaks associated with an interlayer spacing of 15.40 Å can be clearly observed. However, two small satellite peaks (0,0,2)' and (0,0,3)' associated with an interlayer spacing of 14.40 Å, the “pentacene bulk phase”, could also be observed. The intensity of these two peaks is two orders of magnitudes lower when compared to their corresponding 15.40 Å Bragg peaks.

In a GIXD measurement shown in figure 4.6, only Bragg peaks associated with the *thin-film* phase were found. Thus, the GIXD Bragg peak intensities of the bulk phase crystallites are too weak to be detected. The unit-cell of the pentacene *thin-film* phase on OTS substrate was determined in the same way as on  $a - SiO_2$  and found to be equal.

However, the molecular orientation of the pentacene molecules on an OTS substrate determined from the GI-CTRs measurements and shown in figure 4.7 differs from the ones determined on  $a - SiO_2$  substrate. The fit results of the molecular orientation are summarized in table 4.3.

## 4.3 Crystal structure on Topas substrate

Figure 4.8 shows an X-ray reflectivity measurement of the pentacene *thin-film* phase on Topas gate dielectric. Five distinct Bragg peaks associated with an interlayer spacing of  $d_{00l} = 15.40$  Å can be clearly observed. No signal of bulk phase Bragg peaks could be observed. Again, the unit-cell parameters of the *thin-film* phase were determined in the same way as it was done for  $a - SiO_2$  and OTS substrate. Figure 4.9 shows the corresponding GIXD measurement and figure 4.10 the corresponding GI-CTR measurements and the best



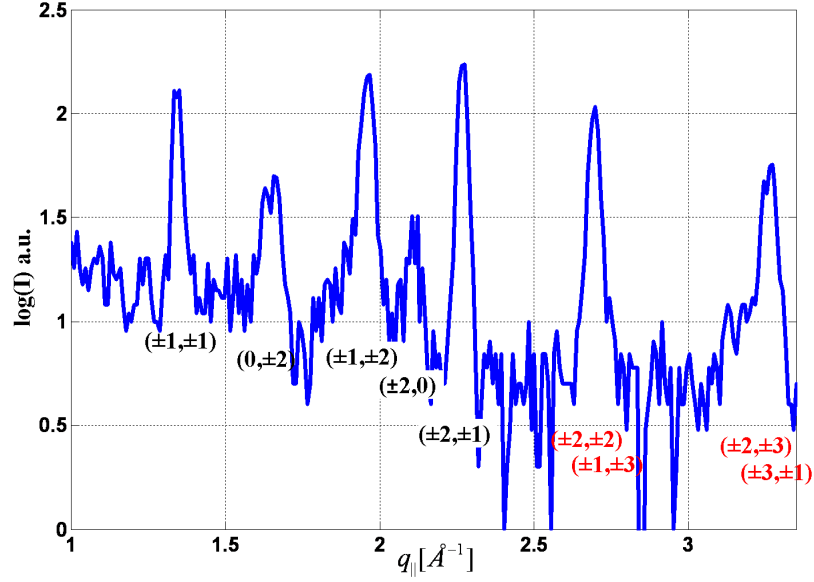


Figure 4.6: GIXD measurement of a 480 Å pentacene thin film on OTS gate dielectric.

Substrate: OTS	
$\theta_{hr gb}$	$55.8 \pm 2.0^\circ$
$\theta_{zA}$	$-1.4 \pm 0.5^\circ$
$\theta_{yA}$	$6.2 \pm 0.7^\circ$
$\theta_{zB}$	$-3.0 \pm 0.5^\circ$
$\theta_{yB}$	$6.1 \pm 0.5^\circ$
$U_{iso}$	$0.08 \pm 0.01$
$\sigma$	$0.24 \pm 0.02$

Table 4.3: Molecular orientation parameters of the pentacene *thin-film* phase grown on OTS.

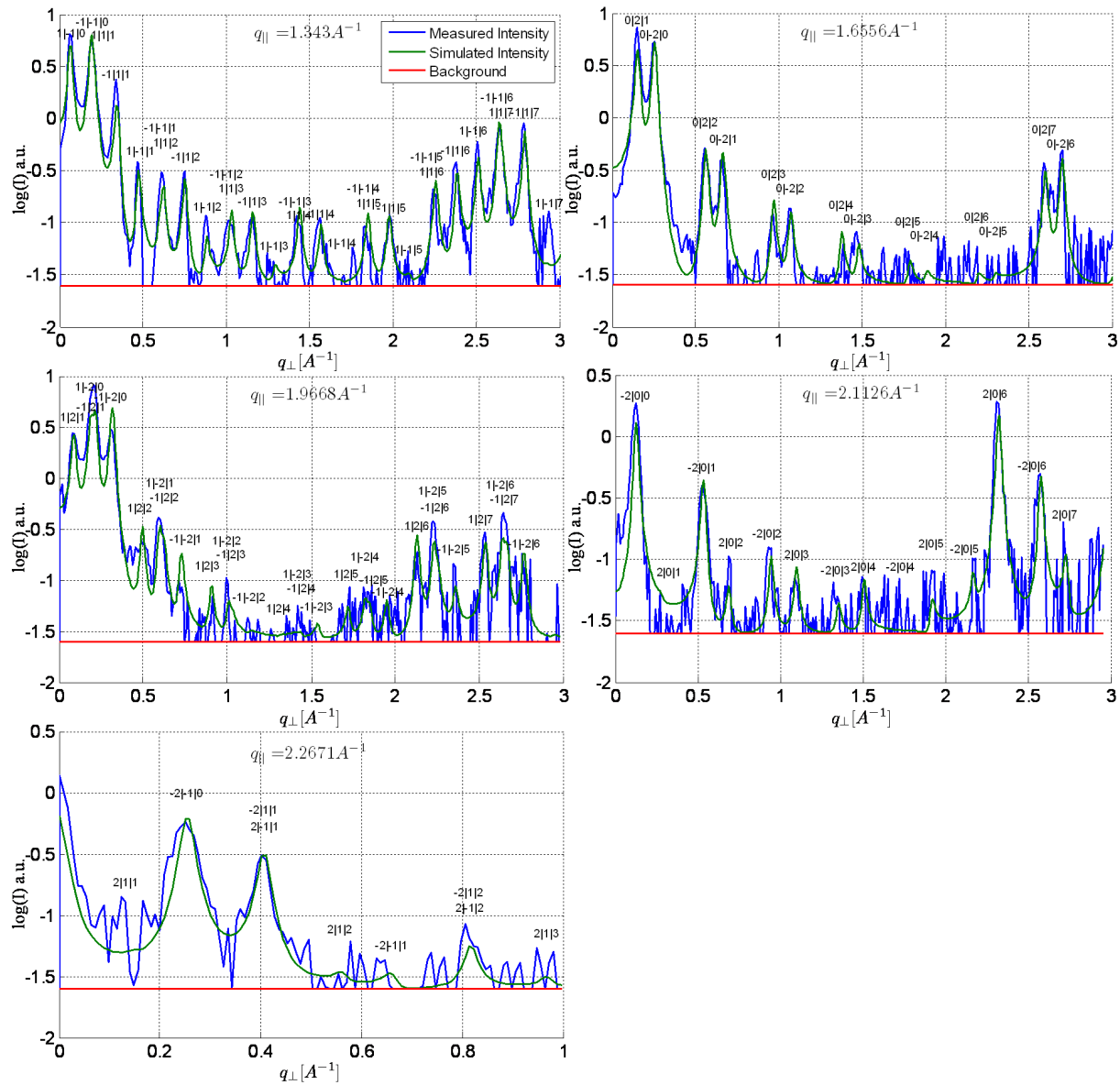


Figure 4.7: GI-CTR measurements of a 480 Å pentacene thin film on OTS gate dielectric.

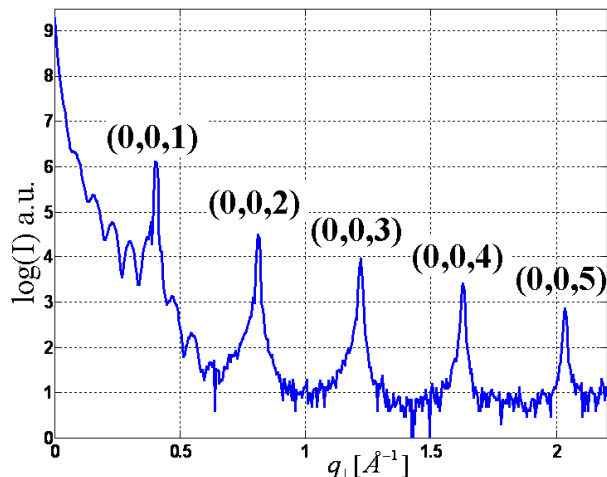


Figure 4.8: X-ray reflectivity measurement of a 480 Å pentacene thin film on Topas gate dielectric.

Substrate: Topas	
$\theta_{hr gb}$	$59.4 \pm 1.3^\circ$
$\theta_{zA}$	$-1.4 \pm 0.4^\circ$
$\theta_{yA}$	$5.4 \pm 0.5^\circ$
$\theta_{zB}$	$-2.0 \pm 0.5^\circ$
$\theta_{yB}$	$6.0 \pm 0.4^\circ$
$U_{iso}$	$0.05 \pm 0.01$
$\sigma$	$0.27 \pm 0.01$

Table 4.4: Molecular orientation parameters of the pentacene *thin-film* phase grown on Topas.

fit plots. The unit-cell parameters on Topas substrate were found to be equal to those on *a* – *SiO*<sub>2</sub> and OTS substrates.

However, the molecular orientation of the pentacene molecules on Topas substrate shown in figure 4.10, differs from the ones determined on *a* – *SiO*<sub>2</sub> and OTS substrate. The fit results of the molecular orientation are summarized in table 4.4.

## 4.4 Crystal structure on PS substrate

The X-ray diffraction measurements of the pentacene *thin-film* phase on polystyrene substrate were performed in air. The X-ray reflectivity measurement is shown in figure 4.11. Here, six Bragg peaks could be observed associated with to the 15.40 Å pentacene *thin-film* phase. No bulk Bragg peaks could be observed. The GIXD measurement is shown in figure 4.12. As the diffraction signal is not limited by the 270° beryllium window, an extra GIXD Bragg peak associated with a Miller index of ( $\pm 1, \pm 4$ ) could be observed. The unit-cell

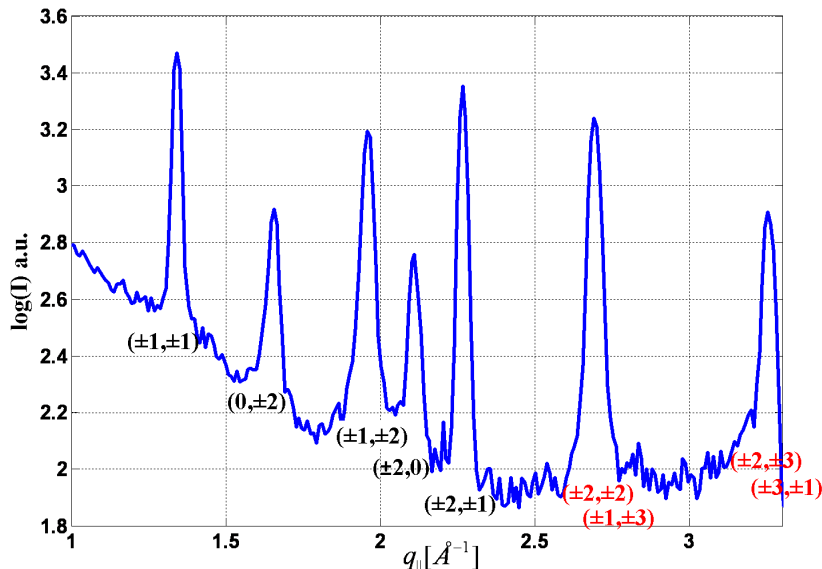


Figure 4.9: GIXD measurement of a 480 Å pentacene thin film on Topas gate dielectric.

substrate	$\theta_{hr gb.} [^\circ]$	$\theta_{zA} [^\circ]$	$\theta_{yA} [^\circ]$	$\theta_{zB} [^\circ]$	$\theta_{yB} [^\circ]$	$U_{iso}$	$\sigma$
$a - SiO_2$	$54.3 \pm 1.3$	$-1.0 \pm 0.4$	$5.6 \pm 0.5$	$-1.6 \pm 0.4$	$5.8 \pm 0.4$	$0.04 \pm 0.01$	$0.23 \pm 0.02$
OTS	$55.8 \pm 2.0$	$-1.4 \pm 0.5$	$6.2 \pm 0.7$	$-3.0 \pm 0.5$	$6.1 \pm 0.5$	$0.08 \pm 0.01$	$0.24 \pm 0.02$
Topas	$59.4 \pm 1.3$	$-1.4 \pm 0.4$	$5.4 \pm 0.5$	$-2.0 \pm 0.5$	$6.0 \pm 0.4$	$0.05 \pm 0.01$	$0.27 \pm 0.01$
polystyrene	$55.1 \pm 0.9$	$-1.5 \pm 0.2$	$5.5 \pm 0.3$	$-1.6 \pm 0.2$	$5.8 \pm 0.2$	$0.08 \pm 0.01$	$0.20 \pm 0.02$

Table 4.5: Molecular orientation fit results of the pentacene *thin-film* phase on various gate dielectrics

was determined in the same way it was done for the other three samples, except that one additional GIXD peak and one additional GI-CTR measurement using this Bragg peak as a starting position was measured and used for fitting. It was found that the unit-cell is identical to the unit-cell found for the other three substrates, even though the measurement was performed in air.

However, the molecular orientation was found to be different from the other three substrates. The fit results of the molecular orientation parameters of the pentacene *thin-film* phase on polystyrene substrate is given in table 4.5 together with the values found for the other three samples for comparison.

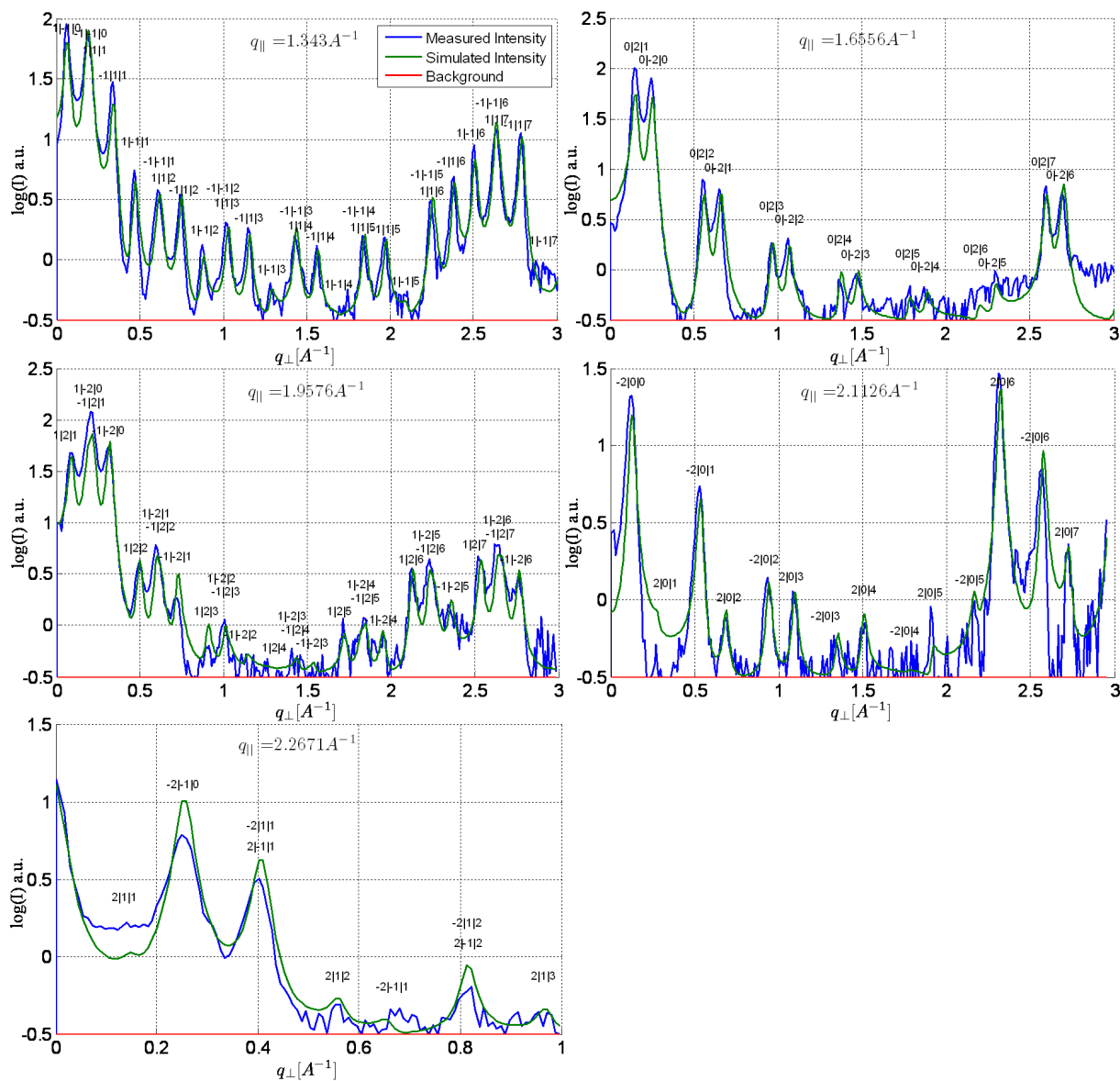


Figure 4.10: GI-CTR measurements and best fit plots of a 480 Å pentacene thin film on Topas gate dielectric.

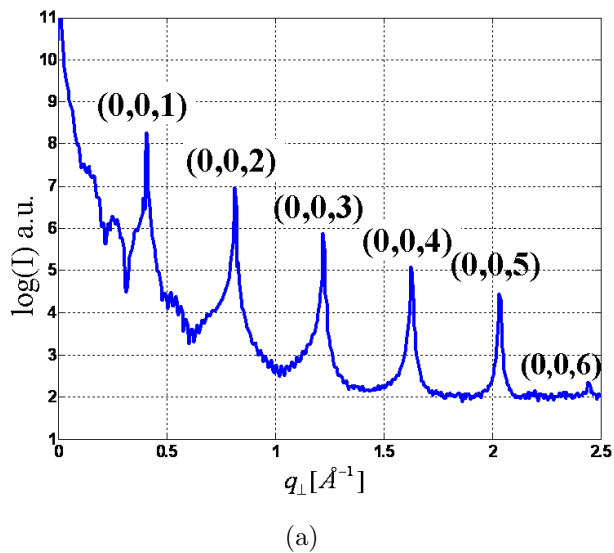


Figure 4.11: X-ray reflectivity measurement of a 480 Å pentacene thin film on polystyrene gate dielectric.

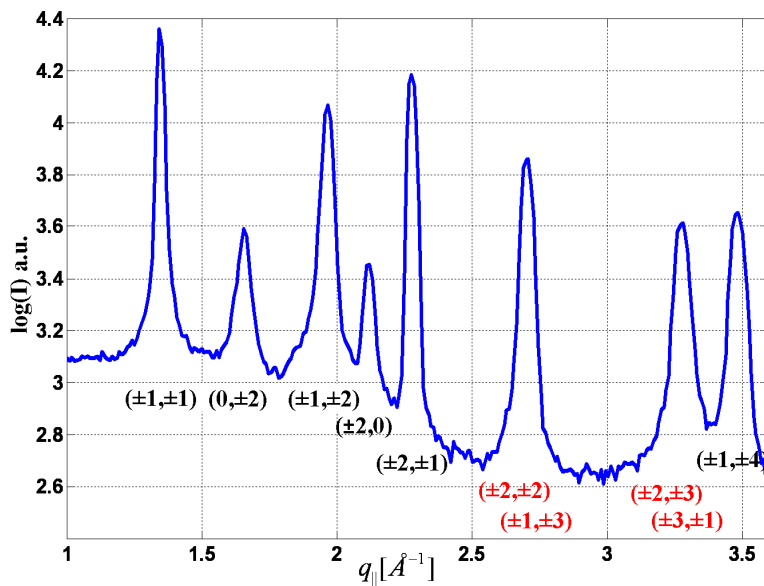


Figure 4.12: GIXD measurement of a 480 Å pentacene thin film on polystyrene gate dielectric.

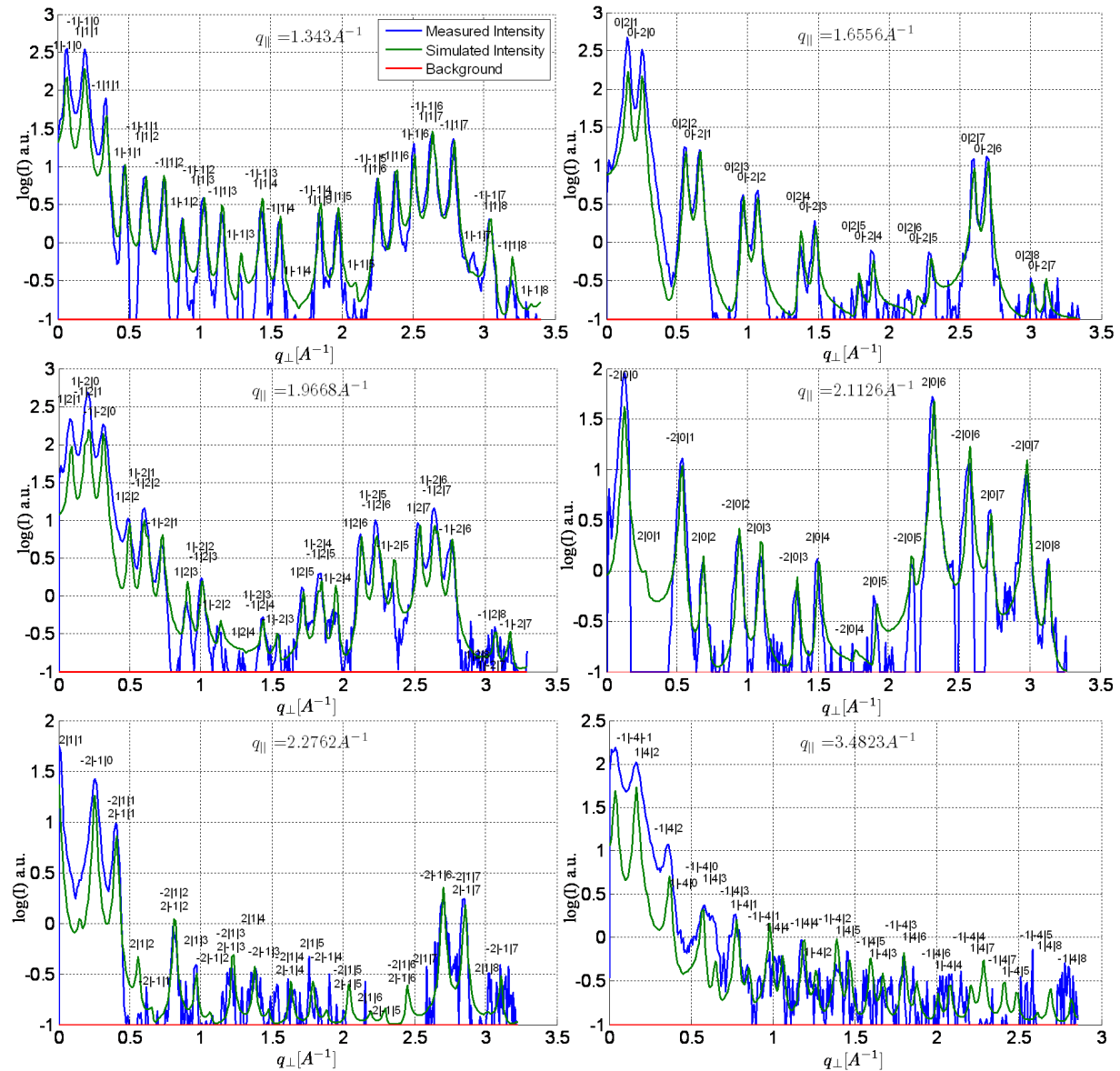


Figure 4.13: GI-CTR measurements and best fit plots of a 480 Å pentacene thin film on polystyrene gate dielectric.





# Chapter 5

## Discussion

### 5.1 Crystal structure

It was found, that the unit cell parameters are identical within measurement precision on all measured substrates. The crystal structure belongs to the space group P-1 and was found to be triclinic with the lattice parameters given in table 5.1. The unit cell volume  $V = 697\text{\AA}^3$  is the largest of all pentacene polymorphs reported so far. The unit-cell parameters a, b and  $\gamma$  differ slightly from values reported from previous studies[32, 33, 34, 7] (comparison see table 5.1). One reason could be, that the GIXD peaks in these studies were not distinguished between those that could be assigned unambiguously to a Miller index and those that have two or more overlapping Bragg peaks.

A full set of unit-cell parameters was recently reported by Yoshida et.al.[7], which only differs slightly from the values reported in this thesis. The reason of this discrepancy could be due to fact that an in-house X-ray setup was used. Yoshida et.al. could only measure a few Bragg peaks with low intensity in a range of  $l = \pm 1$ . Moreover, some Bragg peaks were assigned different Miller indices in this study, which leads to slightly different unit-cell parameters. A table of measured and simulated Bragg peaks positions including the assigned Miller indices are given in appendix B.

	This thesis	Matt.'03[5]	Ruiz'04[32]	Fritz'04[33]	Yang'05[34]	Yosh.'07[7]
a	$5.958 \pm 0.005 \text{ \AA}$	<i>5.77 \AA</i>	5.91 \AA	5.916 \AA	$5.90 \pm 0.01 \text{ \AA}$	5.93 \AA
b	$7.596 \pm 0.008 \text{ \AA}$	<i>7.49 \AA</i>	7.58 \AA	7.588 \AA	$7.51 \pm 0.01 \text{ \AA}$	7.56 \AA
c	$15.61 \pm 0.01 \text{ \AA}$	<i>17.2 \AA</i>	-	-	-	15.65 \AA
$\alpha$	$81.25 \pm 0.04^\circ$	<i>73.5^\circ</i>	-	-	-	81.4^\circ
$\beta$	$86.56 \pm 0.04^\circ$	<i>75.3^\circ</i>	-	-	-	86.7^\circ
$\gamma$	$89.80 \pm 0.10^\circ$	<i>91.2^\circ</i>	$90 \pm 0.2^\circ$	89.95^\circ	$89.92 \pm 0.01^\circ$	89.8^\circ
V	$697.0 \text{ \AA}^3$	-	$691.2 \text{ \AA}^3$	-	-	$693 \text{ \AA}^3$

Table 5.1: Comparison of unit-cell parameters for the pentacene *thin-film* phase reported in previous studies (unit cell parameters in italics are predicted values).

substrate	$\theta_{hr gb} [^\circ]$	$\varphi_A$ ,	$\varphi_B$ ,
$a - SiO_2$ (Yoshida et.al.)	50.0	$5.7^\circ$	$6.8^\circ$
$a - SiO_2$	$54.3 \pm 1.3$	$5.6^\circ \pm 0.5$	$6.0^\circ \pm 0.4$
OTS	$55.8 \pm 2.0$	$6.4^\circ \pm 0.7$	$6.8^\circ \pm 0.5$
Topas	$59.4 \pm 1.3$	$5.6^\circ \pm 0.5$	$6.3^\circ \pm 0.4$
polystyrene	$55.1 \pm 0.9$	$5.7^\circ \pm 0.3$	$6.0^\circ \pm 0.2$

Table 5.2: Fit results of the molecular orientation of the pentacene *thin-film* phase on various gate dielectrics compared to the theoretical calculations of Yoshida et.al.[7]

Up to now, there is no study which directly extracted the molecular orientation of the two pentacene molecules within the unit-cell from x-ray data only. Yoshida et.al. used theoretical calculations based on the “*Dreiding Force Field*” method to predict the molecular orientation of the two pentacene molecules and calculated the resulting diffraction pattern to be compared with the observed data. They report a herringbone angle of  $\theta_{hr gb} = 50.0^\circ$  and the the long molecular axis tilted from the surface normal of  $\varphi_A = 5.7^\circ$  for the pentacene molecule at the (0,0,0) position and  $\varphi_B = 6.8^\circ$  for the pentacene molecule at (1/2 1/2 0) position. In this thesis, the herringbone angle  $\theta_{hr gb}$  and the tilts of the two long molecular axes  $\varphi_A$  and  $\varphi_B$  were found to be substrate dependent as shown in table 5.2. The herringbone angle  $\theta_{hr gb}$  is significantly different from the predicted value. The measured tilt angles  $\varphi_A$  and  $\varphi_B$  differ slightly from the predicted values, but cannot be compared directly, as the direction of the tilts were not reported by Yoshida. This indicates that substrate effects have to be included if one aims to understand the molecular structure of the *thin-film* phase in detail.

The herringbone angles of the pentacene *thin-film* polymorphs investigated in this thesis are larger when compared to the other pentacene polymorphs which exhibit herringbone angles in a range of  $51^\circ$ - $53^\circ$ [5]. The tilt angles  $\varphi_A$  and  $\varphi_B$  are much smaller than the tilt angles of  $25^\circ$  and  $21^\circ$  reported for the single crystal[30, 31] and the bulk phases[25, 26], respectively. A comparison of the 3D structures of the pentacene *thin-film* phase on  $a-SiO_2$  substrate and the single crystal phase is shown in figure 5.1.

## 5.2 Charge transport mechanism

An extensive understanding of the charge transport in organic semiconductors is a significant intellectual challenge and, at the same time, is crucial for further advances in the field of organic electronics[69]. The crystal structures reported here (atomic coordinates are given in the appendix C in cif format) provide a basis to apply techniques such as density functional methods to investigate intrinsic charge transport properties[3, 12] of organic thin film devices on a molecular level.

Organic crystals in general are usually lacking main valence bonds between their constituent molecular repeat units. Hence, there is typically only weak electronic overlap between the molecules. The interactions are mainly due to van der Waals forces in the

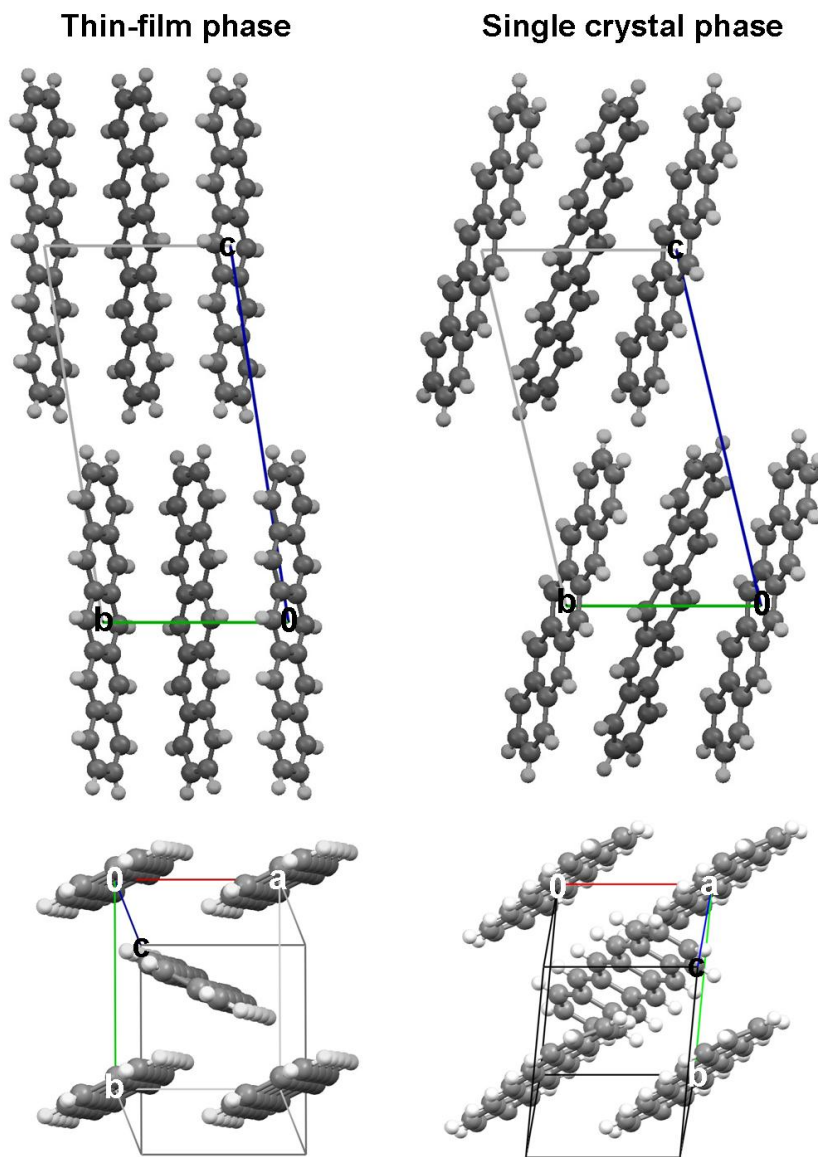


Figure 5.1: Comparison of the 3D crystal structure of the pentacene *thin-film* polymorph on *a* -  $SiO_2$  and the pentacene single crystal phase.

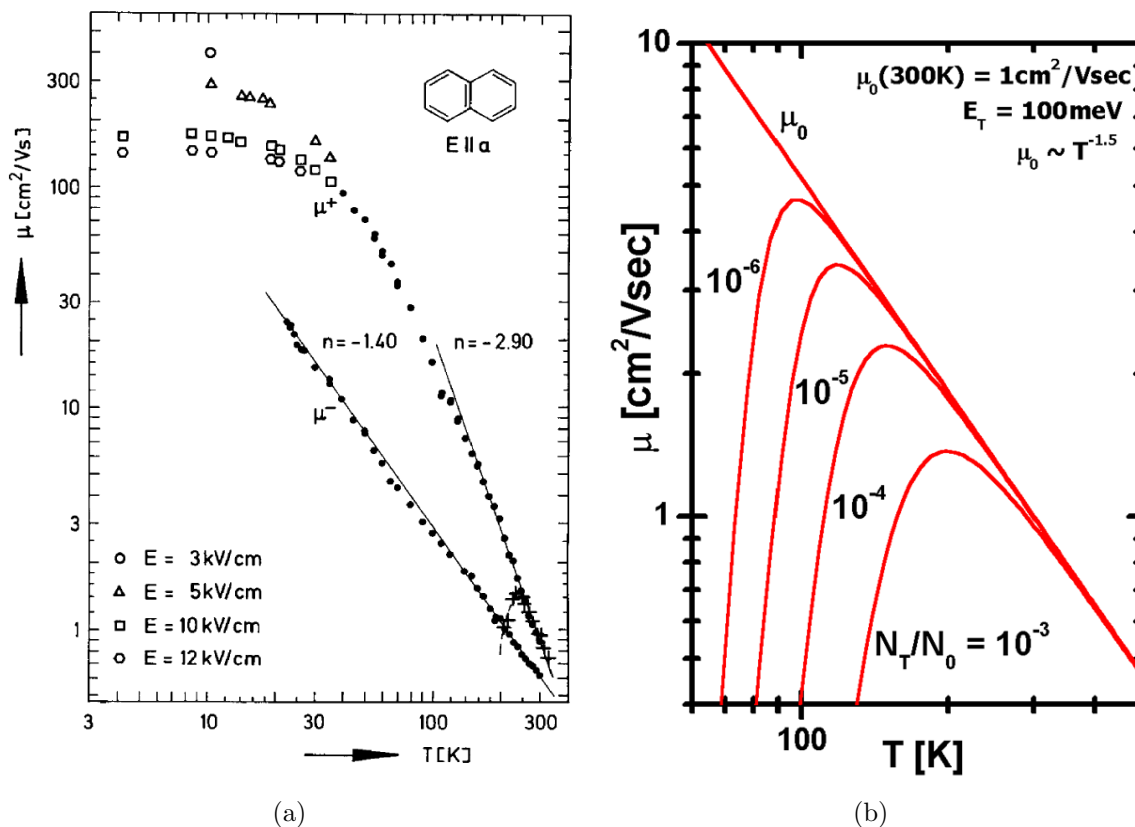


Figure 5.2: (a) Electron and hole mobilities  $\mu$  in the a-direction of a highly purified naphthalene crystal (open symbols and bold dots) as a function of temperature  $T$  from Time of flight measurements. For comparison, data obtained with less purified material (crosses), (figure taken from [2]). (b) Simulation of the charge carrier mobility  $\mu$  as a function of temperature  $T$  using the multiple trapping and release (MTR) model for different trapping vs. conduction states  $N_T/N_0$  (figure by J. Pflaum).

large class of neutral molecular crystals, which are therefore called *van der Waals crystals*. The exchange of a conduction electron or hole between adjacent molecules in such crystals is not very efficient and in general very slow. As the charge carriers are localized on individual molecules, local changes like the nuclear position, vibrational frequencies and electronic wavefunctions by polarization interactions considerably affect the charge transport mechanism in the crystal. The strong localization of the charge carriers is macroscopically reflected by strong inertial resistance against acceleration of the applied electric field, that is formally described by a high *effective mass* of the charge carrier.

Upon cooling, the vibrations are gradually freezing out, which allows the charge carrier to move faster. This in consequence leads to an increased mobility or a reduction of the effective mass. The charge carrier transport in highly perfect organic crystals at low temperature can be almost as fast as in silicon at room temperature [70]. Figure 5.2a shows the electron and hole mobilities in the a-direction of a highly purified naphthalene

single crystal as a function of temperature  $T$ . The straight lines in the  $\log \mu$  vs.  $\log T$  plot indicate an inverse power law temperature dependence  $\mu \propto T^{-n}$  which is indicative of band transport, rather than stochastic hopping. However, the charge transport mechanism in the practical more relevant organic thin films used in OTFTs is impaired by traps caused by the thin film - gate dielectric interface, dislocations and impurities, boundaries between individual crystal grains and by the fiber structure of the thin film. Especially at room temperature, the relation between the contribution of the coherent bandlike transport and that of the incoherent hopping-related transport to the entire charge transport mechanism remains an open question in van der Waals crystals and especially in thin films, composed of van der Waals crystal grains. Figure 5.2a shows the mobility obtained for a single crystal grown from less purified organic material (crosses). Here the mobility reaches a maximum around room temperature and drops by either cooling or heating the organic crystal. This behavior can be described by the multiple trapping and release (MTR) model, which is derived from that developed for hydrogenated amorphous silicon[71]. It assumes that charge transport occurs via delocalized state, but is limited by a distribution of traps located near the transport band (valence or conduction band, depending on electron or hole transport.) As for hopping transport at high temperature, the mobility is thermally activated. Furthermore, the MTR model predicts that for an exponential distribution of traps, mobility is gate voltage dependent following a power law[72]. Figure 5.2b shows a simulation of the charge carrier mobility  $\mu$  as a function of temperature  $T$  using the multiple trapping and release (MTR) model for different trapping vs. conduction states  $N_T/N_0$ .

A promising direct experimental approach to measure the contribution of the coherent bandlike transport and that of the incoherent hopping-related transport to the entire charge transport mechanism in organic thin films is the use of angle-resolved photoelectron spectroscopy (ARPES) measurements. This technique allows to measure the two-dimensional electronic band structure in the a-b plane, which is essential to fully understand the charge transport mechanism of a van der Waals crystal.

So far only two experimental measurements of the band structure of pentacene thin films have been performed with ARPES on the rather exotic substrates graphite[73] and bismuth[74]. The main reasons for this is that ARPES measurements require that the momentum transfer of the photo-electron is assigned to a position within the Brillouin zone. This has only been achieved for pentacene thin films grown on highly oriented pyrolytic graphite and on a Bi(001) surface. However, the crystal structures of pentacene on these surfaces are quite different from e.g. the technologically more relevant 15.4 Å pentacene *thin-film* phase.

In the study of the band structure of pentacene grown on graphite[73] a large band dispersion along the unit cell b-axis direction in this pentacene thin film polymorph at room temperature was observed, which suggests that the bandlike charge transport should play a major part at room temperature, even though the charge carriers may be strongly influenced by a considerable density of defects [75, 59] and are scattered by lattice vibration [76]. The band structure of a pentacene thin film grown on Bi(001) [74] which was measured in the whole a-b plane of the thin film by ARPES measurements, indicates also a bandlike

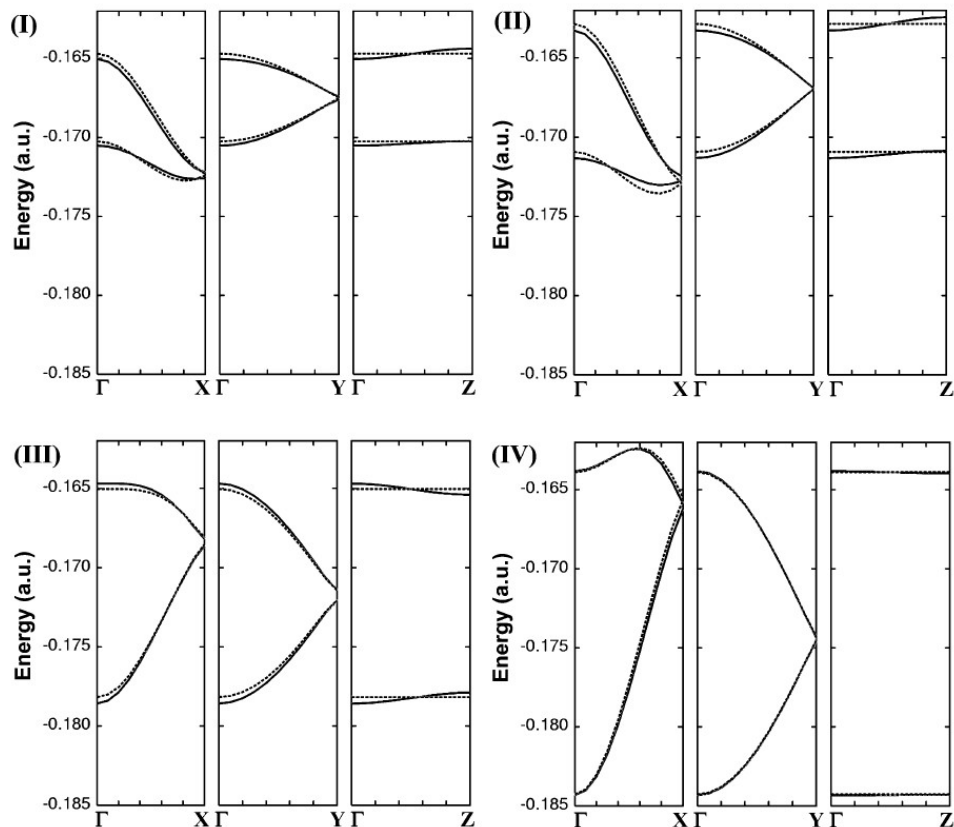


Figure 5.3: Simulation of the two highest occupied bands for the four pentacene polymorphs I-IV corresponding to a distance  $d_{(001)}$  of 14.1 Å, 14.4 Å, 15.0 Å, and 15.4 Å by Troisi et al.[3]. The crystal structures of the 15.0 Å and 15.4 Å polymorphs used for the simulation are based on the predicted crystal structure taken from [4, 5].

charge transport in this specific pentacene thin film polymorph.

Although, these studies give evidence for band-like charge transport in pentacene thin-films, a direct experimental method to measure the band structure of the 15.4 Å pentacene *thin-film* phase in a-b direction may never come due to the fiber structure of the thin-film, which makes a specific crystallographic orientation of the thin film impossible. Note, that the same difficulty could be resolved for X-ray diffraction in this thesis only due to the relatively sharp Bragg peaks of the pentacene *thin-film* polymorphs. Yet, the only approach to access the band structure is by using the indirect method of simulating the band structure by numerical methods based on the crystal structure. This was first performed for pentacene polymorphs by Troisi et.al. [3] (figure 5.3). However, the crystal structures of the substrate induced 15.0 Å and 15.4 Å pentacene thin film polymorphs used for the simulation in this study are based on the predicted crystal structures taken from [4, 5] (table 5.1), which are quite different from the experimental crystal structures reported in this thesis.

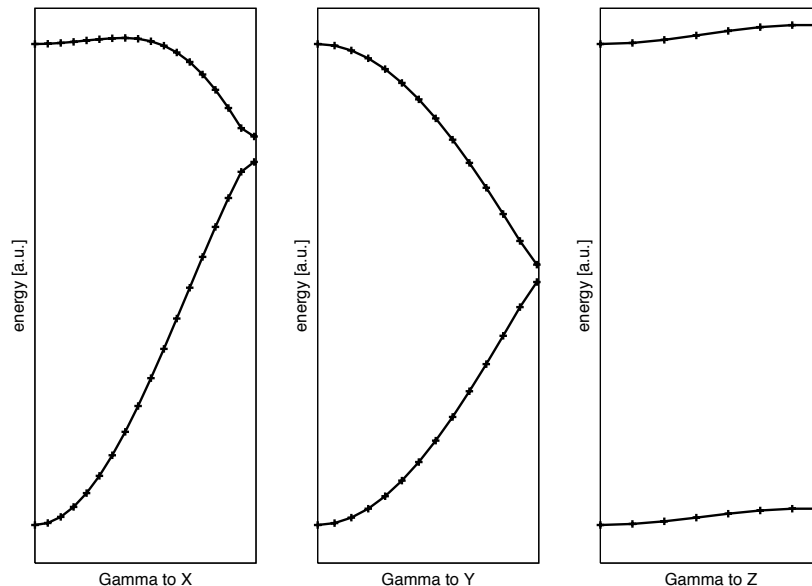


Figure 5.4: Simulation of the two highest occupied bands of the pentacene *thin-film* polymorph grown on  $a - SiO_2$  by density functional theory using the software tool SIESTA[6] (by C. Erlen, TU-München).

Very recently, the crystal structure of the pentacene *thin-film* polymorph reported in this thesis grown on  $a - SiO_2$  was used to calculate the the two highest occupied bands by density functional methods using the software tool SIESTA[6]. The simulations were performed by Christoph Erlen from the department of electrical engineering at the Technische Universität München. A preliminary result is shown in figure 5.4. The results strongly suggest band like charge transport in the a-b plane of the 15.4 Å pentacene *thin-film* phase. It should be noticed, that the band structure is similar to the predicted band structures of the 15.0 Å and 15.4 Å polymorphs shown in figure 5.3.

Band structure simulations of the 15.4 Å pentacene polymorphs grown on other technologically relevant substrates investigated in this thesis are on its way. In previous studies it was observed that different substrates vary the charge carrier mobility in OTFTs[45]. The substrate dependent crystal structures observed here could be one reason for this variation. This topic may lead ultimately to a controlled fine-tuning of intrinsic charge transport properties.





# Chapter 6

## Outlook

As mentioned in the introduction, the research and development in the field of organic semiconductors is rapidly growing. More and more organic semiconducting materials and gate dielectric materials are being investigated. Based on the experimental approach developed in this work, the crystal structure of a wide range of organic thin film systems used in organic electronic devices can be solved. However, solving the crystal structure of an organic thin film system alone only provides a basis to understand the charge transport mechanisms in such systems. The following projects seem promising in order to get a more complete picture of the charge transport mechanism in the substrate induced pentacene *thin-film* polymorphs and in organic thin films in general.

### Density functional simulations based on Siesta

Preliminary results of the band structure of the pentacene *thin-film* polymorph on  $a-SiO_2$  based on the software tool Siesta were shown in figure 5.4. The band structure of the pentacene polymorphs grown on OTS, Topas and polystyrene are on the way. The results and the calculation of the mobility tensor will provide a deep insight into how much the intrinsic charge transport properties are altered by the substrate. In preliminary studies in our lab we found that OTFTs where pentacene was grown Topas show significantly higher mobilities when compared to  $a-SiO_2$  substrate.

### Crystal defects in organic thin films

The relation between the contribution of the coherent bandlike transport and that of the incoherent hopping-related transport to the entire charge transport mechanism remains an open question in organic crystals. The presence of chemical defects and impurities and especially the grain boundaries in the pentacene thin film are thought to be the main drivers for the hopping-related charge transport mechanism. The defect density of pentacene thin films can be investigated by X-ray diffraction with the so called rocking curve technique. In a previous study it was shown, that the defect density of the pentacene thin films also

varies among substrates[75]. The precise analysis of the defect densities in combination with the crystal structure can be used to gain a more complete picture of the charge transport mechanism. Preliminary results of rocking scans performed at the synchrotron beamline W1 at HasyLab Hamburg show, that the defect density in pentacene thin film grown on Topas are about 40% lower than on  $a - SiO_2$ .

## Thin film growth on other gate dielectric materials

A promising path to high-mobility and low-voltage organic transistors is the use of gate dielectric materials that provide a low capacitance per area. In this study it was shown that the crystal structure of an organic thin film can be solved on any gate dielectric material. Of course, there are many more promising gate dielectric materials[36, 37, 38, 39, 40] than the four model systems investigated in this study. Moreover, new gate dielectric materials are developed day-to-day. In the search for the “ideal” gate dielectric material, one question to solve concerns the mechanism with which the substrate induces a specific polymorph. This problem could be addressed experimentally by investigating the crystal structure of organic thin films grown on other promising gate dielectric materials.

## Crystal structure of other organic thin film systems

As mentioned above, the experimental approach developed in this work can be used to solve the crystal structure of a wide range of organic thin film systems. Recently, a thin film growth study about coronene was carried out in our lab and showed that coronene crystallizes in a herringbone structure when deposited as a thin film on  $a - SiO_2$ . Preliminary GIXD and CTR measurements seem to be promising techniques to reveal the thin film structure of Coronene.



# Appendix A

## Detailed Parratt32 fit results

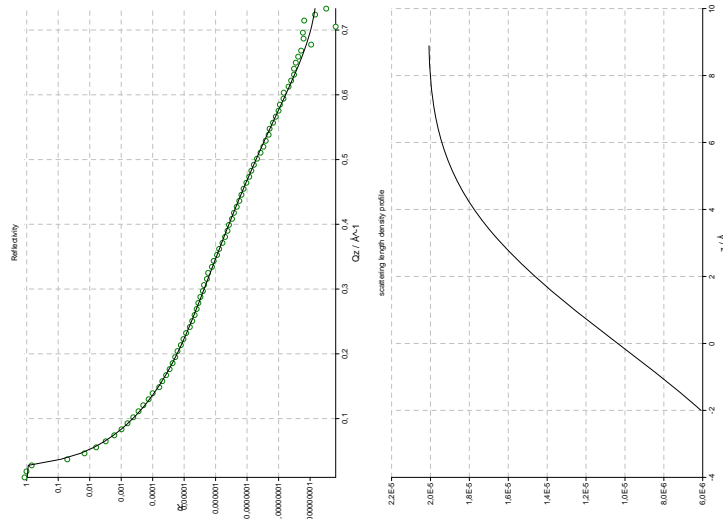
Parratt32 data output sheet

18.05.2007 18:10:36

Datafile: Z:\Messdaten\Project-Studies\0001\Topas\_Layer\_Thickness and Smoothness by Spincoating\0104\_nativ.dat

sample parameters are:

	d / Å	$\rho / \text{Å}^{-2}$	$\text{Im}(\rho) / \text{Å}^{-2}$	$\sigma / \text{Å}$
air	N/A	0E+00	0E+00	N/A
1	7.51	2.081E-5	5.401E-06	3.674
bulk	N/A	1.98E-5	2.732E-08	4.226



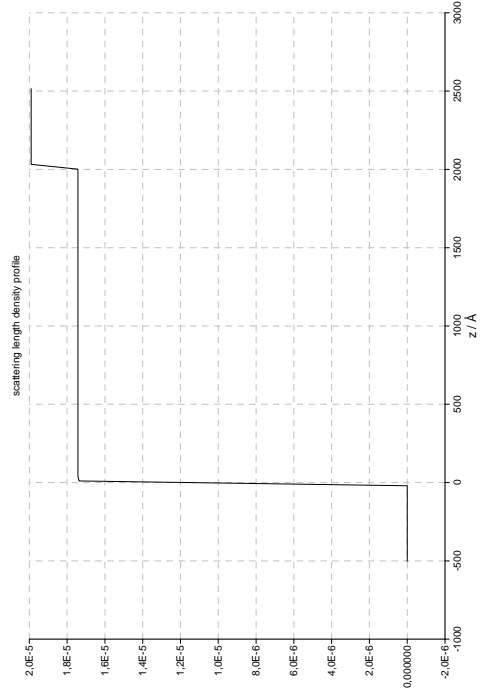
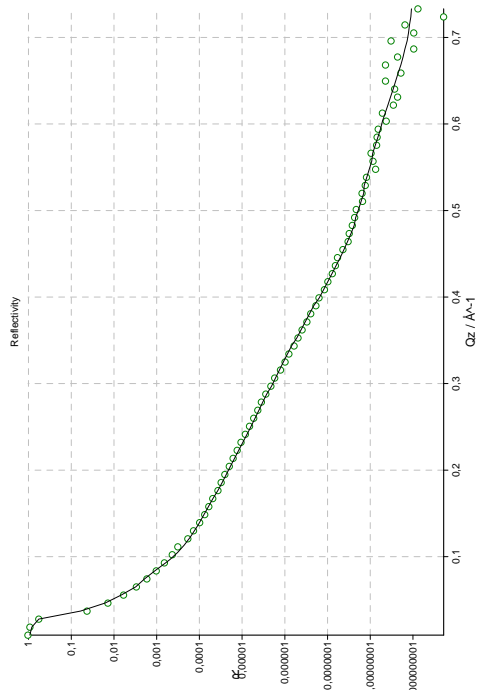
Parratt32 data output sheet

18.05.2007 17:49:10

Datafile: Z:\Messdaten\Project-Studies\0001.Topas.Layer.Thickness.and.Smoothness.by.Spincoating\0106\_self.dat

sample parameters are:

	d / Å	rho / Å <sup>-2</sup>	Im(rho) / Å <sup>-2</sup>	sigma / Å
air	N/A	0E+00	0E+00	N/A
1	2011.97	1.743E-5	1.905E-06	3.711
bulk	N/A	1.99E-5	2.732E-08	3.075



Parratt32 data output sheet

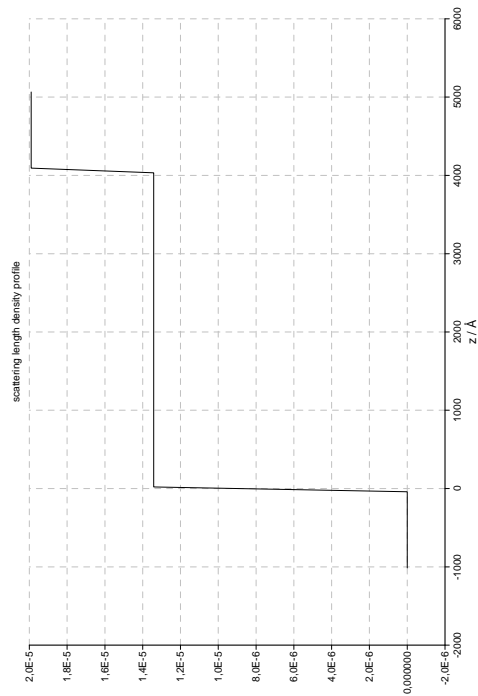
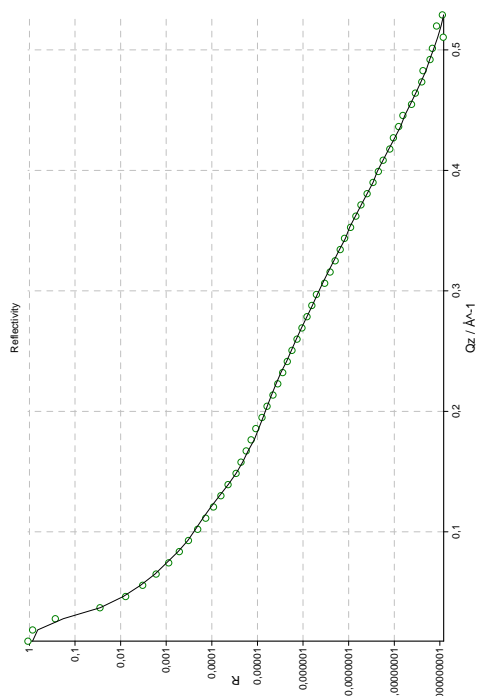
18.05.2007 17:47:51

Datafile: Z:\Messdaten\Project-Studies\0001.Topas.Layer.Thickness.and.Smoothness.by.Spincoating\0105\_com.dat

The logarithmically weighted  $\chi^2$  of the fit is: 2.3549E-03

sample parameters are:

	d / Å	$\rho$ / Å <sup>-2</sup>	$\text{Im}(\rho) / \text{Å}^{-2}$	sigma / Å
air	N/A	0E+00	0E+00	N/A
1	4053.05	1.342E-5	2.895E-06	5.303
bulk	N/A	1.99E-5	2.732E-08	4.955



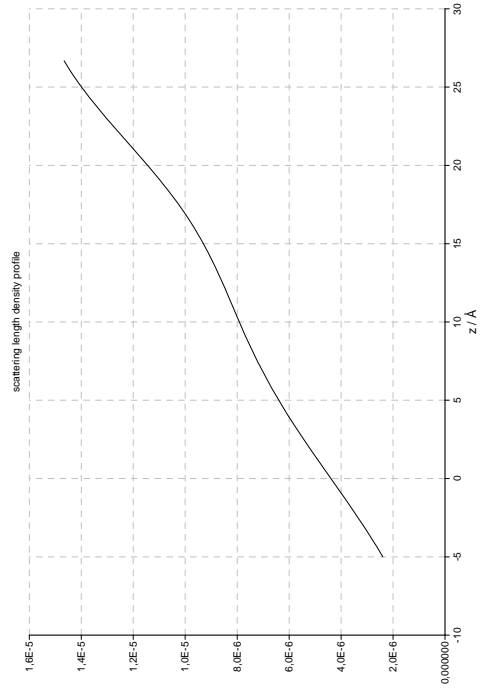
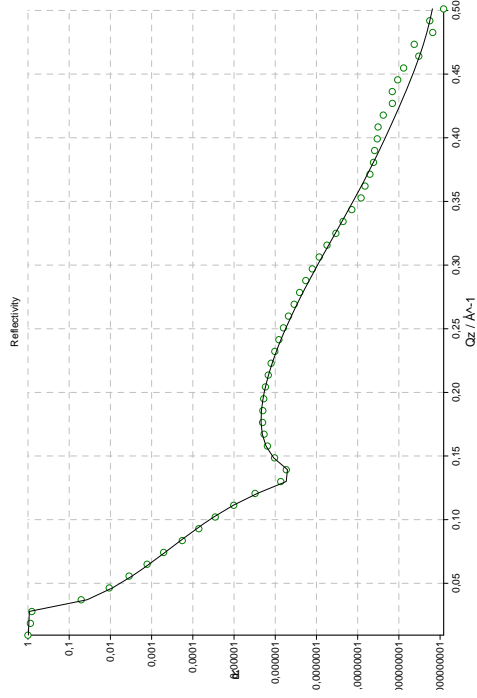
Parratt32 data output sheet

18.05.2007 18:01:03

Datafile: Z:\Messdaten\Project-Studies\0001.Topas.Layer.Thickness.and.Smoothness.by.Spincoating\0120\_OT5.dat

sample parameters are:

air	d / Å	rho / Å <sup>-2</sup>	Im(rho) / Å <sup>-2</sup>	sigma / Å
1	N/A	0E+0	0E+00	N/A
bulk	21.76	8.781E-6	9.724E-07	8.259
	N/A	1.604E-5	1.725E-18	5.592



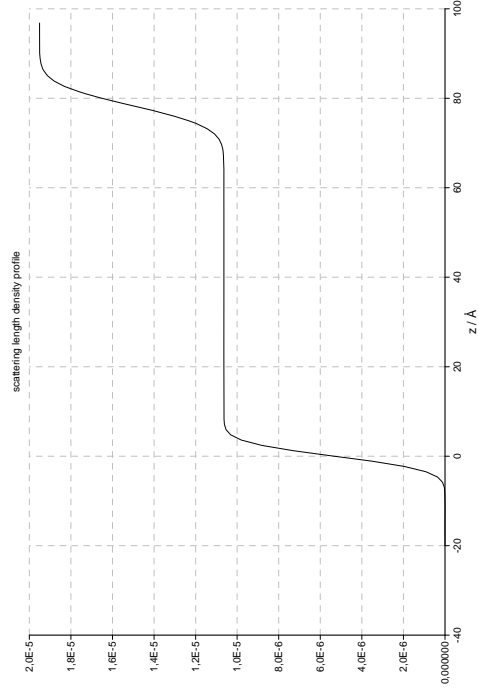
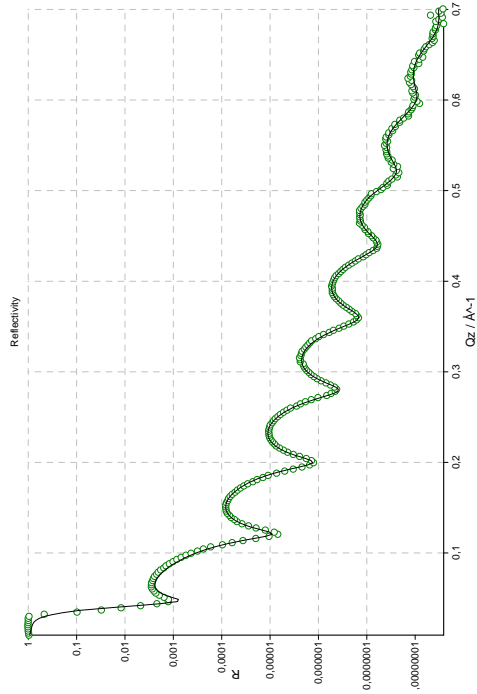
Parratt32 data output sheet

18.05.2007 18:02:57

Datafile: Z:\Messdaten\Project-Studies\0001.Topas.Layer.Thickness.and.Smoothness.by.Spincoating\0025\_025%25\_Topas.dat

sample parameters are:

	d / Å	rho / Å <sup>-2</sup>	Im(rho) / Å <sup>-2</sup>	sigma / Å
air	N/A	0E+00	0E+00	N/A
1	78.39	1.064E-5	1.216E-06	2.548
bulk	N/A	1.951E-5	7.002E-07	3.882





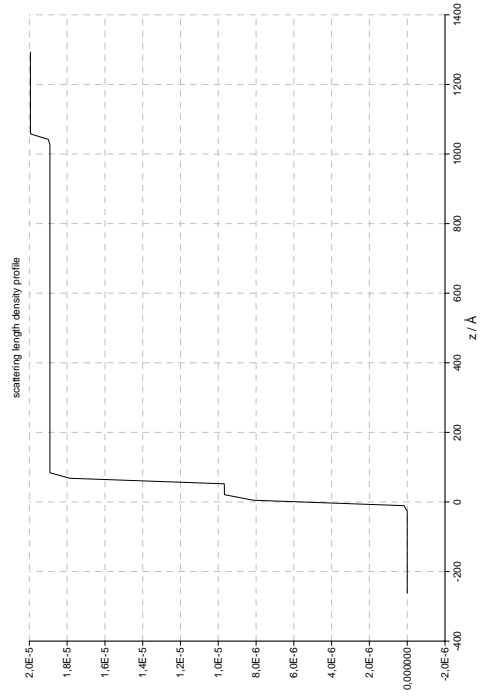
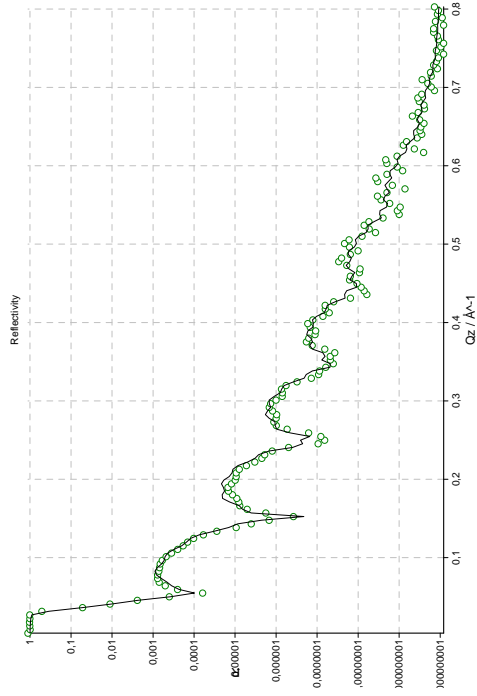
Parratt32 data output sheet

18.05.2007 17:59:45

Datafile: Z:\Messdaten\Project-Studies\0001.Topas.Layer.Thickness.and.Smoothness.by.Spincoating\0130\_PS.dat

sample parameters are:

	d / Å	rho / Å <sup>-2</sup>	Im(rho) / Å <sup>-2</sup>	sigma / Å
air	N/A	0E+00	0E+00	N/A
1	63.57	9.676E-6	1.007E-08	5.062
2	983.77	1.891E-5	7.384E-07	3.614
bulk	N/A	1.994E-5	2.111E-07	3.943





# Appendix B

## Detailed fit results of Bragg peak positions

$q_{  }$ measured [ $\text{\AA}^{-1}$ ]	$q_{  }$ simulated [ $\text{\AA}^{-1}$ ]	h	k
1.343	1.342496	-1	1
1.654	1.654316	0	-2
1.959	1.958774	-1	-2
2.109	2.109106	-2	0
2.268	2.268163	-2	1

Table B.1: Measured and simulated Bragg peak positions and assigned Miller indices observed in GIXD measurements of the pentacene *thin-film* phase.

$q_{\perp}$	$q_{\parallel}$	$q_{\perp}$	$q_{\parallel}$	h	k	l
measured		simulated				
0.061	1.3425	0.063837	1.342496	1	-1	0
0.347	1.3425	0.344162	1.342496	-1	1	1
0.4663	1.3425	0.471836	1.342496	1	-1	1
0.7538	1.3425	0.752161	1.342496	-1	1	2
0.886	1.3425	0.879835	1.342496	1	-1	2
1.1619	1.3425	1.160160	1.342496	-1	1	3
1.294	1.3425	1.287835	1.342496	1	-1	3
1.5714	1.3425	1.568159	1.342496	-1	1	4
1.978	1.3425	1.976158	1.342496	-1	1	5
2.3902	1.3425	2.384157	1.342496	-1	1	6
2.5158	1.3425	2.511832	1.342496	1	-1	6
2.7949	1.3425	2.792156	1.342496	-1	1	7
0.1598	1.6543	0.153154	1.654316	0	2	1
0.2567	1.6543	0.254845	1.654316	0	-2	0
0.5671	1.6543	0.561153	1.654316	0	2	2
0.6642	1.6543	0.662844	1.654316	0	-2	1
0.9755	1.6543	0.969152	1.654316	0	2	3
1.0713	1.6543	1.07084	1.654316	0	-2	2
1.3809	1.6543	1.377151	1.654316	0	2	4
1.4808	1.6543	1.478842	1.654316	0	-2	3
2.6068	1.6543	2.601148	1.654316	0	2	7
2.704	1.6543	2.702839	1.654316	0	-2	6

Table B.2: Measured and simulated Bragg peak positions and assigned Miller indices observed in GI-CTR measurements of the pentacene *thin-film* phase (part 1).

$q_{\perp}$	$q_{\parallel}$	$q_{\perp}$	$q_{\parallel}$	h	k	l
measured		simulated				
0.061	1.3425	0.063837	1.342496	1	-1	0
0.347	1.3425	0.344162	1.342496	-1	1	1
0.4663	1.3425	0.471836	1.342496	1	-1	1
0.7538	1.3425	0.752161	1.342496	-1	1	2
0.886	1.3425	0.879835	1.342496	1	-1	2
1.1619	1.3425	1.160160	1.342496	-1	1	3
0.0953	1.9588	0.089569	1.958774	1	2	1
0.3214	1.9588	0.31843	1.958774	-1	-2	0
0.5033	1.9588	0.497568	1.958774	1	2	2
0.7302	1.9588	0.726429	1.958774	-1	-2	1
0.91231	1.9588	0.905567	1.958774	1	2	3
1.7237	1.9588	1.72157	1.958774	1	2	5
1.967	1.9588	1.950426	1.958774	-1	-2	4
2.1328	1.9588	2.129564	1.958774	1	2	6
2.54	1.9588	2.537563	1.958774	1	2	7
2.7733	1.9588	2.766424	1.958774	-1	-2	6
0.1309	2.1091	0.127170	2.109106	-2	0	0
0.5391	2.1091	0.535169	2.109106	-2	0	1
0.6931	2.1091	0.68883	2.109106	2	0	2
0.9452	2.1091	0.943168	2.109106	-2	0	2
1.1002	2.1091	1.096827	2.109106	2	0	3
2.3234	2.1091	2.320824	2.109106	2	0	6
2.5768	2.1091	2.575164	2.109106	-2	0	6
2.7324	2.1091	2.728823	2.109106	2	0	7
0.2623	2.2682	0.254593	2.268163	-2	-1	0
0.4118	2.2682	0.407747	2.268163	-2	1	1

Table B.3: Measured and simulated Bragg peak positions and assigned Miller indices observed in GI-CTR measurements of the pentacene *thin-film* phase (part 2).



# Appendix C

## Cif files of pentacene *thin-film* polymorphs

### C.1 Cif Header

The cif header of the produced cif files given here is the same for all files.

```
data_global
_publ_requested_journal J.Am.Chem.Soc.
_publ_contact_author_name 'Nickel, Bert'
_publ_contact_author_address
;Department f\"ur Physik
Ludwig Maximilians Universit\"at M\"unchen
Geschwister-Scholl-Platz 1
D-80539 M\"unchen
Germany
;
_publ_contact_author_email nickel@lmu.de
_publ_contact_author_phone +49(0)89-2180-1460
loop_
_publ_author_name
_publ_author_address
'Schiefer, Stefan'
;Department f\"ur Physik
Ludwig Maximilians Universit\"at M\"unchen
Geschwister-Scholl-Platz 1
D-80539 M\"unchen
Germany
;
'Huth, Martin'
;Department f\"ur Physik
Ludwig Maximilians Universit\"at M\"unchen
Geschwister-Scholl-Platz 1
D-80539 M\"unchen
Germany
;
'Dobrinevski, Alexander'
;Department f\"ur Physik
Ludwig Maximilians Universit\"at M\"unchen
Geschwister-Scholl-Platz 1
D-80539 M\"unchen
Germany
;
'Nickel, Bert'
```

```
;Department für Physik
Ludwig Maximilians Universität München
Geschwister-Scholl-Platz 1
D-80539 München
Germany
;
_audit_creation_method Matlab
_audit_creation_date 2007-03-18
data_Pentacene_on_SiO2
_chemical_name_systematic pentacene
_chemical_name_common pentacene
_chemical_formula_moiety 'C22 H14'
_chemical_formula_sum 'C22 H14'
_chemical_formula_structural ?
_chemical_formula_weight 278.35
_chemical_melting_point 573
_symmetry_cell_setting triclinic
_symmetry_space_group_name_H-M 'P -1'
_symmetry_int_tables_number 2
_symmetry_space_group_name_Hall '-P 1'
loop_
_symmetry_equiv_pos_as_xyz
x,y,z
-x,-y,-z
_cell_length_a 5.958
_cell_length_b 7.596
_cell_length_c 15.6096
_cell_angle_alpha 81.25
_cell_angle_beta 86.56
_cell_angle_gamma 89.80
_cell_volume 696.953
_cell_formula_units_Z 2
_cell_measurement_reflns_used 42
_cell_measurement_temperature 293
_exptl_crystal_description 'fibre structured thin film'
_exptl_crystal_colour violet
_diffraction_ambient_temperature 293
_diffraction_radiation_probe X-ray
_diffraction_radiation_type synchrotron
_diffraction_radiation_wavelength 1.1810
_diffraction_source synchrotron
_diffraction_source_type 'HASYLab Beamline W1'
_diffraction_measurement_device_type
;
HASYLab, Hamburg, W1 Beamline
;
_diffraction_reflns_limit_h_min -3
_diffraction_reflns_limit_h_max 3
_diffraction_reflns_limit_k_min -4
_diffraction_reflns_limit_k_max 4
_diffraction_reflns_limit_l_min 0
_diffraction_reflns_limit_l_max 8
_diffraction_reflns_reduction_process
;
Intensity data were corrected for Lorentz and polarization effects,
area factor and interception of scattering rod
;
_chemical_compound_source 'Sigma Aldrich'
_exptl_crystal_recrystallization_method 'Molecular beam deposition'
_diffraction_ambient_pressure 0.00000001
```



## C.2 Atomic positions for $a - SiO_2$ substrate

```
loop-
_atom_site_label
_atom_site_type_symbol
_atom_site_fract_x
_atom_site_fract_y
_atom_site_fract_z
_atom_site_U_iso_or_equiv
_atom_site_thermal_displace_type
_atom_site_occupancy
C1 C 0.2107 -0.0830 -0.0070 0.0373 Uiso 1.0000
C2 C 0.1185 -0.0666 0.0758 0.0373 Uiso 1.0000
C3 C 0.2245 -0.1278 0.1522 0.0373 Uiso 1.0000
C4 C 0.1271 -0.1085 0.2334 0.0373 Uiso 1.0000
C5 C 0.2409 -0.1703 0.3115 0.0373 Uiso 1.0000
C6 C 0.1479 -0.1506 0.3900 0.0373 Uiso 1.0000
C7 C -0.0693 -0.0675 0.3979 0.0373 Uiso 1.0000
C8 C -0.1802 -0.0072 0.3255 0.0373 Uiso 1.0000
C9 C -0.0875 -0.0232 0.2397 0.0373 Uiso 1.0000
C10 C -0.1947 0.0375 0.1660 0.0373 Uiso 1.0000
C11 C -0.0998 0.0189 0.0830 0.0373 Uiso 1.0000
C12 C 0.7104 0.5869 -0.0091 0.0373 Uiso 1.0000
C13 C 0.6200 0.5248 0.0746 0.0373 Uiso 1.0000
C14 C 0.7271 0.5446 0.1499 0.0373 Uiso 1.0000
C15 C 0.6310 0.4811 0.2322 0.0373 Uiso 1.0000
C16 C 0.7428 0.5052 0.3092 0.0373 Uiso 1.0000
C17 C 0.6495 0.4452 0.3887 0.0373 Uiso 1.0000
C18 C 0.4349 0.3541 0.3987 0.0373 Uiso 1.0000
C19 C 0.3250 0.3300 0.3274 0.0373 Uiso 1.0000
C20 C 0.4160 0.3932 0.2406 0.0373 Uiso 1.0000
C21 C 0.3082 0.3718 0.1680 0.0373 Uiso 1.0000
C22 C 0.4025 0.4345 0.0840 0.0373 Uiso 1.0000
H1 H 0.3496 -0.1379 -0.0122 0.0373 Uiso 1.0000
H3 H 0.3636 -0.1829 0.1485 0.0373 Uiso 1.0000
H5 H 0.3805 -0.2244 0.3073 0.0373 Uiso 1.0000
H6 H 0.2238 -0.1907 0.4395 0.0373 Uiso 1.0000
H7 H -0.1335 -0.0553 0.4525 0.0373 Uiso 1.0000
H8 H -0.3199 0.0459 0.3317 0.0373 Uiso 1.0000
H10 H -0.3338 0.0923 0.1708 0.0373 Uiso 1.0000
H12 H 0.8496 0.6441 -0.0158 0.0373 Uiso 1.0000
H14 H 0.8662 0.6016 0.1448 0.0373 Uiso 1.0000
H16 H 0.8812 0.5633 0.3036 0.0373 Uiso 1.0000
H17 H 0.7235 0.4624 0.4376 0.0373 Uiso 1.0000
H18 H 0.3719 0.3118 0.4540 0.0373 Uiso 1.0000
H19 H 0.1870 0.2710 0.3349 0.0373 Uiso 1.0000
H21 H 0.1692 0.3145 0.1742 0.0373 Uiso 1.0000
```

## C.3 Atomic positions for OTS substrate

```
loop-
_atom_site_label
_atom_site_type_symbol
_atom_site_fract_x
_atom_site_fract_y
_atom_site_fract_z
_atom_site_U_iso_or_equiv
_atom_site_thermal_displace_type
_atom_site_occupancy
C1 C 0.2093 -0.0850 -0.0073 0.0819 Uiso 1.0000
C2 C 0.1197 -0.0662 0.0755 0.0819 Uiso 1.0000
C3 C 0.2270 -0.1270 0.1517 0.0819 Uiso 1.0000
```

```

C4 C 0.1322 -0.1053 0.2330 0.0819 Uiso 1.0000
C5 C 0.2472 -0.1666 0.3108 0.0819 Uiso 1.0000
C6 C 0.1568 -0.1447 0.3893 0.0819 Uiso 1.0000
C7 C -0.0590 -0.0596 0.3976 0.0819 Uiso 1.0000
C8 C -0.1710 0.0004 0.3255 0.0819 Uiso 1.0000
C9 C -0.0810 -0.0180 0.2396 0.0819 Uiso 1.0000
C10 C -0.1895 0.0423 0.1661 0.0819 Uiso 1.0000
C11 C -0.0971 0.0214 0.0831 0.0819 Uiso 1.0000
C12 C 0.7089 0.5893 -0.0105 0.0819 Uiso 1.0000
C13 C 0.6201 0.5301 0.0737 0.0819 Uiso 1.0000
C14 C 0.7274 0.5551 0.1483 0.0819 Uiso 1.0000
C15 C 0.6329 0.4943 0.2311 0.0819 Uiso 1.0000
C16 C 0.7448 0.5238 0.3073 0.0819 Uiso 1.0000
C17 C 0.6531 0.4664 0.3874 0.0819 Uiso 1.0000
C18 C 0.4402 0.3728 0.3989 0.0819 Uiso 1.0000
C19 C 0.3302 0.3437 0.3284 0.0819 Uiso 1.0000
C20 C 0.4195 0.4038 0.2410 0.0819 Uiso 1.0000
C21 C 0.3115 0.3774 0.1691 0.0819 Uiso 1.0000
C22 C 0.4042 0.4373 0.0846 0.0819 Uiso 1.0000
H1 H 0.3472 -0.1412 -0.0128 0.0819 Uiso 1.0000
H3 H 0.3651 -0.1834 0.1478 0.0819 Uiso 1.0000
H5 H 0.3860 -0.2220 0.3064 0.0819 Uiso 1.0000
H6 H 0.2335 -0.1845 0.4387 0.0819 Uiso 1.0000
H7 H -0.1214 -0.0458 0.4522 0.0819 Uiso 1.0000
H8 H -0.3099 0.0549 0.3319 0.0819 Uiso 1.0000
H10 H -0.3276 0.0984 0.1711 0.0819 Uiso 1.0000
H12 H 0.8469 0.6482 -0.0181 0.0819 Uiso 1.0000
H14 H 0.8654 0.6138 0.1423 0.0819 Uiso 1.0000
H16 H 0.8822 0.5835 0.3008 0.0819 Uiso 1.0000
H17 H 0.7271 0.4870 0.4357 0.0819 Uiso 1.0000
H18 H 0.3783 0.3323 0.4545 0.0819 Uiso 1.0000
H19 H 0.1933 0.2832 0.3368 0.0819 Uiso 1.0000
H21 H 0.1736 0.3184 0.1762 0.0819 Uiso 1.0000

```

## C.4 Atomic positions for Topas substrate

```

loop_
  _atom_site_label
  _atom_site_type_symbol
  _atom_site_fract_x
  _atom_site_fract_y
  _atom_site_fract_z
  _atom_site_U_iso_or_equiv
  _atom_site_thermal_displace_type
  _atom_site_occupancy
C1 C 0.2057 -0.0905 -0.0060 0.0482 Uiso 1.000
C2 C 0.1149 -0.0692 0.0763 0.0482 Uiso 1.000
C3 C 0.2176 -0.1327 0.1532 0.0482 Uiso 1.000
C4 C 0.1217 -0.1083 0.2340 0.0482 Uiso 1.000
C5 C 0.2320 -0.1725 0.3125 0.0482 Uiso 1.000
C6 C 0.1406 -0.1480 0.3906 0.0482 Uiso 1.000
C7 C -0.0717 -0.0572 0.3975 0.0482 Uiso 1.000
C8 C -0.1793 0.0056 0.3246 0.0482 Uiso 1.000
C9 C -0.0879 -0.0153 0.2392 0.0482 Uiso 1.000
C10 C -0.1918 0.0476 0.1650 0.0482 Uiso 1.000
C11 C -0.0983 0.0241 0.0825 0.0482 Uiso 1.000
C12 C 0.7054 0.5943 -0.0096 0.0482 Uiso 1.000
C13 C 0.6180 0.5299 0.0743 0.0482 Uiso 1.000
C14 C 0.7234 0.5545 0.1493 0.0482 Uiso 1.000
C15 C 0.6305 0.4885 0.2318 0.0482 Uiso 1.000
C16 C 0.7403 0.5176 0.3085 0.0482 Uiso 1.000
C17 C 0.6500 0.4552 0.3882 0.0482 Uiso 1.000
C18 C 0.4408 0.3565 0.3988 0.0482 Uiso 1.000

```

```
C19 C 0.3328 0.3277 0.3277 0.0482 Uiso 1.000
C20 C 0.4206 0.3931 0.2407 0.0482 Uiso 1.000
C21 C 0.3146 0.3670 0.1684 0.0482 Uiso 1.000
C22 C 0.4057 0.4320 0.0842 0.0482 Uiso 1.000
H1 H 0.3413 -0.1504 -0.0106 0.0482 Uiso 1.000
H3 H 0.3534 -0.1927 0.1502 0.0482 Uiso 1.000
H5 H 0.3685 -0.2316 0.3090 0.0482 Uiso 1.000
H6 H 0.2143 -0.1898 0.4404 0.0482 Uiso 1.000
H7 H -0.1349 -0.0416 0.4518 0.0482 Uiso 1.000
H8 H -0.3159 0.0638 0.3301 0.0482 Uiso 1.000
H10 H -0.3276 0.1074 0.1692 0.0482 Uiso 1.000
H12 H 0.8411 0.6564 -0.0166 0.0482 Uiso 1.000
H14 H 0.8591 0.6164 0.1439 0.0482 Uiso 1.000
H16 H 0.8753 0.5805 0.3026 0.0482 Uiso 1.000
H17 H 0.7227 0.4756 0.4369 0.0482 Uiso 1.000
H18 H 0.3799 0.3126 0.4541 0.0482 Uiso 1.000
H19 H 0.1982 0.2639 0.3356 0.0482 Uiso 1.000
H21 H 0.1790 0.3047 0.1749 0.0482 Uiso 1.000
```

## C.5 Atomic positions for polystyrene substrate

```
loop_
  _atom_site_label
  _atom_site_type_symbol
  _atom_site_fract_x
  _atom_site_fract_y
  _atom_site_fract_z
  _atom_site_U_iso_or_equiv
  _atom_site_thermal_displace_type
  _atom_site_occupancy
C1 C 0.2100 -0.0843 -0.0063 0.0786 Uiso 1.000
C2 C 0.1175 -0.0658 0.0761 0.0786 Uiso 1.000
C3 C 0.2226 -0.1262 0.1529 0.0786 Uiso 1.000
C4 C 0.1249 -0.1047 0.2338 0.0786 Uiso 1.000
C5 C 0.2377 -0.1656 0.3122 0.0786 Uiso 1.000
C6 C 0.1445 -0.1439 0.3903 0.0786 Uiso 1.000
C7 C -0.0720 -0.0594 0.3976 0.0786 Uiso 1.000
C8 C -0.1819 0.0001 0.3249 0.0786 Uiso 1.000
C9 C -0.0890 -0.0180 0.2393 0.0786 Uiso 1.000
C10 C -0.1953 0.0418 0.1653 0.0786 Uiso 1.000
C11 C -0.1000 0.0211 0.0827 0.0786 Uiso 1.000
C12 C 0.7097 0.5880 -0.0091 0.0786 Uiso 1.000
C13 C 0.6196 0.5255 0.0746 0.0786 Uiso 1.000
C14 C 0.7262 0.5460 0.1499 0.0786 Uiso 1.000
C15 C 0.6305 0.4821 0.2322 0.0786 Uiso 1.000
C16 C 0.7417 0.5070 0.3092 0.0786 Uiso 1.000
C17 C 0.6488 0.4465 0.3887 0.0786 Uiso 1.000
C18 C 0.4350 0.3542 0.3988 0.0786 Uiso 1.000
C19 C 0.3255 0.3295 0.3274 0.0786 Uiso 1.000
C20 C 0.4162 0.3930 0.2406 0.0786 Uiso 1.000
C21 C 0.3088 0.3710 0.1680 0.0786 Uiso 1.000
C22 C 0.4028 0.4341 0.0840 0.0786 Uiso 1.000
H1 H 0.3484 -0.1401 -0.0111 0.0786 Uiso 1.000
H3 H 0.3612 -0.1821 0.1496 0.0786 Uiso 1.000
H5 H 0.3769 -0.2206 0.3084 0.0786 Uiso 1.000
H6 H 0.2198 -0.1834 0.4401 0.0786 Uiso 1.000
H7 H -0.1363 -0.0458 0.4519 0.0786 Uiso 1.000
H8 H -0.3213 0.0542 0.3306 0.0786 Uiso 1.000
H10 H -0.3339 0.0975 0.1697 0.0786 Uiso 1.000
H12 H 0.8483 0.6460 -0.0158 0.0786 Uiso 1.000
H14 H 0.8648 0.6038 0.1448 0.0786 Uiso 1.000
H16 H 0.8796 0.5658 0.3036 0.0786 Uiso 1.000
H17 H 0.7224 0.4642 0.4376 0.0786 Uiso 1.000
```

H18 H 0.3721 0.3117 0.4540 0.0786 Uiso 1.000  
H19 H 0.1880 0.2698 0.3349 0.0786 Uiso 1.000

## C.6 Comments on cif file checking

The A-alerts occur, because the method of the structure determination is non standard (i.e. not 'four- circle single crystal diffractometry'):

- *ATOM007\_ALERT\_1\_A \_atom\_site\_aniso\_label is missing unique label identifying the atom site:*

This is because only an overall isotropic Debye-Waller factor was employed in the calculations. Anisotropic Debye-Waller factors would cause too many variables for the present experimental data.

- *GEOM001\_ALERT\_1\_A \_geom\_bond\_atom\_site\_label\_1 is missing label identifying the atom site 1.*

*GEOM003\_ALERT\_1\_A \_geom\_bond\_distance is missing distance between atom sites 1 and 2.*

*GEOM006\_ALERT\_1\_A \_geom\_angle\_atom\_site\_label\_2 is missing label identifying the atom site 2.*

This is because bonding between atoms is not described here as the pentacene molecular geometry was taken from literature and kept fixed.

- *PLAT027\_ALERT\_3\_A \_diffn\_reflns\_theta\_full (too) Low: 0.00 Deg.*  
*PLAT029\_ALERT\_3\_A \_diffn\_measured\_fraction\_theta\_full Low: 0.00*

Single crystal diffraction data completeness is not available because this is not a standard 4-circle diffractometry experiment.

- *PLAT201\_ALERT\_2\_A Isotropic non-H Atoms in Main Residue(s): 22*

This is because only an overall isotropic Debye-Waller factor was employed

Concerning C-Alerts: estimated standard deviations on atomic positions are not given because the molecule taken from the literature was assumed to be rigid.

# Appendix D

## Publications

- B. Nickel, M. Fiebig, S. Schiefer, M. Goellner, Martin Huth, C. Erlen, and P. Lugli  
"Pentacene devices: molecular structure, charge transport and photo response"  
Physica Status Solidi, (2007) accepted
- H. Marciniak, M. Fiebig, M. Huth, S. Schiefer, B. Nickel, S. Lochbrunner  
"Ultrafast Formation of Charge Transfer Excitons in Microcrystalline Pentacene Films"  
Physical Review Letters, (2007) accepted
- S. Schiefer, M. Huth, A. Dobrinevski, B. Nickel  
"Determination of the Crystal Structure of Substrate Induced Pentacene Polymorphs in Fiber Structured Thin Films"  
Journal of the American Chemical Society, vol.129, issue 34, (2007)
- C. Erlen, P. Lugli, M. Fiebig, S. Schiefer, B. Nickel  
"Transient TCAD simulation of three-stage organic ring oscillator"  
Journal of Computational Electronics, vol. 5, nr. 4: 345-348, (2006)
- C. Erlen, F. Brunetti, P. Lugli, M. Fiebig, S. Schiefer, B. Nickel, B.  
"Trapping Effects in Organic Thin Film Transistors"  
Sixth IEEE Conference on Nanotechnology 2006, IEEE-NANO, vol. 1: 82-85, (2006)
- M. Tanaka, S. Schiefer, C. Gege, R.R. Schmidt, G.G. Fuller  
"Influence of Subphase Conditions on Interfacial Viscoelastic Properties of Synthetic Lipids with Gentiobiose Head Groups"  
Journal of Physical Chemistry, vol. 108 (10): 3211-3214, (2004)



# Bibliography

- [1] H. Yanagisawa, T. Tamaki, M. Nakamura, and K. Kudo. Structural and electrical characterization of pentacene films on sio2 grown by molecular beam deposition. *Thin Solid Films*, 464-65:398–402, 2004.
- [2] N. Karl. Charge carrier transport in organic semiconductors. *Synthetic Metals*, 133:649–657, 2003.
- [3] A. Troisi and G. Orlandi. Band structure of the four pentacene polymorphs and effect on the hole mobility at low temperature. *Journal Of Physical Chemistry B*, 109(5):1849–1856, 2005.
- [4] C. C. Mattheus, A. B. Dros, J. Baas, G. T. Oostergetel, A. Meetsma, J. L. de Boer, and T. T. M. Palstra. Identification of polymorphs of pentacene. *Synthetic Metals*, 138(3):475–481, 2003.
- [5] C. C. Mattheus, G. A. de Wijs, R. A. de Groot, and T. T. M. Palstra. Modeling the polymorphism of pentacene. *Journal Of The American Chemical Society*, 125(20):6323–6330, 2003.
- [6] J. M. Soler, E. Artacho, J. D. Gale, A. Garcia, J. Junquera, P. Ordejon, and D. Sanchez-Portal. The siesta method for ab initio order-n materials simulation. *Journal of Physics-Condensed Matter*, 14(11):2745–2779, 2002.
- [7] H. Yoshida, I Katsuhiko, and N. Sato. X-ray diffraction reciprocal space mapping study of the thin film phase of pentacene. *Applied Physics Letters*, 90:181930, 2007.
- [8] C. K. Chiang, C. R. Fincher, Y. W. Park, A. J. Heeger, H. Shirakawa, E. J. Louis, S. C. Gau, and A. G. Macdiarmid. Electrical-conductivity in doped polyacetylene. *Physical Review Letters*, 39(17):1098–1101, 1977.
- [9] H. Shirakawa, E. J. Louis, A. G. Macdiarmid, C. K. Chiang, and A. J. Heeger. Synthesis of electrically conducting organic polymers - halogen derivatives of polyacetylene, (ch)x. *Journal of the Chemical Society-Chemical Communications*, (16):578–580, 1977.
- [10] A. Tsumura, H. Koezuka, and T. Ando. Macromolecular electronic device - field-effect transistor with a polythiophene thin-film. *Applied Physics Letters*, 49(18):1210–1212, 1986.

- [11] H. Klauk, M. Halik, U. Zschieschang, G. Schmid, W. Radlik, and W. Weber. High-mobility polymer gate dielectric pentacene thin film transistors. *Journal Of Applied Physics*, 92(9):5259–5263, 2002.
- [12] A. Troisi and G. Orlandi. Charge-transport regime of crystalline organic semiconductors: Diffusion limited by thermal off-diagonal electronic disorder. *Physical Review Letters*, 96(8):4, 2006.
- [13] J. Cornil, J. P. Calbert, and J. L. Bredas. Electronic structure of the pentacene single crystal: Relation to transport properties. *Journal Of The American Chemical Society*, 123(6):1250–1251, 2001.
- [14] J. Cornil, D. Beljonne, J. P. Calbert, and J. L. Bredas. Interchain interactions in organic pi-conjugated materials: Impact on electronic structure, optical response, and charge transport. *Advanced Materials*, 13(14):1053–1067, 2001.
- [15] Swensberg C.E. Pope M. *Electronic processes in organic crystals and polymers*, volume 2 ed. Oxford University Press, 1999.
- [16] A. F. Hebard, M. J. Rosseinsky, R. C. Haddon, D. W. Murphy, S. H. Glarum, T. T. M. Palstra, A. P. Ramirez, and A. R. Kortan. Superconductivity at 18-k in potassium-doped c-60. *Nature*, 350(6319):600–601, 1991.
- [17] A. R. Brown, A. Pomp, D. M. deLeeuw, D. B. M. Klaassen, E. E. Havinga, P. Herwig, and K. Mullen. Precursor route pentacene metal-insulator-semiconductor field-effect transistors. *Journal Of Applied Physics*, 79(4):2136–2138, 1996.
- [18] A. J. Salih, S. P. Lau, J. M. Marshall, J. M. Maud, W. R. Bowen, N. Hilal, R. W. Lovitt, and P. M. Williams. Improved thin films of pentacene via pulsed laser deposition at elevated substrate temperatures. *Applied Physics Letters*, 69(15):2231–2233, 1996.
- [19] W. A. Schoonveld, J. Vrijmoeth, and T. M. Klapwijk. Intrinsic charge transport properties of an organic single crystal determined using a multiterminal thin-film transistor. *Applied Physics Letters*, 73(26):3884–3886, 1998.
- [20] G. B. Blanchet, C. R. Fincher, and I. Malajovich. Laser evaporation and the production of pentacene films. *Journal of Applied Physics*, 94(9):6181–6184, 2003.
- [21] S. F. Nelson, Y. Y. Lin, D. J. Gundlach, and T. N. Jackson. Temperature-independent transport in high-mobility pentacene transistors. *Applied Physics Letters*, 72(15):1854–1856, 1998.
- [22] A. Gavezzotti and G. R. Desiraju. A systematic analysis of packing energies and other packing parameters for fused-ring aromatic-hydrocarbons. *Acta Crystallographica Section B-Structural Science*, 44:427–434, 1988.



- [23] G. R. Desiraju and A. Gavezzotti. Crystal-structures of polynuclear aromatic-hydrocarbons - classification, rationalization and prediction from molecular-structure. *Acta Crystallographica Section B-Structural Science*, 45:473–482, 1989.
- [24] Y. Y. Lin, D. J. Gundlach, S. F. Nelson, and T. N. Jackson. Stacked pentacene layer organic thin-film transistors with improved characteristics. *Ieee Electron Device Letters*, 18(12):606–608, 1997.
- [25] R. B. Campbell, J. Trotter, and J. M. Robertson. Crystal and molecular structure of pentacene. *Acta Crystallographica*, 14(7):705–&, 1961.
- [26] R. B. Campbell, J. Trotter, and Monteath.J. Crystal structure of hexacene, and a revision of crystallographic data for tetracene and pentacene. *Acta Crystallographica*, 15(3):289–&, 1962.
- [27] T. Minakata, I. Nagoya, and M. Ozaki. Highly ordered and conducting thin-film of pentacene doped with iodine vapor. *Journal Of Applied Physics*, 69(10):7354–7356, 1991.
- [28] T. Minakata, M. Ozaki, and H. Imai. Conducting thin-films of pentacene doped with alkaline-metals. *Journal Of Applied Physics*, 74(2):1079–1082, 1993.
- [29] C. D. Dimitrakopoulos, A. R. Brown, and A. Pomp. Molecular beam deposited thin films of pentacene for organic field effect transistor applications. *Journal Of Applied Physics*, 80(4):2501–2508, 1996.
- [30] D. Holmes, S. Kumaraswamy, A. J. Matzger, and K. P. C. Vollhardt. On the nature of nonplanarity in the [n]phenylenes. *Chemistry-A European Journal*, 5(11):3399–3412, 1999.
- [31] C. C. Mattheus, A. B. Dros, J. Baas, A. Meetsma, J. L. de Boer, and T. T. M. Palstra. Polymorphism in pentacene. *Acta Crystallographica Section C-Crystal Structure Communications*, 57:939–941, 2001.
- [32] R. Ruiz, A. C. Mayer, G. G. Malliaras, B. Nickel, G. Scoles, A. Kazimirov, H. Kim, R. L. Headrick, and Z. Islam. Structure of pentacene thin films. *Applied Physics Letters*, 85(21):4926–4928, 2004.
- [33] S. E. Fritz, S. M. Martin, C. D. Frisbie, M. D. Ward, and M. F. Toney. Structural characterization of a pentacene monolayer on an amorphous sio2 substrate with grazing incidence x-ray diffraction. *Journal Of The American Chemical Society*, 126(13):4084–4085, 2004.
- [34] H. C. Yang, T. J. Shin, M. M. Ling, K. Cho, C. Y. Ryu, and Z. N. Bao. Conducting afm and 2d gixd studies on pentacene thin films. *Journal Of The American Chemical Society*, 127(33):11542–11543, 2005.

- [35] L. F. Drummy and D. C. Martin. Thickness-driven orthorhombic to triclinic phase transformation in pentacene thin films. *Advanced Materials*, 17(7):903–+, 2005.
- [36] A. Facchetti, M. H. Yoon, and T. J. Marks. Gate dielectrics for organic field-effect transistors: New opportunities for organic electronics. *Advanced Materials*, 17(14):1705–1725, 2005.
- [37] J. Collet, O. Tharaud, A. Chapoton, and D. Vuillaume. Low-voltage, 30 nm channel length, organic transistors with a self-assembled monolayer as gate insulating films. *Applied Physics Letters*, 76(14):1941–1943, 2000.
- [38] M. Halik, H. Klauk, U. Zschieschang, G. Schmid, C. Dehm, M. Schutz, S. Maisch, F. Effenberger, M. Brunnbauer, and F. Stellacci. Low-voltage organic transistors with an amorphous molecular gate dielectric. *Nature*, 431(7011):963–966, 2004.
- [39] M. H. Yoon, A. Facchetti, and T. J. Marks. sigma-pi molecular dielectric multilayers for low-voltage organic thin-film transistors. *Proceedings Of The National Academy Of Sciences Of The United States Of America*, 102(13):4678–4682, 2005.
- [40] Y. D. Park, D. H. Kim, Y. Jang, M. Hwang, J. A. Lim, and K. Cho. Low-voltage polymer thin-film transistors with a self-assembled monolayer as the gate dielectric. *Applied Physics Letters*, 87(24):3, 2005.
- [41] A. Dodabalapur, H. E. Katz, L. Torsi, and R. C. Haddon. Organic heterostructure field-effect transistors. *Science*, 269(5230):1560–1562, 1995.
- [42] W. Kern and D. A. Puotinen. Cleaning solutions based on hydrogen peroxide for use in silicon semiconductor technology. *Rca Review*, 31(2):187–&, 1970.
- [43] D. W. Schubert and T. Dunkel. Spin coating from a molecular point of view: its concentration regimes, influence of molar mass and distribution. *Materials Research Innovations*, 7(5):314–321, 2003.
- [44] T. Minakata, H. Imai, and M. Ozaki. Electrical-properties of highly ordered and amorphous thin-films of pentacene doped with iodine. *Journal Of Applied Physics*, 72(9):4178–4182, 1992.
- [45] M. Shtein, J. Mapel, J. B. Benziger, and S. R. Forrest. Effects of film morphology and gate dielectric surface preparation on the electrical characteristics of organic-vapor-phase-deposited pentacene thin-film transistors. *Applied Physics Letters*, 81(2):268–270, 2002.
- [46] X. D. Xiao, G. Y. Liu, D. H. Charych, and M. Salmeron. Preparation, structure, and mechanical stability of alkylsilane monolayers on mica. *Langmuir*, 11(5):1600–1604, 1995.

- [47] J. B. Brzoska, I. Benazouz, and F. Rondelez. Silanization of solid substrates - a step toward reproducibility. *Langmuir*, 10(11):4367–4373, 1994.
- [48] Christoph Strobl. *Mikro- und Nanofluidik auf piezoelektrischen Substraten*. Phd thesis, Ludwig-Maximilians-Universität München, 2005.
- [49] M. B. Hochrein, C. Reich, B. Krause, J. O. Radler, and B. Nickel. Structure and mobility of lipid membranes on a thermoplastic substrate. *Langmuir*, 22(2):538–545, 2006.
- [50] C. Jung, A. Maliakal, A. Sidorenko, and T. Siegrist. Pentacene-based thin film transistors with titanium oxide-polystyrene/polystyrene insulator blends: High mobility on high k dielectric films. *Applied Physics Letters*, 90(6):3, 2007.
- [51] G. Binnig, C. F. Quate, and C. Gerber. Atomic force microscope. *Physical Review Letters*, 56(9):930–933, 1986.
- [52] L. G. Parratt. Surface studies of solids by total reflection of x-rays. *Physical Review*, 95(2):359–369, 1954.
- [53] T. W. Kelley, P. F. Baude, C. Gerlach, D. E. Ender, D. Muyres, M. A. Haase, D. E. Vogel, and S. D. Theiss. Recent progress in organic electronics: Materials, devices, and processes. *Chemistry Of Materials*, 16(23):4413–4422, 2004.
- [54] S. R. Forrest. Ultrathin organic films grown by organic molecular beam deposition and related techniques. *Chemical Reviews*, 97(6):1793–1896, 1997.
- [55] M. Shtein, P. Peumans, J. B. Benziger, and S. R. Forrest. Micropatterning of small molecular weight organic semiconductor thin films using organic vapor phase deposition. *Journal of Applied Physics*, 93(7):4005–4016, 2003.
- [56] K. H. Probst and N. Karl. Energy-levels of electron and hole traps in band-gap of doped anthracene-crystals. *Physica Status Solidi a-Applied Research*, 27(2):499–508, 1975.
- [57] L. B. Roberson, J. Kowalik, L. M. Tolbert, C. Kloc, R. Zeis, X. L. Chi, R. Fleming, and C. Wilkins. Pentacene disproportionation during sublimation for field-effect transistors. *Journal of the American Chemical Society*, 127(9):3069–3075, 2005.
- [58] A. V. Dzyabchenko, V. E. Zavodnik, and V. K. Belsky. 6,13-pentacenequinone - molecular packing analysis. *Acta Crystallographica Section B-Structural Science*, 35(SEP):2250–2253, 1979.
- [59] O. D. Jurchescu, J. Baas, and T. T. M. Palstra. Effect of impurities on the mobility of single crystal pentacene. *Applied Physics Letters*, 84(16):3061–3063, 2004.

- [60] R. Ruiz, D. Choudhary, B. Nickel, T. Toccoli, K. C. Chang, A. C. Mayer, P. Clancy, J. M. Blakely, R. L. Headrick, S. Iannotta, and G. G. Malliaras. Pentacene thin film growth. *Chemistry Of Materials*, 16(23):4497–4508, 2004.
- [61] S. Pratontep, M. Brinkmann, F. Nuesch, and L. Zuppiroli. Nucleation and growth of ultrathin pentacene films on silicon dioxide: effect of deposition rate and substrate temperature. *Synthetic Metals*, 146(3):387–391, 2004.
- [62] D. Knipp, R. A. Street, A. Volkel, and J. Ho. Pentacene thin film transistors on inorganic dielectrics: Morphology, structural properties, and electronic transport. *Journal of Applied Physics*, 93(1):347–355, 2003.
- [63] D. Knipp, R. A. Street, and A. R. Volkel. Morphology and electronic transport of polycrystalline pentacene thin-film transistors. *Applied Physics Letters*, 82(22):3907–3909, 2003.
- [64] B.E. Warren. *X-ray diffraction*. Dover Publications, Inc., New York, 1990.
- [65] E. Prince. *International Tables for Crystallography Vol. C*. Springer, 2004.
- [66] D. M. Smilgies. Geometry-independent intensity correction factors for grazing-incidence diffraction. *Review of Scientific Instruments*, 73(4):1706–1710, 2002.
- [67] I. K. Robinson and D. J. Tweet. Surface x-ray-diffraction. *Reports on Progress in Physics*, 55(5):599–651, 1992.
- [68] A. Savitzky and M. J. E. Golay. Smoothing and differentiation of data by simplified least squares procedures. *Analytical Chemistry*, 36(8):1627–&, 1964.
- [69] S. R. Forrest. The path to ubiquitous and low-cost organic electronic appliances on plastic. *Nature*, 428(6986):911–918, 2004.
- [70] W. Warta, R. Stehle, and N. Karl. Ultrapure, high mobility organic photoconductors. *Applied Physics a-Materials Science & Processing*, 36(3):163–170, 1985.
- [71] P. G. Lecomber and W. E. Spear. Electronic transport in amorphous silicon films. *Physical Review Letters*, 25(8):509–&, 1970.
- [72] G. Horowitz, R. Hajlaoui, and P. Delannoy. Temperature-dependence of the field-effect mobility of sexithiophene - determination of the density of traps. *Journal De Physique Iii*, 5(4):355–371, 1995.
- [73] N. Koch, A. Vollmer, I. Salzmann, B. Nickel, H. Weiss, and J. P. Rabe. Evidence for temperature-dependent electron band dispersion in pentacene. *Physical Review Letters*, 96(15):4, 2006.

- 
- [74] H. Kakuta, T. Hirahara, Matsuda I., Nagao T., Hasegawa S., Ueno N., and Sakamoto K. Electronic structure of the highest occupied molecular orbital bands of a pentacene ultrathin film. *Physical Review Letters*, 98(24), 2007.
- [75] B. Nickel, R. Barabash, R. Ruiz, N. Koch, A. Kahn, L. C. Feldman, R. F. Haglund, and G. Scoles. Dislocation arrangements in pentacene thin films. *Physical Review B*, 70(12), 2004.
- [76] K. Hannewald, V. M. Stojanovic, J. M. T. Schellekens, P. A. Bobbert, G. Kresse, and J. Hafner. Theory of polaron bandwidth narrowing in organic molecular crystals. *Physical Review B*, 69(7):7, 2004.



# List of Figures

1.1	a) Passive polymer RFID tag (Source: PolyIC). b) Four generations of lighting technologies: incandescent light bulb, fluorescent, compact fluorescent and the new Organic Light Emitting Diode in different colors (Source: Philips). c) Flexible Display (Source: Universal Display Corporation). d) Electronic paper device (Source: Philips). . . . .	4
1.2	Lewis structure of a) polyacetylene b) pentacene and c) C60. . . . .	5
1.3	3D Atomic force microscopy (AFM) micrograph of a 480 Å pentacene thin film on a Topas substrate. Edge length is 5 μm. The crystalline areas (grains) with a diameter of ~ 2 μm are clearly visible. Terrace height corresponds to a pentacene monolayer with a $d_{(00l)}$ spacing of 15.4 Å. The crystal grains are forming a typical fiber structure. The fiber axes are parallel to the substrate surface normal. Also clearly visible is the surface roughness, that characteristically shapes the whole thin film. . . . .	7
1.4	The four crystal packings observed for (almost) planar aromatic hydrocarbon crystals. a) Classical herringbone structure (Naphthalene) b) Sandwich herringbone (Pyrene) c) $\gamma$ -structure (Benzopyrene) d) $\beta$ -structure (Violanthrene). . . . .	8
1.5	Equipment built during this thesis: a) In-house 4-circle X-ray diffractometer. b) Mobile ultra high vacuum growth chamber. c) Mobile ultra high vacuum growth chamber mounted on W1 diffractometer at HASYLab, Hamburg. d) Reconstructed molecular beam deposition chamber. . . . .	10
1.6	Screenshots of versatile software packages, that have been developed throughout this thesis. (a) Manual mode of thin film deposition software (TFDS) developed for the portable vacuum growth chamber (PGC) coded with NI LabView 6. (b) Software developed to solve the crystal structure of fiber structured organic thin films by X-ray diffraction. . . . .	12
2.1	Illustration of the layered structure used in OTFTs. The structure consists of the silicon substrate, gate dielectric layer and the pentacene thin film layer. The insulating gate dielectric materials can be divided into three main categories: inorganic, self-assembled mono and multilayers (SAMs) and polymers. . . . .	14

2.2	Spin coating a dissolved polymer on a substrate is a three step process a) Dispense: defines initial amount of solution b) Ramp-up (accelerating $\omega$ ): spreads the solution c) Constant $\omega$ : dry spin coated thin film. . . . .	16
2.3	Structure of octadecyltrichlorosilane (OTS). . . . .	17
2.4	Self assembled monolayer of OTS on $a - SiO_2$ substrate. . . . .	17
2.5	Chemical structure of Topas, purchased from Ticona, Germany. . . . .	18
2.6	Chemical structure of the aromatic polymer polystyrene. . . . .	18
2.7	AFM contact mode. . . . .	20
2.8	AFM tapping mode. . . . .	20
2.9	Fresnel X-ray reflectivity of a bare substrate with a surface roughness of 5 Å. . . . .	22
2.10	X-ray reflectivity of a flat surface covered with a surface layer of $d=100$ Å thickness and an interface roughness of 5 Å. . . . .	23
2.11	Schematic drawing of the in-house 4-circle X-ray setup. The diffractometer is employed for reflectivity studies from surfaces and thin films (figure by C. Reich). . . . .	24
2.12	3D AFM micrographs of wafers before (a) and after (b) the growth of 200 nm of $a - SiO_2$ in our RTP oven. (note that the z-axis scaling is different from the x- and y-axis scaling). . . . .	25
2.13	X-ray reflectivity (W1). Silicon wafer with an initially 7.5 Å native $a - SiO_2$ layer, after the growth of 200 nm $a - SiO_2$ in the RTP oven and for comparison a commercially purchased wafer with a 400 nm $a - SiO_2$ layer. Data fits are illustrated by solid lines. . . . .	26
2.14	3D AFM micrograph of an OTS treated $a - SiO_2$ wafer. The needle like surface is clearly visible, which suggests, that the surface is not fully covered with an OTS monolayer. (note that the z-axis scaling is different from the x- and y-axis scaling). . . . .	27
2.15	(a) X-ray reflectivity (W1). OTS treated $a - SiO_2$ sample (circles). The data fit (solid line) revealed an OTS monolayer of $d = 21.8$ Å and a surface roughness of 8.2 Å. . . . .	27
2.16	X-ray reflectivity measurements (in-house). Topas films coated on $a - SiO_2$ wafers with concentrations of Topas dissolved in toluene as indicated. The thickness can be tuned almost linearly within a concentration range of 5.00 % down to 0.25 %. Concentrations $> 5$ % were beyond the resolution of the in-house 4-circle X-ray setup. . . . .	28
2.17	X-ray reflectivity measurements (in-house). Topas film before (black line) and after the treatment of 10min on a hotplate with $T=110^\circ C$ (red line). The periodicity of the Kiessig fringes indicates that the Topas layer thickness is not affected by heating up to $110^\circ C$ . . . . .	29
2.18	3D AFM micrograph of a Topas film spin coated on a silicon wafer. The polymer film has surface roughness of $R_q = 2.0$ Å measured by AFM. (note that the z-axis scaling is different from the x- and y-axis scaling). . . . .	30



2.19	X-ray reflectivity (W1). Spin coated Topas film with a concentration of $c = 0.25\%$ dissolved in toluene after one minute of annealing at a temperature of $T = 80^\circ\text{C}$ . The data fit (solid line) revealed a film thickness of $d = 78.9\text{\AA}$ and a surface roughness of $2.5\text{\AA}$ . . . . .	30
2.20	3D AFM micrograph of a polystyrene film spin coated on a $a - \text{SiO}_2$ wafer. The polymer film has a surface roughness of $R_q = 3.4\text{\AA}$ measured by AFM. (note that the z-axis scaling is different from the x- and y-axis scaling). . .	31
2.21	X-ray reflectivity (W1). Polystyrene film spin coated on a commercially purchased $a - \text{SiO}_2$ wafer with a concentration of $0.10\text{ weight } \%$ dissolved in toluene after one minute of annealing at a temperature of $T = 80^\circ\text{C}$ . The data fit (solid line) revealed a film thickness of $d = 63.6\text{\AA}$ and a surface roughness of $5.1\text{\AA}$ . . . . .	31
2.22	Sketch of the setup used for temperature gradient sublimation. . . . .	34
2.23	Lewis structure of 6,13-pentacenequinone. When pentacene is exposed to light and oxygen, it oxidizes to 6,13-pentacenequinone. . . . .	34
2.24	(a) Custom-made, portable vacuum growth chamber (PGC). (b) Rack of electric equipment used to operate the PGC. . . . .	35
2.25	Sketch of the evaporation source. A tantalum bag is produced by spot-welding a tantalum foil and is filled with the previously purified organic semiconducting material. The bag is heated by an electric current and the organic material evaporates and streams out of the loophole producing a point-source organic molecular beam. . . . .	35
2.26	Custom-made rotatable sample holder. (a) Mounted with four samples. Each sample is heated using a 20W halogen light bulb. The temperature of the substrate surface is measured by a thermo couple. (b) Mounted with shadow masks for growing organic thin films on TFT structures. . . . .	36
2.27	Electric wiring of the PGC setup. The setup consists of two major proportional-integral-derivative (PID) control loop feedback circuits indicated in red and green. . . . .	37
2.28	TFDS configuration: (a) Configuration of deposition material (left) and substrate material (right). (b) Macro script editor to enter commands for the deposition process, that are executed one after an other in macro-mode. . . . .	38
2.29	Screenshot of temper GUI. The temper command allows controlled predeposition treatments, such as annealing. It displays pressure, temperature and used heating power over time. . . . .	40
2.30	Screenshot of ramp GUI. The ramp command allows the deposition rate at the beam shutter to be set to a specific value and to become stable before the thin film deposition. . . . .	41
2.31	Screenshot of deposit GUI. The deposition command is responsible for the actual thin film deposition process and allows the user to set deposition rate at the substrate surface, thin film thickness and/or deposition time. . . . .	42

2.32	Screenshot of the manual mode. All parameters like pressure, temperature, electric power of the substrate heating, film-thickness, deposition rate and electric power of the evaporation source are displayed over time. The control buttons are located on the left of each diagram, that allow the user to experiment with deposition parameters. . . . .	43
2.33	Effect of growth temperature and deposition rate on average grain size and polymorph of the resulting pentacene thin film grown on $a - SiO_2$ with surface roughness of 6 Å (figure from [1]). The red dot indicates the parameters used to grow pentacene thin films in this thesis. . . . .	45
2.34	Schematic illustration of the growth of the different pentacene polymorphs on $a - SiO_2$ . . . . .	45
2.35	AFM micrograph of a 240 Å pentacene thin film deposited on (a) custom-made $a - SiO_2$ and (b) commercially purchased $a - SiO_2$ . . . . .	46
2.36	3D AFM micrographs of a 480 Å pentacene thin film deposited at $T=30^\circ C$ on different gate dielectric substrates: (a) $a - SiO_2$ (b) OTS treated $a - SiO_2$ (c) Topas (d) Polystyrene. The terraces correspond to a pentacene monolayer with a $d_{(001)}$ spacing of 15.4 Å. (note, that (d) is only a $3 \times 3 \mu m$ section, resulting in optical smaller grains when compared to $5 \times 5 \mu m$ sections). . .	48
3.1	(a) Schematic representation of the unit cell, illustrating the unit cell vectors $\vec{a}$ , $\vec{b}$ and $\vec{c}$ and their respective angles $\alpha$ , $\beta$ and $\gamma$ . (b) Schematic representation of $d_{001}$ . . . . .	50
3.2	Illustration of crystallographic planes with their corresponding Miller indices notation (1 1 1) and (0 1 0). . . . .	50
3.3	Vector representation of Bragg's Law. . . . .	52
3.4	Simulated Bragg peak positions and their corresponding Miller indices found using equations 3.14 and 3.15. As $\gamma = 90^\circ$ , Bragg peaks with equal modulus of $h$ and $k$ share the same $q_{  }$ (marked by orange boxes). Bragg peaks with $h = 0$ or $k = 0$ always share the same $q_{  }$ independent of $\gamma$ (marked by red boxes). For Bragg peaks with $h = k = 0$ , $q_{  } = 0$ (marked by green boxes). These peaks are observed in X-ray reflectivity measurements. . . . .	54
3.5	Simulated Bragg peak positions and their corresponding Miller indices found using equations 3.14 and 3.15 and $\gamma = 85^\circ$ . Bragg peaks with equal modulus of $h$ and $k$ (marked by orange boxes) now split up in $q_{  }$ by $\pm 2hkba \cdot \cos \gamma$ when compared to $\gamma = 90^\circ$ (figure 3.4), while the other Bragg peaks do not split up in $q_{  }$ . . . . .	55
3.6	X-ray absorption edges of the elements. . . . .	58
3.7	3D AFM micrograph of a pentacene crystal grain grown on a Topas. The graph on the left shows a height profile along a pyramid plane marked in blue. The steps of the pyramid terraces have a height of $\sim 1.5 nm$ which corresponds to the length of a pentacene molecule. . . . .	59

3.8	Simulation of the intensity $I(\vec{q})$ along a (11 <i>l</i> ) Bragg peak series with surface roughness $\sigma = 0.05$ (blue line) and $N_c = 30$ . The structure factor is plotted in red and masks the intensity $I(\vec{q})$ . . . . .	60
3.9	Simulation of the intensity $I(\vec{q})$ along a (11 <i>l</i> ) Bragg peak series with different surface roughness $\sigma$ and $N_c = 30$ . . . . .	61
3.10	Illustration of planes defined by Miller indices in the unit cell. The red plane (1,-1,0) is parallel to the blue (-1,1,0) plane. The crystal directions are oriented in opposite directions, which also applies for the parallel planes (1,1,0) in yellow and (-1,-1,0) in green. . . . .	62
3.11	Simulation of the individual intensity contributions of the fiber structure and their sum $I(\vec{q})$ of a pentacene thin film using equation 3.28 along the ( $ 1   1  l$ ) direction. ( $\sigma = 0.3, U_{iso} = 0.05$ ). . . . .	64
3.12	Refraction of the incoming wavevector $\vec{k}_i$ at the air/vacuum - pentacene thin film interface. . . . .	64
3.13	Photon flux of the DORIS W1 wiggler. The experiments were carried out at an energy of 10500 eV, where the photon flux reaches a maximum of $2 \cdot 10^{15} \text{ photons/s} \cdot \text{mrad}^2 \cdot 0.1\%$ bandwidth (figure by P. Gurtler, HASYLab). . . . .	66
3.14	Sketch of W1 beamline (sketch from HASYLab homepage). . . . .	66
3.15	PGC mounted on W1 diffractometer. . . . .	67
3.16	Setup of W1 diffractometer at HASYLab W1 beamline, Hamburg and motor names as used in calculations. . . . .	68
3.17	Momentum transfer during an X-ray reflectivity measurement. . . . .	70
3.18	Sketch of a GIXD geometry. . . . .	71
3.19	Sketch of the GI-CTR geometry using spherical coordinates. . . . .	73
3.20	Evolution of the detector position when traveling in $q_{\perp}$ along a given rod for different fixed $q_{\parallel}$ values according to equations 3.37 ( $\delta, \gamma$ ) as red lines and 3.38 (FTR, TT) as blue lines. $\alpha_i$ is fixed at $0.15^\circ$ . . . . .	74
3.21	Evolution of the Polarization factor $P$ plotted vs. the detector angle $\gamma$ during a GI-CTR measurement. The detector position ( $\delta, \gamma$ ) was simulated as illustrated in figure 3.20 for $\delta' = 15^\circ, \gamma = [0^\circ, 40^\circ]$ and $\alpha_i$ fixed at $0.15^\circ$ . . . . .	75
3.22	Evolution of the Lorentz factor $L$ plotted vs. the detector angle $\gamma$ during a GI-CTR measurement. The detector position ( $\delta, \gamma$ ) was simulated as illustrated in figure 3.20 for $\delta' = 15^\circ, \gamma = [0^\circ, 40^\circ]$ and $\alpha_i$ fixed at $0.15^\circ$ . . . . .	76
3.23	(a) Evolution of the active area $A$ during a GI-CTR measurement. The substrate area illuminated by the incident beam is red. The area, that the detector “sees” is blue. The intersection of the two rectangles is green. The detector position ( $\delta, \gamma$ ) was simulated as illustrated in figure 3.20 for $\delta' = 15^\circ$ and $\gamma = [14^\circ, 40^\circ]$ . $\alpha_i$ is fixed at $0.15^\circ$ . (b) Plot of the active area vs. $\gamma$ (as simulated on the left) during a GI-CTR measurement. . . . .	77

3.24	Evolution of the L-, P-, A- and R-factor plotted vs. the detector angle $\gamma$ during a GI-CTR measurement. The detector position $(\delta, \gamma)$ was simulated as illustrated in figure 3.20 for $\delta' = 15^\circ$ , $\gamma = [0^\circ, 40^\circ]$ and $\alpha_i$ fixed at $0.15^\circ$ . The solid line represents the product of L, P, A, and R factors. Note: For better visualization, the A factor was multiplied by 0.1 and the LPAR factor by 0.02. . . . .	79
3.25	Schematic drawing of the X-ray setup for GIXD and GI-CTR measurements using an image plate to record the Bragg peaks. . . . .	79
3.26	2D image plate scan of a 480 Å pentacene thin film and simulated Bragg peak pattern (shifted to the right). (a) Zoom of the $(\pm 1, \pm 1, 1)$ rod indicating a left shifted Bragg peak. (b) Zoom of $(\pm 1, \pm 2, 1)$ rod indicating a right shifted Bragg peak. (c) The yellow boxes mark the area scanned by a GI-CTR measurement. The left shifted box marks the area, where the background scan of the $(0, \pm 2, 1)$ rod was performed. . . . .	81
3.27	3D visualization of a image plate scan of 480 Å pentacene thin film. The green line indicates a profile scan, which is inset in the top left. The lines left and right of the Bragg peaks series mark the relevant area scanned during a GI-CTR measurement. . . . .	82
3.28	Screenshot of the (a) X-ray diffraction simulation module and the (b) Bragg peak position fit module using the curve fitting tool from the curve fitting toolbox by Mathworks. . . . .	84
3.29	Screenshot of the unit-cell solver module. . . . .	85
3.30	Flowchart of the algorithm to fit data in FiberRod. . . . .	86
3.31	Screenshot of the molecular orientation solver module. . . . .	87
3.32	(a) Side view and (b) top view of a pentacene unit-cell arranged in a herringbone structure. The long molecular axis (LMA) is illustrated as a red dotted line. The herringbone angle between the two molecule planes is illustrated in green. . . . .	89
3.33	Schematic illustration of the automatic assignment of Miller indices to a measured data point. The green dotted line illustrates the path of a GI-CTR measurement. The blue dots represent the centers of the Bragg peaks. Data points within the red ellipses, illustrating the “catch area”, are assigned the Miller indices of the respective Bragg peak. . . . .	90
3.34	Screenshot of the crystal structure visualizer and the crystal structure export module. . . . .	91
3.35	Plot of the GI-CTR fit results after clicking the “Plot & Sim TR” button. . . . .	92
4.1	X-ray reflectivity measurement of a 480 Å pentacene thin film on $a - SiO_2$ gate dielectric. . . . .	94
4.2	GIXD measurement of a 480 Å pentacene thin film on $a - SiO_2$ gate dielectric. . . . .	94
4.3	GI-CTR measurements and best fit plots of a 480 Å pentacene thin film on $a - SiO_2$ gate dielectric. . . . .	96

4.4	Impact of the herringbone angle $\theta_{hr gb}$ on the (a) $(0, \pm 2)$ and (b) $(\pm 2, \pm 1)$ rods. Impact of the tilt angle (c) $\theta_{AY}$ on the $(\pm 1, \pm 2)$ and (d) $\theta_{BY}$ on the $(\pm 1, \pm 1)$ rod. (e) Impact of the tilt angle $\theta_{AZ}$ on the $(\pm 1, \pm 1)$ and (f) $\theta_{BZ}$ on the $(\pm 1, \pm 2)$ rod. . . . .	97
4.5	X-ray reflectivity measurement of a 480 Å pentacene thin film on OTS gate dielectric. . . . .	98
4.6	GIXD measurement of a 480 Å pentacene thin film on OTS gate dielectric.	99
4.7	GI-CTR measurements of a 480 Å pentacene thin film on OTS gate dielectric.	100
4.8	X-ray reflectivity measurement of a 480 Å pentacene thin film on Topas gate dielectric. . . . .	101
4.9	GIXD measurement of a 480 Å pentacene thin film on Topas gate dielectric.	102
4.10	GI-CTR measurements and best fit plots of a 480 Å pentacene thin film on Topas gate dielectric. . . . .	103
4.11	X-ray reflectivity measurement of a 480 Å pentacene thin film on polystyrene gate dielectric. . . . .	104
4.12	GIXD measurement of a 480 Å pentacene thin film on polystyrene gate dielectric. . . . .	104
4.13	GI-CTR measurements and best fit plots of a 480 Å pentacene thin film on polystyrene gate dielectric. . . . .	105
5.1	Comparison of the 3D crystal structure of the pentacene <i>thin-film</i> polymorph on $a-SiO_2$ and the pentacene single crystal phase. . . . .	109
5.2	(a) Electron and hole mobilities $\mu$ in the a-direction of a highly purified naphthalene crystal (open symbols and bold dots) as a function of temperature T from Time of flight measurements. For comparison, data obtained with less purified material (crosses), (figure taken from [2]). (b) Simulation of the charge carrier mobility $\mu$ as a function of temperature T using the multiple trapping and release (MTR) model for different trapping vs. conduction states $N_T/N_0$ (figure by J. Pflaum). . . . .	110
5.3	Simulation of the two highest occupied bands for the four pentacene polymorphs I-IV corresponding to a distance $d_{(001)}$ of 14.1 Å, 14.4 Å, 15.0 Å, and 15.4 Å by Troisi et al.[3]. The crystal structures of the 15.0 Å and 15.4 Å polymorphs used for the simulation are based on the predicted crystal structure taken from [4, 5]. . . . .	112
5.4	Simulation of the two highest occupied bands of the pentacene <i>thin-film</i> polymorph grown on $a-SiO_2$ by density functional theory using the software tool SIESTA[6] (by C. Erlen, TU-München). . . . .	113



# List of Tables

2.1	Comparison of surface roughnesses of $a - SiO_2$ wafers before and after the growth of a $a - SiO_2$ layer and commercially purchased $a - SiO_2$ wafers measured by AFM ( $R_q$ ) and X-ray reflectivity $\sigma$ . . . . .	25
2.2	Comparison of the surface roughness $R_q$ measured by AFM, $\sigma$ measured by X-ray reflectivity and layer thickness $d_{layer}$ , also measured by X-ray reflectivity. Topas has the lowest surface roughness, followed by custom-made $a - SiO_2$ , polystyrene and OTS. . . . .	32
2.3	Comparison of surface roughnesses and layer thickness of the gate dielectric substrates measured by AFM and X-ray reflectivity . Also given the average crystal grain diameter and the thin film roughness after the growth of a 480 Å pentacene thin film. Deposition rate was set to 1.7 nm/min for polystyrene and 0.5 nm/min for the other substrates. Substrate temperature was set to 30°C. . . . .	47
3.1	Cromer-Mann coefficients of carbon (C) and hydrogen (H). . . . .	56
4.1	Unit-cell parameters of the pentacene <i>thin-film</i> phase grown on $a - SiO_2$ . .	95
4.2	Molecular orientation parameters of the pentacene <i>thin-film</i> phase grown on $a - SiO_2$ . . . . .	95
4.3	Molecular orientation parameters of the pentacene <i>thin-film</i> phase grown on OTS. . . . .	99
4.4	Molecular orientation parameters of the pentacene <i>thin-film</i> phase grown on Topas. . . . .	101
4.5	Molecular orientation fit results of the pentacene <i>thin-film</i> phase on various gate dielectrics . . . . .	102
5.1	Comparison of unit-cell parameters for the pentacene <i>thin-film</i> phase reported in previous studies (unit cell parameters in italics are predicted values).	107
5.2	Fit results of the molecular orientation of the pentacene <i>thin-film</i> phase on various gate dielectrics compared to the theoretical calculations of Yoshida et.al.[7] . . . . .	108
B.1	Measured and simulated Bragg peak positions and assigned Miller indices observed in GIXD measurements of the pentacene <i>thin-film</i> phase. . . . .	125

- B.2 Measured and simulated Bragg peak positions and assigned Miller indices observed in GI-CTR measurements of the pentacene *thin-film* phase (part 1).126
- B.3 Measured and simulated Bragg peak positions and assigned Miller indices observed in GI-CTR measurements of the pentacene *thin-film* phase (part 2).127



# Vielen Dank...

**Joachim Rädler**, für die Möglichkeit die Doktorarbeit an seinem Lehrstuhl durchzuführen, sein entgegengebrachtes Vertrauen, die vielen Freiheiten, die er mir ließ und für die vielfältige Unterstützung die ich von ihm erhalten habe.

**Bert Nickel**, für die ausgezeichnete Betreuung dieser Doktorarbeit, unendlich viel Geduld und Zeit bei Erklärungen und Diskussionen und das exzellente Teamwork (auch beim Kickern am HASYLab :)).

**Prof. Wolfgang Schmahl**, für die großartige Hilfe bei der Erstellung der cif files, die Einführung in die Kristallographie Standards und die Bereitschaft als Experte diese Doktorarbeit zu beurteilen.

**LS Jörg Kotthaus und Mitarbeiter**, für die Mitnutzung des Reinraumes und für die vielfältige Unterstützung in Sachen Probenpräparation.

**Willi Fenzl**, für die sehr hilfreichen Diskussionen über Röntgenstreuung.

**Martin Huth**, für ein sehr gutes Teamwork, die super Zeit als Schreibtischnachbar und dass die Strahlzeiten am HASYLab alles andere als langweilig waren!

**Nok Tsao und Matthias Fiebig**, für die viele und gute Hilfe bei der Probenpräparation und bei Messungen.

**Alexander Dobrinevski**, für die große Hilfe bei der Implementierung in Matlab.

**Christoph Erlen**, für die vielen netten Diskussionen rund um Pentacene und die wertvollen Simulationen. (Expresso?).

**Jens Pflaum**, für die reibungslose Zusammenarbeit und die professionelle Aufreinigung

von Pentacene.

**Stefan Lochbrunner**, für angenehme Zusammenarbeit und interessante Diskussionen.

**Markus Tober**, für die großartige Hilfe bei der Implementierung in LabView.

**Simon Youssef**, für die vielen nützlichen Tipps und Diskussionen.

**Matthew Ware und Margaret Horton**, für das Korrekturlesen und für viele hilfreiche Kommentare.

**Margarete Meixner, Eva Natzer, Marie-Christine Blüm und Evelyn Morgenroth**, für Hilfe und Beistand bei organisatorischen und finanziellen Fragen.

**Gerlinde Schwake und Susi Kempter**, für den täglichen Kampf gegen das Chaos im Labor.

**Christian Neubert und der Mechanikwerkstatt**, für die sehr gute Arbeit und Unterstützung bei den vielen Mechanikkonstruktionen (“Bis wann brauchts’n des?”).

**Tobi Göpel, Lea Hoffmann, Markus Schäffeler, Maxl und Willy**, für Verständnis und Unterstützung.

**Dem gesamten Lehrstuhl Rädler** für die nette und entspannte Arbeitsatmosphäre (Kuchen?).

Der **DFG SP1121**, dem **Elitenetzwerk Bayern** und dem **IDK NanoBio Technology** und dem **CeNS** für finanzielle Unterstützung.

**Yvonne**, für sehr viel Liebe, Unterstützung und unendlich viel Geduld.

**Meine Eltern**, meiner **Schwester Silke** und meine **Freunde**, auf die ich mich immer verlassen konnte.

# Curriculum vitae

## Stefan Rudolf Schiefer

geboren am 11.10.1975 in Freilassing (Obb.)

### Hochschulausbildung

---

- 6/2003 - 10/2007 Promotion in Physik an der Ludwig Maximilians  
Universität München bei Prof. Rädler.
- 4/2002 - 10/2002 Diplomarbeit an der Stanford University, CA am Depart-  
ment of Chemical Engineering bei Prof. G.G. Fuller.  
Thema: "Rheology of glyocalix model systems"
- 1996 - 2002 Studium der allgemeinen Physik an der Technischen  
Universität München. Abschluss: "Dipl. Phys. Univ."

### Schulische Ausbildung

---

- 1986 - 1995 Karls gymnasium, Bad Reichenhall.  
Mathematisch-naturwissenschaftlicher Zweig.  
Abschluss: "Allgemeine Hochschulreife"

### Wehrdienst

---

- 7/1995 - 4/1996 Gebirgsjägerbataillon 231, Bad Reichenhall